Control of Propeller Cavitation in Operational Conditions

Control of Propeller Cavitation in Operational Conditions

Proefschrift

ter verkrijging van de graad van doctor
aan de Technische Universiteit Delft,
op gezag van de Rector Magnificus prof. dr. ir. J. T. Fokkema,
voorzitter van het College voor Promoties,
in het openbaar te verdedigen

op dinsdag 30 juni 2009 te 14.00 uur

door

Arthur VRIJDAG

maritiem ingenieur
geboren te Hellevoetsluis

Dit proefschrift is goedgekeurd door de promotoren:

Prof. ir. D. Stapersma
Prof. dr. ir. T. J. C. van Terwisga

Samenstelling promotiecommissie:

Rector Magnificus,	voorzitter
Prof. ir. D. Stapersma,	Technische Universiteit Delft, promotor
Prof. dr. ir. T. J. C. van Terwisga,	Technische Universiteit Delft, promotor
Prof. M. Atlar, BSc, MSc, PhD,	Newcastle University
Prof. Dr.-Ing. H. Rulfs,	Technische Universität Hamburg-Harburg
Prof. ir. J. Klein Woud,	Technische Universiteit Delft
Prof. ir. O. H. Bosgra,	Technische Universiteit Delft
Dr. ir. ing. H. T. Grimmelius,	Technische Universiteit Delft
Prof. ir. J. J. Hopman	Technische Universiteit Delft, reservelid

Published by:

VSSD
Leeghwaterstraat 42
2628 CA Delft
The Netherlands
Tel. +31152782124
Fax. +31152787585
E-mail: hlf@vssd.nl
internet: http://vssd.nl/hlf

ISBN 978-90-6562-202-0
NUR 969

Keywords: ship propulsion control, cavitation, controllable pitch propeller, signature management, validation, uncertainty analysis, operational conditions

©Arthur Vrijdag, 2009

All rights reserved. No part of this publication may be reproduced, stored in a retrieval system, or transmitted, in any form or by any means, electronic, mechanical, photocopying, recording or otherwise, without the prior written permission of the publisher.

Contents

1 **Introduction** **1**

1.1 Background and Relevance . . . 1

1.2 Literature Review . . . 3

1.3 Research Objectives . . . 4

1.4 Outline . . . 5

2 **The Simulation Model** **7**

2.1 Introduction . . . 7

2.2 Simulation Model Goals . . . 8

2.3 Propulsion Plant Description . . . 9

2.4 The Conceptual Propulsion Plant Model . . . 11

2.4.1 The Propeller Model . . . 13

2.4.2 The Diesel Engine Model . . . 16

2.4.3 The Ship Model . . . 20

2.4.4 The Propulsion Control System Model . . . 20

2.5 Mathematical Framework for the Conceptual Model . . . 22

3 **Model Verification** **25**

3.1 Introduction . . . 25

3.2 Verification of Static Operating Points . . . 26

3.3 Verification of Dynamic Behaviour . . . 30

3.4 Conclusions . . . 34

4 **Model Calibration** **35**

4.1 Introduction . . . 35

4.2 Model Calibration Procedure . . . 36

4.2.1 Calibration Experiment Description . . . 36

4.2.2 The Engine Submodel . . . 37

4.2.3 The Propeller Submodel . . . 41

4.2.4 The Ship Submodel 45
4.3 Final Total Model Calibration 45
4.4 Discussion 53

5 Model Validation 55
5.1 Introduction 55
5.2 Validation 56
5.2.1 Theory of Validation of Static Operating Points 57
5.2.2 Theory of Validation of Dynamic Behaviour 64
5.2.3 The Validation Experiment 69
5.2.4 Validation of Static Behaviour 73
5.2.5 Validation of Dynamic Behaviour 78
5.3 Conclusions 80

6 Prediction of Cavitation Inception 83
6.1 Introduction 83
6.2 Propeller Cavitation Inception 83
6.3 Requirements on Inception Prediction 86
6.4 Computational Cavitation Inception Prediction 86
6.4.1 Lifting Surface Methods 87
6.4.2 Panel Methods 90
6.4.3 Viscous Methods 95
6.5 Experimental Cavitation Inception Prediction Methods 97
6.5.1 Vortex Cavitation Inception 100
6.6 Assessment of Applicability 101
6.7 Conclusions and Recommendations 103

7 Controller Development 105
7.1 Introduction 105
7.2 General Controller Considerations 105
7.2.1 Conventional Ship Propulsion Control: Feedforward 106
7.2.2 Experimental Ship Propulsion Control: Noise Feedback 108
7.2.3 Combined Feedback and Feedforward 108
7.3 New Controller Concept 109
7.3.1 Control of Ship Speed 111

7.3.2 Control of Effective Angle of Attack: α_{eff} 111

7.4 Relation between α_{eff} and the Engine Diagram 123

7.5 Controller Implementation 123

7.5.1 Ship Speed Feedback Controller 124

7.5.2 Angle of Attack Feedback Controller 125

7.5.3 Overall Blockdiagram 125

7.6 PCS+ Parametric study 127

7.7 Possible Controller Extensions 128

7.7.1 Turning Circles 128

7.7.2 Pressure Variations 132

7.8 Conclusions 133

8 Experimental Setup **135**

8.1 Introduction 135

8.2 General Layout 135

8.3 The Control Computer System 137

8.4 The Sensor System 138

8.4.1 Engine Room Location 140

8.4.2 Aft Measurement Location 141

9 Measurement Analysis **145**

9.1 Introduction 145

9.2 Test Overview 145

9.3 Environmental Conditions 147

9.4 Measurement Analysis 147

9.4.1 The α-bucket Test 147

9.4.2 The Acceleration Test 150

9.4.3 The Deceleration Test 164

9.4.4 The Forced Over-and Underloading Test 177

9.4.5 The Seaway Test 181

9.4.6 The Turning Circle Test 189

9.5 Trial Conclusions and Recommendations 196

10 Alternative Use **199**

10.1 Introduction 199

10.2 Fuel Efficiency 200

10.2.1 Efficiency Definitions 200

10.2.2 Verification and Validation 202

10.2.3 Conclusions and Recommendations 203

10.3 Thermal Overloading 205

10.3.1 λ in Static Conditions 207

10.3.2 λ during Acceleration 208

10.3.3 Conclusions and Recommendation 208

10.4 Manoeuvring Behavior 209

10.4.1 PCS Modifications 210

10.4.2 Application of Manoeuvring Predictions 210

10.4.3 Conclusions and Recommendation 212

10.5 Life Cycle Applications 212

10.5.1 Design Phase 213

10.5.2 Engineering Phase and Component Acceptance Tests 213

10.5.3 Sea Trials 213

10.5.4 Pre- and Post Maintenance Performance Tests 214

10.5.5 Conclusions and Recommendation 214

11 Conclusions and Recommendations **215**

11.1 Modeling, Verification, Calibration and Validation 215

11.1.1 Conclusions 215

11.1.2 Recommendations 216

11.2 Cavitation Inception Predictions 217

11.3 Newly Developed Propulsion Controller 217

11.3.1 Conclusions 217

11.3.2 Recommendations 218

11.4 Full Scale Measurement Results 219

11.5 Alternative Use of the Simulation Model 220

A Engine Lookup Tables **223**

B Validation Data **227**

C Scaling of Vortex Cavitation Inception **231**

D Trial List **233**

E Seaway Test time traces **235**

References **246**

Nomenclature **247**

Acronyms **251**

Summary **253**

Samenvatting **255**

Acknowledgements **257**

Curriculum Vitae **259**

Chapter 1

Introduction

1.1 Background and Relevance

Because of the shift of naval operations towards shallow coastal waters and the associated increasing mine threat, underwater signature management is of growing importance for naval ships. At the same time the number of countries that operate submarines is growing, suggesting that navies should be prepared for possible increased torpedo threat.

Due to the resulting strict demands on inboard as well as outboard noise levels, increasing effort is being put into the investigation, monitoring and control of noise sources, such as vibrating machinery and cavitation of the propellers. For naval vessels, acoustic signature management serves multiple goals. First of all, the risk of being detected by acoustic sensors of the opponent (including acoustically triggered mines and torpedoes), is greatly dependent on the acoustic signature. Secondly the own acoustic detection range is decreased by self-noise, which increases the chance of *being* detected before *having* detected.

From full scale measurements it is known that off-design conditions have a considerable influence on cavitation performance of ships propellers, and thus on the ships acoustic signature. The effects of seastate and manoeuvring are for instance reported in Verkuyl and Van Terwisga (2000). Measurements onboard the oceanographic research vessel HNLMS Tydeman of the Royal Netherlands Navy, show that, compared to the calm water condition, the cavitation inception speed is reduced by as much as 75% in bow quartering waves, seastate 5. As can be seen in Fig 1.1, headwaves result in a decrease of 100%: no cavitation free range is left for this condition. The use of 20 degrees rudder in calm seas is reported to give a decrease of as much as 55%, as can be seen in Fig 1.2.

The introduction of the Controllable Pitch Propeller (CPP) offered the possibility to adjust propeller pitch in addition to shaft speed, which has great advantages with regards to manoeuvrability. A reversible coupling was not needed anymore, and low ship speeds could be sustained for long periods. These two aspects combined greatly simplified the manoeuvring of ships in constrained waters, such as for instance in port. *Despite the advantages, the possibilities of controllable pitch propellers are still not used to their full extent nowadays, as will be demonstrated in this thesis.*

In principle the CPP gives the operator the freedom to achieve the same ship speed with many combinations of shaft speed and propeller pitch. Low shaft speed and high pitch can

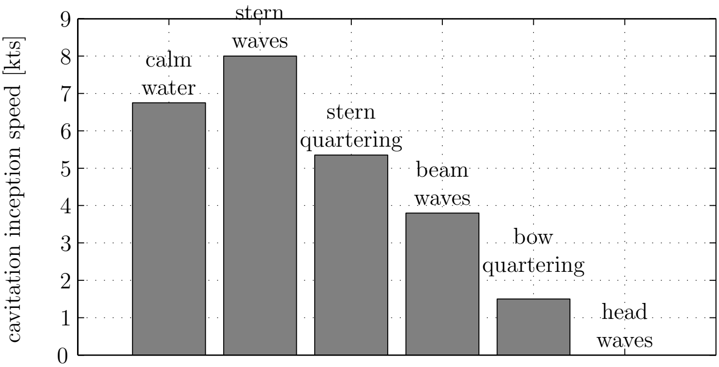

Figure 1.1: Effect of wave direction on Cavitation Inception Speed. Reproduced from Verkuyl and Van Terwisga (2000)

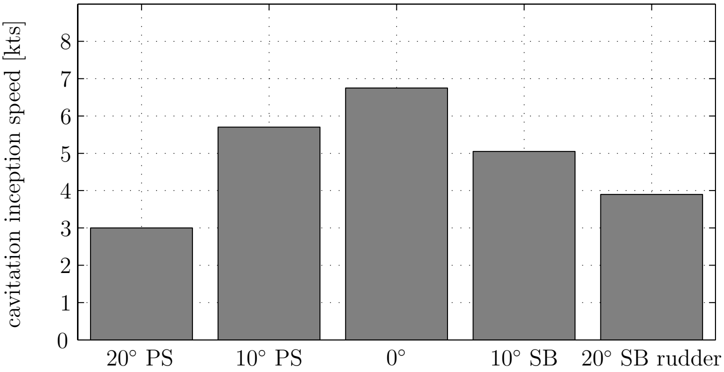

Figure 1.2: Effect of rudder angle on Cavitation Inception Speed. Reproduced from Verkuyl and Van Terwisga (2000)

give the same ship speed as high shaft speed and low pitch. By making use of this freedom one can strive for a secondary goal besides sustaining the desired mean ship speed.

A possible secondary goal could for instance be to sail at the most fuel efficient shaft speed-pitch combination, independent of the actual loading condition or environmental conditions. Other possible secondary goals might for instance relate to minimal engine wear or optimal manoeuvring capabilities. From the viewpoint of acoustic signature reduction, another goal might be to sail with a shaft speed-pitch combination that gives least or no propeller cavitation. When sailing in operational conditions, continuous adjustment of the shaft speed-pitch combination might be used to match the propeller inflow as good as possible. The latter is expected to help to increase the cavitation free time in operational conditions, and is the subject of this dissertation.

1.2 Literature Review

Due to the multidisciplinary character of this research, a complete literature review of the vast field of ship propulsion plant modeling, ship propulsion control, and propeller cavitation in operational conditions would in itself fill this thesis. Therefore only the most important or illustrative results from previous research are shortly discussed here.

Already in 1490 it was Leonardo Da Vinci who wrote:

> *"If you cause your ship to stop, and place the head of a long tube in the water and place the outer extremity to your ear, you will hear ships at a great distance from you."*

Although this type of passive sonar system suffers from low sensitivity and cannot indicate the direction of the source, its principle is still used in todays (military) acoustic underwater sensors. With the increasing role of submarines in WWI, research into active and passive sonar system strongly expanded, leading to various types of acoustic underwater sensors. A towed array that was named the "eel" was extensively deployed, and could easily be fitted to existing escort ships. By making cross bearings with two or more array-equipped ships, the surface fleet could localize underwater contacts. (Urick (1983))

Since then the available technology has evolved, and warships and submarines are commonly fitted with both active and passive sonar systems. With the increasing sensitivity of passive sonar systems, it became important to decrease the acoustic signature of naval ships and submarines. On the one hand this acoustic signature is governed by machinery noise, of which the reduction receives significant attention nowadays. On the other hand the interest of navies to decrease the underwater acoustic signature has led to extensive research into the fundamental physics of cavitation and its associated noise. Since WWII a great amount of effort has been put into the design of (naval) propellers with improved cavitation behaviour, besides other requirements on for instance propulsive efficiency and strength. With the development of more advanced model scale testing facilities and computer programs aiming at prediction of propeller (cavitation) performance, the propeller designs have been improved, and further improvements are continuously being made.

To investigate the effects of waves on the propeller performance, Aalbers and Van Gent (1984) determined the unsteady wake velocities in waves by means of model experiments as well as computations. They found that the effect of waves on the angle of attack of the blade sections is considerable, and suggested that by taking the average wave climate into account during propeller design, the long term propeller cavitation behaviour can be improved. This suggestion was taken up by for instance Jessup and Wang (1996), who assessed the effect of simple propeller modifications on the off-design cavitation behaviour. They concluded that improvement of off-design cavitation behaviour had to be traded off against other effects such as cavitation induced thrust breakdown at higher ship speeds.

Besides the possible gains in cavitation behaviour by means of improved propeller geometry, one can also consider the effect of the propulsion control system on cavitation. As will be discussed more thoroughly later on, De Mulder and De Nies (1987) developed and tested a ship propulsion control system that aimed at reduction of acoustic signature. Their system made use of accelerometers above the propellers, and adjusted both pitch and shaft speed in order to find the most silent combination of the two. Although gains are reported, this system did not remain active within the Royal Netherlands Navy (RNLN).

By means of a simplified simulation tool, Van Terwisga (2000) analyzed the effect of resistance increase and combinator curve on engine loading and propeller cavitation. In Van Terwisga et al. (2004) a more hydrodynamic-oriented simulation model that includes wave induced wakefield disturbances, is described. By showing the effect of various simplified propulsion control systems, possible gains in cavitation behaviour are investigated.

The use of simulation models to predict ship propulsion system behaviour is common nowadays. There are however great differences in the complexity of such models, since the necessary complexity is dependent on the goals that one pursues with the model. A clear description of the main dynamics of the ship propulsion system is given in Stapersma (2000). Practical use of ship propulsion models is for instance reported in Campora and Figari (2003), Routhier and Horning (2006), Altosole et al. (2008) and Altosole et al. (2009), but many more examples can be found. However, too often the simulation models are not validated very thoroughly, which can have its consequences on the ultimate performance of a model based design. A validation procedure of (ship propulsion) simulation models is therefore necessary and is thoroughly described in Schulten (2005), Schulten and Stapersma (2007) and Vrijdag et al. (2007).

1.3 Research Objectives

Operational conditions, as opposed to laboratory or trial conditions, include ship manoeuvres, waves, wind and possibly fouling of the hull. Although these conditions are always present in reality, most ship propulsion research considers only static operating conditions. This focus on static conditions holds both for the hydrodynamic as for the mechanical aspects of the ship propulsion system.

An objective of this thesis is to increase the knowledge of the behaviour of the total ship propulsion system in real conditions by combined analysis of full scale measurements and computer simulations. Use of a *simulation model*-instrument necessitates development, verification, calibration and validation of this model. Only after these laborious tasks the simulation model can rightfully be used to make predictions prior to, or instead of full scale measurements.

As a next step, the second objective is to develop and test a propulsion control system which results in improved (dynamic) behaviour of the total system in operational conditions. The third objective is to investigate the effects of operational conditions on the performance of the propulsion system by means of full scale trials.

Since many possible controller goals can be pursued, it is chosen to limit the practical implementation to a controller aiming at an increase of cavitation free time, while preventing thermal overloading of the engine, and keeping manoeuvring characteristics within acceptable limits. The research is further limited with respect to the type of operational conditions that are considered. Due to the immaturity of propeller cavitation inception predictions for ships in a turn, it is chosen to limit the current research to straight line manoeuvring characteristics.

The objectives and their related research questions are summarized by:

- *Create a ship propulsion simulation model that represents reality accurate enough to make it useful for controller development.*

  - What is the validity of this model with respect to: propeller cavitation inception, diesel engine behaviour and straight line manoeuvring characteristics?

- *Use the simulation model to develop a propulsion control system that aims at increased cavitation free time in operational conditions, and test this propulsion control system on full scale.*
  - How should ship propulsion simulation models be used in order to have maximum benefit during development and testing of a practically applicable ship propulsion control system?
  - How should a newly developed propulsion control system be tested in order to asses its performance?

- *Investigate the effects of operational conditions on the performance of the propulsion system.*
  - What is the effect of acceleration and deceleration on the system performance?
  - What is the effect of added resistance (due to for instance wind or fouling) on the system performance?
  - What is the effect of waves on the propulsion system performance?

1.4 Outline

This dissertation is structured into 11 chapters. Chapters 2, 3, 4 and 5 deal with the development of the simulation model. Chapter 2 is used to derive the conceptual model through analysis of reality. The resulting simulation model is verified in Chapter 3, after which calibration is carried out in Chapter 4. The agreement of the simulations with reality is formally assessed in Chapter 5. These first chapters are necessary to rightfully use the simulation model for propulsion controller development and testing in further chapters.

The capabilities of existing cavitation inception prediction methods are discussed in Chapter 6. They are assessed by making use of verification and validation studies found in literature.

Chapter 7 deals with the development of a propulsion control system aiming at increased cavitation free time in operational conditions. The approach is considered original, and therefore can be seen as the most important novelty of this work.

A description of the full scale test setup is given in Chapter 8. The full scale trial results are discussed in Chapter 9, where the performance of the developed control system is verified. The experimental data includes simultaneous measurements of Controllable Pitch Propeller (CPP) and Diesel Engine (DE) related variables, as well as synchronized video recordings of the propeller.

Chapter 10 does not directly contribute to achieving the research goals, but should be seen as additional material to demonstrate possible other applications of the simulation model.

This dissertation is ended with Chapter 11, in which the results are summarized, conclusions are drawn, and recommendations are given.

Chapter 2

The Simulation Model

2.1 Introduction

The need for a simulation model for controller development is widely acknowledged. One of the reasons for this is that the use of a simulated plant model is without risk. It is possible to simulate situations that one would not dare to test in real life due to possible risks for material or personnel. Use of scale models can be too costly, too complex, or even impossible due to scaling issues. Simulations can be used to investigate system behaviour long before a system is actually built. Simulations are often faster than real-time, increasing the amount of tests that can be carried out. Sufficient testing in a simulation environment decreases the full scale tuning and testing time. This can significantly reduce costs since the full scale system is needed for less dedicated testing time, subsequently reducing the need for personnel.

The use of simulation models for controller development and tuning also helps to increase the performance of the final system. On board tuning and testing during commissioning is a stressful job, especially when considering the constraints in available time and the risks during the commissioning phase. This easily leads to too a conservative tuning, resulting in unnecessary loss of system performance.

The foregoing shows the benefits of using a simulation model. However, a big disadvantage of using a simulation model is that one has to build one! Building a simulation model often is a time consuming task itself, with difficult choices on model adequacy, complexity, structure and required accuracy. When the physical processes in the plant are not fully understood, more time-intensive analysis is needed to come to a conceptual model. Ultimately the modeler's task is to ensure that the simulations represent reality to a sufficiently accurate level, in order to use them with considerable profit.

This chapter deals with the extraction of a conceptual model from reality, as is illustrated in Fig 2.1. This process requires analysis and understanding of the real system and the involved phenomena that drive system behaviour. The conceptual model of a system can be of various levels of complexity. A task of the modeler is to "qualify" the model, which is defined by the Society for Computer Simulation (SCS) as:

> *Qualification: Determination of adequacy of the conceptual model to provide an acceptable level of agreement for the domain of intended application.*

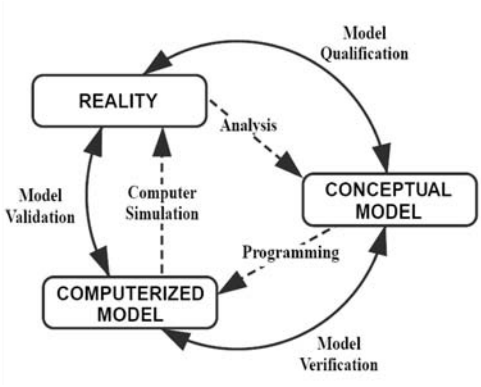

Figure 2.1: From reality to the conceptual model. Source: Schlesinger (1979)

This definition implies that the simulation goals should be driving the extraction of the conceptual model from reality. This might seem trivial, but often modelers are tempted to use legacy codes that were developed earlier, sometimes by others, with other goals in mind, which can easily lead to non-adequate computer codes.

The process of extracting a conceptual model from reality can be divided in several phases. First of all the modeling goals have to be set. In other words one has to determine what the model should be able to. Thereafter the reality has to be studied in order to identify the relevant features that need to be modeled. Through analysis of the real system, in combination with the modeling goals, the conceptual model can now be developed.

This chapter is ended with a description of the mathematical framework that contains the developed conceptual model. This framework is introduced here since it will be used in the calibration and validation phase.

2.2 Simulation Model Goals

As argued before, the necessary level of complexity of a simulation model depends on the goals that are pursued with the model. For rough estimates of main system performance one can often use a system model based on simplified concepts. The same holds for simulation models that are used for educational purposes. In such cases the trends are more important than the actual quantitative results. On the other side of the spectrum, where in-depth analysis of complex processes is desired, one needs to model these complex processes in detail. Examples are easily found: for educational purposes a ship propulsion simulation model can be fitted with a parabolic resistance curve without problems. For a complex task as studying the effect of small appendages on the resistance curve, one needs a specialized model that captures the relevant physical processes in detail. When detailed physical processes have a big effect on the overall system behaviour, it should be considered whether a simplified submodel of the complex sub-process can still give good overall results.

The simulation model used in this thesis is built with these considerations on necessary model complexity in mind. On an abstract level, the goal of this model can be summarized as follows:

> *The ship propulsion simulation model should represent reality accurate enough to make it useful for the development of a propulsion controller. This controller should aim at increasing cavitation free time in operational conditions by active control of both shaft speed and propeller pitch. The model should also give sufficiently accurate output to enable judgment of diesel engine loading, propeller behaviour, and straight line manoeuvring characteristics.*

This abstract goal includes the somewhat vague descriptions *"sufficiently accurate"*, *"useful"*, and *"operational conditions"*. To come to clear specifications of the simulation model an interpretation of the high level goal is made here:

- *Create a model containing the following submodels: diesel engine, propeller, and manoeuvring model*
- *Accuracy of the propeller model should be such that conclusions with respect to cavitation inception can be drawn*
- *Accuracy of the diesel engine model should be such that the currently used (static) engine overloading-criterion of the diesel engines can be checked*
- *Accuracy of the manoeuvring model should be such that conclusions with respect to straight line manoeuvring behaviour can be drawn*
- *The model should accommodate for the simulation of increased ship resistance and a fluctuating wakefield due to a seaway*

These specifications give a starting point for setting up the simulation model. A more detailed specification is not given here since this would easily lead to a specification as big as (or possible bigger than) the model itself.

Whether the resulting total simulation model gives outputs with sufficient accuracy cannot easily be said beforehand due to uncertainty propagation through the various submodels. A mathematical approach to uncertainty propagation through various coupled submodels is discussed in Vrijdag et al. (2007) and Schulten and Stapersma (2007), and is discussed in Section 5.2.1 of the chapter on model validation.

2.3 Propulsion Plant Description

The ship propulsion system that is to be modeled here is based on the Multipurpose Frigate (M-frigate) of the Royal Netherlands Navy, shown in Fig 2.2. This ship type is chosen since early on in the project it was decided that full scale trials were to be carried out onboard an M-frigate.

The layout of the propulsion system of the M-frigate is shown in Fig 2.3, with some general data given in Table 2.1. The ship is approximately 120 meters long and 14 meters wide, and has a displacement of approximately 3300 tons. It is a twin shaft ship, with both shafts linked to a dedicated Combined Diesel or Gas (CODOG) installation. The 4-stroke turbocharged diesel engines run in the medium speed range ($<$ 1000rpm), and are capable of propelling the ship up to speeds of approximately 20 kts. Two Rolls Royce gas turbines are capable of driving the ship up to $\approx$ 29 kts in calm water conditions.

Figure 2.2: Multipurpose frigate. Source: RNLN

Ship length overall	122 m
Breadth	14.4 m
Displacement	3300 tons
Crew	max 154
Maximum speed	29 kts
Propulsion system	2 SW280 diesel engines 2 Rolls Royce Spey gas turbines

Table 2.1: General M-frigate data

Both shafts are fitted with a 5 bladed Controllable Pitch Propeller (CPP) rotating inward over the top. These propellers have been optimized for high Cavitation Inception Speed (CIS) and for high propeller efficiency. Two inclined rudders are fitted directly behind the propellers, capable of roll-reduction by continuous active rudder adjustments (Van Amerongen (1982) and Van Der Klugt (1987)).

The propulsion system of the M-frigate can be operated in various configurations. Apart from a Diesel Engine (DE) or Gas Turbine (GT) driven shaft, it is also possible to sail with one non-driven shaft which is beneficial during prolonged operation at low ship speed, because it reduces fouling and running hours of the diesel engines. The non-driven shaft can be chosen to run freely at low rotating speed (trailing), or can be locked by a shaft brake. In the latter case the propeller is often feathered to reduce resistance.

Only the double DE configuration is to be simulated with the ship propulsion simulation model, while GT operation is not required. This is a choice that is based on the goals that are pursued with the model. In this case the choice is made to only consider the DE-configuration because the ship speed at which gains in cavitation free time are expected lies in the DE operating range. Prolonged GT operation during the full scale testing period was considered too expensive considering the low fuel efficiency of the GT at relative low ship speeds.

It is acknowledged that the need for increased cavitation free time also holds when sailing on GT's. Due to their nature, GT's in general produce less underwater noise (compared to the DE's at same ship speed). Therefore RNLN-procedures often require GT-configuration for ships involved in missions that require low underwater noise. It is expected that findings

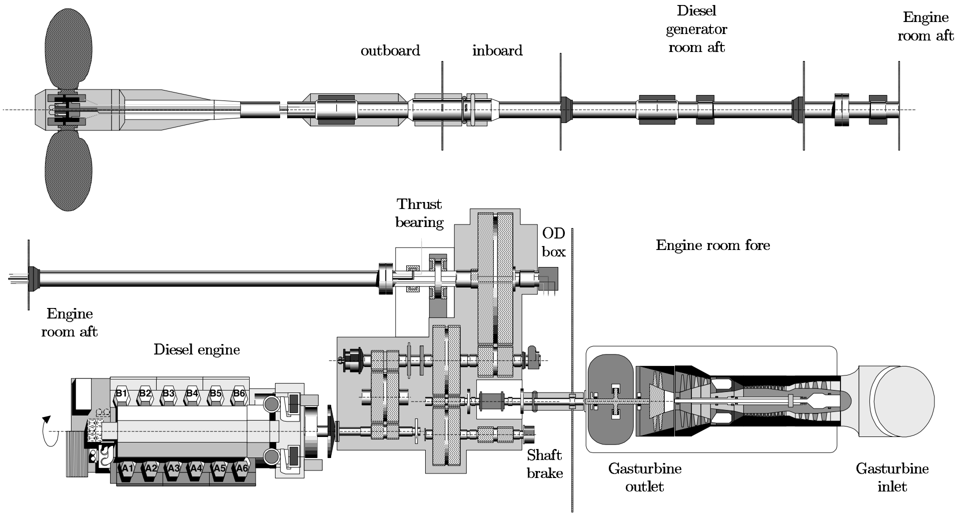
outboard
inboard
Diesel generator room aft
Engine room aft
Thrust bearing
OD box
Engine room fore
Engine room aft
Diesel engine
B1
B2
B3
B4
B5
B6
A1
A2
A3
A4
A5
A6
Shaft brake
Gasturbine outlet
Gasturbine inlet

Figure 2.3: Propulsion plant layout of the M-frigate (port side). Source: RNLN

of this project can also be used for further development of control of a GT-driven ship.

2.4 The Conceptual Propulsion Plant Model

The general structure of the ship propulsion simulation model is shown in Fig 2.4. This blockdiagram is built up from various submodels that in principle can all be of selected degree of complexity. The submodels and the total model should however be adequate to provide an acceptable level of agreement for the domain of intended application. Since the level of uncertainty in total simulation output cannot easily be determined beforehand, it can easily happen that a suitable total model is only found after various iterations of the modeling-loop shown in Fig 2.1. Experience with, and knowledge of submodel sensitivities and uncertainties can however help to decrease the number of necessary iterations.

The actual ship under consideration has a similar installation for port and starboard side. Only one side is shown here. Note that the gearbox is part of the engine-block and that the hydraulic pitch actuating system is part of the pitch control system block.

The two most important differential equations that govern the dynamic behaviour of the ship propulsion plant are shown in the blockdiagram, and are dealt with in some detail here.

On the right hand side of Fig 2.4, the ship translation loop is shown. On a conceptual level it is assumed that structural axial dynamics of the shaft and of the ship play no role so that the thrust of the propeller is directly transferred to the thrust block. Note that with this choice of conceptual model, no axial vibrations of the shaft can be predicted by the model. The ship structure is assumed rigid, and its speed is based on a force balance between

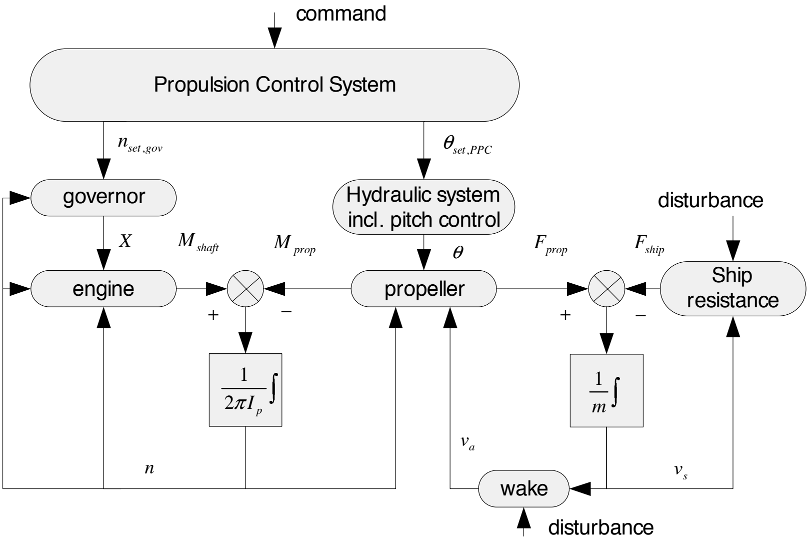
command
Propulsion Control System
n set,gov
θ set,PPC
governor
Hydraulic system incl. pitch control
disturbance
X
M shaft
M prop
θ
F prop
F ship
engine
propeller
Ship resistance
+
−
+
−
1/(2πI_p) ∫
1/m ∫
v a
n
v s
wake
disturbance

Figure 2.4: General blockdiagram of a ship propulsion plant

propeller thrust F_{prop} and ship force F_{ship}. When F_{prop} and F_{ship} are out of balance, a net force will result in an acceleration or deceleration of the ship. Integration of acceleration gives ship speed:

$$v_s = \frac{1}{m}\int_0^T F dt + v_{s,0} \tag{2.1}$$

where v_s is ship speed (having initial value $v_{s,0}$ at time $t = 0$). F is the sum of all forces working in the longitudinal direction of the ship and m is the total mass of the ship including added mass, both assumed constant.

On the left hand side the shaft rotation loop is shown, dealing with the balance between propeller and shaft torque. On a conceptual level it is chosen to assume a rigid shaft. This simplification causes that torsional vibrations are not included in the model. Furthermore the torsional damper that is installed in reality is not modeled.

In the same way as in the ship translation loop, a net torque will cause an acceleration or deceleration of the shaft. Integration of angular acceleration gives shaft speed:

$$n = \frac{1}{2\pi I_p}\int_0^T M dt + n_0 \tag{2.2}$$

where n is shaft speed (having initial value n_0 at time $t = 0$), M is the sum of all torques working on the shaft and I_p is the effective rotational inertia of the shaft system (including engine and gearbox, shaft, propeller and entrained water, all assumed constant and rigid).

In the middle the propeller is shown. The propeller is linked to the other systems via the propeller thrust F_{prop} and torque M_{prop}. Other systems provide a certain shaft speed n, advance speed v_a and actual propeller pitch θ to the propeller model.

A more complete description of this general propulsion blockdiagram is given in Stapersma (2000). The general blockdiagram can be extended to multiple shafts, simplified to FPP's, or modified to different kinds of propulsors such as water jets or podded propellers. The prime mover can be tailored to the case under consideration.

The simulation model that is developed here is not the first in its type. Use of ship propulsion simulation models is widespread and literature reveals many different variants of basically the same system. Common features are the differential equations for ship and shaft speed, which are clearly modeled by the two integrators shown in Fig 2.4 and equivalently expressed in equations (2.1) and (2.2).

Differences often lie in the type and complexity of the various submodels. This difference is (or should be) driven by the goals that one pursues with the model. There are ship propulsion simulation models that include relatively complex thermodynamic models of (diesel) engine processes, such as reported in Schulten (2005) and the Motor Thermodynamics (MoTher)-model, developed at the Marine Engineering group of the National Technical University of Athens. Some simulation models have complex propeller and wakefield models, such as for instance Van Terwisga et al. (2004). Other simulation models use a multi-degree of freedom manoeuvring model, such as reported in Schulten (2005), enabling manoeuvres that deviate from the straight path. Finally there is a big difference in the completeness of the modeled control system, even though this system has a big effect on the dynamic behaviour of the total system. Serious effort to model the control system into detail is found in for instance Altosole et al. (2008).

In order to reach the simulation goals, it is chosen to keep the various submodels as simple as possible, whilst pursuing *"adequate"* and *"sufficiently accurate"* simulation results in terms of both static and dynamic behaviour. The accuracy of the simulation output can however only be assessed after the validation phase, which is put in perspective in Fig 2.1. The conceptual submodels that are used for this research are described in the following sections.

2.4.1 The Propeller Model

In this section the propeller model in a broad sense is covered. Not only the hydrodynamic propeller model is dealt with, but also the hydraulic pitch actuation system is covered. The Propeller Pitch Controller (PPC), which is the link between the Propulsion Control System (PCS) and the hydraulic propeller actuating system, is also dealt with here.

The Propeller Hydrodynamic Model

The propeller is the link between the inboard machinery and the outboard environment. A basic feature of the propeller model should be that it provides thrust F_{prop} and torque M_{prop} for a wide range of pitch angles θ and advance ratios J.

Since this research is on the prevention of cavitation, it is tempting to incorporate a complex hydrodynamic computer program to predict propeller performance. Such a program generally not only delivers thrust and torque, but also gives detailed information on for instance the pressure distribution over the propeller surface and possibly about the occurrence and inception of various types of cavitation.

On the downside, these programs typically require high computational power which is especially burdensome for the development and tuning phase of a propulsion control system, since this decreases the advantage of fast development by using a simulation tool.

Complex hydrodynamic propeller performance prediction programs generally aim at accurate prediction of local flow phenomena, such as local separation and vorticity generation (Van Terwisga et al. (2006)). Such predictive capabilities are important to create a deeper understanding of the involved physical phenomena, but are hard to verify and validate.

In this thesis the goal of the simulation model is to design working equipment, which influences the type of tools that the modeler should use. It therefore is decided to use a propeller model based on the open water diagram. This choice of conceptual model has the consequence that the model does not capture possible dynamic effects on propeller performance, and cannot show performance fluctuations due to blade passages. Instead quasi-steady performance is assumed. Further on in this thesis it is shown how the relatively simple open water diagram can still be used to get an indication of cavitation onset in operational conditions as dictated by the preset goals.

The hydrodynamic propeller model as used is shown in Fig 2.5. Advance ratio J is defined as: $J = \frac{v_a}{nD}$, where the advance speed v_a is related to ship speed via the wake fraction w by $v_a = v_s(1 - w)$. The open water propeller diagram gives the relation between advance ratio J and thrust and torque coefficient k_t and k_q dependent on the actual pitch angle: $k_t = f(\theta, J)$ and $k_q = g(\theta, J)$. From these coefficients the open water thrust and torque can be calculated as: $F_{prop} = k_t \rho n^2 D^4$ and $Q = k_q \rho n^2 D^5$. Rotating in behind conditions, the propeller torque is slightly modified due to propeller-wake interaction effects. The relative rotative efficiency η_r is defined as the ratio between in-behind torque and open water torque, so that the torque that the propeller requires in behind conditions equals: $M_{prop} = \frac{Q}{\eta_r}$.

There exist various approaches to simulate the wakefield disturbances that are shown in Fig 2.5. An approach might be to directly model such disturbances by inclusion of complex hydrodynamic submodels. Such an approach has the disadvantage that it in general has a negative effect on the simulation speed. A workaround can be to generate appropriate time series by use of a standalone (specialized) hydrodynamically oriented program. A time trace can then be used multiple times, while the computational costs during the actual simulation are minimal. The approach that is taken here is to generate the timeserie inside the actual model, but by means of a very simple submodel. On the one hand regular waves are implemented as sinusoidal disturbances with appropriate amplitude and frequency. On the other hand a slightly more complex irregular disturbance "generator" is modeled based on Fossen (2002). This model can be summarized as a *second order wave response transfer function approximation*, and is convenient due to its simplicity. The transfer function with shape

$$h(s) = \frac{K_w s}{s^2 + 2\lambda\omega_0 s + \omega_0^2}$$

in fact is a second order filter. Feeding zero-mean white noise into this filter results in a time realization of a spectrum that, dependent on parameter settings, can approximate both a Modified Pierson Moskowitz (MPM) and a JONSWAP spectrum. If one assumes that the wave disturbances follow the same spectral distribution, this model can be used to simulate irregular wave induced wake disturbances. Realistic disturbance amplitudes and frequencies were obtained by manual tuning of the coefficients.

The CPP Actuating System

Closely related to the propeller model is the hydraulic actuation model. This hydraulic system that actuates the CPP is shown in Fig 2.6.

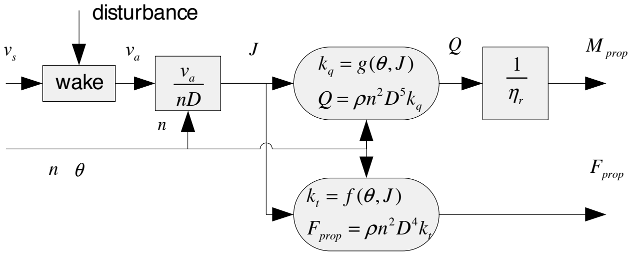
disturbance
v_s
wake
v_a
$\frac{v_a}{nD}$
n
J
$k_q = g(\theta, J)$
$Q = \rho n^2 D^5 k_q$
Q
$\frac{1}{\eta_r}$
M_{prop}
n θ
F_{prop}
$k_t = f(\theta, J)$
$F_{prop} = \rho n^2 D^4 k_t$

Figure 2.5: Hydrodynamic Propeller blockdiagram

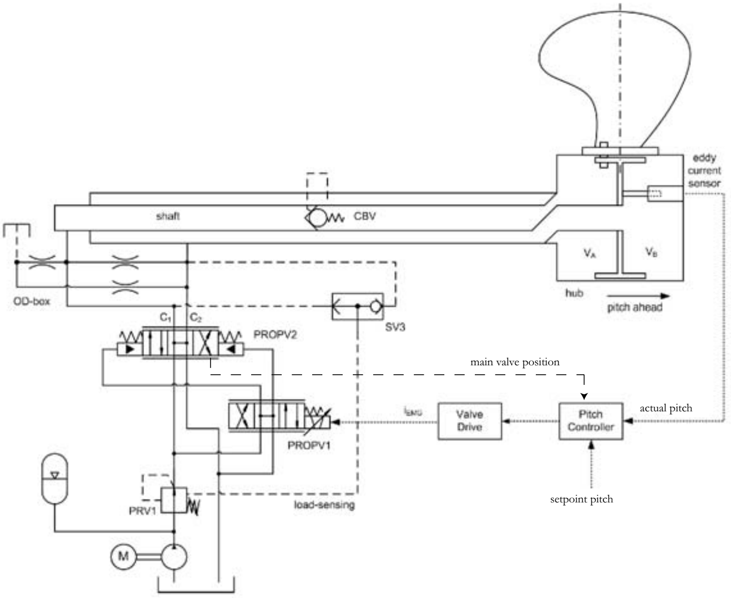
eddy current sensor
shaft
CBV
V_A
V_B
hub
pitch ahead
OD-box
C_1
C_2
PROPV2
SV3
main valve position
actual pitch
i_{EMG}
Valve Drive
Pitch Controller
PROPV1
load-sensing
PRV1
M
setpoint pitch

Figure 2.6: Simplified hydraulic CPP system. Source: Huijbers (2008)

The hydraulic system starts with the pilot valve drive. This drive electrically actuates the pilot valve (PROPV1) in order to control the position of the main proportional valve x_m (PROPV2). It is necessary to use a pilot valve for controlling the main valve because the forces for setting the main valve are too high to be generated electrically within a small construction. An off-center position of the main valve results in an oil flow via the Oil Distribution box (OD box) through the propeller shaft, resulting in a pressure difference over the yoke. This pressure difference is converted to blade spindle torque via a pin slot mechanism. When opposing forces are overcome, the yoke and thus the propeller blades will start to move. A counterbalance valve (CBV) is included in the shaft to lock up the propeller pitch if no actuation is required. The "load sensing" capability is implemented to achieve a constant pressure drop along the main valve at every arbitrary valve opening. Its purpose is to ensure a limited flow to the hub, so that the speed of the yoke is restricted independent of the load. (Huijbers (2008))

The hydraulic CPP submodel that is used in this thesis was provided by a third party.In

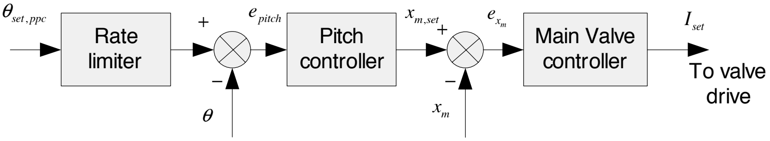

Figure 2.7: Propeller Pitch Controller (PPC) blockdiagram

the following chapters the most important CPP variables are verified and validated, which should reveal whether the main performance of the model agrees with reality. However, the validity with respect to detailed internal hydraulic variables is not considered. This is justified by the fact that high confidence predictions of internal hydraulic variables are not considered a goal for this thesis. It was found that in this case, largely independent of the model and parameters of the hydraulic system, the low level pitch controller ensured that the pitch moved as ordered, which is sufficient for the goals as were set for this simulation model.

If a more specialized CPP-controller is to be developed it is evident that internal variables of the hydraulic system need to be modeled, verified and validated in more detail. Such detailed modeling (and control) effort is described in for instance Bakker et al. (2006) and Huijbers (2008).

The Propeller Pitch Controller (PPC)

The PPC is the link between the PCS and the hydraulic system as described before. Its functional location is shown in Fig 2.6, showing inputs *measured pitch* θ and *setpoint pitch* $\theta_{set,ppc}$. As shown in the detailed blockdiagram in Fig 2.7, the input to this system is the pitch setpoint $\theta_{set,ppc}$ as ordered by the PCS. To effectuate this setpoint the actual pitch θ and the position of the main proportional valve x_m are also input to the PPC as shown in Fig 2.6. The output is a current setpoint I_{set} to the valve-drive.

The first part of the PPC is a rate limiter on the pitch setpoint $\theta_{set,ppc}$. This ensures that the pitch will never be actuated such that the maximum allowed pitch rate is exceeded. The rest of the PPC is basically a two stage controller for the pitch: The middle part is a proportional pitch controller. The error in pitch e_{pitch} is multiplied by a gain, resulting in a setpoint for the main valve position $x_{m,set}$. The final part is the proportional main valve controller. The main valve position error e_{x_m} is multiplied by a second gain, and the resulting signal I_{set} is output to the valve-drive that electrically actuates the pilot valve.

A complete description of the PPC is given in Visser and Pol (1996).

2.4.2 The Diesel Engine Model

The "governed" diesel engine (DE) blockdiagram is shown in Fig 2.8. It contains the (electronic) governor, the actuator that actuates the fuel rack rod, the fuelpumps, and the engine itself. The system boundaries are chosen such that they include the gearbox and the rotating shaft system. The various submodels that are included in the DE model are subsequently discussed here:

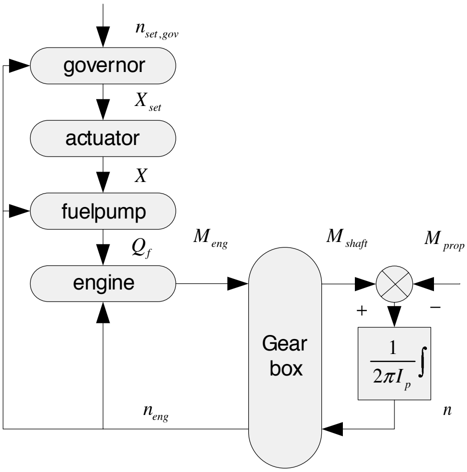

Figure 2.8: Blockdiagram of a "governed" diesel engine

The Governor Model

The inputs to the governor are the actual and the desired engine speed: n_{eng} and $n_{set,gov}$. Following a PI- process with engine speed dependent fuelrack-limitation (as a final protection against overloading), the governor calculates the desired fuelrack setpoint X_{set} that is input for the actuator.

The Actuator Model

Based on verbal communication with the manufacturer, the actuator is modeled as a first order linear system with a time constant of 20 ms. This gives a settling time (98%) of $\approx 80ms$. A reported delay of $5ms$ is considered negligible, and is disregarded.

Via mechanic levers, the hydraulic actuator actuates the fuelrack rod, resulting in a fuel rack position X in mm. Subsequently the fuel rack position X is used as an input to the fuel pumps.

The Fuel Pump Model

The fuelrack position, together with the actual engine speed n_{eng}, determines the volume of fuel (per cycle) that is injected by the engine driven (plunger) fuel pumps. These fuel pumps are modeled as lookup tables. Based on the inputs X and n_{eng}, the injected volume of fuel per cycle Q_f is determined. The 2-D lookup table includes the effect of internal leakage of the fuelpumps.

The Diesel Engine Model

A variety of engine models can be chosen from, which is comparable to the selection of a suitable hydrodynamic propeller model. On the one hand complex CFD-based models exist that are intended to analyze and understand combustion phenomena in detail. On the other hand there exist lookup-table approaches that give accurate results in the domain for which input lookup-data is available. As mentioned by Schulten (2005), such look-up table models clearly have disadvantages. They are not generic: every engine-model needs other lookup tables for which data needs to be available.

The mentioned disadvantage only partly holds for this research: engine lookup tables for this specific engine are available, and there was no need to vary the engine type or model. The engine model outputs as required by the goals, can all be delivered via the existing lookup-table set. Some engine-model outputs would have been "nice to have", but are not necessarily available. This for instance holds for the exhaust gas temperature which might be a better indicator for thermal engine overloading than the currently applied overloading criterion (which is discussed later). Such an indicator was however not set as a goal.

Based on Deleroi (1995), the engine is modeled as a set of lookup tables (shown in Appendix A). On a top level the model has engine speed n_{eng} and volume fuelflow per cycle Q_f as inputs, as shown in Fig 2.9, and inlet receiver pressure p_{ir} and turbocharger speed n_{tc} as outputs.

Output of lookup-table 1 is the static mean effective pressure $p_{me,s}$. The p_{me} includes the mechanical losses in the engine due to for instance friction and power take-offs for cooling water and fuel pumps. Other losses due to work on the cylinder valves are also included. The engine torque M_{eng} is related to p_{me} via

$$M_{eng} = \frac{p_{me} \cdot i \cdot V_s}{2\pi \cdot k}$$

where $k = 2$ for 4 stroke engines, i is the number of cylinders, and V_s is the swept volume of the cylinder, which is the product of bore area and stroke length. This value of M_{eng} is used as input to the gearbox model.

Besides the lookup table for mean effective pressure, a simplified turbocharging model is also included, as shown in Fig 2.9. The turbocharger loop including its driving forces is modeled in a daring way, by means of 4 lookup tables of which 2 are equal. These 2 equal tables (2A and 2B) contain the static relation between the inlet receiver pressure p_{ir}, and n_{eng} and p_{me}, as can be determined by engine tests. There is however a difference with respect to the input signals to tables 2A and 2B. Table 2A is driven by the actual engine speed and the actual p_{me}, resulting in the inlet receiver pressure $p_{ir,s}$ as would be found in static conditions when the turbocharger is rotating at steady speed. Table 2B is also driven by the actual engine speed, but then by the so called dynamic mean effective pressure $p_{me,d}$. This $p_{me,d}$ is generated by table 3. Table 3 relates the actual turbocharger speed n_{tc} and actual engine speed n_{eng} to the p_{me} that would be found if the engine was operating with these two enforced rpm's. Since this p_{me} is dependent on the actual dynamic rotation speed of the turbocharger, it is noted as $p_{me,d}$. This signal is now fed into table 2B, resulting in $p_{ir,d}$, which represents the dynamic inlet pressure. The dynamics due to the turbocharger inertia are included in this signal since (via table 3) it is driven by the actual turbocharger speed n_{tc}.

To determine the driving torques of the turbocharger, one in principle should make use of the compressor and turbine maps. To keep the model simple it is chosen to follow the approach suggested by Deleroi (1995). There, an approximate turbocharger model is proposed, assuming that the driving forces are proportional to $p_{ir,s}$ and $p_{ir,d}$. The in-between variables that should in principle be necessary to come to something like a turbine and compressor torque, are lumped together with the turbocharger inertia I_{tc}, in

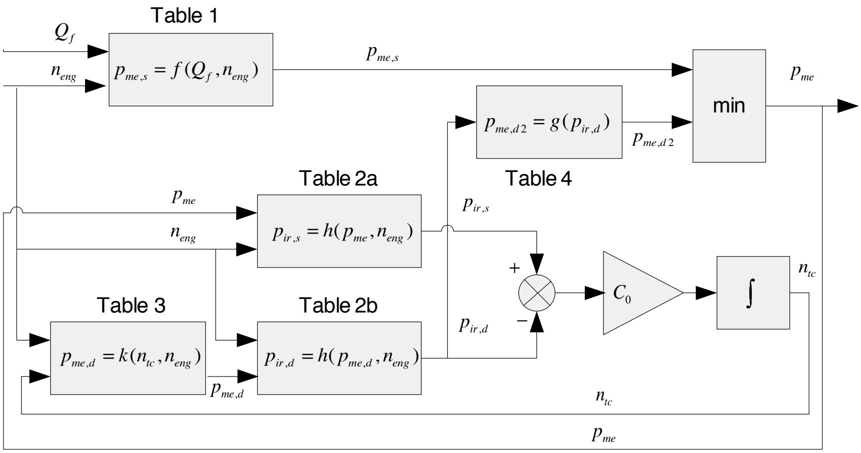
Table 1
Q_f
n_{eng}
$p_{me,s} = f(Q_f, n_{eng})$
$p_{me,s}$
min
p_{me}
$p_{me,d2} = g(p_{ir,d})$
$p_{me,d2}$
Table 2a
Table 4
p_{me}
n_{eng}
$p_{ir,s} = h(p_{me}, n_{eng})$
$p_{ir,s}$
+
−
C_0
$\int$
n_{tc}
Table 3
Table 2b
$p_{ir,d}$
$p_{me,d} = k(n_{tc}, n_{eng})$
$p_{ir,d} = h(p_{me,d}, n_{eng})$
$p_{me,d}$
n_{tc}
p_{me}

Figure 2.9: Engine blockdiagram in detail

the constant C_0. This variable can be tuned to obtain the approximate correct dynamics of the turbocharger loop.

The model also facilitates for the simulation of reduced engine torque due to lack of available combustion air. This is modeled by means of the *min*-block in conjunction with table 4. This table relates the dynamic inlet pressure $p_{ir,d}$ to the maximum achievable effective pressure $p_{me,d2}$. If $p_{me,d2}$ is less than $p_{me,s}$, this means that the engine output is limited due to lack of available air, and the effective pressure is reduced.

It is finally noted that the model including lookup table data was already available at the start of this project and no further tuning of C_0 was necessary. Where necessary some outliers in the lookup table data where removed/ modified to prevent unrealistic engine behaviour in specific operating points.

The Gearbox Model

The gearbox model that is used in the simulation is rather simple. It is assumed that the power leaving the gearbox equals the power entering the gearbox multiplied by a constant gearbox efficiency. This gives:

$$P_{shaft} = P_{eng} \cdot \eta_{gb}$$

so that with gearbox ratio $i_{gb} = \frac{n_{eng}}{n}$,

$$M_{shaft} = M_{eng} \cdot \frac{n_{eng}}{n} \cdot \eta_{gb} = M_{eng} \cdot i_{gb} \cdot \eta_{gb}$$

Relatively high losses are expected for this specific gearbox, due to the three geartrains as shown in Fig 2.3. Gearbox losses up to 7% are reported for CODOG installations (Hoppe (2008)).

2.4.3 The Ship Model

The ship resistance curve is modeled as a lookup table, that is based on towing tank measurements reported in Sinnema (1986). Corrections due to the thrust deduction factor t (also taken from Sinnema (1986)) are applied as follows:

$$F_{ship,0} = \frac{R_{ship}}{(1-t)}$$

where R_{ship} is the resistance without propeller at the static speed under consideration, as found from the resistance test. $F_{ship,0}$ is the calm water resistance including the effects of propeller-hull interaction. Extra resistance can be added via multiplication of, and/or by addition to, the calm water resistance $F_{ship,0}$:

$$F_{ship} = \alpha_R F_{ship,0} + R_0 + \Delta R$$

where the tuning parameters α_R and R_0 can be used dependent on the character of the extra resistance. ΔR can be used to simulate resistance variations, due to for instance second order wave drift forces, which are however not modeled in detail. To study the effect of such disturbances on the system, a sinusoidal signal with a period of 20-50s is proposed. An appropriate amplitude can for instance be determined by means of expert opinion or by use of a suitable hydrodynamic program.

2.4.4 The Propulsion Control System Model

A ship propulsion plant is normally not operated without a PCS. A clear exception is the occurrence of a (partial) failure of the PCS, necessitating manual control of the propulsion plant. In normal conditions however, the PCS is the link between the commands of the user and the underlying parts of the propulsion system.

The complexity of a PCS varies per ship(type). More complexity of the propulsion system almost automatically leads to more complexity in the control system. Especially the ability to sail with various propulsion configurations (of for instance CODOG or CODAG installations), including necessary transitions between them, adds to the complexity. Furthermore the presence of a CPP increases the complexity, since this increases the number of controllable inputs of the plant. On the other end of the spectrum, a PCS can solely consist of a governor connected to a command lever.

In Chapter 7 of this thesis a new control system is developed and tested on the plant model, followed by full scale testing. In order to validate the plant model that is used for the controller development it was decided to model the currently applied propulsion control system of the M-frigate first. This has increased the confidence in the ability of the total simulation model to represent full scale behaviour, while it also forced the modeler to learn from the experience that was put into the existing control system.

It is noted here that the step from an existing real PCS to the conceptual model in fact is not taken here. True analysis of the system in the sense of understanding the physical background such that relevant phenomena can be modeled does not apply here. Having the right documentation at hand, the modeling task is basically reduced to a programming-task. Following this line of thought it can be said that no parameter or model uncertainty is introduced in this step since no extraction of a conceptual model from reality is necessary.

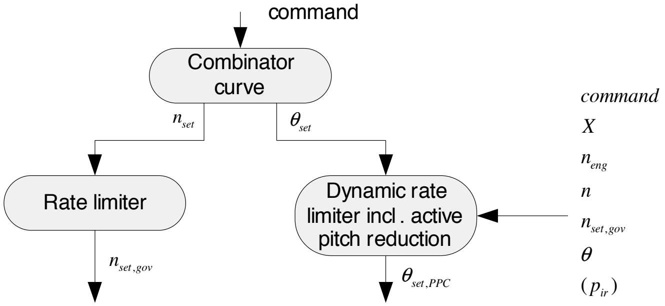

Figure 2.10: A simplified blockdiagram of the Propulsion Control System (PCS)

Nevertheless the PCS model is dealt with here to show the basic working principles. It should be noted that only the relevant parts of the PCS are discussed: parts that are only relevant for GT-configuration or transitions between various configurations are not discussed.

A simplified blockdiagram of the PCS of the M-frigate (Version 6.3, Brouwer and Dupré (2004)) is shown in Fig 2.10. Several elements are clearly defined:

the combinator curve: As shown schematically in the figure, the starting point of the PCS is the single lever command given by the operator. This command is translated to two separate high level setpoints. One for the engine/shaft speed, and one for the propeller pitch. This process is based on two lookup tables for which the parameters are dependent on the propulsion system configurations, and the desired controller mode. These lookup tables fix the static working points of propeller pitch and shaft speed, as long as no further limitation is applied further downstream the path.

the setpoint generator for the governor of the DE: The high level setpoint for the engine speed is not passed directly to the governor. To keep shaft accelerations in hand, the PCS applies rate limiting before the setpoint is transferred to the governor. The parameters that determine the shaft acceleration rate $\dot{n}_{set,gov,max}$ and the maximum shaft speed n_{max} are mentioned here since they will be used for controller tuning in a later phase.

the setpoint generator for the PPC: The implementation of the pitch-branch of the PCS is more complex. The high level pitch setpoint is rate limited dynamically. This means that the rate at which the propeller pitch setpoint $\theta_{set,ppc}$ is allowed to change is made dependent on the actual condition of the propulsion plant. It would lead too far to give an in-depth description here, but some system measurements and control system variables that have effect on the pitch rate are: engine margin against overloading, actual governor setpoint, and actual fuelrack position. The engine margin against overloading is expressed by the amount of fuelrack (mm) that can be added until some engine limit is reached. These limits are related to the reduction of time between overhaul, if the engine is operated there for a prolonged period. These limiting lines in the engine diagram are called the Reduced Time Between Overhaul (RTBO)-lines.

A short summary of the characteristics of the dynamic pitch rate-limiter is given here:

- As an overall measure the pitch rate is made dependent on the actual virtual shaft speed. For high virtual shaft speeds the rate is drastically limited. The concept of "virtual shaft speed" has not been explained yet, but is discussed in Chapter 7.
- The pitch rate is further decreased if available engine margin is small.
- The pitch rate is decreased if there is a big difference between the actual engine speed and the speed setpoint that is input to the governor.
- If due to a step in the command, a big change in shaft speed is required, the pitch rate is decreased (even before there is a difference between actual engine speed and the governor setpoint).
- If the DE has to accelerate, and the engine operating point is close to the RTBO-line, a negative pitch rate is enforced, resulting in active pitch reduction.
- If dynamic propeller loading due to waves is such that the RTBO line is regularly crossed, a negative pitch rate is enforced. By application of a pitch recovery algorithm, the pitch is temporarily kept at the reduced value. The same algorithm gradually relaxes the pitch reduction until the process starts over again.
- A pitch rate limitation based on inlet receiver pressure p_{ir} is also available. Parameter settings however are such that this rate limitation is not active.
- If a second RTBO line (RTBO2) is crossed for a period longer that 2 seconds, pitch is immediately reduced with the highest allowable rate.
- If during a commanded deceleration the pitch is drastically reduced, this can result in a temporary increase in shaft speed. This effect is called the windmill-effect. If the windmill-effect is so strong that the shaft speed exceeds the maximum allowable value, the pitch decrease is halted until the shaft speed drops again.

The complexity of the currently applied PCS has evolved over the years. Parts have been removed or added, dependent on the problems that occurred during the lifetime of the M-frigate propulsion plant. Engine overloading problems in the past have resulted in a PCS that drastically relieves the DE's from high loading during both static and dynamic conditions.

2.5 Mathematical Framework for the Conceptual Model

In the previous sections the complete conceptual model is treated. The various submodel boundaries are chosen based on the functional relations between the models. Where possible, the submodels are chosen such that they are intrinsically stable. Furthermore the variables that link the various submodels together are chosen such that they can be measured on full scale. These two characteristics of the submodels and their linking variables will prove valuable during calibration and validation.

In the following chapters on verification, calibration and validation, these system boundaries and their input-output connections play an important role. In this section the developed model is put in a mathematical framework, paving the way for the following chapters.

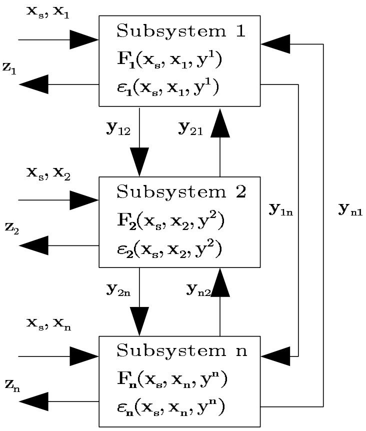

Figure 2.11: Coupled subsystems, reproduced from Du and Chen (2002)

The notation used here is based on the notation of Du and Chen (2002), which was already applied to a ship propulsion system in Vrijdag et al. (2007). First of all, the general mathematical framework is described. After this the simulation model used in this thesis is put into the system's notation.

Let us first assume a general system that is built up out of n interconnected subsystems, as shown in Fig 2.11. Common input parameters to all subsystems are called shared variables and denoted $\boldsymbol{x}_s$. Input parameters particular to a certain subsystem are denoted by $\boldsymbol{x}_i$, where i denotes the subsystem under consideration. Outputs of a particular submodel i are denoted $\boldsymbol{z}_i$.

Linking variables are denoted $\boldsymbol{y}_{ij}$, $i \neq j$, and are interconnecting the various subsystems, where the signal goes from subsystem i to subsystem j. For ease of notation Du and Chen introduce $\boldsymbol{y}_i$, as the set of linking variables coming from subsystem i, as input to all other subsystems. Outputs coming from all subsystems except subsystem i , used as input to subsystem i are abbreviated as $\boldsymbol{y}^i = \{y_1, \dots, y_{i-1}, y_{i+1}, \dots, y_n\}$.

Introducing the notation $\boldsymbol{F}_{yi}$ for the subsystem model algorithm, and $\boldsymbol{\epsilon}_{yi}$ for the corresponding model error, the linking variables are described by:

$$\boldsymbol{y}_i = \boldsymbol{F}_{yi}\left(\boldsymbol{x}_s, \boldsymbol{x}_i, \boldsymbol{y}^i\right) + \boldsymbol{\epsilon}_{yi}\left(\boldsymbol{x}_s, \boldsymbol{x}_i, \boldsymbol{y}^i\right)$$

As an equivalent for the outputs $\boldsymbol{z}_i$ of the subsystem i we find:

$$\boldsymbol{z}_i = \boldsymbol{F}_{zi}\left(\boldsymbol{x}_s, \boldsymbol{x}_i, \boldsymbol{y}^i\right) + \boldsymbol{\epsilon}_{zi}\left(\boldsymbol{x}_s, \boldsymbol{x}_i, \boldsymbol{y}^i\right)$$

It is noted that linking variables follow from the subsystem boundaries and are not freely chosen. Output variables can be chosen freely by the user and can also include the linking variables.

When the introduced notation is applied to the ship propulsion system the blockdiagram as shown in Fig 2.12 arises. Note that the variables $\boldsymbol{x}_s$ and $\boldsymbol{x}_i$ are kept generic because they include all the model parameters. $\boldsymbol{z}_i$ is also kept generic since it represents all model outputs.

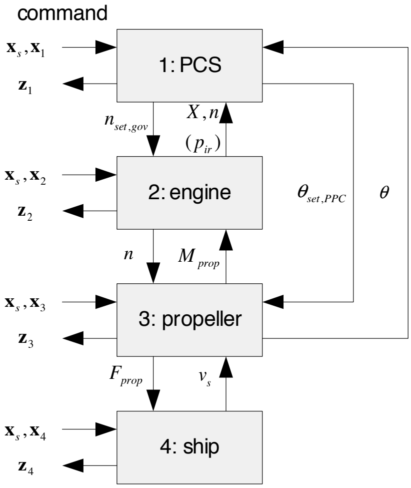
command
$\mathbf{x}_s, \mathbf{x}_1$
$\mathbf{z}_1$
1: PCS
$n_{set,gov}$
X, n
(p_{ir})
$\mathbf{x}_s, \mathbf{x}_2$
$\mathbf{z}_2$
2: engine
$\theta_{set,PPC}$
θ
n
M_{prop}
$\mathbf{x}_s, \mathbf{x}_3$
$\mathbf{z}_3$
3: propeller
F_{prop}
v_s
$\mathbf{x}_s, \mathbf{x}_4$
$\mathbf{z}_4$
4: ship

Figure 2.12: Blockdiagram of coupled subsystems of the conceptual ship propulsion plant, including linking variables

Chapter 3

Model Verification

3.1 Introduction

In the previous chapter the conceptual model was developed. This conceptual model is programmed in a simulation environment, resulting in the starting point of this chapter: the simulation model. The programming step often is not thoroughly discussed: it is simply not interesting from an academic point of view. Nevertheless the programming phase can seriously influence the outcome of the simulation model. The focus of this chapter lies on the verification of the ship propulsion simulation model, which is put in perspective in Fig 3.1. A definition of verification as used here is taken from ASME (2006):

> *Verification: The process of determining that a computational model accurately represents the underlying mathematical model and its solution.*

As discussed in Oberkampf et al. (2003), verification is preferably carried out by comparison against analytical solutions. Comparisons against other highly accurate numerical solutions can also be made, but in this case the quality of the accurate model output is of great importance.

Unfortunately analytical solutions to complex nonlinear systems are hard, if not impossible, to derive. Highly accurate numerical solutions may be present for specific sub-models, but not for the complete simulation model. Because of these difficulties in the formal verification of the ship propulsion simulation model, this chapter deals with a less formal verification: the results of the simulation model are checked for resemblance with the expectations of the modeler, without paying much attention to quantitative model output.

Another verification issue that is further left untouched here is the dependency of model output on the numerical solver and the solver-settings that are used. It should be ensured that the solution of the differential equations, given by the numerical solver, is independent of solver-choice and associated settings. This is comparable to required grid-independence of CFD model output. Solver difficulties related to stiff differential equations are dealt with in for instance Garfinkel et al. (1977). Modern simulation tools mostly include specialized stiff equation solvers that help to prevent numerical errors in the model output.

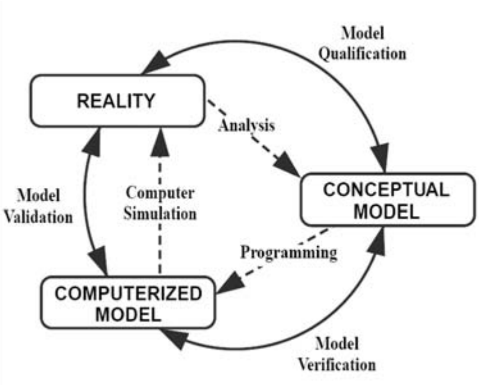

Figure 3.1: The relation between the conceptual model and the computerized simulation model. Source: Schlesinger (1979)

For complex systems it is advisable to verify the various sub-models individually before connecting them all together. In this case the verification of the individual sub-models was an ongoing process during the programming phase, of which the specific results are not shown here: the total simulation model is verified here at once. Since the static *and* the dynamic simulation results are of importance, it is chosen to verify them both. This requires two distinct types of tests:

1. First of all the static tests, that will reveal if trends in static behaviour are credible.
2. Secondly a dynamic test is carried out to investigate whether the dynamic behaviour of the system is credible.

3.2 Verification of Static Operating Points

In this section the static working points of the plant model are verified. Because the model is developed to be used in a wide variety of operating conditions, the verification domain is chosen large. Using crude calculation power, the model outputs for many static operating points are calculated. This necessitates the PCS to be disconnected from the plant model since the PCS simply does not allow for all desired operating points that need to be verified. Subsequently a set of 400 different governor- and pitch setpoints ($n_{set,gov}$ and $\theta_{set,ppc}$) are enforced as input to the uncontrolled model, while the resulting steady state system variables are stored in memory. It is noted that for the sole purpose of this test, the maximum allowed pitch angle limitation in the Propeller Pitch Controller (PPC) is relaxed by a parameter change.

In principle all stored variables can now be checked for their credibility. In this case it is chosen to focus on the linking variables between the various sub-models, as were shown in Fig 2.12 on page 24. The linking variables between the three lower sub-systems are: shaft speed n, pitch θ, propeller thrust F_{prop}, ship speed v_s, fuelrack position X, and propeller torque M_{prop}. For ease of verification the results are presented as contour plots in the phase plane spanned by the two enforced inputs $n_{set,gov}$ and $\theta_{set,ppc}$.

The results are shown in Fig 3.2 to 3.7. The following observations are made:

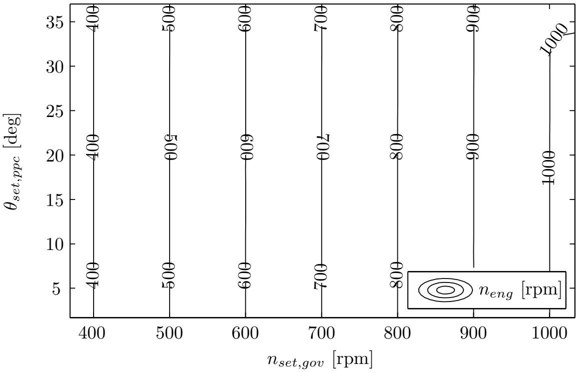

Figure 3.2: Static verification: engine speed n_{eng}

Shaft speed n: The shaft speed contours show that over almost the complete domain, the governor setpoint is reached. Only at the highest load the setpoint is not reached due to a fuel rack limitation in the governor. Note that in fact the engine speed is shown in Fig 3.2.

Pitch angle θ: The pitch angle contours show that the PPC in combination with the pitch hydraulics is capable of realization of the enforced pitch setpoint $\theta_{set,ppc}$ over the complete domain.

Single propeller thrust F_{prop}: Propeller thrust shows no irregularities, and as expected rises monotonously with pitch and shaft speed. As expected, zero thrust is found around 1.7 degrees pitch.

Ship speed v_s: Ship speed shows smooth monotonous behaviour in both directions, which agrees with the expectations.

Fuelrack position X: The fuelrack behaviour at higher loads agrees with the expectations. However, the unexpected non-monotonous behaviour around the low load and low speed (contourline of 8 mm) is given further attention. Inspection shows that this is caused by the fuelpump model: The engine driven fuelpump performance is relatively poor at low speeds: equal fuelrack setting at low engine speed results in less fuel injection per cycle than it would at higher engine speed. The result is that at equal pitch setting, a lower shaft speed needs more fuelrack.

The three small irregularities around 5 deg pitch are attributed to small irregularities in the lookup tables of the simulation model. These irregularities are not considered of importance since, in future simulations and measurements, operating points in this area are not expected.

Propeller torque M_{prop}: It is observed that propeller torque behaves well over the complete domain. Two small unexpected humps are visible around 5 degrees pitch angle. They are attributed to small irregularities in the lookup tables of the simulation model. These irregularities are not considered of importance since, in future simulations and measurements, operating points in this area are not expected.

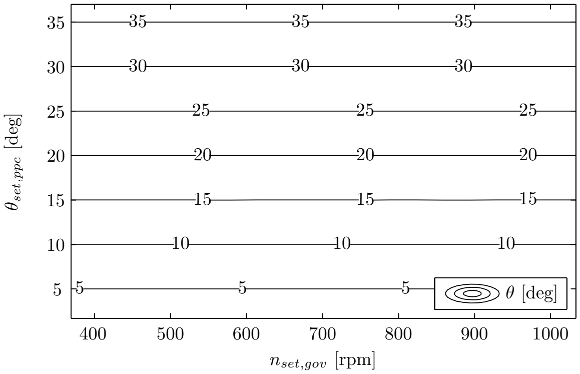

Figure 3.3: Static verification: propeller pitch θ

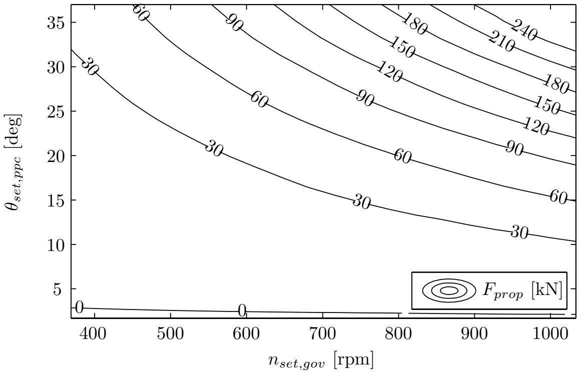

Figure 3.4: Static verification: single propeller thrust F_{prop}

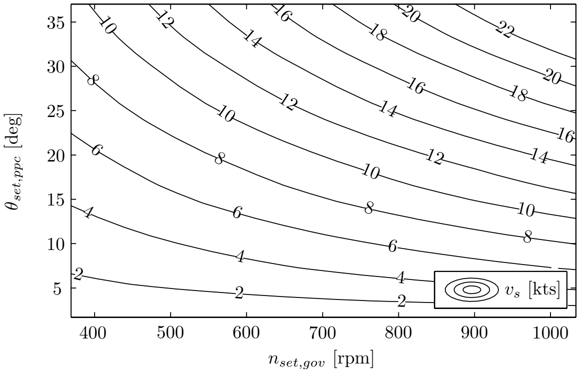

Figure 3.5: Static verification: ship speed v_s

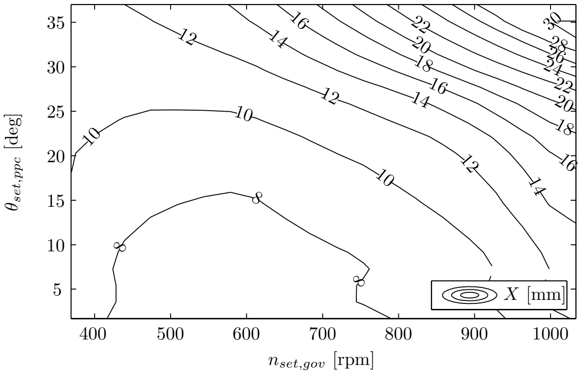

Figure 3.6: Static verification: fuel rack position X

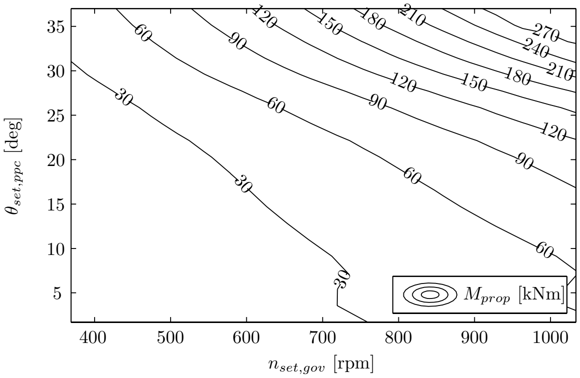

Figure 3.7: Static verification: propeller torque M_{prop}

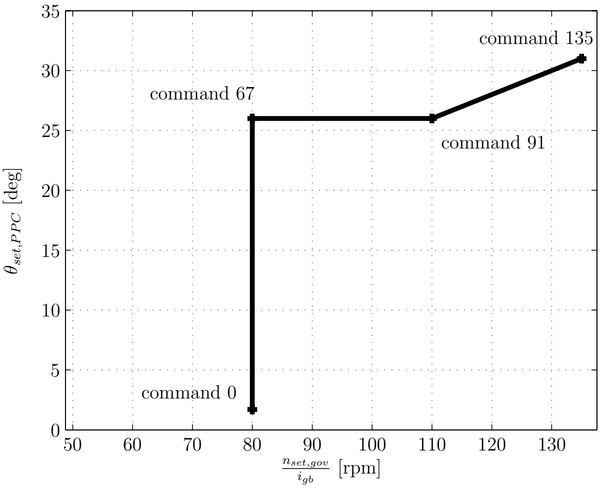

Figure 3.8: The combinator curve in the $n_{set,gov}$-$\theta_{set,ppc}$ plane. Note that $n_{set,gov}$ is scaled down to shaft speed

3.3 Verification of Dynamic Behaviour

In this section the dynamic behaviour of the propulsion plant is verified. Since the PCS has a big influence on the system dynamics, it is reconnected again so that the system as shown on page 24 can be verified as a whole.

Because it would be impossible to simulate all transients and the resulting unsteady system states, this verification is limited to some characteristic accelerations and decelerations. These manoeuvres are chosen such that they capture the three ”propulsion control regimes” that are dictated by the PCS. These three regimes are shown in Fig 3.8, by means of the so called combinator curve. This combinator curve shows the locus of static working points that the control system will try to effectuate, dependent on the command given by the user. First of all there is the constant shaft speed regime, where only pitch is increased with increasing command. Secondly there is the constant pitch regime, where only shaft speed is changed. Finally there is the regime where both shaft speed and pitch are changed following a change in command. The transition points between these three regimes are called (combinator)-nodes.

The characteristic manoeuvres that are considered for the dynamic verification are some of the transitions between the combinator nodes. The system variables that are verified here, are the same as in the previous section on static verification: fuelrack position X, propeller torque M_{prop}, propeller thrust F_{prop}, shaft speed n, propeller pitch θ and ship speed v_s. Since the system that is verified here includes the PCS, the following linking variables are added: setpoint governor $n_{set,gov}$ and the pitch setpoint $\theta_{set,ppc}$.

The *command*- input to the system is shown in Fig 3.9. As shown the following sequence of commands is simulated: $0 - 67 - 91 - 135 - 91 - 67 - 0 - 135 - 0$ rpm. Results of the manoeuvres are shown in Figs 3.10 to 3.15. The following observations are made:

Commanded and realized virtual shaft speed $n_{virt,set}$ and n_{virt}: The command is realized gradually. Sudden small hick ups around $t = 300s$ and $t = 450s$ occur

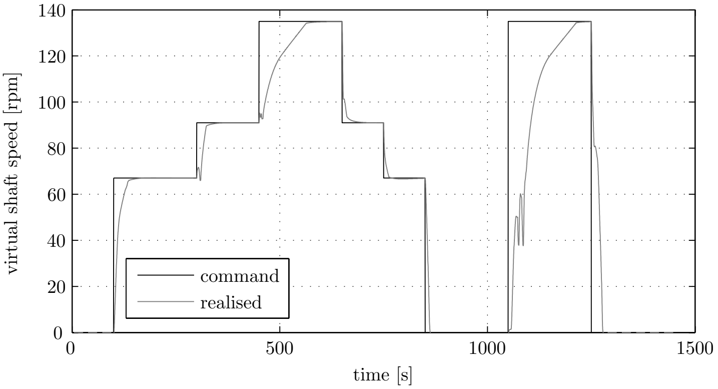

Figure 3.9: The verification of dynamic behaviour: virtual shaft speed n_{virt}

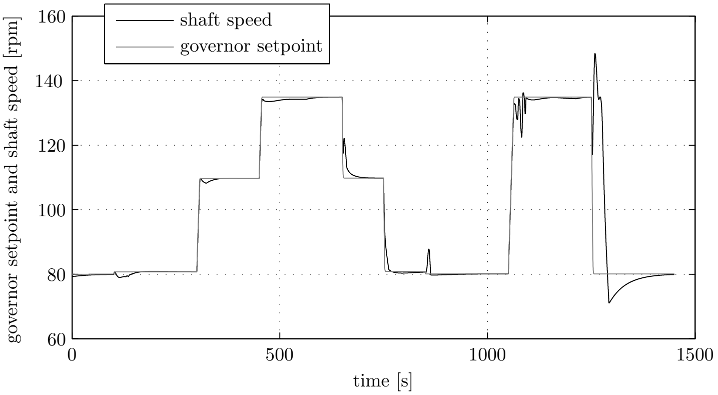

Figure 3.10: The verification of dynamic behaviour: shaft speed n

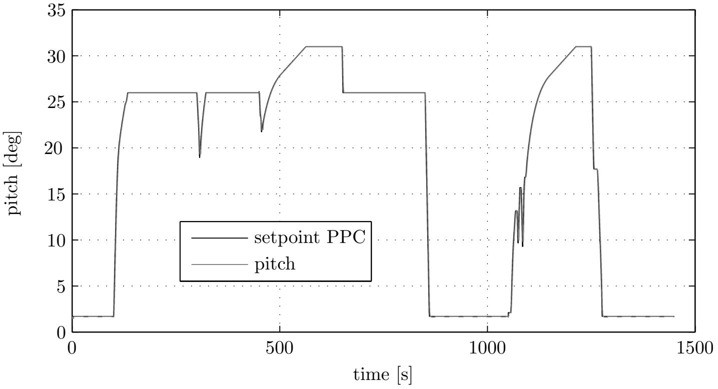

Figure 3.11: The verification of dynamic behaviour: pitch θ

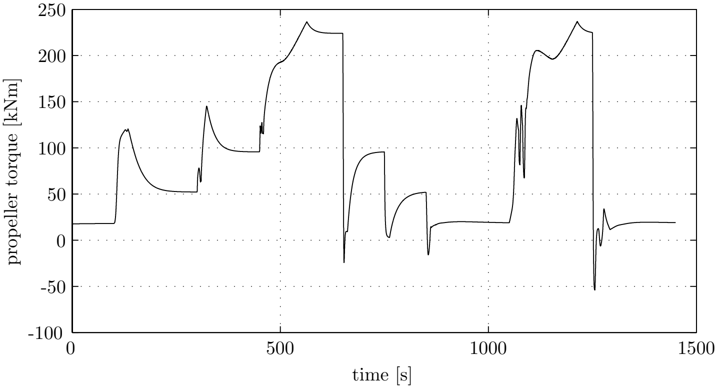

Figure 3.12: The verification of dynamic behaviour: propeller torque M_{prop}

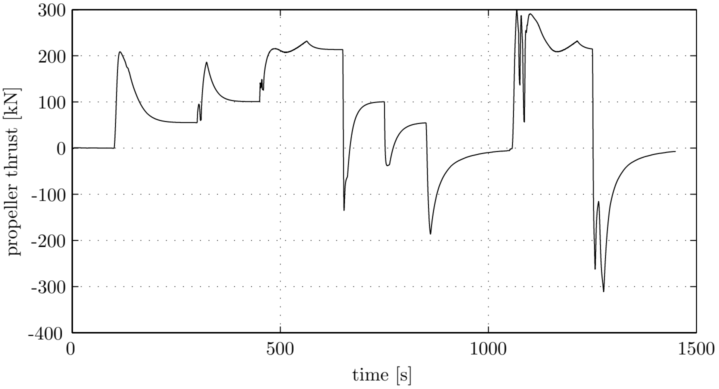

Figure 3.13: The verification of dynamic behaviour: thrust F_{prop}

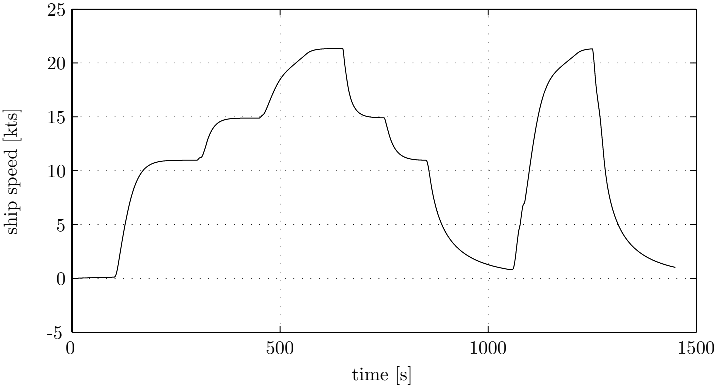

Figure 3.14: The verification of dynamic behaviour: ship speed v_s

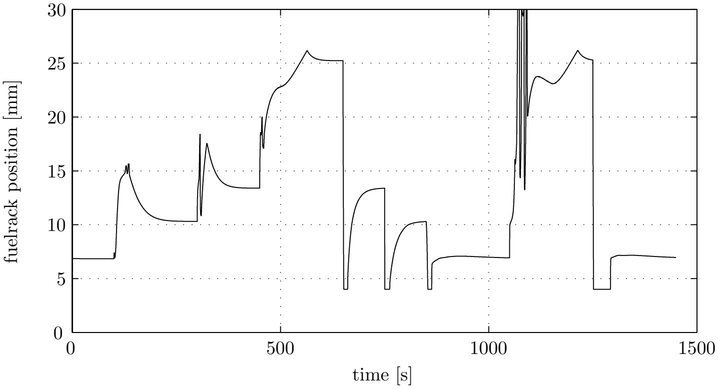

Figure 3.15: The verification of dynamic behaviour: fuelrack position X

during the start of an acceleration. They are caused by the active pitch reduction that is commanded by the PCS during the accelerations. Another oscillatory type of hick up occurs around $t = 1075s$, which is the result of a temporal shortage of available combustion air during the acceleration. This shortage leads to a temporal physical limitation of the delivered engine torque, while the governor increases the fuel injection. The increase of fuelrack is sensed by the PCS, resulting in a reduction of pitch to decrease the load. As the turbocharger picks up speed, more combustion air comes available, and the pitch can increase again.

Governor setpoint $n_{set,gov}$ and shaft speed n: The shaft speed follows the governor setpoint (reduced to shaft speed) well. On three occasions the windmill effect is visible. The first two times the upspin is relatively small compared to the third time. There, a big shaft speed increase up to 147 rpm is shown during the deceleration. This effect seems to be exaggerated compared to reality, but this issue is dealt with in the validation phase, where it will be shown that the predicted windmill behaviour in calm water agrees well with calm water measurements. As a result of the temporal shortage of combustion air, small shaft speed oscillations are visible around $t = 1075s$.

Pitch setpoint $\theta_{set,ppc}$ and pitch θ: The setpoint to the PPC shows big dips during accelerations around $t = 250s$ and $t = 450s$. This may seem strange for those without experience with the M-frigate-PCS, but active pitch reduction is one of the measures that has been taken to prevent engine overloading during acceleration. Around $t = 1075s$, the pitch shows a short oscillatory behaviour, which is commanded by the PCS to reduce the engine load, until sufficient combustion air is available.
The pitch follows the pitch setpoint with an approximate delay of 1 second. This seems credible.

Propeller torque M_{prop}: Propeller torque shows no unexpected behaviour except for the small irregularity around $t = 300s$, $t = 450s$ and $t = 1075s$, caused by active pitch reduction.

Propeller thrust F_{prop}: Just as the propeller torque, the propeller thrust shows no unexpected behaviour except for the small irregularity around $t = 300s$, $t = 450s$ and $t = 1075s$, also caused by active pitch reduction.

Ship speed v_s: Ship speed behaves as expected, although it seems that the maximum speed when sailing on the DE's is over-predicted. This is however not an issue for the verification phase but for the validation phase.

Fuelrack position X: The small irregularities around $t = 300s$ and $t = 450s$ are caused by active pitch reduction. The oscillations around $t = 1075s$ are the result of incomplete combustion, governor action and the resulting active pitch reduction. The oscillations that are predicted here are expected to be higher than in reality, since due to the simplicity of the engine model, the transitions between complete and incomplete combustion is of the on/off type here, while in reality it is expected that this is a gray area. A more complex simulation model is necessary to make accurate predictions under such conditions.

It is concluded that the dynamic results contain some features (the overestimated windmill effect) that not fully align with expectations. On the other hand, at this phase this cannot be settled as a modeling-flaw or fault. Only in a later phase of this project it was found that the predicted calm water windmill behaviour does agree well with reality.

It is noted that sometimes the process of verification, calibration and validation can be iterative since errors or shortcomings might only be identified in a later stage. Too often modeling errors are only found after a simulation model has been in use for many years.

3.4 Conclusions of the verification phase

Verification of complex non-linear dynamic systems is never complete. This is caused by the large amount of possible (un)steady system states that can never be checked in the complete application domain. Nevertheless the verification process does increase the confidence in the correct implementation of the conceptual model.

Both the static and dynamic behaviour of the simulation model are partially verified. Although some minor issues remain, results are satisfactory, meaning that the observed trends are credible and that the dynamic behaviour as observed largely agrees with the expected behaviour of the conceptual model that the author has in mind. It is acknowledged that this might not be obvious for those not familiar with the M-frigate propulsion control system.

Chapter 4

Model Calibration

4.1 Introduction

With the verified model available, the next step is to calibrate the simulation model. The calibration phase is necessary to improve agreement between the computational results and the experimental data that were obtained in a calibration experiment. By adjusting uncertain parameters of the simulation model, the level of agreement can often be improved significantly. It should however be kept in mind that shortsighted use of model calibration may result in the right model output for the wrong reason. Too often, model calibration is (unintentionally) used to cover up the weaknesses of the underlying conceptual (sub)models.

A definition of calibration is given in Thacker (2004):

> *Calibration: Process of adjusting numerical or physical modeling parameters in the computational model for the purpose of improving agreement with experimental data.*

Calibration is often referred to as tuning, matching or as parameter estimation or identification. These terms all refer to the same activity.

Calibration of a simulation model is only possible if measurements of the (partial) real system are available. For ship propulsion models, this is mostly the case. Even if the ship is not built yet, data on for instance engine performance or open water propeller data will already be available in some preliminary form. In this research project the ship under consideration was available for dedicated calibration measurements, which is a luxurious circumstance.

The design and execution of good calibration experiments should not be underestimated: often calibration is carried out using coincidentally available data, from non-dedicated trials, covering only small parts of the intended application domain of the simulation model. Good calibration experiments should be designed in such a way that they cover a large domain of the intended use of the model. Furthermore the experiments should focus on obtaining data that is useful for calibration of the unknown or uncertain parameters for which the model output is most sensitive. Pre-calibration simulations can help to reveal such parameters.

As will be shown in this chapter, calibration measurements should preferably capture all the linking variables between the submodels as well as the output variables that are related to the intended goals of the simulation model. In this way calibration of submodels can be performed individually, which helps to discover submodel weaknesses. This greatly decreases the risk of obtaining the right model output for the wrong reason.

Onboard "field experiments" evidently suffer from the lack of controlled conditions as opposed to "laboratory experiments". Use of rudder to stay on course, as well as wind and seastate can for instance not be canceled out during full scale experiments. Furthermore a "field measurement setup" has effect on the quality of the measured signals, especially because onboard data gathering is often restricted to the sensors that are already integrated in the propulsion plant. These issues with regard to onboard data gathering should be taken into consideration during the calibration and validation process.

4.2 Model Calibration Procedure

For reasons explained above, the subsystems as shown in Fig 2.12 on page 24 are calibrated independently. The PCS submodel is an exception: there is no need for calibration since it only contains exactly known mathematical equations and parameters.

Adopting the notation as introduced in Section 2.5, the procedure for calibration of an individual submodel i is as follows: Submodel i is disconnected from the bigger model, and measured linking variables $\boldsymbol{y}^i$ that are input to this subsystem are used as enforced input. By tuning one or more calibration parameters chosen from $\boldsymbol{x}_i$, it is attempted to get sufficient agreement for the linking variables $\boldsymbol{y}_i$ and all output variables $\boldsymbol{z}_i$ that are output of this subsystem. The amount of tuning that is applied should be dependent on both the desired quality of the model itself, as on the accuracy of the measurements.

If required agreement cannot be found for reasonable settings of $\boldsymbol{x}_i$, the conceptual model should be reconsidered through re-analysis of reality. This might possibly lead to adjustment of the conceptual model, and re-programming of parts of the simulation model.

4.2.1 Calibration Experiment Description

For the calibration of the various submodels a dedicated full scale calibration measurement was carried out. The manoeuvre that was performed is a so called piecewise acceleration/ deceleration test that was already introduced in Section 3.3. This test was designed and chosen since it captures both low, middle and high ship speeds and accompanying static working points. Several types of relatively small transients are included as well as two big transients. The test is relatively simple to perform, since the same commands are used multiple times as input to the PCS.

During the calibration measurements on the North Sea the seastate was significant (seastate 4-5), which emphasizes the field-experiment character of the test. Onboard sensors were calibrated before departure, using standard calibration procedures. However, even after calibration of the sensors, the thrust and torque measurements remain quite uncertain because no accurate reference measurements were available.

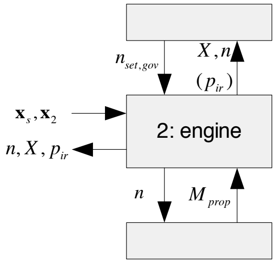

Figure 4.1: Engine submodel that is to be calibrated

4.2.2 The Engine Submodel

The general calibration procedure that was described above is now applied to the engine submodel shown in Fig 4.1. The output variables $\boldsymbol{z}_i$ of this submodel are: shaft speed n, fuelrack position X, and inlet receiver pressure p_{ir}.

As the introduced calibration procedure dictates, the engine submodel is disconnected from the total model. Measured values of linking variables that are input to this subsystem ($n_{set,gov}$ and M_{prop}) are fed into the disconnected submodel, and are shown in Figs 4.2 and 4.3. By tuning with the calibration variables for which the output variables are expected to be sensitive, it is attempted to get good overall agreement. Resulting agreement between measurement and simulated output variables is shown in Figs 4.4 to 4.6. To obtain this agreement the parameters gearbox efficiency η_{gb} and fuelpump leakage factor $\eta_{fuelpump}$ had to be adjusted, as listed in Table 4.1. Note that $\eta_{fuelpump}$ is defined as an overall multiplication factor to the fuelpump lookup table output.

Shaft speed n in general aligns well with the measurements. Measured shaft speed seems to exceed the simulated value by approximately 1 rpm, which might easily be caused by inaccurate sensor calibration. Around $t = 1520s$ the windmill effect makes the shaft spin up only slightly in reality, but the simulation seriously exaggerates the windmill-effect here. Although in this phase this might indicate a modelling flaw or fault, other (calm water) measurements presented in Fig 7.10 in Chapter 7 reveal that the predicted windmill effect agrees well with reality. This indicates that the small measured windmill effect that is presented here can be attributed to dynamic wave induced propeller torque variation. It is expected that a comparable deceleration in the same seastate, at another point in time can easily lead to a measured windmill effect that is greater that predicted.

Closer inspection of the shaft speed does show another difference between measurement and simulation. Over the complete interval the measured shaft speed shows more variations than the simulated shaft speed. This seems strange since the fuelrack position does show good agreement (except for three specific intervals). A possible explanation is given here. First of all the good agreement in fuelrack position indicates that the same engine torque is generated. Because not only the driving engine torque, but also the propeller torque is the same for the simulation and for the measurement, no difference in shaft speed should be expected. If the propeller torque is well measured and the engine torque is well modeled, the difference in shaft speed behaviour might be explained by torsional vibrations of the shaft system, which end up in the shaft speed measurement. Due to the rigid shaft approach, such vibrations are not included in the model.

A different type of difference is visible in the fuelrack graph. The fuelrack position aligns

	Original value	Adjusted value
η_{gb}	1	0.93
$\eta_{fuelpump}$	1	0.9

Table 4.1: Calibrated Engine submodel parameters

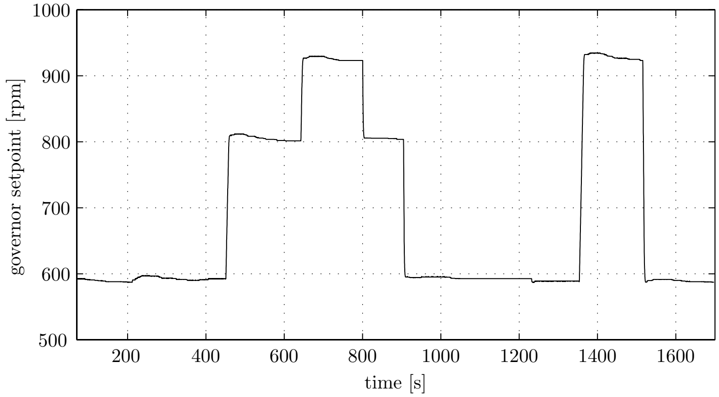

Figure 4.2: Enforced input of the engine model: governor setpoint $n_{set,gov}$

well in the range above $10mm$. In the intervals 100-200s, 1250-1350s and 1550-1700s the simulation shows a wiggle that is not present in reality. This oscillation stems from the measured propeller torque that is enforced onto the engine model. It is hypothesized that in those intervals, the measured torque oscillation does not accurately represent the actual propeller torque during the trial. This thought is strengthened by the fact that during these intervals the oscillations in measured thrust and torque show completely different periods, while these periods largely align in the intermediate intervals (measured thrust is shown in Fig 4.12). The relatively coarse signal resolution of the torque measurement might play a role here.

The inlet receiver pressure p_{ir} aligns reasonably well over the complete range.

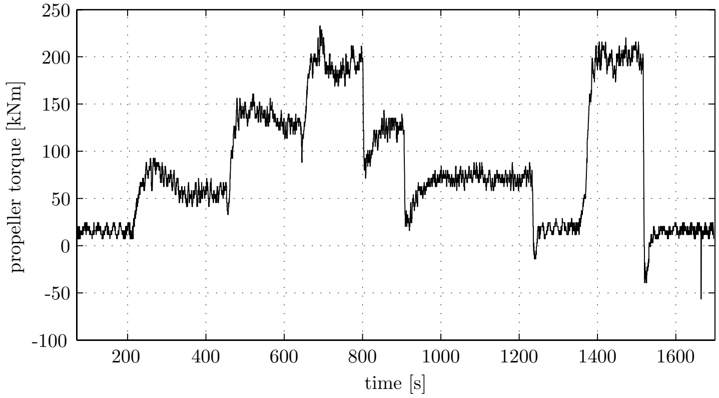

Figure 4.3: Enforced input of the engine model: propeller torque M_{prop}

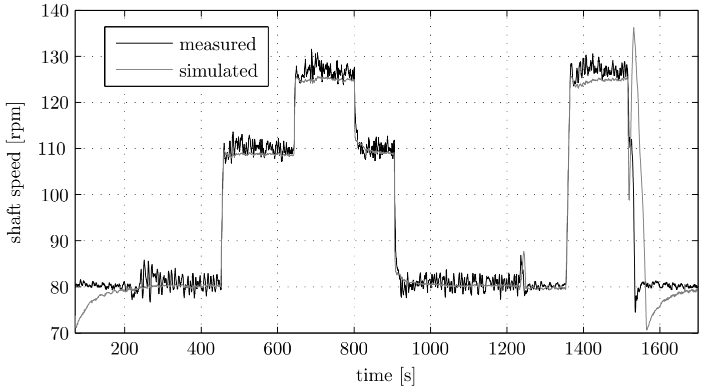

Figure 4.4: Output of the calibrated engine model: shaft speed n

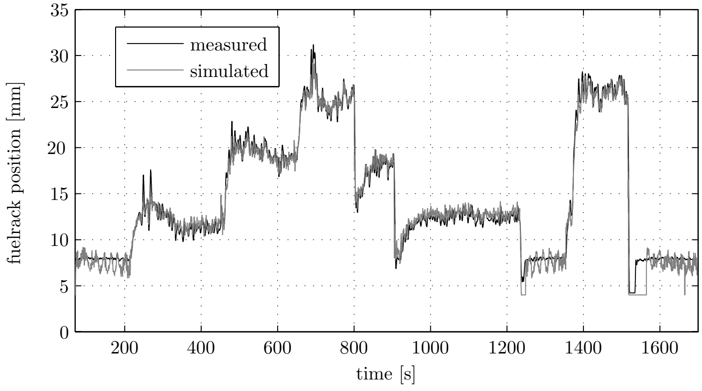

Figure 4.5: Output of the calibrated engine model: fuelrack position X

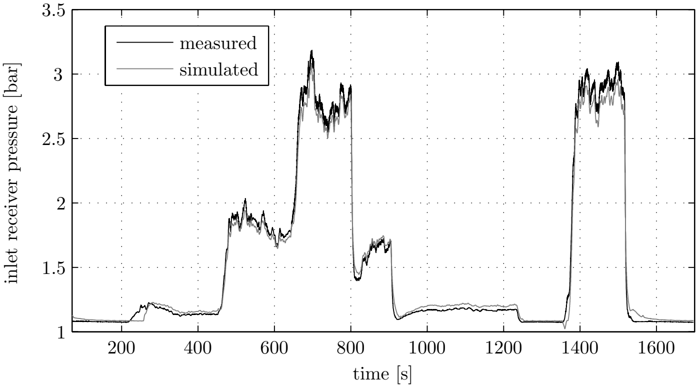

Figure 4.6: Output of the calibrated engine model: inlet receiver pressure p_{ir}

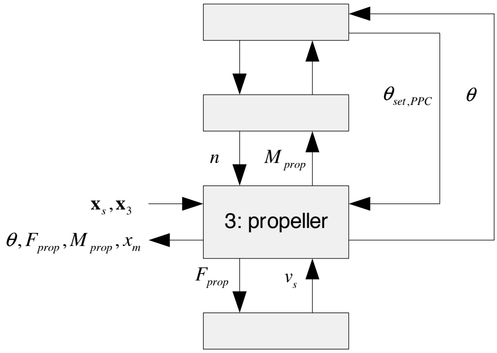

Figure 4.7: The propeller submodel that is to be calibrated

4.2.3 The Propeller Submodel

The blockdiagram of the propeller model is shown in Fig 4.7. The actual measured variables n, v_s and $\theta_{set,ppc}$ are fed into the disconnected propeller model and are shown in Figs 4.8, 4.9 and 4.10. The output variables of this subsystem are: pitch θ, propeller torque M_{prop}, propeller thrust F_{prop} and main valve position x_m, which are shown in Figs 4.11 to 4.14. Note that no calibration is applied to this submodel, because the uncalibrated model outputs already agree well with the calibration-measurement data.

Fig 4.11 shows that propeller pitch aligns well. Small differences are attributed to uncertainty in pitch measurement, and to a lesser extent to a small dead band in the Propeller Pitch Controller (PPC). Simulated thrust shown in Fig 4.12 seems to be on the low side at lower values, but has good agreement at higher values. The same observation is made for the propeller torque signal shown in Fig 4.13. Especially the low simulation results around $t = 800 - 1200s$ seem to be caused by a small differences in pitch angle that is visible in that interval.

Furthermore it is observed that, in specific time-intervals, the simulated torque values are more noisy than the measured torque values. Inspection of the enforced input signals shows that this is caused by the noisy enforced inputs n and v_s. Especially the measured ship speed signal v_s is uncertain. First of all the ship speed through the water is measured midships, by means of an Electro Magnetic (EM)-log. This type of device measures the speed of the water flow by means of an induced potential difference between two pickup points that are submerged in the water. This means that local disturbances due to ship motions, manoeuvres and/or orbital velocities end up in the speed signal. In the simulation model the measured signal is used as input to the simple wakefield model given by $v_a = v_s(1 - w)$. Since v_a is used in the calculation of propeller thrust and torque, differences can thus partly be attributed to the source of the signal v_s.

Taking into account the uncertainty in measured signals v_s, M_{prop} and F_{prop}, as well as θ, no calibration is applied to the propeller model. True need for calibration can only be assessed if calm water measurements, using well calibrated sensors, are available.

To get a feeling for the quality of the simulated CPP-main-valve-position x_m, its agreement with reality is presented in Fig 4.14. Its excursions seem to be simulated quite well, but its behaviour around the neutral position differs. First of all the mean position during the measurement doesn't lie at 0 mm, which indicates leakage in the hydraulic system

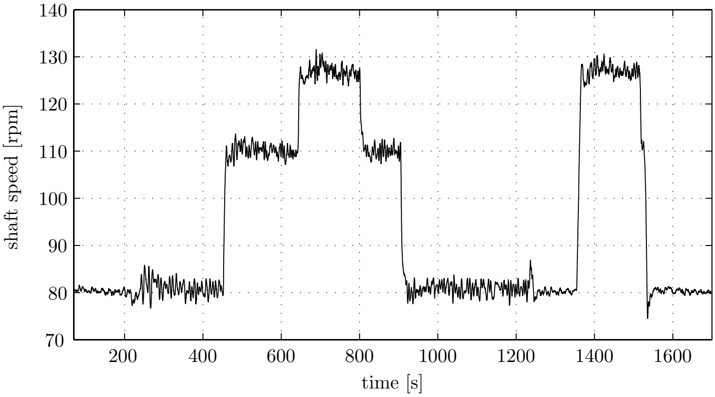

Figure 4.8: Enforced input of the propeller model: shaft speed n

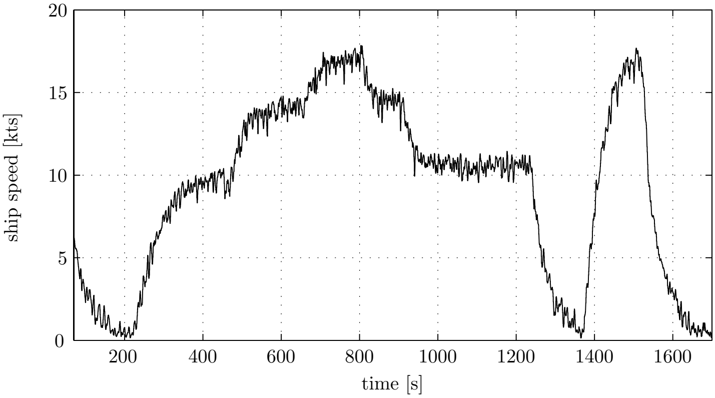

Figure 4.9: Enforced input of the propeller model: ship speed v_s

or possibly a sensor-calibration bias. Another difference is the nervous behaviour of the simulation around the neutral position. This is explained by the fact that the simulation model does not contain a Counter Balance Valve (CBV) in the hydraulic system, so that the modeled main hydraulic valve is continuously balancing the oil flow to and from the yoke. This signal is however not further dealt with since it was not directly related to the modeling goals.

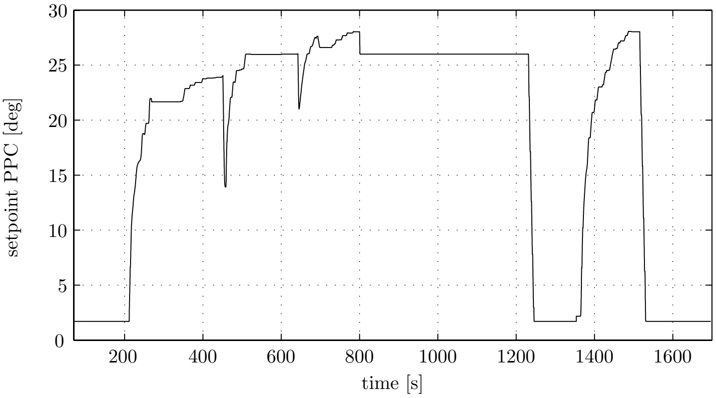

Figure 4.10: Enforced input of the propeller model: pitch setpoint $\theta_{set,ppc}$

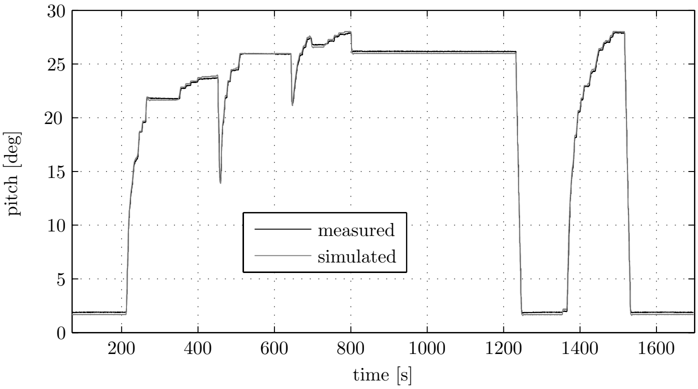

Figure 4.11: Output of the calibrated propeller model: pitch θ

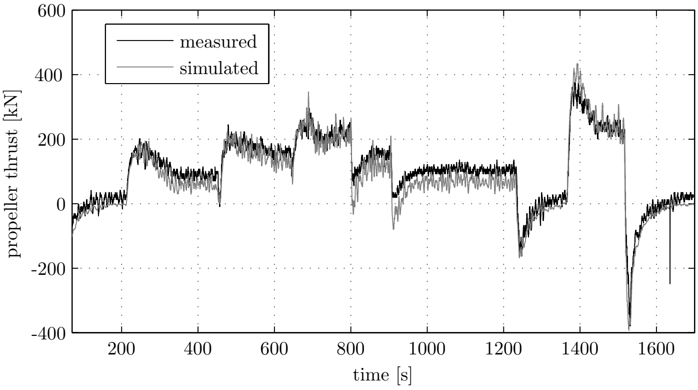

Figure 4.12: Output of the calibrated propeller model: single propeller thrust F_{prop}

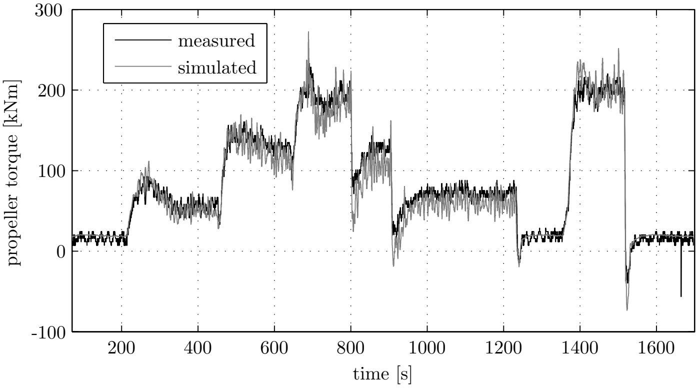

Figure 4.13: Output of the calibrated propeller model: torque M_{prop}

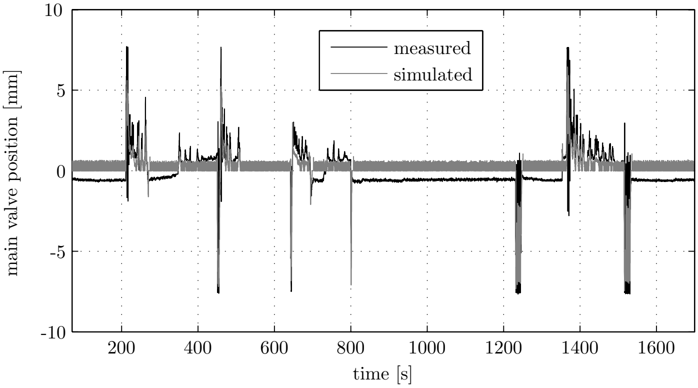

Figure 4.14: Output of the calibrated propeller model: main valve position x_m

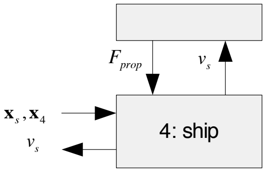

Figure 4.15: The ship submodel that is to be calibrated

	original value	calibrated setting
α_R	1	1.35
R_0	0 [kN]	30 [kN]

Table 4.2: Calibrated ship-sub model parameters

4.2.4 The Ship Submodel

The blockdiagram of the ship submodel is shown in Fig 4.15. Although this blockdiagram only shows one input F_{prop}, it is emphasized that this is the sum of port- and starboard thrust $F_{prop,ps}$ and $F_{prop,sb}$, which are both shown in Fig 4.16. The resulting ship speed is calibrated using the resistance disturbance parameters α_R and R_0 that have effect on ship resistance via:

$$F_{ship} = \alpha_R F_{ship,0} + R_0$$

It is found that reasonable agreement of measured and simulated ship speed is achieved by setting $\alpha_R = 1.35$, and $R_0 = 30kN$, as listed in Table 4.2. A resistance increase of 35% may seem high, but it should be kept in mind that the calibration test was carried out in seastate 4-5.

The measured and simulated ship speed are shown in Fig 4.17. Ship speed discrepancies are quite large around $t = 350s$ and $t = 1450s$. Further analysis showed that this was caused by use of ≈ 35 degrees rudder as ordered by the helmsman as shown in Fig 4.18. The use of rudder was necessary to bring the ship back on course after a period of low ship speed. Other discrepancies around $t = 200s$, $t = 1100s$ and $t = 1350s$ are likely caused by unknown, un-modeled (dynamic) resistance sources such as for instance resistance disturbances caused by fluctuating wind loads or (second order) wave forces acting on the hull.

The noisy ship speed measurement is explained by the nature of the ship speed sensor, as discussed in the section on propeller-model calibration.

4.3 Final Total Model Calibration

Based on the presented submodel calibration results, it might be expected that the reconnected total model gives approximately the same agreement between computation and measurement. This is however not necessarily true due to the propagation of errors. To demonstrate this, let us consider a steady state operating point of the blockdiagram shown in Fig 4.19. Let us assume that the unknown exact model has parameters $a = 2$ and $b = 3$. Further assume that the measurements during the calibration experiment contain no uncertainty. We now start calibrating parameters a and b at submodel level, and we

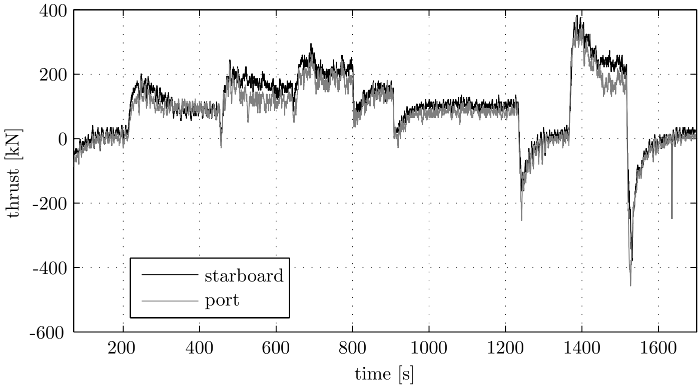

Figure 4.16: Enforced inputs of the ship model: portside and starboard propeller thrust F_{prop}

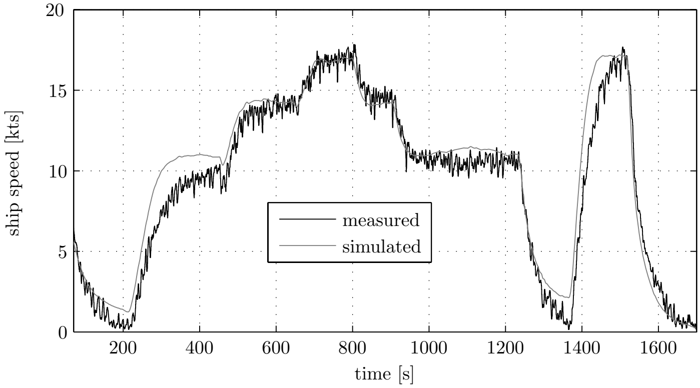

Figure 4.17: Output of the ship model: ship speed v_s

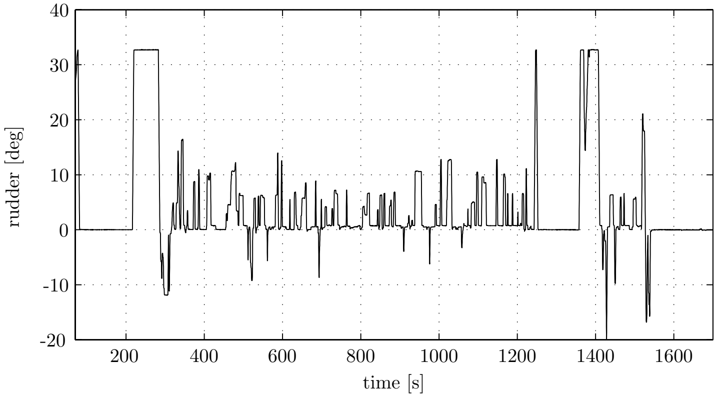

Figure 4.18: Use of rudder during the full scale calibration experiment. Since the two rudders were operated simultaneously (coupled mode) only the mean rudder angle δ is shown

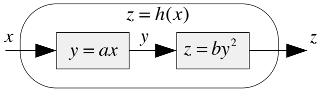

Figure 4.19: Effect of local sensitivities on model calibration

stop with adjusting the estimated parameters $\tilde{a}$ and $\tilde{b}$ as soon as the submodel outputs have a relative error of 5%. For sub model 1 this means that:

$$\frac{\tilde{y}(x)}{y(x)} = \frac{\tilde{a}x}{ax} = 0.95 \Rightarrow \tilde{a} = 0.95a$$

In the same way we find:

$$\frac{\tilde{z}(y)}{z(y)} = \frac{\tilde{b}y^2}{by^2} = 0.95 \Rightarrow \tilde{b} = 0.95b$$

Using these estimated parameters $\tilde{a}$ and $\tilde{b}$, we now determine the relative error between simulated and measured total model output noted by $\tilde{h}$ and h:

$$\frac{\tilde{h}(x)}{h(x)} = \frac{\tilde{b}\tilde{a}^2x^2}{ba^2x^2} = \frac{\tilde{b}}{b} \cdot \left(\frac{\tilde{a}}{a}\right)^2$$

The latter equation shows that the relative error has increased from 5% at submodel level to

$$100\% \cdot \left(1 - 0.95 \cdot 0.95^2\right) \approx 14\%$$

at the total model level. Submodel sensitivities determine the propagation of errors through the model. This includes both the parameters sensitivities as sensitivities to linking variables. A mathematical approach to determine the propagation of uncertainty through complex multidisciplinary simulation models is described and applied in Vrijdag et al. (2007). There, the uncertainty propagation is used to determine the uncertainty in computational output, as will be shown to be necessary for validation at a reasonable quality level. From the simplified example given here, it becomes clear that propagation of uncertainty and bias-errors are already important in the calibration phase, and not only in the validation phase. Good calibration at submodel level does not necessarily mean good calibration at total model level. It might be questioned whether a calibration at submodel level is still worth the effort, if it is unclear whether a good calibration will result in a good overall calibration. The answer is that the big advantage of calibration at submodel level is that it can ensure that disagreements between simulation and measurement are attributed to the right submodel. It might however be necessary to fine-tune the calibration parameters in a total (re-connected) model to compensate for insufficiently accurate submodel calibration or for inaccurate or biased calibration measurements.

To test whether further fine-tuning of parameters is necessary, the 4 submodels are reconnected (including the PCS), and the same calibration simulation as before is run again. The results show that, even though the submodel calibration is qualitatively judged as *very good*, there is a significant increase of disagreement between the simulation and the measurement. Further inspection showed that the disagreement is most probably caused by the underestimated values of F_{prop} and M_{prop}. In hindsight this might already have been

	original value	calibrated setting
η_{gb}	1	0.93
$\eta_{fuelpump}$	1	0.9
α_R	1	1.35
R_0	0 [kN]	30 [kN]
α_w	1	1.2

Table 4.3: Overview of all model parameters that were used for calibration

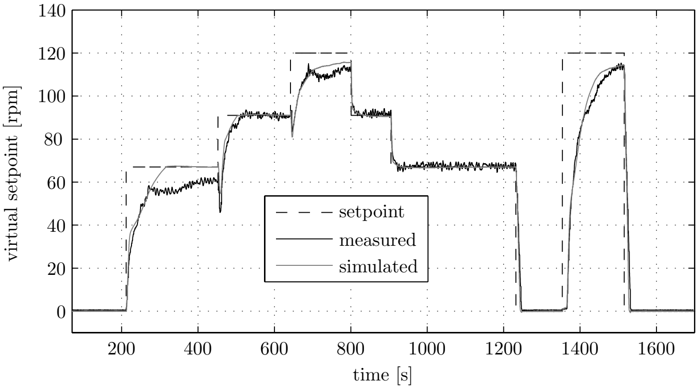

Figure 4.20: Input and realisation of the total model: command $n_{virt,set}$ and virtual shaft speed n_{virt}

concluded from Figs 4.12 and 4.13. In that phase however no calibration of the propeller submodel was applied: this was considered inappropriate because of the observed level of agreement combined with the assumed uncertainty in the measurements.

To improve the agreement in thrust and torque an appropriate calibration parameter is sought. It is reasoned that the small disagreement is likely to be caused by the parameter settings of the wakefield model. To calibrate this model, a calibration parameter α_w is introduced, which is applied as follows:

$$v_a = v_s \cdot (1 - \alpha_w w)$$

By trial and error it is found that good overall agreement is found for $\alpha_w = 1.2$. It is however noted that the agreement of thrust and torque could also be improved by calibrating the open water diagram itself.

The final parameter settings of the calibrated total model are presented in Table 4.3. Final overall calibration results are presented in Figs 4.21 to 4.30. These results have been obtained using the command as given in Fig 4.20. Note that the measured rudder signal as used during the calibration experiment was already shown in Fig 4.18 on page 46.

The measured propeller pitch is lagging in the interval 250-450s, which is the result of the reaction of the PCS on the temporary high engine load due to the use of rudder. The simulated shaft speed again shows an exaggerated windmill effect around t=1500s, of which the reason was given in this chapter. Other variables show agreement that will be quantified in the validation phase.

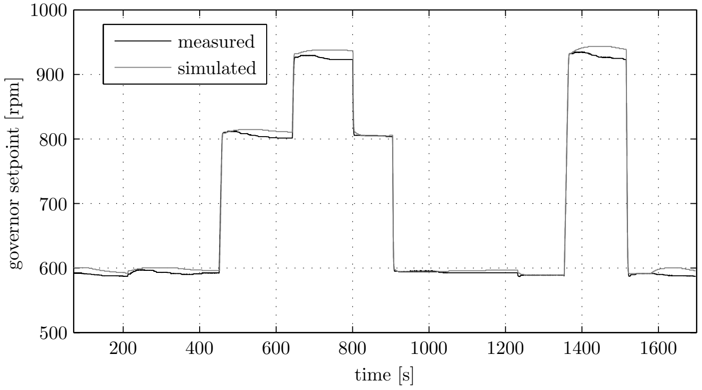

Figure 4.21: Total model output: setpoint governor $n_{set,gov}$

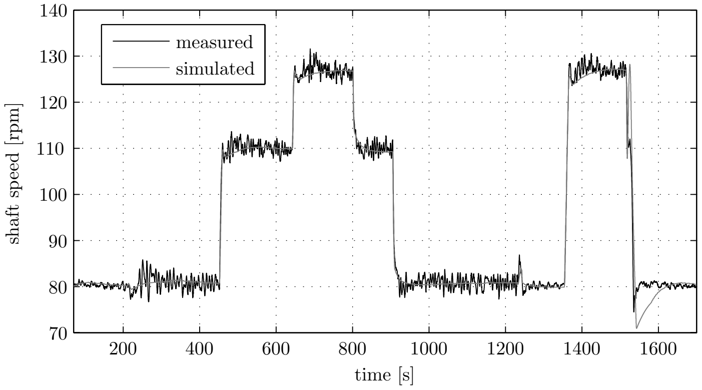

Figure 4.22: Total model output: shaft speed n

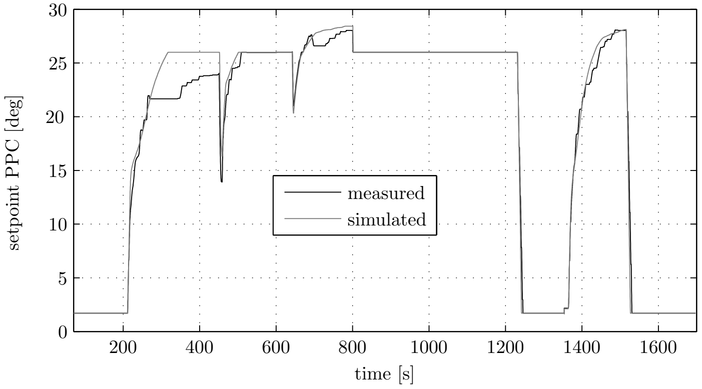

Figure 4.23: Total model output: setpoint Propeller Pitch Controller (PPC) $\theta_{set,PPC}$

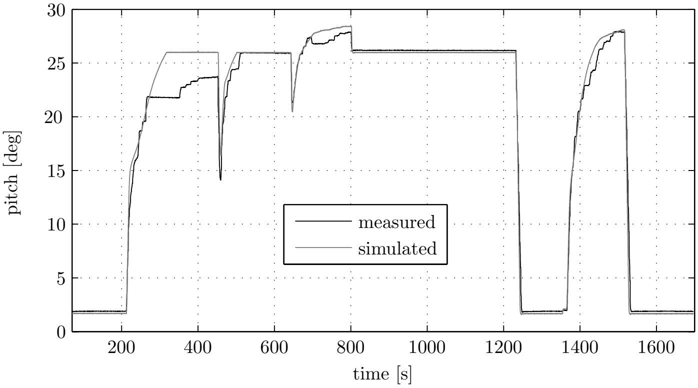

Figure 4.24: Total model output: propeller pitch θ

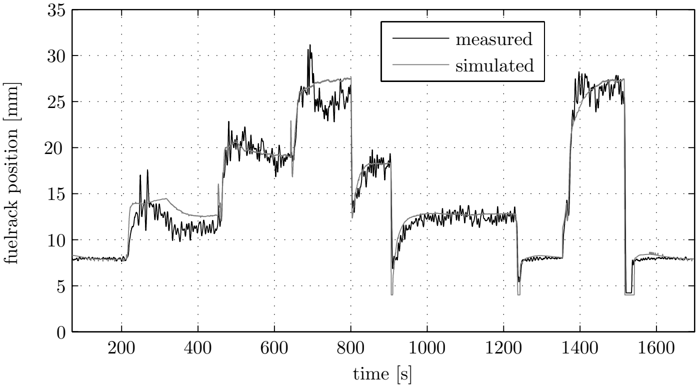

Figure 4.25: Total model output: fuelrack position X

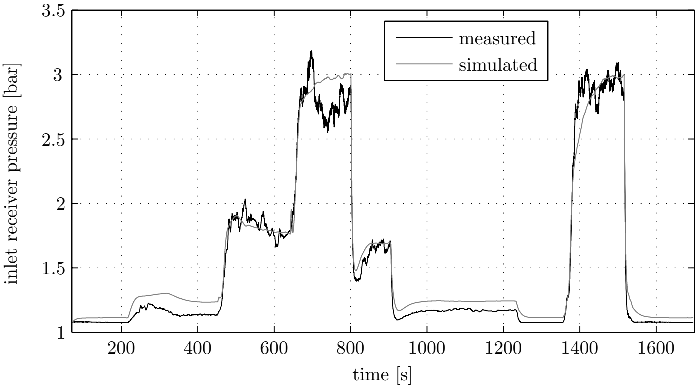

Figure 4.26: Total model output: inlet receiver pressure p_{ir}

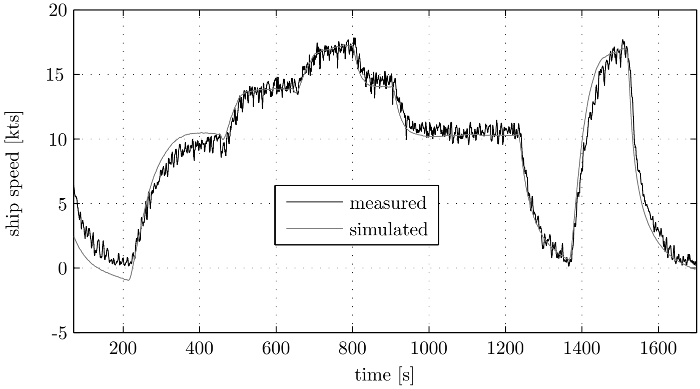

Figure 4.27: Total model output: ship speed v_s

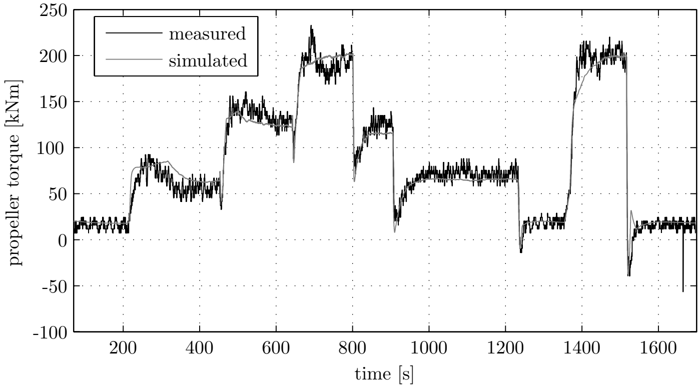

Figure 4.28: Total model output: propeller torque M_{prop}

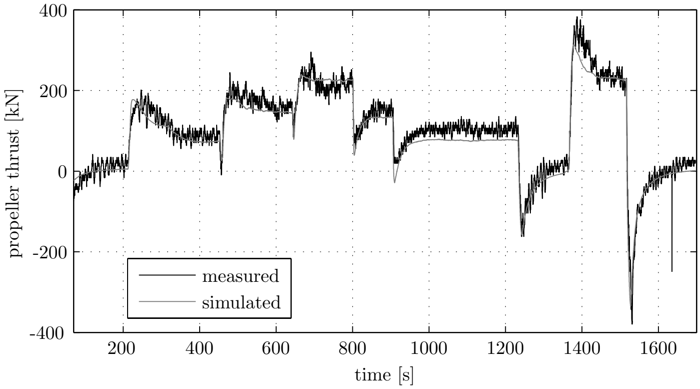

Figure 4.29: Total model output: propeller thrust F_{prop}

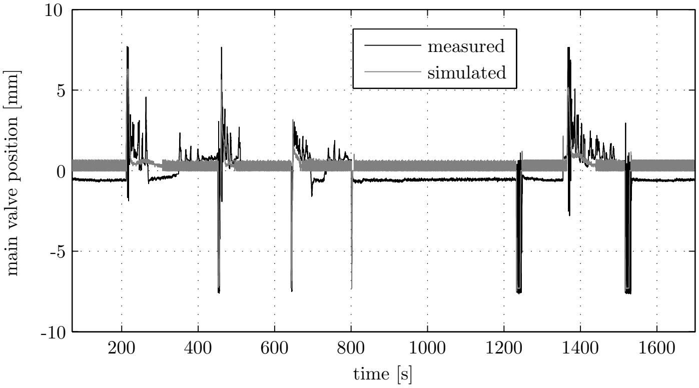

Figure 4.30: Total model output: main valve position x_m

4.4 Discussion

Calibration is an overdetermined optimization problem since it has more tunable input parameters than output variables that need to agree with full-scale measurements. This gives the user the freedom to pick specific calibration parameters that are deemed suited for the job.

The task of calibration is greatly simplified if the linking variables $\boldsymbol{y}_{ij}$ between the various submodels have been measured during the calibration experiment. Submodels can then be calibrated individually, so that model-issues can be attributed to specific submodels.

There is a balance between the number of individual submodels that should be defined, and the level at which calibration is performed. On the one hand a coarse submodel distribution can easily result in good results for the wrong reason. Possibly a very fine submodel distribution can prevent this. In that case however, good calibration can only take place if many variables (including all linking variables) have been measured in the calibration experiment.

Due to sensitivity of submodel i for its input variables $\boldsymbol{y}^i$, it might occur that after reconnecting the calibrated submodels, unexpected disagreement between measurement and total model computations occur. A final calibration step is then necessary to improve the agreement. This issue shows that model sensitivities are not only important for validation, but can also already play a big role in the calibration phase.

Even if perfect measurements of all the necessary variables would be available, it is still impossible to obtain a perfectly calibrated model simply because a simulation model can never capture all phenomena that are of influence to the ship propulsion performance. This is the most important reason why the calibrated model as developed here does not give a perfect match in all operating points. Nevertheless the agreement seems to be acceptable from a qualitative point of view, which will be quantified in the next chapter on validation.

Chapter 5

Model Validation

5.1 Introduction

The goal of a simulation model is to make predictions of real life system behaviour. Since a simulation model can never fully capture the complex physical phenomena that contribute to this system behaviour, simulation predictions are always wrong, in the sense that they never perfectly agree with reality. Nevertheless simulation models can still be used, as long as the user has some idea of how well the model-predictions agree with reality.

Validation assesses the agreement of simulation results with experimental data (see Fig 5.1). The purpose of this validation is to justify a certain level of confidence in model predictions. The better the overlap between the validated domain and the application domain, and the better the understanding of the underlying physical (and mathematical) principles, the stronger the inferences with respect to model prediction accuracy can be. Fig 5.2 illustrates the effect of validation and application domain on the strength of inference. Clearly the inference in the non-overlap case can be less firm, than in the full-overlap case. The relation between validation, prediction and inference, is put in perspective in Fig 5.3.

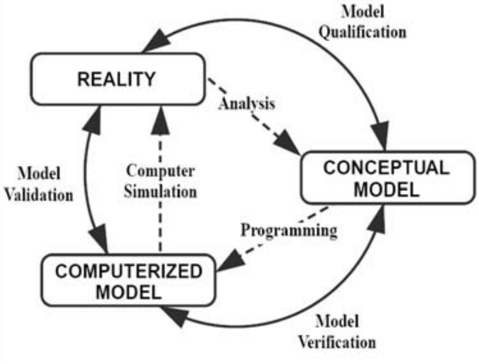
Model
Qualification
REALITY
Analysis
CONCEPTUAL
MODEL
Model
Validation
Computer
Simulation
Programming
COMPUTERIZED
MODEL
Model
Verification

Figure 5.1: Validation of the simulation model. Source: Schlesinger (1979)

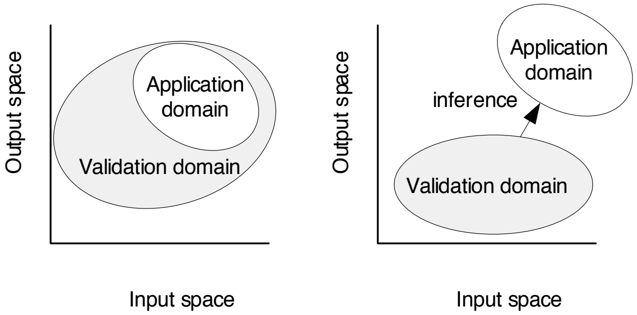

Figure 5.2: Difference in justified confidence level based on validation and application domain. Figure based on Easterling (2001) and Oberkampf et al. (2003)

The upper part of the figure illustrates the prediction process, while the lower part deals with the validation process. Validation takes place by quantification of the agreement between experimental data and data generated by the computational model. This gives some idea of the accuracy of the simulation results. Predictions are made by using the simulation model for cases without available experimental validation data. The notion of accuracy of the simulations that was obtained by means of validation can then be taken into account while assessing the outcome of model predictions.

A possible definition of validation is given in ASME (2006):

> *Validation: The process of determining the degree to which a model is an accurate representation of the real world from the perspective of the intended uses of the model.*

Based on Trucano et al. (2006) a prediction is defined here as follows:

> *Prediction: A calculation that predicts a number or quantity or a collection of these quantities prior to or instead of their physical measurement.*

5.2 Validation

In validation, the quantification of the ”degree of agreement” takes place using so called validation metrics. Validation metrics are computable measures that quantify the agreement between computational and experimental results. One or more validation metrics can thus quantitatively define the ”degree of agreement”, and should preferably take into account the uncertainties involved in the comparison of computational results and experimental data.

Traditionally applied validation metrics mostly focus on the validation of one or more steady state operating points. This process is illustrated in Fig 5.4, showing increasing quality of validation. In the first level, where contour plots of specific output variables in a specific input-domain are compared side by side, one can hardly speak of validation. The comparison is very subjective, with the result depending on the eyes and mindset of the

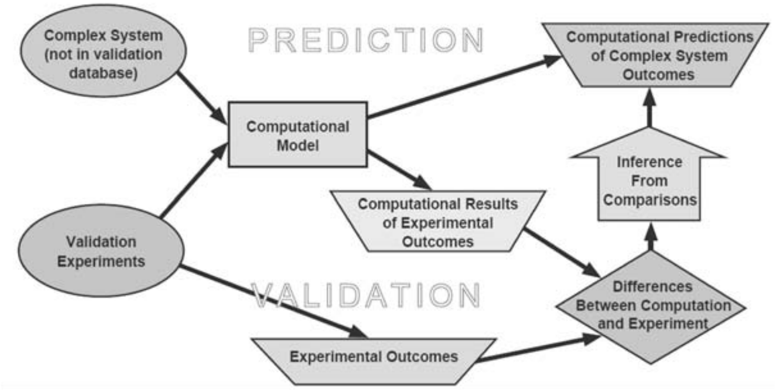
Complex System (not in validation database)
PREDICTION
Computational Predictions of Complex System Outcomes
Computational Model
Inference From Comparisons
Computational Results of Experimental Outcomes
Validation Experiments
VALIDATION
Differences Between Computation and Experiment
Experimental Outcomes

Figure 5.3: Relationship between validation and prediction. Source: Oberkampf and Trucano (2002)

observer. The most common type of validation is shown in the second figure, comparing computed and measured results without showing extra information on the uncertainty intervals. Also in this type of validation, the outcome is dependent on the observer, who may subjectively state that the results "match reasonably well", and show "the right trend". Further figures show increasing levels of validation quality, where figures e and f basically give the same information, showing the uncertainties in measurements and simulations, both in the output as in the input direction. From this discussion on the relation between uncertainty quantification and validation it should become clear that uncertainty analysis is a necessary activity to enable fair validation.

Validation of dynamic model output is a less explored field than the validation of static operating points. Often, dynamic behaviour of a simulation model is judged qualitatively by means of comparison of measured and simulated time-histories. Experts express their opinion on correspondence in terms as "reasonably well" or "fairly good", without quantitatively defining the level of agreement.

In this chapter both the static and the dynamic behaviour of the simulation model are validated. To asses the "static" validity at a reasonable quality level, an uncertainty analysis is carried out. Uncertainty in measured system outputs is quantified by means of expert opinion. A validation metric that takes uncertainty in both model and measurement into account is used to quantify the local ("static") model validity.

To quantify the agreement of transient responses, two other validation metrics are found in literature and will be used here. Development and use of such "dynamic" metrics is not yet as widespread as for the "static" metrics, and their early stage of development is reflected by their inability to incorporate model- and measurement uncertainties. It is however expected that the growing need for objective agreement-quantifiers will drive further development in the future.

5.2.1 Theory of Validation of Static Operating Points

Validation of static operating points concerns the quantification of agreement of computed and measured static operating points. In the following sections the approach to this quan-

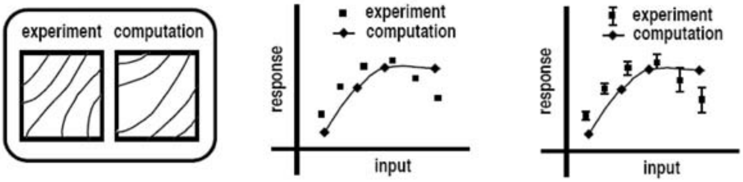

(a) Viewgraph Norm (b) Deterministic (c) Experimental Uncertainty

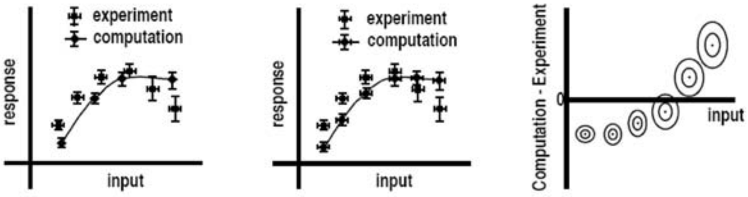

(d) Numerical Error (e) Nondeterministic Computation (f) Quantitative Comparison

Figure 5.4: Increasing quality of validation, taken from Oberkampf et al. (2003)

tification is described. First of all the uncertainty in the simulated outputs is determined, based on parameter- (and possibly model-) uncertainties that play a role in the simulation. Secondly the uncertainty in measurements is quantified by means of expert opinion. Finally the validity of the simulation outputs is objectively quantified by means of a validation metric that takes the uncertainties in both measurement and simulation into account.

The Uncertainty in Computational Data

The accumulated uncertainty in simulation results is the result of various uncertainty sources, as discussed in Schulten (2005) and Schulten and Stapersma (2007). In this research the System Uncertainty Analysis (SUA) method as described in Du and Chen (2002) is used. This method was already applied to a ship propulsion simulation model in Vrijdag et al. (2007) where it was shown to give comparable results as another (less computationally efficient) uncertainty analysis method. Most of the following on the mathematical uncertainty analysis procedure is taken directly from Vrijdag et al. (2007).

The objective of uncertainty analysis is to provide a notion of the possible range of the model output in relation with "true values"(Schulten (2005)). There is a certain vagueness in 'provide a notion of the possible range...'. This implies that output uncertainty cannot unambiguously be represented by one single hard number. This *uncertainty in uncertainty analysis* is caused by several assumptions that are often made in uncertainty analysis methods:

- Uncertain input parameters follow a normal distribution. The central limit theorem says that input parameters that are influenced by many small and unrelated random effects are approximately normally distributed. Whether this holds for the

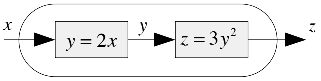

Figure 5.5: Local and Global sensitivities

input parameters remains to be seen, but it would be very difficult to determine the probability density function for each parameter by expert opinion or by measurement series.

- The system may be linearised, so that the sensitivities around the working point are fixed. This is only true for infinitesimal small input parameter variations.
- Related with the previous assumption, it is often assumed that the outputs follow a normal distribution when the input parameters are normally distributed. This is true for a linearised system, but in a non-linear real system this is not the case.

Monte Carlo Simulation (MCS) is a method that does not need these assumptions. The MCS method randomly generates values for uncertain input parameters (according to their probability density function) over and over again to simulate the modelled system under consideration. After many simulations a probability density function of the model output is available. The outcome of this method can be considered as the 'true' uncertainty, since none of the foregoing assumptions are made. For complex multidisciplinary simulation models however this method is not practical, if not impossible, due to the computational costs of the large amount of simulations.

Since MCS often not is an option, users and developers have been searching for other methods to efficiently quantify the uncertainty in model output. Du and Chen (2002) describe two methods: the System Uncertainty Analysis (SUA) and the Concurrent Sub-System Uncertainty Analysis (CSSUA). A summary of the SUA method is given here. The CSSUA, which is a refinement of the SUA, is not considered further.

The SUA approach uses local sensitivities determined at subsystem level to find the uncertainties of the outputs at system level. Alternatively one could determine global sensitivities, using the complete simulation model. The difference between local sensitivities and global sensitivities is illustrated in Fig 5.5, where analytic functions are known for the submodels. The local sensitivities of submodel 1 and submodel 2 are given by $\frac{\partial y}{\partial x} = 2$ and $\frac{\partial z}{\partial y} = 6y$.

When not distinguishing the two submodels, the analytic function of the total system is given by: $z = 12x^2$. The global sensitivity covering the complete system is then given by $\frac{\partial z}{\partial x} = 24x$. The main idea of the SUA approach is that only local sensitivities have to be determined. As will be shown, these local sensitivities will be combined, and the result will deliver the global sensitivities indirectly. The SUA approach has some advantages over the global sensitivity approach:

- First of all the sensitivities can be determined using only one subsystem at a time. This means that the time needed for a single sensitivity assessment is less than for a global sensitivity assessment (lower computational costs).
- Secondly, since the determination of sensitivities of the various submodels is decoupled, various specialists can work with the submodel of their own discipline. This parallel approach may speed up the laborious task of a total uncertainty analysis.

- Furthermore, the division in various submodels facilitates a clear demarcation of responsibilities. Responsibilities are unambiguously limited by the subsystem boundaries, which can be a great advantage in large multidisciplinary simulation projects where various parties deliver particular submodels.

On the other hand, compared to the global sensitivity approach, more local sensitivities have to be determined per submodel in order to correctly incorporate the uncertainty propagation between the various submodels. This is clearly illustrated by the example given above: With the total model approach, only one differentiation is needed to obtain $\frac{\partial z}{\partial x}$. Using the SUA approach, one needs to differentiate twice after which the global sensitivity still is to be derived from the two local sensitivities.

General description of a multidisciplinary system with uncertainties Fig 5.6 shows a total system built up out of n interconnected subsystems. This system and its notation was shortly introduced in Section 2.5, and is described here in more detail:

Common parameter inputs to all subsystems are called *shared variables* and denoted $\boldsymbol{x}_s$. Parameter-inputs particular to a certain subsystem are denoted by $\boldsymbol{x}_i$, where $i = 1, n$ denotes the subsystem under consideration.
Linking variables are denoted $\boldsymbol{y}_{ij}, i \neq j$, and are interconnecting the various subsystems, where the signal goes from subsystem i to subsystem j.
For ease of notation Du and Chen (2002) introduce $\boldsymbol{y}_i = \left\{ \boldsymbol{y}_{ij} \,|j = 1, n, i \neq j \right\}$, as the set of linking variables coming from subsystem i, as input to all other subsystems. Outputs coming from all subsystems except subsystem i, used as input to subsystem i are abbreviated as $\boldsymbol{y}^i = \left\{ \boldsymbol{y}_1, \ldots, \boldsymbol{y}_{i-1}, \boldsymbol{y}_{i+1}, \ldots, \boldsymbol{y}_n \right\}$.
Introducing the notation $\boldsymbol{F}_{yi}$ for the subsystem model, and $\boldsymbol{\varepsilon}_{yi}$ for the corresponding model error, the linking variables are described by:

$$\boldsymbol{y}_i = \boldsymbol{F}_{yi}\left(\boldsymbol{x}_s, \boldsymbol{x}_i, \boldsymbol{y}^i\right) + \boldsymbol{\varepsilon}_{yi}\left(\boldsymbol{x}_s, \boldsymbol{x}_i, \boldsymbol{y}^i\right) \tag{5.1}$$

As an equivalent for the outputs $\boldsymbol{z}_i$ of the subsystem i we find:

$$\boldsymbol{z}_i = \boldsymbol{F}_{zi}\left(\boldsymbol{x}_s, \boldsymbol{x}_i, \boldsymbol{y}^i\right) + \boldsymbol{\varepsilon}_{zi}\left(\boldsymbol{x}_s, \boldsymbol{x}_i, \boldsymbol{y}^i\right) \tag{5.2}$$

Summarizing, the goal of uncertainty analysis is to find the mean values $\boldsymbol{\mu}_{yi}$ and $\boldsymbol{\mu}_{zi}$ and accompanying standard deviations $\boldsymbol{\sigma}_{yi}$ and $\boldsymbol{\sigma}_{zi}$ of linking and output variables $\boldsymbol{y}_i$ and $\boldsymbol{z}_i$, given the mean values and standard deviations of input parameters and model errors $\boldsymbol{\mu}_{xs}$, $\boldsymbol{\mu}_{xi}$, $\boldsymbol{\sigma}_{xs}$, $\boldsymbol{\sigma}_{xi}$, $\boldsymbol{\mu}_{\varepsilon yi}$, $\boldsymbol{\mu}_{\varepsilon zi}$, $\boldsymbol{\sigma}_{\varepsilon yi}$ and $\boldsymbol{\sigma}_{\varepsilon zi}$.

Evaluating mean values Before the total model can be split up into the several submodels, the means of the linking variables $\boldsymbol{y}_i$ and outputs $\boldsymbol{z}_i$ have to be known in the operating point under consideration. Using the same notation as was just introduced:

$$\boldsymbol{\mu}_{yi} = \boldsymbol{F}_{yi}\left(\boldsymbol{\mu}_{xs}, \boldsymbol{\mu}_{xi}, \boldsymbol{\mu}_y^i\right) + \boldsymbol{\mu}_{\varepsilon yi} \tag{5.3}$$

$$\boldsymbol{\mu}_{zi} = \boldsymbol{F}_{zi}\left(\boldsymbol{\mu}_{xs}, \boldsymbol{\mu}_{xi}, \boldsymbol{\mu}_y^i\right) + \boldsymbol{\mu}_{\varepsilon zi} \tag{5.4}$$

In the SUA method, the evaluation of these mean values $\boldsymbol{\mu}_{yi}$ and $\boldsymbol{\mu}_{zi}$ requires one (computationally expensive) simulation at the system level.

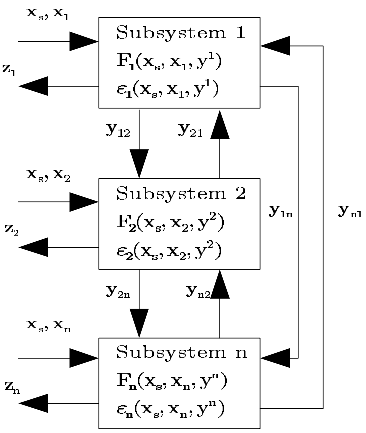

Figure 5.6: Coupled multidisciplinary subsystems, reproduced from Du and Chen (2002)

Deriving System Variance This section presents a summary of the SUA method by Du and Chen (2002):

To obtain the variances of system outputs, first, linking variables $\boldsymbol{y}_i, i = 1, n$, are linearised by the first order Taylor approximations expanded at the mean values identified in Eq. 5.1 through systemlevel evaluations. Multiple linking variables are derived simultaneously based on a set of linear equations. Second, we approximate a system output by the first-order Taylor expansion with respect to input variables $\boldsymbol{x}_s$ and $\boldsymbol{x}_i$ and linking variables $\boldsymbol{y}_i$ in each subsystem. After substituting $\boldsymbol{y}_i$ with the approximation derived earlier, we have the approximation of a system output as the function of input variables $\boldsymbol{x}_s$ and $\boldsymbol{x}_i$ only. Finally, based on the approximated system output, its variance is evaluated. The detailed procedure is as follows.
From Eq. 5.1, the linking variables $\boldsymbol{y}_i$ are approximated using Taylor's expansion as:

$$\Delta \boldsymbol{y}_i = \sum_{\substack{j=1 \\ j \neq i}}^{n} \frac{\partial \boldsymbol{F}_{yi}}{\partial \boldsymbol{y}_j} \Delta \boldsymbol{y}_j + \frac{\partial \boldsymbol{F}_{yi}}{\partial \boldsymbol{x}_s} \Delta \boldsymbol{x}_s + \frac{\partial \boldsymbol{F}_{yi}}{\partial \boldsymbol{x}_i} \Delta \boldsymbol{x}_i + \Delta \boldsymbol{\varepsilon}_{yi} \qquad (i = 1, n) \tag{5.5}$$

which can be written in matrix form as:

$$\boldsymbol{A} \Delta \boldsymbol{y} = \boldsymbol{B} \Delta \boldsymbol{x}_s + \boldsymbol{C} \Delta \boldsymbol{x} + \boldsymbol{D} \tag{5.6}$$

where

$$\boldsymbol{A} = \begin{bmatrix} \boldsymbol{I}_1 & -\frac{\partial \boldsymbol{F}_{y1}}{\partial \boldsymbol{y}_2} & \cdots & -\frac{\partial \boldsymbol{F}_{y1}}{\partial \boldsymbol{y}_n} \\ -\frac{\partial \boldsymbol{F}_{y2}}{\partial \boldsymbol{y}_1} & \boldsymbol{I}_2 & \cdots & -\frac{\partial \boldsymbol{F}_{y2}}{\partial \boldsymbol{y}_n} \\ \cdots & \cdots & \cdots & \cdots \\ -\frac{\partial \boldsymbol{F}_{yn}}{\partial \boldsymbol{y}_1} & -\frac{\partial \boldsymbol{F}_{yn}}{\partial \boldsymbol{y}_2} & \cdots & \boldsymbol{I}_n \end{bmatrix} \qquad \boldsymbol{B} = \begin{bmatrix} \frac{\partial \boldsymbol{F}_{y1}}{\partial \boldsymbol{x}_s} \\ \frac{\partial \boldsymbol{F}_{y2}}{\partial \boldsymbol{x}_s} \\ \cdots \\ \frac{\partial \boldsymbol{F}_{yn}}{\partial \boldsymbol{x}_s} \end{bmatrix}$$

$$\boldsymbol{C} = \begin{bmatrix} \frac{\partial \boldsymbol{F}_{y1}}{\partial \boldsymbol{x}_1} & 0 & \dots & 0 \\ 0 & \frac{\partial \boldsymbol{F}_{y2}}{\partial \boldsymbol{x}_2} & \dots & 0 \\ \dots & \dots & \dots & \dots \\ 0 & 0 & \dots & \frac{\partial \boldsymbol{F}_{yn}}{\partial \boldsymbol{x}_n} \end{bmatrix} \qquad \boldsymbol{D} = \begin{bmatrix} \boldsymbol{\varepsilon}_{y1} - \boldsymbol{\mu}_{\varepsilon y1} \\ \boldsymbol{\varepsilon}_{y2} - \boldsymbol{\mu}_{\varepsilon y2} \\ \dots \\ \boldsymbol{\varepsilon}_{yn} - \boldsymbol{\mu}_{\varepsilon yn} \end{bmatrix}$$

$$\Delta \boldsymbol{x}_s = \boldsymbol{x}_s - \boldsymbol{\mu}_{xs} \qquad \Delta \boldsymbol{x} = \begin{bmatrix} \boldsymbol{x}_1 - \boldsymbol{\mu}_{x1} \\ \boldsymbol{x}_2 - \boldsymbol{\mu}_{x2} \\ \dots \\ \boldsymbol{x}_n - \boldsymbol{\mu}_{xn} \end{bmatrix} \qquad \Delta \boldsymbol{y} = \begin{bmatrix} \boldsymbol{y}_1 - \boldsymbol{\mu}_{y1} \\ \boldsymbol{y}_2 - \boldsymbol{\mu}_{y2} \\ \dots \\ \boldsymbol{y}_n - \boldsymbol{\mu}_{yn} \end{bmatrix}$$

in which $\boldsymbol{I}_i, i = 1, n$, are the identity matrices.(Quoted from Du and Chen (2002).)
Since the variances in linking variables $\boldsymbol{y}_i$ are sought after, Eq. 5.6 can now be written as:

$$\Delta \boldsymbol{y} = \boldsymbol{A}^{-1} \boldsymbol{B} \Delta \boldsymbol{x}_s + \boldsymbol{A}^{-1} \boldsymbol{C} \Delta \boldsymbol{x} + \boldsymbol{A}^{-1} \boldsymbol{D} \tag{5.7}$$

Using a similar procedure, the error in system outputs $\boldsymbol{z}_i$ is derived. As follows from Eq. 5.2:

$$\Delta \boldsymbol{z}_i = \sum_{\substack{j=1 \\ j \neq i}}^{n} \frac{\partial \boldsymbol{F}_{zi}}{\partial \boldsymbol{y}_j} \Delta \boldsymbol{y}_j + \frac{\partial \boldsymbol{F}_{zi}}{\partial \boldsymbol{x}_s} \Delta \boldsymbol{x}_s + \frac{\partial \boldsymbol{F}_{zi}}{\partial \boldsymbol{x}_i} \Delta \boldsymbol{x}_i + \Delta \boldsymbol{\varepsilon}_{zi} \qquad (i = 1, n) \tag{5.8}$$

which is written in matrix form as:

$$\Delta \boldsymbol{z} = \boldsymbol{E} \Delta \boldsymbol{y} + \boldsymbol{F} \Delta \boldsymbol{x}_s + \boldsymbol{G} \Delta \boldsymbol{x} + \boldsymbol{H} \tag{5.9}$$

Substitution of Eq. 5.7 into Eq. 5.9 delivers:

$$\Delta \boldsymbol{z} = \boldsymbol{E} \left[\boldsymbol{A}^{-1} \boldsymbol{B} \Delta \boldsymbol{x}_s + \boldsymbol{A}^{-1} \boldsymbol{C} \Delta \boldsymbol{x} + \boldsymbol{A}^{-1} \boldsymbol{D} \right] + \boldsymbol{F} \Delta \boldsymbol{x}_s + \boldsymbol{G} \Delta \boldsymbol{x} + \boldsymbol{H} \tag{5.10}$$

Regrouping per uncertainty source results in:

$$\begin{aligned} \Delta \boldsymbol{z} = {} & \left[\boldsymbol{E} \left(\boldsymbol{A}^{-1} \boldsymbol{B} \right) + \boldsymbol{F} \right] \Delta \boldsymbol{x}_s + \\ & \left[\boldsymbol{E} \left(\boldsymbol{A}^{-1} \boldsymbol{C} \right) + \boldsymbol{G} \right] \Delta \boldsymbol{x} + \\ & \left(\boldsymbol{E} \boldsymbol{A}^{-1} \right) \boldsymbol{D} + \boldsymbol{H} \end{aligned} \tag{5.11}$$

where:

$$\boldsymbol{E} = \begin{bmatrix} 0 & \frac{\partial \boldsymbol{F}_{z1}}{\partial \boldsymbol{y}_2} & \dots & \frac{\partial \boldsymbol{F}_{z1}}{\partial \boldsymbol{y}_n} \\ \frac{\partial \boldsymbol{F}_{z2}}{\partial \boldsymbol{y}_1} & 0 & \dots & \frac{\partial \boldsymbol{F}_{z2}}{\partial \boldsymbol{y}_n} \\ \dots & \dots & \dots & \dots \\ \frac{\partial \boldsymbol{F}_{zn}}{\partial \boldsymbol{y}_1} & \frac{\partial \boldsymbol{F}_{zn}}{\partial \boldsymbol{y}_2} & \dots & 0 \end{bmatrix} \qquad \boldsymbol{F} = \begin{bmatrix} \frac{\partial \boldsymbol{F}_{z1}}{\partial \boldsymbol{x}_s} \\ \frac{\partial \boldsymbol{F}_{z2}}{\partial \boldsymbol{x}_s} \\ \dots \\ \frac{\partial \boldsymbol{F}_{zn}}{\partial \boldsymbol{x}_s} \end{bmatrix}$$

$$\boldsymbol{G} = \begin{bmatrix} \frac{\partial \boldsymbol{F}_{z1}}{\partial \boldsymbol{x}_1} & 0 & \dots & 0 \\ 0 & \frac{\partial \boldsymbol{F}_{z2}}{\partial \boldsymbol{x}_2} & \dots & 0 \\ \dots & \dots & \dots & \dots \\ 0 & 0 & \dots & \frac{\partial \boldsymbol{F}_{zn}}{\partial \boldsymbol{x}_n} \end{bmatrix} \qquad \Delta \boldsymbol{z} = \begin{bmatrix} \boldsymbol{z}_1 - \boldsymbol{\mu}_{z1} \\ \boldsymbol{z}_2 - \boldsymbol{\mu}_{z2} \\ \dots \\ \boldsymbol{z}_n - \boldsymbol{\mu}_{zn} \end{bmatrix}$$

$$\boldsymbol{H} = \begin{bmatrix} \boldsymbol{\varepsilon}_{z1} - \boldsymbol{\mu}_{\varepsilon z1} \\ \boldsymbol{\varepsilon}_{z2} - \boldsymbol{\mu}_{\varepsilon z2} \\ \dots \\ \boldsymbol{\varepsilon}_{zn} - \boldsymbol{\mu}_{\varepsilon zn} \end{bmatrix}$$

From standard error propagation theory it is known that the variance of the sum p_3 of two stochastic distributed parameters p_1 and p_2 is generally given by:

$$\sigma_{p_3}^2 = \left(\frac{\partial p_3}{\partial p_1}\right)^2 \sigma_{p_1}^2 + \left(\frac{\partial p_3}{\partial p_2}\right)^2 \sigma_{p_2}^2 + 2\sigma_{p_1 p_2}\left(\frac{\partial p_3}{\partial p_1}\right)\left(\frac{\partial p_3}{\partial p_2}\right) \tag{5.12}$$

Application of Eq. 5.12 to the summation carried out in Eq. 5.11 is simplified since the four sources of uncertainty $\boldsymbol{x}_s$, $\boldsymbol{x}$, $\boldsymbol{D}$ and $\boldsymbol{H}$ are mutually independent. This implies that the covariance-term $\sigma_{p_1 p_2}$ in Eq. 5.12 equals 0, and the variance of the system outputs can be written as a summation of individual uncertainty contributions:

$$\boldsymbol{D}_z = \boldsymbol{I}\boldsymbol{D}_{xs} + \boldsymbol{J}\boldsymbol{D}_x + \boldsymbol{K}\boldsymbol{D}_{y\varepsilon} + \boldsymbol{D}_{z\varepsilon} \tag{5.13}$$

in which:

$$\boldsymbol{I} = \{i_{ij}\}, \qquad i_{ij} = \left\{\boldsymbol{E}\left(\boldsymbol{A}^{-1}\boldsymbol{B}\right) + \boldsymbol{F}\right\}_{ij}^2$$
$$\boldsymbol{J} = \{j_{ij}\}, \qquad j_{ij} = \left\{\boldsymbol{E}\left(\boldsymbol{A}^{-1}\boldsymbol{C}\right) + \boldsymbol{G}\right\}_{ij}^2$$
$$\boldsymbol{K} = \{k_{ij}\}, \qquad k_{ij} = \left\{\boldsymbol{E}\boldsymbol{A}^{-1}\right\}_{ij}^2 \tag{5.14}$$

and

$$\boldsymbol{D}_z = \begin{bmatrix} \boldsymbol{\sigma}_{z1}^2 \\ \boldsymbol{\sigma}_{z2}^2 \\ \dots \\ \boldsymbol{\sigma}_{zn}^2 \end{bmatrix} \qquad \boldsymbol{D}_x = \boldsymbol{\sigma}_x^2 \qquad \boldsymbol{D}_{xs} = \begin{bmatrix} \boldsymbol{\sigma}_{x1}^2 \\ \boldsymbol{\sigma}_{x2}^2 \\ \dots \\ \boldsymbol{\sigma}_{xn}^2 \end{bmatrix}$$

$$\boldsymbol{D}_{y\varepsilon} = \begin{bmatrix} \boldsymbol{\sigma}_{y\varepsilon 1}^2 \\ \boldsymbol{\sigma}_{y\varepsilon 2}^2 \\ \dots \\ \boldsymbol{\sigma}_{y\varepsilon n}^2 \end{bmatrix} \qquad \boldsymbol{D}_{z\varepsilon} = \begin{bmatrix} \boldsymbol{\sigma}_{z\varepsilon 1}^2 \\ \boldsymbol{\sigma}_{z\varepsilon 2}^2 \\ \dots \\ \boldsymbol{\sigma}_{z\varepsilon n}^2 \end{bmatrix}$$

Vectors $\boldsymbol{D}_z$, $\boldsymbol{D}_{xs}$, $\boldsymbol{D}_x$, $\boldsymbol{D}_{y\varepsilon}$ and $\boldsymbol{D}_{z\varepsilon}$ describe the variances of the various variables. Matrices $\boldsymbol{I}$, $\boldsymbol{J}$, and $\boldsymbol{K}$ are the squared *global sensitivity* matrices. These global sensitivities include the propagation of uncertainties over the subsystem boundaries via the matrix $\boldsymbol{A}$. The essence of the SUA method is that the global sensitivities are derived from local sensitivities, thereby saving considerable computational effort if specific individual sub model evaluations are computationally expensive. Further discussion on the computational efficiency of the method can be found in Vrijdag et al. (2007).

The Uncertainty in Experimental Data

The uncertainty in experimental data is estimated by means of expert opinion. This means that one or more experts have to estimate a confidence interval of each measurement that was made.

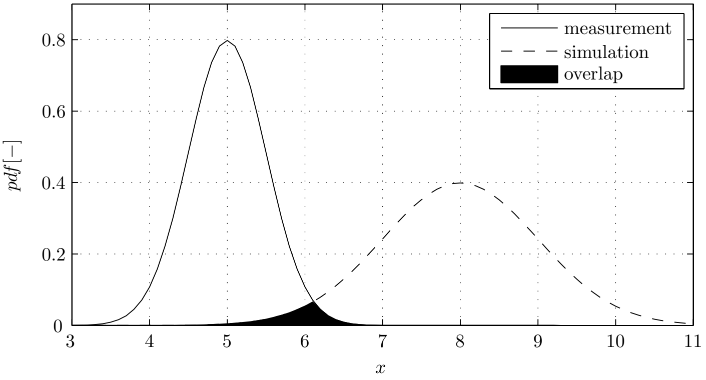

Figure 5.7: Example of static metric definition

A Validation Metric for Static Behaviour

With the estimated probabilistic distributions of measured and simulated output available, the next step is to quantify the agreement between computation and measurement by application of a validation metric. This validation metric in itself does not give a value judgment on the validity of the simulation model. It only quantifies the level of agreement, after which the user can decide whether this agreement is sufficient for the intended use of the model.

The metric that is used in this thesis is visualized in Fig 5.7, showing the normal distributions of both a measured and a simulated output. The validity is quantified by determination of the overlapping surface of the two distributions with Gaussian probability density function pdf, mean μ and standard deviation σ. The overlapping surface is given by:

$$\psi = \int_{-\infty}^{\infty} min\left[pdf(\mu_c, \sigma_c, x), pdf(\mu_m, \sigma_m, x)\right] dx$$

in which the subscript c indicates computation, and m indicates the measurement. For reference the pdf of a normal (Gaussian) distribution is given:

$$pdf(x) = \frac{1}{\sigma\sqrt{2\pi}} \cdot e^{\left(-\frac{(x-\mu)^2}{2\sigma^2}\right)}$$

A value of $\psi = 100\%$ means perfect agreement, while $\psi = 0\%$ means no agreement. The example given in Fig 5.7, with $\mu_m = 5$, $\sigma_m = 0.5$, and $\mu_c = 8$, $\sigma_c = 1$ has a value of $\psi = 4.3\%$. Whether this is sufficient should be decided by the user.

5.2.2 Theory of Validation of Dynamic Behaviour

The need for specific validation metrics to quantify agreement of time-histories is expressed in Oberkampf and Barone (2006). Two types of such metrics developed by Geers (1984), Russel (1997a), Russel (1997b) and Spraque and Geers (2003), are discussed and compared in Schwer (2007). He shows that the analyzed validation metrics can mimic expert opinion well, especially taking into account the variation in the opinion of various experts. Since these types of validation metrics are not commonly known and applied, a summary of theory including some examples is given here. Various other types of metrics are described, tested and compared in Ray et al. (2008), but are not dealt with here.

In the following, two validation metrics are presented. Consider a measured time history $m(t)$ and a corresponding computed time history $c(t)$.

Sprague and Geers define the following integrals over the time span of interest:

$$\vartheta_{mm} = \frac{1}{t_2 - t_1} \int_{t_1}^{t_2} m^2(t)dt$$

$$\vartheta_{cc} = \frac{1}{t_2 - t_1} \int_{t_1}^{t_2} c^2(t)dt$$

$$\vartheta_{mc} = \frac{1}{t_2 - t_1} \int_{t_1}^{t_2} m(t)c(t)dt$$

A magnitude error factor is given by:

$$M_{SG} = \sqrt{\vartheta_{cc}/\vartheta_{mm}} - 1$$

which is the ratio of integrated squared response histories. For two exactly matching signals M_{SG} equals zero, meaning that perfect agreement is obtained. This metric is insensitive to phase errors, which are captured independently by a phase error factor as defined by:

$$P_{SG} = \frac{1}{\pi} \arccos \left(\frac{\vartheta_{mc}}{\sqrt{\vartheta_{mm}\vartheta_{cc}}} \right)$$

This metric is insensitive to errors in magnitude, but focuses on capturing phase shifts such as might be introduced by $c(t) = m(t - \Delta t)$.

The two presented metrics are combined into a *comprehensive error factor* given by:

$$C_{SG} = \sqrt{M_{SG}^2 + P_{SG}^2}$$

This combined metric is just one of many possible ways of combining the magnitude and phase error factors.

Knowles and Gear use a point-to-point approach instead of using time averaged integrals. Just as the approach of Sprague and Geers they use separate metrics for magnitude and phase, which are later combined into a *comprehensive error factor*. The magnitude-metric is basically a normalised weighted sum of squared differences given by:

$$M_{KG} = \sqrt{\sum_{i=1}^{N} \frac{Q_i \cdot (\tilde{c}_i - m_i)^2}{QS}}$$

in which the weight factor Q_i is defined by:

$$Q_i = \left(\frac{|m_i|}{m_{max}} \right)^p \cdot (t_{i+1} - t_{i-1})$$

and the normalisation-factor QS is defined by:

$$QS = \sum_{i=1}^{N} \left(\frac{|m_i|}{m_{max}} \right)^p m_i^2 \cdot (t_{i+1} - t_{i-1})$$

If uniform time sampling is applied the evaluation of M_{KG} simplifies to:

$$M_{KG} = \sqrt{\frac{\sum_{i=1}^{N} \left(\frac{|m_i|}{m_{max}} \right)^p \cdot (\tilde{c}_i - m_i)^2}{\sum_{i=1}^{N} \left(\frac{|m_i|}{m_{max}} \right)^p \cdot (m_i)^2}}$$

A value of $p = 1$ is recommended to put more weight on errors that occur near higher values of $m(t)$ (closer to m_{max}). The signal $\tilde{c}(t)$ is the shifted signal $c(t - \tau)$. By shifting of the signal it is attempted to decouple the magnitude factor from the phase factor. The shift τ is the difference between the so called Time Of Arrival (TOA) of the measured and the computed signal:

$$\tau = TOA_c - TOA_m$$

It is recommended to define the TOA of a transient time history as the time at which some percentage of the maximum value is reached. Use of a range of $5 - 10\%$ of the maximum signal value is recommended. Use of other "conspicious features" of the signals might be necessary to determine the lag between measuremnt and computation.

Instead of using a true phase-metric, this approach uses a TOA-metric defined by:

$$M_{TOA} = \frac{|TOA_c - TOA_m|}{TOA_m}$$

which is a measure of the relative error with respect to TOA_m.

A combination of the magnitude metric and the TOA metric leads to the following combined metric:

$$C_{KG} = \sqrt{\frac{10 M_{KG}^2 + 2 M_{TOA}^2}{12}}$$

The importance factors 10 and 2 for magnitude and TOA as used by Schwer (2007) are adopted here.

Example Applications of Dynamic Validation Metrics

To demonstrate and compare the proposed metrics, Schwer (2007) gives various examples involving an analytical decaying sine wave with structure:

$$m(t) = e^{-(t-\tau)} \sin\left(2\pi(t - \tau)\right)$$

Advantage of such a signal is that it can easily be shifted in time and be given a different amplitude. Examples of a pure magnitude increase, a pure shift in phase, and their combined effect are discusses in the article under consideration. Some illustrative examples are shown in Fig 5.8, of which the resulting metrics are given in Table 5.1.

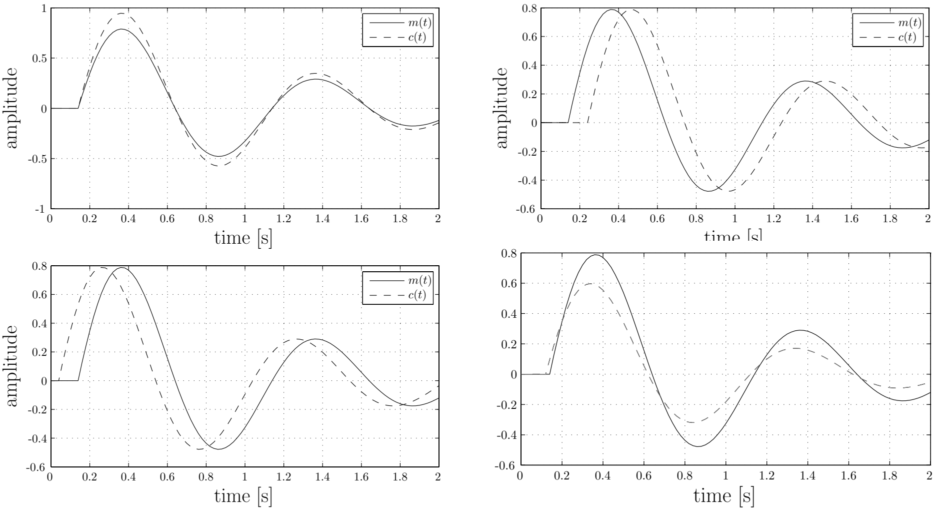

Figure 5.8: Illustration of 20% amplitude error, 20% phase lead and lag, and combined magnitude and phase error

For the pure amplitude-error both methods give approximately the same results, with the combined KG-metric slightly smaller due to the introduction of the *importance factors*. For the lag and lead errors the 63% of the KG-TOA metric is quite high compared to the SG-phase metric. This is caused by the completely different definitions and cannot be compared directly. The combined error shows an important difference: the sign of the SG-amplitude metric does tell whether the simulations are generally too low or too high, while the KG-amplitude metric doesn't indicate whether the computations are too high or too low. -28% indicates that the simulation has less amplitude that the measurements. Such a conclusion could not be drawn from the KG-magnitude metric (with value 27%).

The presented metrics are not only tested on analytical waveforms. Further testing is applied to various truly measured and calculated velocity signals. Comparison with multiple expert opinions is made, and two out of a total of five cases are shown in Fig 5.9. It is shown that the experts give a mean agreements quantification of 0.45 on a scale from 0 to 1 for the first plot, while they give an agreement factor of 0.87 to the second plot.

Fig 5.10 shows that the metric results agree quite well with the expert opinion, especially when taking into account the spread in expert opinion by means of showing error bars with a total length of 2 standard deviations. Note that in this figure the complement of the agreement factor is shown, which is labeled as a *waveform difference*. Also note that only waveform-pairings 2 and 5 are shown in Fig 5.9. The other pairings are shown in the original article.

type of error	**metric**	SG	KG
amplitude error	Magnitude	20%	20%
	Phase or TOA	0%	0%
	Combined	20%	18%
phase error (lead)	Magnitude	0%	1%
	Phase or TOA	20%	63%
	Combined	20%	26%
phase error (lag)	Magnitude	0%	0%
	Phase or TOA	20%	63%
	Combined	20%	26%
combined error	Magnitude	-28%	27%
	Phase or TOA	5%	13%
	Combined	29%	25%

Table 5.1: Validation metrics applied to $m(t)$ and $c(t)$, shown in Fig 5.8. Lead means that $c(t)$ is in advance of $m(t)$. Small differences with Schwer (2007) are attributed to differences in integration method, roundoff errors, and the difference in TOA-determination

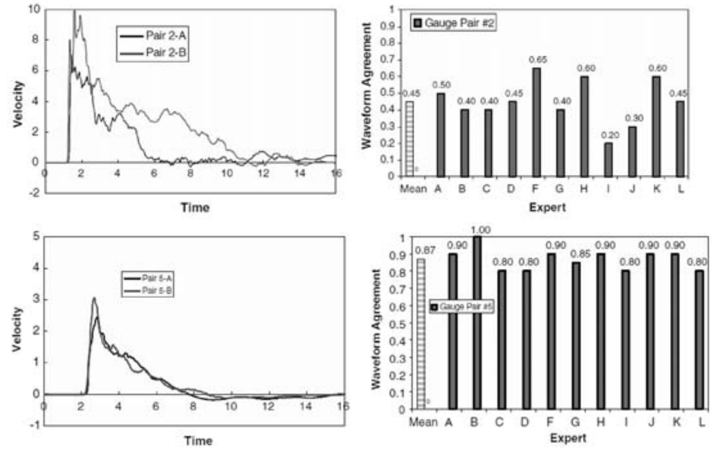

Figure 5.9: Examples of quantified expert opinions (of experts A to L) on agreement between measured and computed velocity transients. Taken from Schwer (2007)

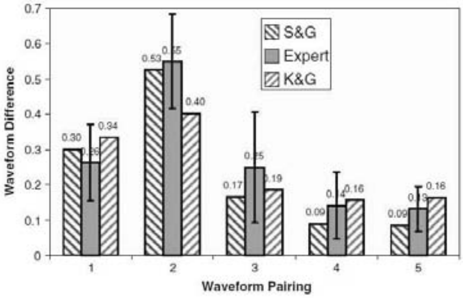

Figure 5.10: Comparison of expert opinion and metric evaluation of five transient pairings. Taken from Schwer (2007)

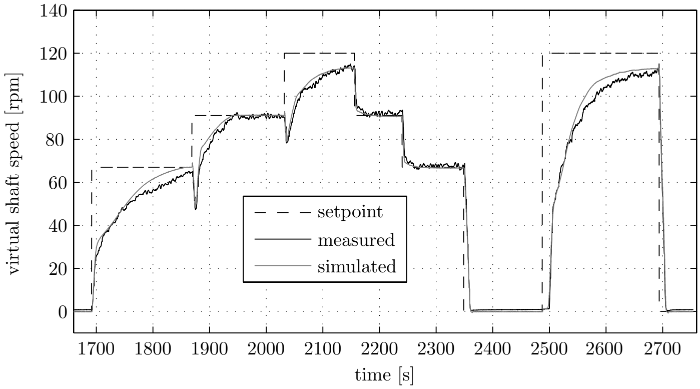

Figure 5.11: Validation input: the command and realised virtual shaft speed

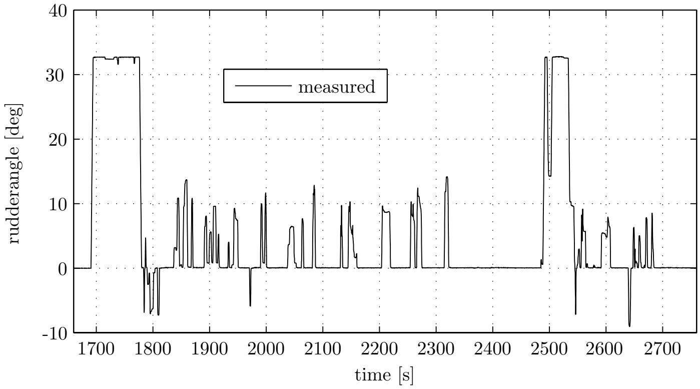

Figure 5.12: Disturbing input during validation experiment: rudder angle

5.2.3 The Validation Experiment

Static measurements are available from a dedicated validation test, that was performed in the North Sea in November 2007, directly after the dedicated calibration test. Due to weather conditions, these measurements could not be carried out in calm water. The ship resistance increase factors α_R and R_0 that were found in the calibration phase, are used here again.

The validation experiment is a repeated version of the calibration experiment as was described in Section 4.2.1. This experiment is chosen since its operating points span a big validation-domain in the $\theta - n$ plane, which is of importance in the light of Fig 5.2.

The computed and measured results of the validation experiment are shown in Figs 5.11 to 5.22. The command input is shown in the Fig 5.11, and the rudder input in Fig 5.12. At the virtual commands 0, 67, 91 and 120 rpm, the steady propulsion variables are determined by averaging over a certain time interval (listed in Table 5.2) at which the mean system behaviour is considered steady.

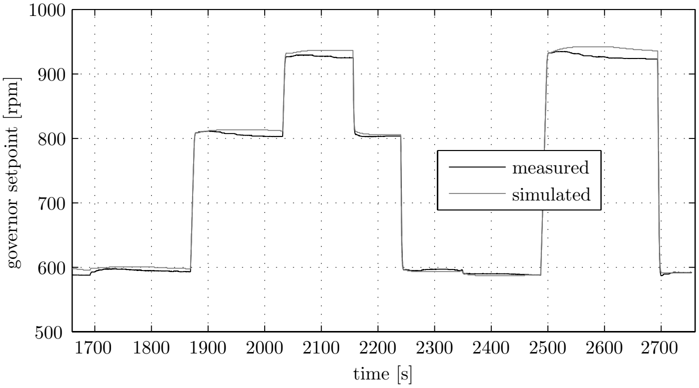

Figure 5.13: Validation: setpoint governor

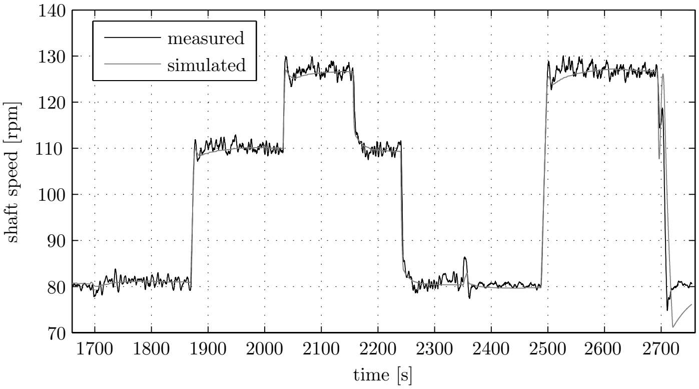

Figure 5.14: Validation: shaft speed

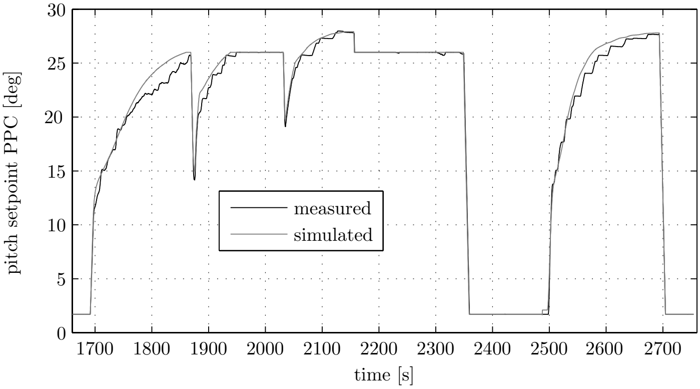

Figure 5.15: Validation: pitch setpoint Propeller Pitch Controller (PPC)

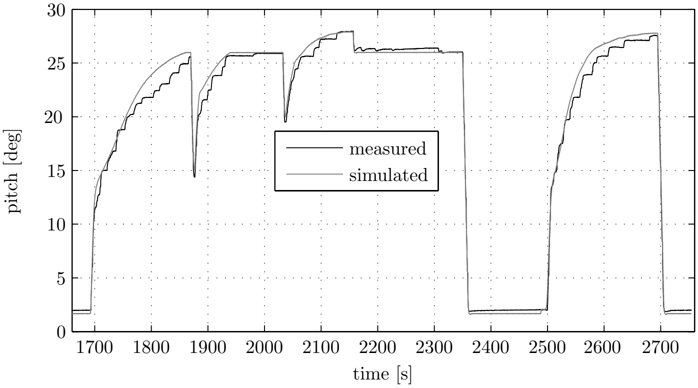

Figure 5.16: Validation: propeller pitch

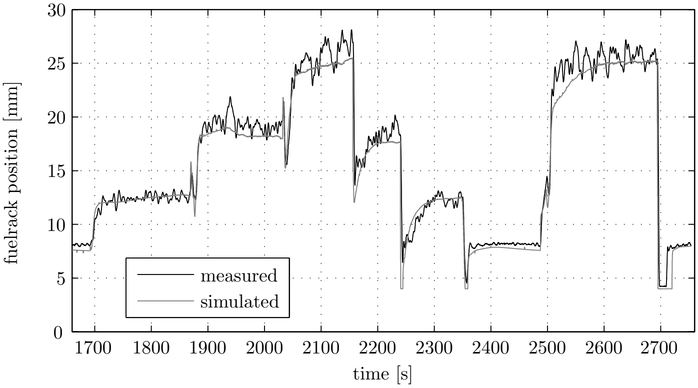

Figure 5.17: Validation: fuelrack position

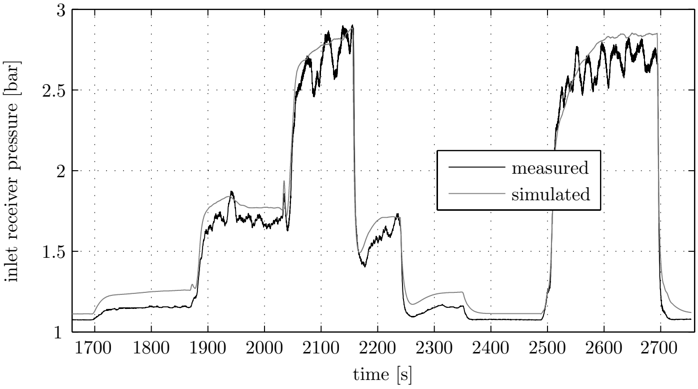

Figure 5.18: Validation: inlet receiver pressure

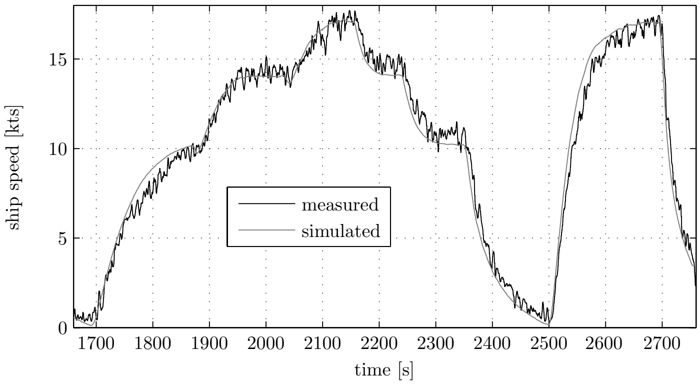

Figure 5.19: Validation: ship speed

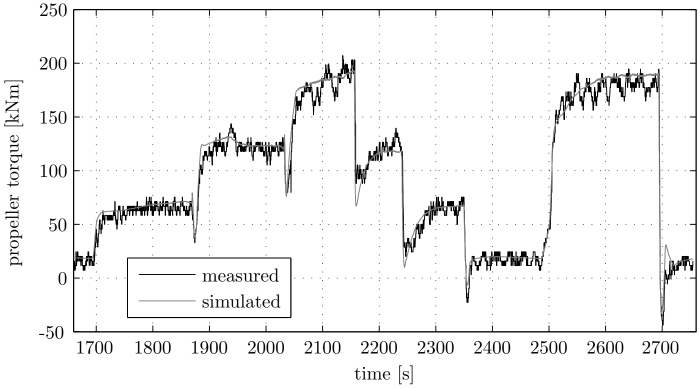

Figure 5.20: Validation: propeller torque

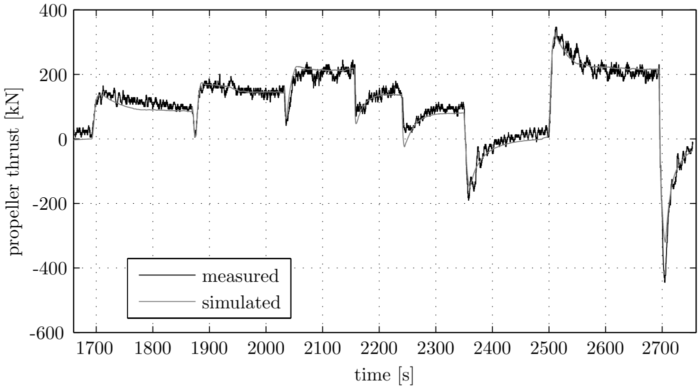

Figure 5.21: Validation: propeller thrust

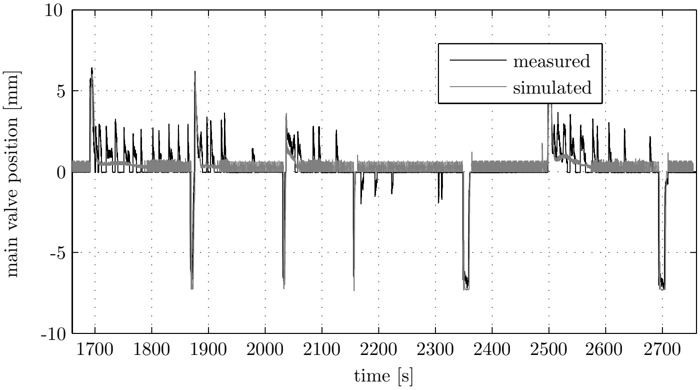

Figure 5.22: Validation: main valve position

operating point	I	II	III	IV
command [rpm]	0	67	91	120
time interval	1640-1680s	2310-2330s	1980-2020s	2675-2690s

Table 5.2: Intervals at which the static operating point values are determined

5.2.4 Validation of Static Behaviour

For the validation of static simulation output, a total of 4 static working points are selected from the validation measurements presented in Section 5.2.3. The selected operating points and their time-intervals are listed in Table 5.2. The steady operating points are determined by averaging over the indicated time intervals. An overview of the agreement including uncertainties is presented in Fig 5.23.

In the following the sources of the shown uncertainty intervals are discussed in more detail. The SUA method as described in Section 5.2.1 is applied to the plant model without the PCS submodel. This is justified because in the static operating points I, II and III, the limitations in the PCS are not active. No limitation of the top level setpoints generated by the combinator-curve causes that (in static non-limited conditions) the two setpoints $n_{set,gov}$ and $\theta_{set,PPC}$ are not sensitive to the PCS-inputs n, X and p_{ir}. Therefore the static outputs of the PCS model are not propagating any uncertainty to the linking variables $n_{set,gov}$ and $\theta_{set,PPC}$, so that $\frac{\partial n_{set,gov}}{\partial n} = 0$, $\frac{\partial n_{set,gov}}{\partial X} = 0$, $\frac{\partial n_{set,gov}}{\partial p_{ir}} = 0$, and $\frac{\partial \theta_{set,PPC}}{\partial n} = \frac{\partial \theta_{set,PPC}}{\partial X} = \frac{\partial \theta_{set,PPC}}{\partial p_{ir}} = 0$.

Besides not propagating any uncertainty, the PCS also does not introduce any uncertainty, since all parameters and equations are set by the programmer of the PCS, and thus are exactly known.

In operating point IV the pitch setpoint is limited by the PCS, resulting in uncertainty propagation through the PCS so that in principle the approach is not valid. However, even if the PCS would be included in the SUA method, the strong one-sided nonlinearity caused by the limiter in the PCS, would also have effect on the SUA-output, so that only a MCS-approach would give valid results. It is decided to analyze operating point IV in the same manner as the other operating points.

The sensitivities of 8 selected output variables to 14 selected input parameters are de-

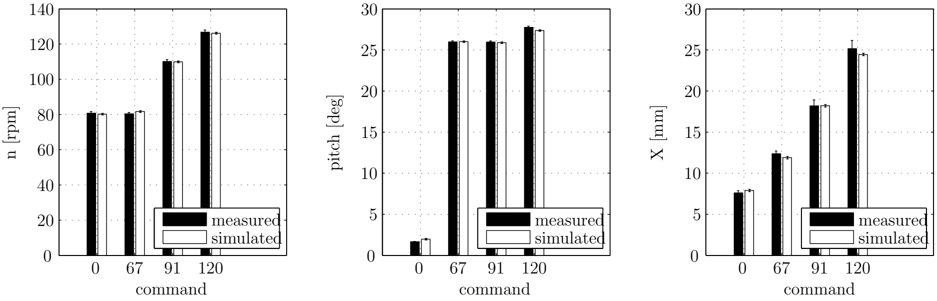

(a) Shaft speed (b) Pitch (c) Fuelrack position

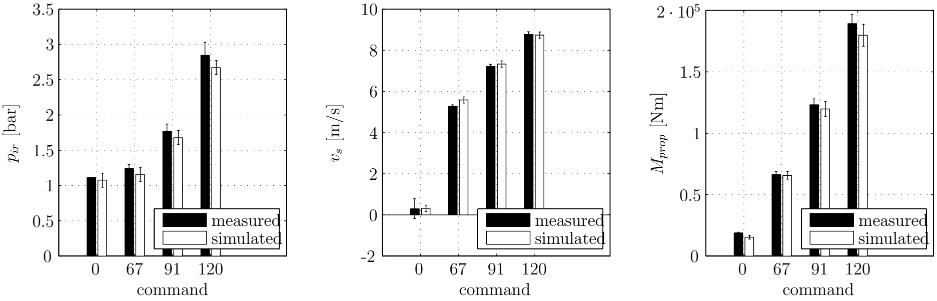

(d) Inlet receiver pressure (e) Ship speed (f) Propeller torque

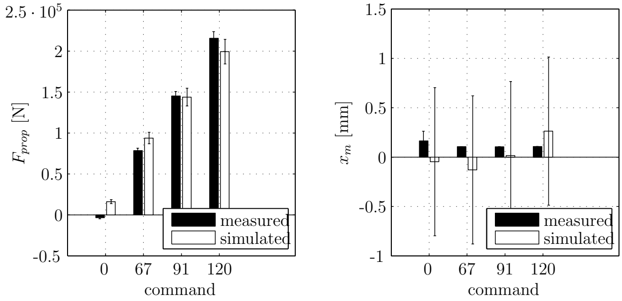

(g) Propeller thrust (h) Main valve position

Figure 5.23: Validation of 4 static operating points. Error bars indicate ± 1 standard deviation

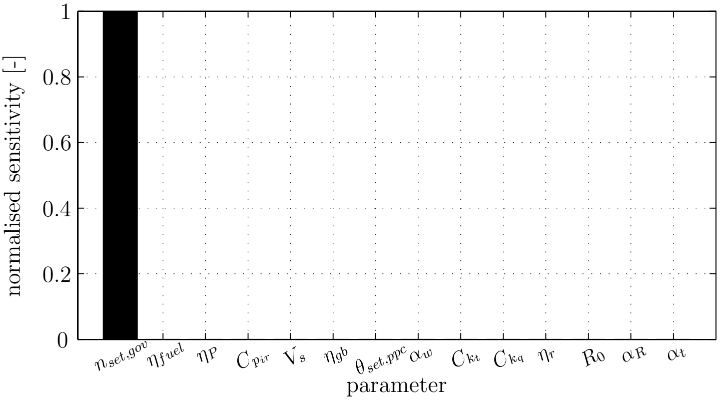

Figure 5.24: Absolute normalised sensitivity of shaft speed n in operating point II

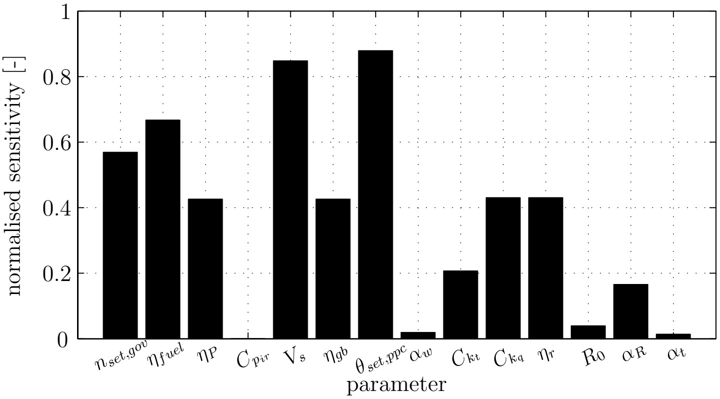

Figure 5.25: Absolute normalised sensitivity of fuelrack position X in operating point II

termined via the SUA method as described in Section 5.2.1. The 8 output variables are selected based on their importance in the overall system behaviour. As an example the sensitivities of shaft speed n and fuelrack position X to the considered input parameters (in operating point II) are presented in Fig 5.24 and Fig 5.25. The meaning of the parameters in these figures is explained in appendix B. Note that the normalized sensitivities are presented: the sensitivity of output z_i to input parameter x_i is given by $\frac{\partial z_i}{\partial x_i}$ and the normalized sensitivity is given by $\frac{\partial z_i}{\partial x_i}\frac{x_i}{z_i}$. As clearly shown in Fig 5.24, the shaft speed of the governed diesel engine is insensitive to parameter uncertainty, except for the governor input parameter $n_{set,gov}$. The fuelrack position however is dependent on many parameters: even though the shaft speed remains constant independent of input parameter uncertainty, the accompanying fuelrack position is affected by most of the input parameters.

As shown by Equation 5.13, the uncertainty of the output variables is a combination of the sensitivities and the input parameter uncertainties. The input parameter uncertainties for operating point II are listed in Table B.1, and are determined by expert opinion.

Operating point II	unit	computation		measured		ψ
		mean	sigma	mean	sigma	
n	[rpm]	80.39	0.80	81.68	0.50	0.31
p_{ir}	[bar]	1.24	0.06	1.16	0.10	0.55
X	[mm]	12.38	0.32	11.88	0.15	0.27
M_{prop}	[Nm]	66320	2572	65629	3000	0.88
F_{prop}	[N]	78489	2905	93817	7000	0.11
θ	[deg]	25.98	0.13	26.01	0.10	0.87
x_m	[mm]	0.11	0.00	-0.13	0.75	0.00
v_s	[m/s]	5.27	0.07	5.59	0.15	0.15

Table 5.3: Steady State validation results of operating point II: command 67

Operating point:	I	II	III	IV
n	0.6	0.3	0.6	0.5
p_{ir}	0.0	0.5	0.6	0.5
X	0.4	0.3	0.4	0.2
M_{prop}	0.1	0.9	0.6	0.6
F_{prop}	0.0	0.1	0.9	0.4
θ	0.0	0.9	0.7	0.1
x_m	0.2	0.0	0.0	0.0
v_s	0.5	0.1	0.6	0.9

Table 5.4: Quantitative validation of 4 operating points by means of metric ψ

The uncertainties in combination with the sensitivities are used to calculate the uncertainty in n and X as well as in the other static output variables. Results are presented in Table 5.3, which hold for operating point II. The table presents the end-results of the computational uncertainty analysis together with the experimental uncertainty. The last column of the table shows the quantified agreement by means of the metric value ψ, that was defined in Section 5.2.1. The static validation metric value gives an objective measure of the agreement between the experiment and the simulation. To get a feeling for the metric ψ, few examples of overlapping Gaussian distributions are shown in Fig 5.26. Best overlap, with highest ψ, is found for M_{prop}, and lowest ψ is found for F_{prop} (not considering x_m).

The analysis of the validity of the static output variables in the other operating points is carried out in the same way. End results are presented in Table 5.4. This table shows that the agreement in general is worse at the low ship speed of operating point I. More detailed data on the derivation of the uncertainties in operating points I, III and IV is given in Appendix B.

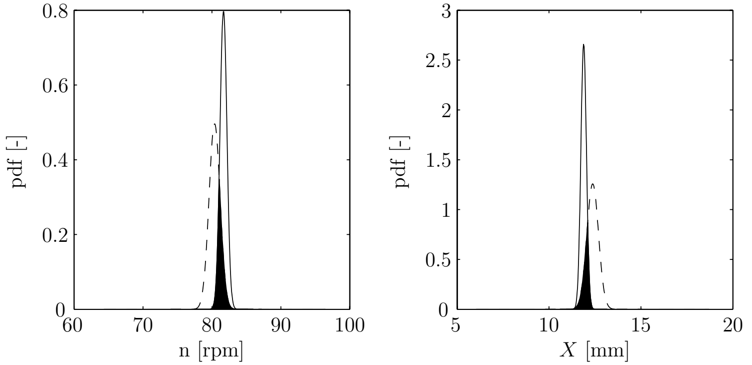

(a) $\psi = 0.31$ (b) $\psi = 0.27$

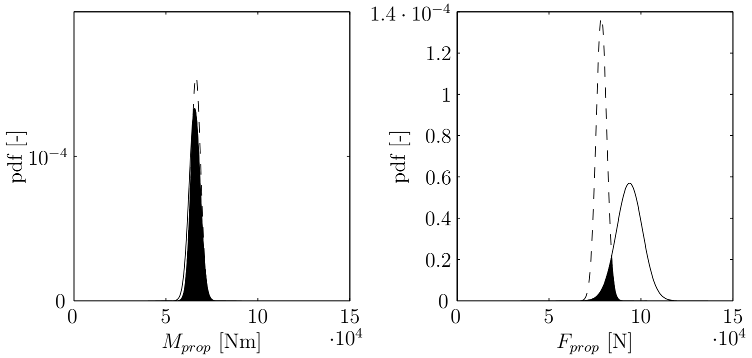

(c) $\psi = 0.88$ (d) $\psi = 0.11$

Figure 5.26: Overlapping normal distributions of n*,* X*,* M_{prop} *and* F_{prop}*. Dashed curve indicates simulation, solid curve indicates measurement*

5.2.5 Validation of Dynamic Behaviour

For the validation of dynamic behaviour, multiple transients are analyzed by means of the "dynamic" metrics as presented in Section 5.2.2. The transients that are analyzed are the up- and down going steps between $0-67-91-120$ rpm, as well as the up- and down transitions between 0 and 120 rpm. The signals n, θ, v_s, X, M_{prop}, and F_{prop} are analyzed.

Calculation of the metrics necessitates the definition of an interval of interest on which the metric is to be based. The interval of interest is however dependent on the type of signal: the ship speed transient simply takes longer than the shaft speed transient. Because the shaft speed transient is in general much faster than the other transients, the interval of interest of n is chosen shorter than the other intervals. The results of the manual interval selection are given in Table 5.5. The start of this interval is the time where the transient is started by means of a new command, while the end is chosen by manual determination of the end of the interval that contains the transient including the settlement phase.

The calculation of the KG-metrics is partly based on the determination of the Time Of Arrival (TOA) of both the measured and the computed signal. Due to non-monotonous behaviour of various signals during the transients, an automatic determination of TOA_m and TOA_c as suggested in Schwer (2007) is not possible. It is chosen to set both TOA_m and TOA_c equal to the start of the interval of interest, so that by definition the TOA-metric of the KG-approach equals 0.

The resulting metrics for a single transient from $0-67$ rpm are shown in Table 5.6. The shaft speed signals have best agreement with combined metric factors of 0.4% vs. 1.1%. Thrust has the worst agreement with combined metrics of 14.1% vs. 16.1%. For this specific manoeuvre the difference between the two methods is small.

Note that Schwer (2007) gives the following rule of thumb on the quality of agreement:

> *"Anything below about 20% is really good. When you get to around 20 to 30%, it is getting fair. When you get above the 30 to 40% range, that is rather poor."*

An overview of the various metrics for all 8 time-intervals is given in the bar-plot shown in Fig 5.27. The figure shows that the comprehensive error factors of the signals n, θ and v_s are always under 10%. In the decelleration from $120-0$ rpm there is quite a difference between C_{SG} and C_{KG} of the shaft speed signal. Further inspection of the shaft speed signal in Fig 5.14 shows that this is caused by a overprediction of the windmill effect by the simulation model, which was discussed in Section 4.2.2. Based on another (full scale) measurement of the windmill effect shown in Fig 7.10 on page 122 it is concluded that the size of the effect is very sensitive to actual inflow conditions. It is likely that both in the calibration experiment and in the validation experiment, wave influence decreased the size of the shaft speed upspin. The calm water measurement presented in Fig 7.10 reveals that a high shaft speed upspin as predicted by the simulation model is possible, and the overpredicted effect in this chapter does not reveal a modelling flaw.

The difference in quantification of the agreement of the shaft speed between the two methods is caused by the application of a weight factor by the KG-method. Due to this factor the KG-method puts more focus on the windmill peak than the SG-method.

The agreement of the signals F_{prop} and M_{prop} is in general less. Also the differences between the two methods are bigger. Further inspection of the relevant intervals shows that the

manoeuvre	t_1	t_2 shaft speed n	t_2 other variables
$0-67$ rpm	1691	1865	1865
$67-91$ rpm	1868	1885	1980
$91-120$ rpm	2030	2045	2155
$120-91$ rpm	2156	2180	2240
$91-67$ rpm	2240	2260	2320
$67-0$ rpm	2349	2370	2480
$0-120$ rpm	2487	2600	2690
$120-0$ rpm	2693	2750	2750

Table 5.5: Intervals of interest for determination of "dynamic" validation metrics

		SG [%]	**KG [%]**
n	**magnitude**	0.0	1.2
	Phase/TOA	0.4	0.0
	Combined	0.4	1.1
θ	**magnitude**	5.7	6.4
	Phase/TOA	0.9	0.0
	Combined	5.8	5.8
v_s	**magnitude**	6.6	8.2
	Phase/TOA	1.9	0.0
	Combined	6.9	7.5
F_{prop}	**magnitude**	-13.5	17.6
	Phase/TOA	3.8	0.0
	Combined	14.1	16.1
M_{prop}	**magnitude**	7.1	10.4
	Phase/TOA	2.9	0.0
	Combined	7.7	9.5
X	**magnitude**	3.6	4.9
	Phase/TOA	1.1	0.0
	Combined	3.7	4.4

Table 5.6: Validation metrics of transition $0-67$ rpm in the interval $1691-1865$ s. Lowest value indicates best agreement

difference between the two methods is likely to be caused by (wave) disturbances in the measurements. These disturbances are not included in the simulations, which causes the general less agreement between measurement and computation. The big difference between the two methods for the fuel rack position X (Fig 5.28) during the deceleration from $120-0$ rpm is related to the overestimated windmill effect: due to the over predicted upspin of the shaft, the simulated fuel rack is decreased to a minimum for a far longer period than in reality. Furthermore the steep decrease of fuel rack position occurs earlier in the simulation than in reality, so that the KG-metric rapidly increases due to large discrepancies in $\tilde{c}_i - m_i$.

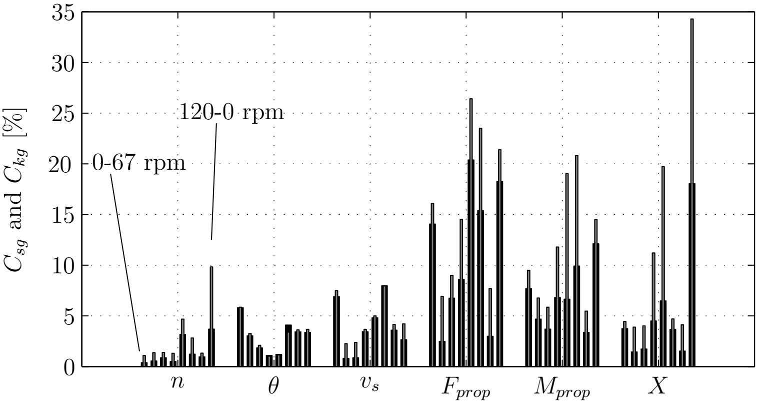

Figure 5.27: Overview of combined metrics C_{SG} (black) and C_{KG} (gray) for all 8 *transients, for* 6 *system variables*

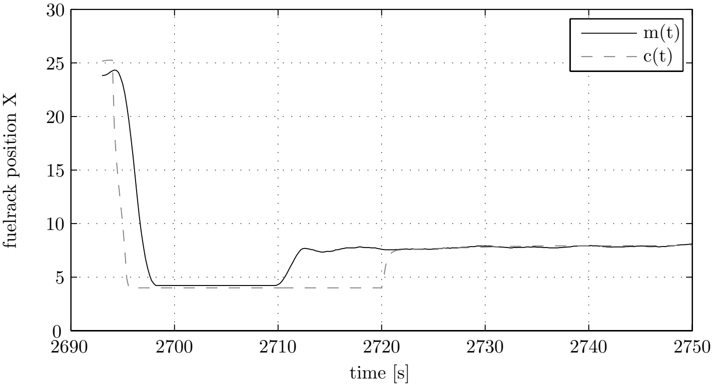

Figure 5.28: Computed and measured X in the interval $2693 - 2750s$.

5.3 Conclusions

This chapter quantified the agreement between measurement and simulation. Four static operating points with a wide spread in the input domain were selected for this analysis. It is acknowledged that the addition of one or more static operating points at high shaft speed combined with low pitch would increase the validation domain even further. On the other hand static model behaviour in this area is of less importance since the installation is not (and is not expected to be) operated in that area.

The static validation domain could also be increased by addition of static operating points at different seastates to the validation database. Measurements in other seastates are however not available. Nevertheless, the understanding of the system is at such a level that quite strong inferences with respect to predictions outside the validated seastate are justified.

It is concluded that the model is suited to make predictions of the static operating points of all validated variables except for the main valve position x_m. Predictions outside the validated domain should (as always) be considered with care. Predictions at low commands (low ship speeds) should also be considered with care, as these predictions are shown to be less accurate.

Furthermore a specific set of transients is validated by means of two "dynamic" validation metrics found in literature. It is found that the variables n, v_s, and θ show an agreement that is quantified by: $C_{KG} < 10\%$ and $C_{SG} < 8\%$. The variables M_{prop}, F_{prop} and X have less agreement, which is quantified by $C_{KG} < 35\%$ and $C_{SG} < 21\%$. For variables n and X less agreement is found in the decelerating transient from command $120 - 0$ rpm. This is caused by the overestimated windmill effect. It is concluded that this is not caused by a modelling flaw, but by a high sensitivity of the effect for the actual inflow due to waves.

The predictive value of the model in the frequency domain has not been explicitly validated. Even though the ship sailed in waves, no fair validation was possible because the wave induced disturbances were not measurable. Predictions of system behaviour in waves should therefore be considered with care.

To validate future ship propulsion models in the frequency domain it is recommended to carry out a full scale experiment with a sinusoidal setpoint variation superimposed on $n_{set,gov}$ or $\theta_{set,PPC}$. By studying the effect of varying amplitude and frequency of the setpoints on the output variables, this type of system behaviour can also be validated, leading to an increased application domain of the model.

Finally at this phase there is little information on the time variance of the system. Wear and tear, as well as other system characteristics that change over time, have effect on the validity of the model. Structured scheduled data gathering over longer time periods might help to create insight in this aspect of model validity.

It is concluded that formal validation by means of validation metrics has the advantage that it allows for objective quantification of agreement. This makes the validation process largely independent of the data presentation, and the eyes and mindset of the observer. This can help to make fair comparisons between various manoeuvres or various models. This does however not mean that expert opinion does not count: validation metrics do not capture all intricacies of model validation.

Chapter 6

Prediction of Cavitation Inception

6.1 Introduction

Because propeller cavitation can have unfavourable consequences, its prediction is an important issue in the field of propeller hydrodynamics. Inception prediction is also important for the development of a propulsion control system aiming at increased cavitation free time, as will be shown in Chapter 7. This chapter attempts to define the required capabilities of inception prediction methods that are necessary for the development of the propulsion controller aiming at increased cavitation free time. The actual predictive capabilities that are available at this stage are shortly discussed. By comparing required and available predictive capabilities, it is assessed which method is most appropriate for the inception prediction task.

6.2 Propeller Cavitation Inception

The first noticeable appearance of cavitation is referred to as cavitation inception. Cavitation is the phenomenon of a phase change from liquid to gas, due to the presence of low pressures in the flow. This is illustrated in Fig 6.1, which relates the state of water to the actual pressure and temperature. A pressure drop from A to B should, according to this figure, result in cavitation. However, this is not necessarily true, since various other factors affect the transition from liquid to gaseous form. The presence of dissolved air, small vapour bubbles, and even small fixed particles cause a difference between the vapour pressure and the pressure at which cavitation starts. The lack of nuclei can result in delay of cavitation inception, because there are no cores that act as starting points for the growth of gas-bubbles. Due to these effects a liquid can sometimes be subjected to pressures much lower than the vapour pressure until at some point the phase-change takes place. Due to the importance of nuclei (distribution) with regard to cavitation inception, Gindroz (1998) concludes that nuclei measurement is necessary in any cavitation inception test. Fig 6.2 illustrates the effect of nuclei content on inception measurements. He also discusses the importance of a good understanding of the nuclei distribution at sea, which is reported to show a wide spread. The latter may well be the reason for differences in full scale inception speed observations of the same ship in different operating areas.

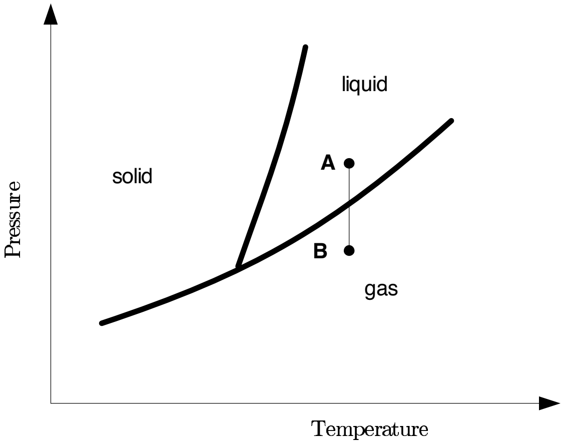

Figure 6.1: Phase diagram of water

Inception occurs both around nuclei in the free stream and around small crevices / irregularities that cover the propeller surface and that act as growth cores. An in depth overview of cavitation inception on a fundamental level is given in for instance Brennen (1995).

Cavitation inception events at (sub)millimeter-scale already result in one of the detrimental effects of cavitation: underwater noise. However, if cavitation inception is observed visually, only cavity sizes of the order of centimeters can be identified in a full scale setup. The limited spatial resolution on full scale is likely the most important cause for reported differences of more than 2 kts between visually observed inception, and acoustically measured propeller cavitation inception. The actual size of the difference is however dependent on the uncertainties related to both methods, and on the visibility of the cavitation bubbles around inception.

Although state-of-the-art flow codes might be able to predict cavitation inception at millimeter scale in the future, this is far from common practice nowadays. Most currently applied analysis programs do not directly take into account the effects of roughness of the propeller surface, and of the amount and size of nuclei in the water, and can therefore only be expected to predict cavitation inception at larger length scales, not being governed by the very local details of flow and geometry.

As far as known to the author, studies on the systematic difference between the acoustic and the visual inception bucket have never been published in the public domain. It is however expected that a certain trend is present. The expected uncertain shape of the acoustically determined inception bucket is shown together with the visually observed inception bucket in Fig 6.3. The locus of the middle of the bucket is expected to remain unchanged.

In the remainder of this chapter mainly the "visual" inception bucket is considered, while it is recognized that the (relevant) "acoustic" bucket is likely to be located well within the visual inception bucket.

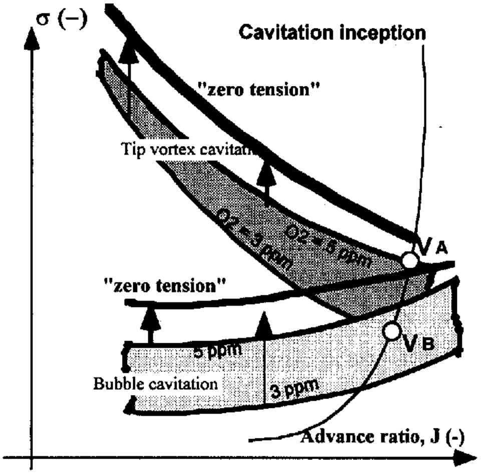
σ (-)
Cavitation inception
"zero tension"
Tip vortex cavitati
O2 = 3 ppm
O2 = 5 ppm
VA
"zero tension"
VB
5 ppm
Bubble cavitation
3 ppm
Advance ratio, J (-)

Figure 6.2: Schematic effect of nuclei distribution on inception bucket. The lower inception lines represent a 3 ppm nuclei density, while the upper lines represent 5 ppm. Furthermore an extrapolated socalled "zero tension" line is shown, which should not be dependent on the test facility. Source: Gindroz (1998)

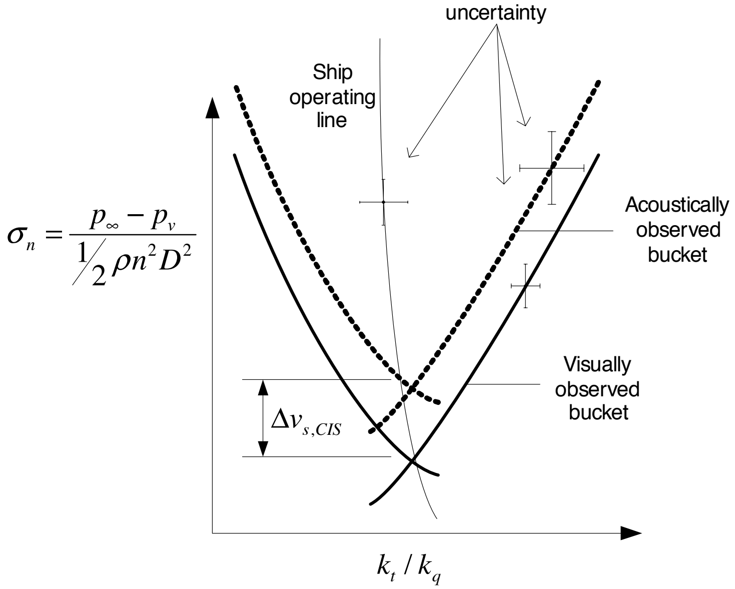
uncertainty
Ship operating line
Acoustically observed bucket
Visually observed bucket
$\Delta v_{s,CIS}$
$\sigma_n = \frac{p_\infty - p_v}{\frac{1}{2}\rho n^2 D^2}$
k_t / k_q

Figure 6.3: Illustration of acoustic and hydrodynamic buckets including uncertainties

6.3 Requirements on Inception Prediction

The starting point of the discussion on required capabilities was already given in the research objectives of this dissertation. These abstract goals (given on page 4) implicitly state that the simulation model should give an indication of propeller cavitation inception in both static and dynamic conditions. Accelerations, decelerations, sailing in high resistance conditions, and sailing in waves are mentioned in particular. No level of required validity is defined, but it is mentioned that the model should represent reality sufficiently accurate to make it useful for controller development. This interpretation of usefulness includes aspects of required accuracy, but also on robustness and necessary computational times. The interpretation also includes that inception predictions should be given for a variety of pitch angles, and not only for nominal pitch.

One of the goals of this research, which should be kept in mind, is to test a cavitation reducing PCS on full scale: Off-line prediction of inception conditions alone might help to increase insight, but does not necessarily lead to a practically applicable propulsion control system.

But to what requirements do these abstract research goals lead? First of all the goal of this research is to develop a propulsion control system that reduces all types of cavitation. In principle no distinction is made between the various possible types of cavitation, although for naval propellers the focus lies on vortex and sheet cavitation since they mostly appear first in practice. Secondly it is required to consider all propeller operating conditions (in this research limited to sailing on a straight line). Finally the aim is not limited to making off-line predictions of cavitation inception, but more importantly to give guidance for practical applications. In other words, the definition of a propeller operating area, that is cavitation free in a great variety of conditions (with a high degree of certainty), is more important than an exact prediction of the inception lines.

Now that the required capabilities have been set, the following sections aim at a description of capabilities of currently applied experimental and computational prediction methods. Computational predictions have the advantage that they (after verification and validation) should be able to give answers without the need to carry out expensive full scale or model scale tests. In this specific research this would be very beneficial since inception conditions for many pitch angles and many conditions are of interest.

6.4 Computational Cavitation Inception Prediction

To assess the available computational cavitation inception (CI) prediction methods, three types of propeller analysis programs are considered: one based on lifting surface theory, two panel methods, as well as three types of viscous flow solvers (DNS, LES, and RANS). These programs are considered representative for the state of the art in their class of methods.

The principle difference between lifting surface and panel methods is the location of the singularity distribution: lifting surface methods distribute the singularities over the camberline, and subsequently make corrections for thickness effects, while panel methods distribute the singularities over the actual propeller surface. Both before mentioned methods belong to the class of Boundary Element Methods (BEMs).

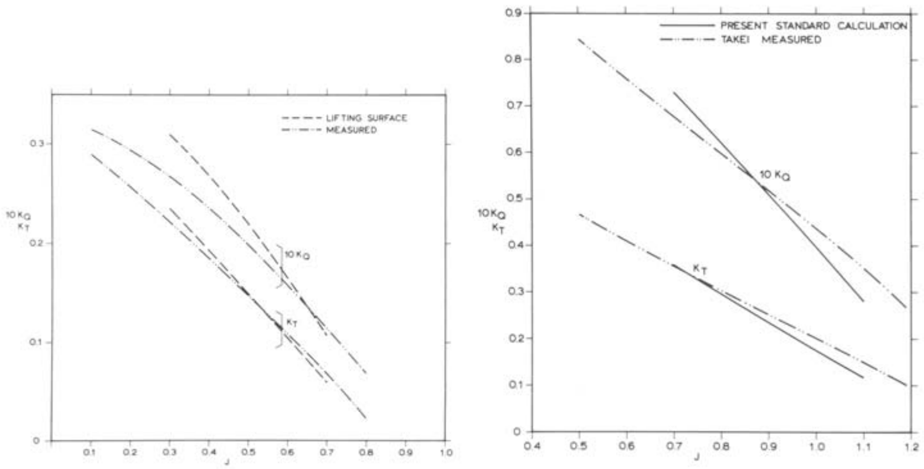

Figure 6.4: Comparison of propeller performance predictions and measurements. Source: Kuiper (1981)

Viscous methods divide the whole flow domain in cells, thereby capturing more flow details at the cost of high necessary computational power. They belong to the class of field methods.

6.4.1 Lifting Surface Methods

This section aims to give an overview of the predictive capabilities (and related validity) that one might expect from a typical lifting surface propeller analysis code. Kuiper (1981) presents an overview of predictive capabilities of such a lifting surface code. Some typical results of open-water propeller curve and pressure distribution predictions are discussed here first. The graphs shown in Fig 6.4 are taken from mentioned source, and give a qualitative idea of the validity of the method. In general the graphs show a better trend for k_t than for k_q. Especially the agreement of k_q becomes worse at lower advance ratios. Whether this specific agreement is sufficient should be decided by the user.

The capability of the program with respect to the prediction of pressure distribution over the propeller surface is also discussed. Such capabilities are assessed by comparing the chordwise pressure distribution at a specific radius against other predictions (verification) as well as against measurements (validation).

A verification of the pressure prediction of the lifting surface code is carried out against multiple other codes, although there is no specific reason to assume that the accuracy of the other lifting surface codes is higher. Results of the pressure distributions over both the face (pressure side) and the back (suction side) are compared in Fig 6.5. As noted by Kuiper, *the shape of the pressure distribution is similar for most calculations, although the minimum pressures at the leading edge can differ widely.* It is further reported that at inner radii the considered calculation method predicts a lower pressure at midchord (on the suction side).

A qualitative validation is shown in Fig 6.6, showing the comparison of predictions and measurements of pressures on the suction side at one single propeller radius. The lack of

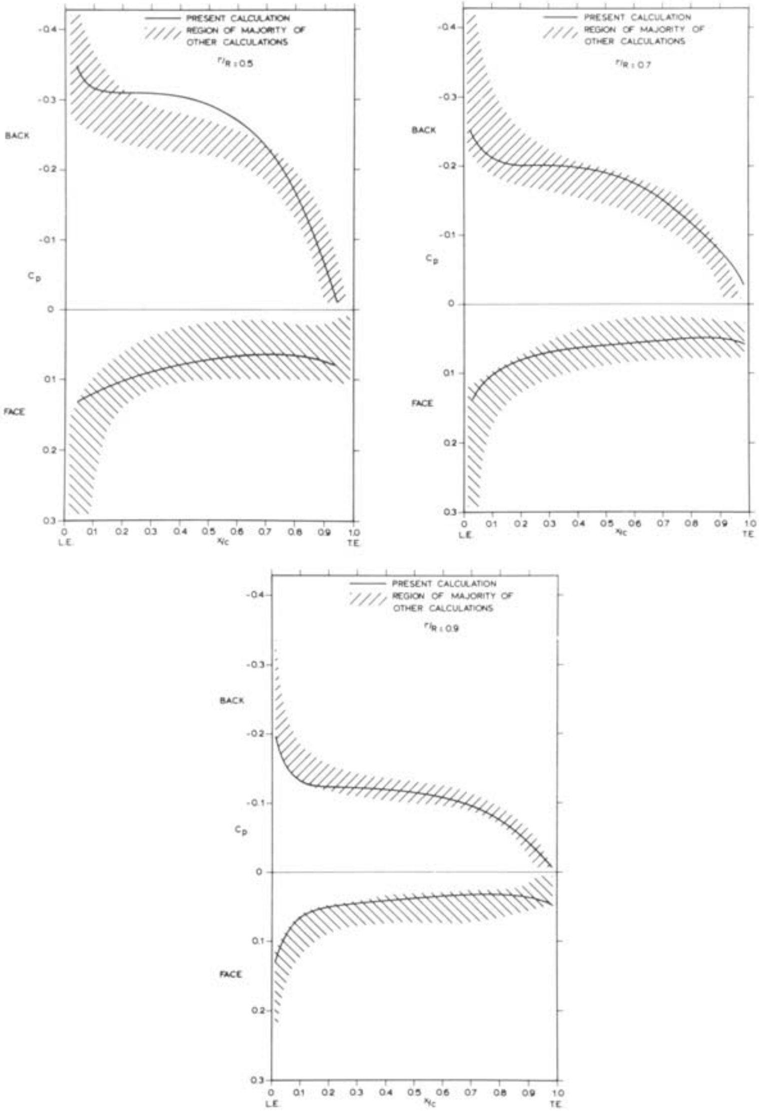

Figure 6.5: Example of verification of the pressure distribution calculation of a lifting surface code. Comparison is made against a number of other calculation methods. $C_p = \frac{p-p_0}{\frac{1}{2}\rho V^2}$*, with* V *the inflow velocity for that section, defined by* $V(r) = \sqrt{U^2 + \left(\frac{r}{R}\pi nD\right)^2}$*. Source: Kuiper (1981)*

measured data at the leading edge is presumably caused by measurement difficulties in the sharp pressure peak. This unfortunately results in a lack of validation data in the first 20% of the chordlength, while in many cases the cavitation inception location lies in this region. In other words: the intended prediction domain lies outside the validation domain.

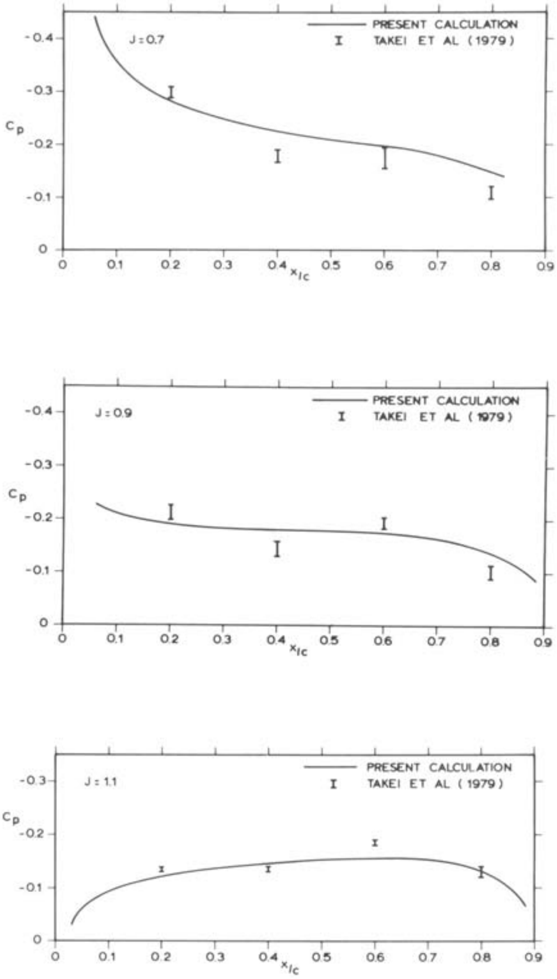

Figure 6.6: Example pressure distribution validation of a lifting surface code: Pressure distributions on the Takei propeller at $r/R = 0.77$*. Source: Kuiper (1981)*

The presented verification and validation results do not justify a strong confidence in the ability of the lifting surface code to predict the pressure distribution over the propeller surface with satisfactory accuracy. Note that this in itself is not a disqualification of lifting surface methods. However, considering the conceptual model behind the code, it is expected that lifting surface codes are not capable of delivering the required information for this project. First of all lifting surface methods are known to suffer from numerical problems in the region of the suction peak. Secondly the modeling of the tip-geometry

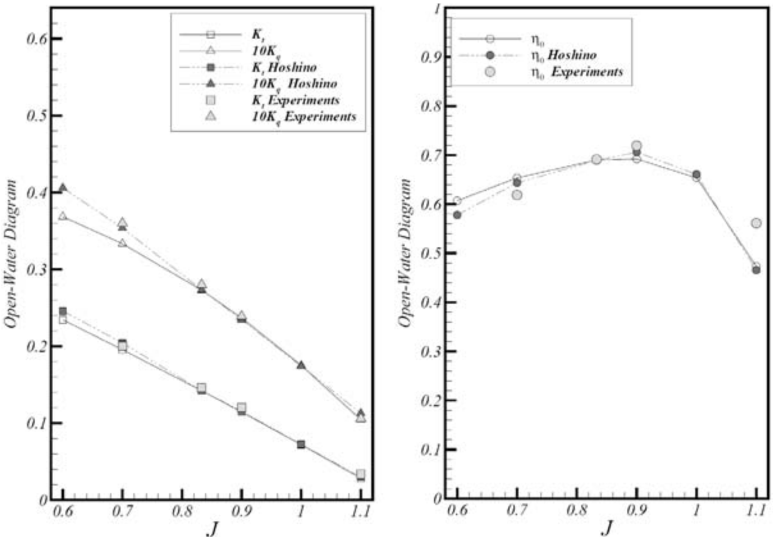

Figure 6.7: Verification and validation of open water performance prediction by a panel method. Source: Vaz (2005)

is known to be a weak point in lifting surface codes. All in all it is concluded that the method is not suited for inception prediction, especially because inception is likely to occur in the first 5% of the chord or in the tip region. Due to the mentioned weaknesses in the conceptual model it is not likely that additional validation studies will reveal otherwise.

6.4.2 Panel Methods

The predictive capabilities of typical panel methods are now discussed. Vaz (2005) presents validation results starting with a rectangular and an elliptical wing. Hereafter a rotating propeller geometry is considered, of which validation (and verification) results of open water propeller performance are shown in Fig 6.7. The openwater diagram shows qualitatively good agreement with experiments at higher advance ratios, with deteriorating agreement of especially k_q at lower advance ratios.

Verification and validation results of the pressure distribution at multiple radii are shown in Fig 6.8. The verification results show good agreement with the numerical results of *Hoshino*. Differences at the trailing edge are reported to possibly be caused by differences in the wake model. The validation results show good agreement at $r = 0.7R$ and $r = 0.9R$. Near the leading edge, which is often important for cavitation inception, the negative pressures are exaggerated, presumably due to the absence of viscosity in the potential code. The inner section at $r = 0.3R$ shows less agreement than the other two radii.

Calculations of a propeller in behind condition are also verified and validated by Vaz. Some representative validation results are shown in Fig 6.9. 0° indicates the top dead centre position, while 90° is the halfway down position. Note that this is an unsteady calculation, since it does take into account the flow dynamics due to the variation in inflow vector during a revolution of the blade(section). These and other results are reported to give the same trend as the measurements, but with quantitative differences. With respect to the validation domain that is covered by the presented results, it is concluded that no validation has been carried out for unsteady pressure prediction near the leading edge ($x/c < 0.1$). This does not mean that the computational predictions in that area are wrong: in this case no experimental data is available that allows for validation in that area.

In the same dissertation by Vaz, additional validation studies are carried out, considering the capability of the propeller analysis program to predict the extent and thickness of propeller cavitation in open water conditions. Such predictions are outside the scope of this research and are not dealt with here.

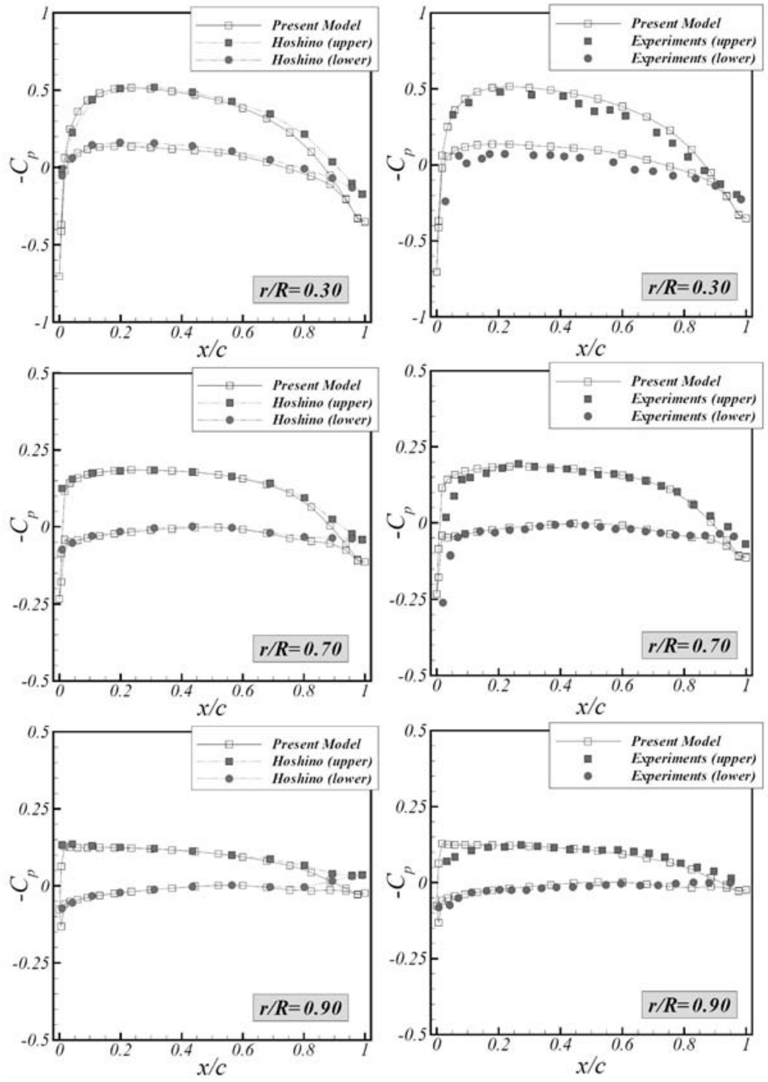

Figure 6.8: Verification and validation of pressure prediction against numerical data by Hoshino and experimental data by Gindroz et al. (1998). Design condition $J = 0.833$*. Source: Vaz (2005)*

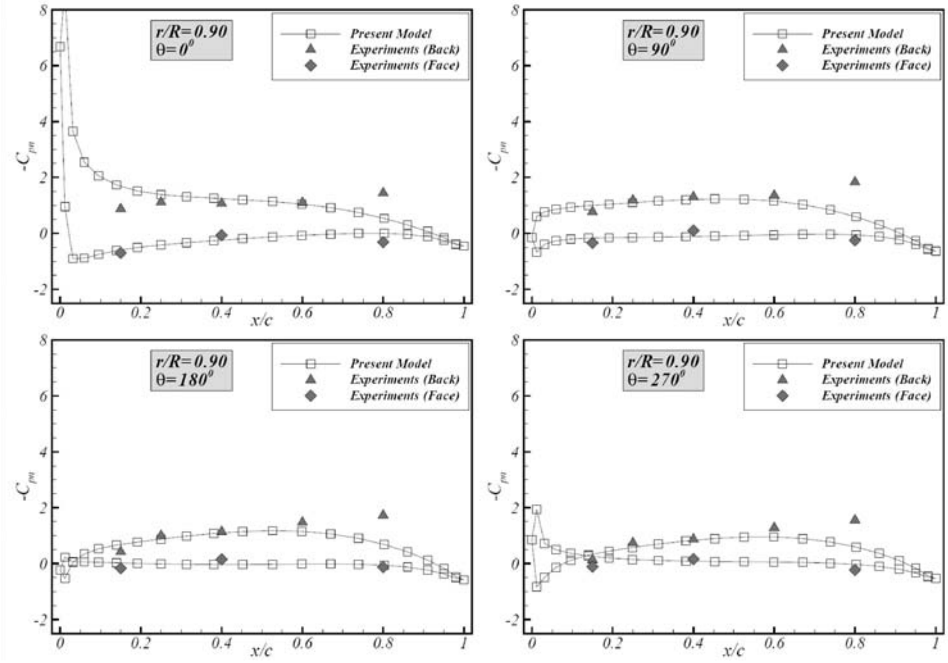

Figure 6.9: Verification and Validation of in behind performance: pressures at r=0.9R, at four different blade angles. Numerical data by Hoshino and experimental data by Gindroz et al. (1998) Source: Vaz (2005)

No validation of inception predictive capabilities is reported by Vaz. Such predictions by means of panel methods are discussed in Noble (1997) and Noble (2005), the latter using the same program as Vaz (2005). Because of the relevance for the current work these studies are considered in the following.

Inception prediction: Panel Method I

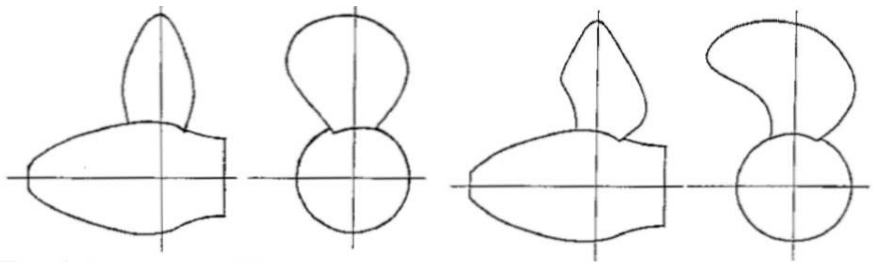

(a) Propeller *A*

(b) Propeller *B*

Figure 6.10: Propellers considered in Noble (1997)

Noble (1997) presents comparisons of cavitation inception predictions between a panel method named ASP-2, model scale experiments, and full scale observations. These comparisons are made for two five bladed controllable pitch propellers A and B, which are schematically shown in Fig 6.10. Only the inception prediction results for propeller A are discussed here.

Fig 6.11 presents validation results of the inception conditions of propeller A. ASP-2 predicts inception of suction side sheet cavitation at 1.8% from the leading edge, at a radius of $r/R = 0.95$, which agrees with both model- and full scale observations. As shown in Fig 6.11a, the qualitative agreement of suction side cavitation inception seems good, although both prediction methods give slightly conservative results when compared to the full scale measurement. The validation domain only consists of one operating point, which is insufficient to draw firm conclusions.

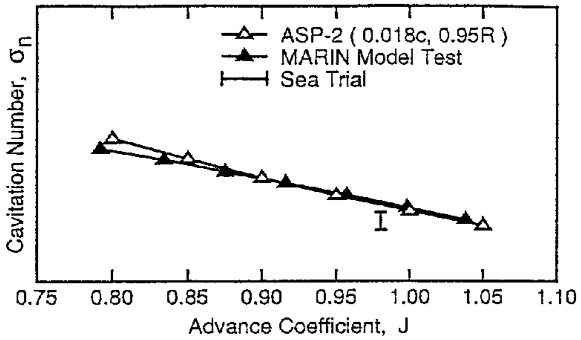

(a) Outer radius suction side sheet cavitation inception

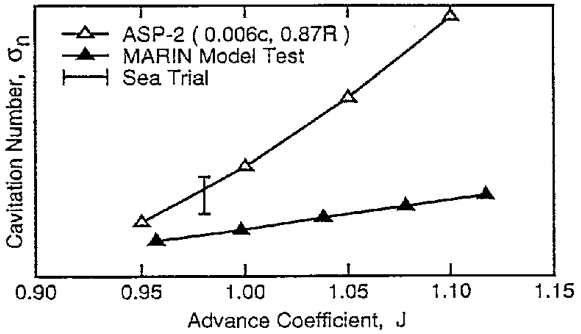

(b) Outer radius pressure side sheet cavitation inception

Figure 6.11: Validation of cavitation inception predictions: propeller A. $\sigma_n = \frac{p_\infty - p_v}{\frac{1}{2}\rho n_i^2 D^2}$. *Source: Noble (1997)*

The pressure side inception predictions are shown in Fig 6.11b. A big difference between model scale predictions and ASP-2 predictions is shown, of which a possible explanation is given in Section 6.5. The single operating point that is validated shows that (in that specific operating point) the ASP-2 prediction has good agreement with full scale observations. With respect to the inception location, ASP-2 predicts inception around 0.6% from the leading edge, at $r/R = 0.87$. This aspect is confirmed by both model scale as full scale experiments.

Although the presented validation material does not justify high expectations for future predictions, it should be noted that due to the sparse full scale observation data and the blanked axes of the graphs, again, no firm conclusions can be drawn from the presented results.

Inception prediction: Panel Method II

A second study on inception prediction by use of a panel method is reported in Noble (2005). Four propellers from a systematic series with skew angles ranging from 0 to 108 degrees are considered, and are shown in Fig 6.12. Each propeller was designed to have the same radial loading distribution and to operate at the same design point. Although not dealt with here, the thrust and torque coefficients of the same propellers where already validated in another report, showing deteriorating agreement for higher skew angles.

Although the report aims at validation of the inception prediction capabilities of the program, the greater part of the report is on verification and calibration. The reported grid refinement activities show that the discrete calculation scheme of the panel method does result in a stable converged solution of the continuous physical problem in the greater part of the domain. However, with each grid refinement the leading edge suction peak keeps growing due to the absence of viscosity. Nevertheless at some stage, where the greater part of the solution has converged, the grid refinement is stopped. These grid-refinement activities fall within the verification phase.

Due to the over predicted suction peak near the leading edge, the inception predictions are too pessimistic. To improve the agreement of inception prediction, a special form of calibration is applied. Since the experimental inception conditions are known, calibration is carried out in the following way: By defining so called *forbidden search regions* for the minimum predicted pressure, the overestimated suction peak is not taken into account for the determination of the minimum pressure. This ensures that the minimum pressure is found away from the suction peak, and quantitative good agreement in inception conditions can be found for a specific operating point. Note that this approach does not capture the intricacies of the pressure distribution near the leading edge and the tip, and that the definition of a specific forbidden search region is grid dependent.

The calibration procedure is carried out per propeller per side (back or face), after which some validation is carried out for other operating points of the same propellers. Examples of results for both the zero-skew and the high skew propeller are shown in Fig 6.13. Results are good for the low skew propeller, with deteriorating agreement for higher skew. In general the suction side predictions are slightly better than the pressure side predictions. In both figures the inception line is calibrated at $J = 0.8$ for suction side and $J = 1.1$ for pressure side inception. Note that the figures present results for multiple grids.

An important remark is made with regard to the type of cavitation that is being predicted here. The model scale sheet cavitation inception data that is shown in Fig 6.13 stems from model scale experiments that are documented in Boswell (1971). In that report the inception lines of various types of cavitation are shown, revealing that, in case of the 36°, 72° and 108°-skewed propellers, the inception bucket of vortex cavitation is more narrow than the inception bucket of sheet cavitation. This reveals that even if accurate predictions of sheet cavitation are possible, due to vortex cavitation inception, the true cavitation free operating area is likely to be more restrictive.

As concluded in the report, *"The restricted search procedure outlined in this report can be considered an interim approach that can hopefully be replaced in the future with suitable* *corrections to potential flow results for Reynolds number scale effects."* The opinion of the author of this thesis is that the demonstrated approach is too laborious, and needs too much calibration data, to be used frequently. The validation domain is restricted to 4 propellers from the same series, which have various common characteristics, and no off-design pitch angles are validated. It is therefore concluded that the considered panel method in combination with the proposed inception prediction method is not yet at a stage at which it can be used as a reliable predictive tool for the determination of cavitation inception in operational conditions.

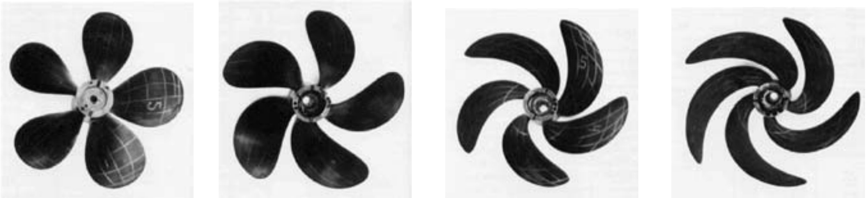
(a) 0 deg skew (b) 36 deg skew (c) 72 deg skew (d) 108 deg skew

Figure 6.12: Photographs of propeller series. Source: Noble (2005)

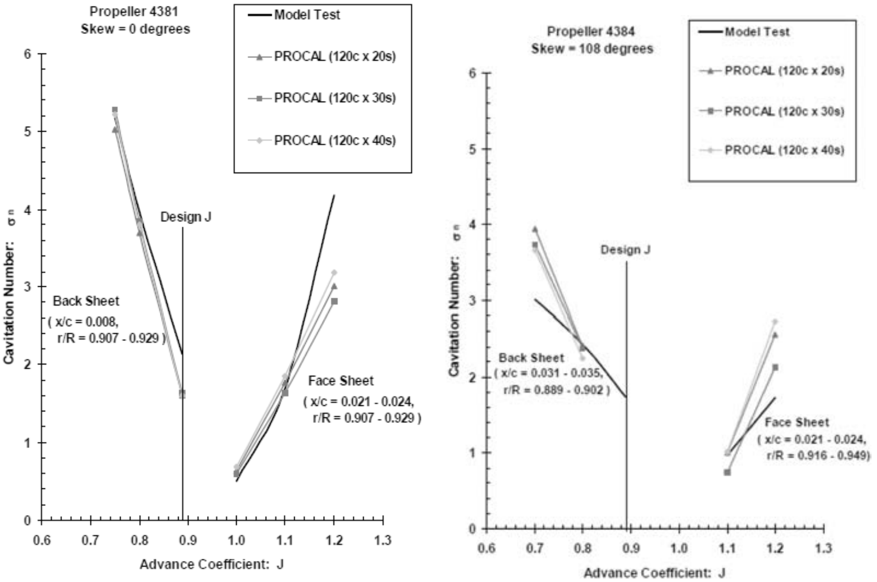

Figure 6.13: Prediction of the Cavitation Inception Characteristics for two propellers using Blade Grids with 120 Chord-wise Panels. $\sigma_n = \frac{p_\infty - p_v}{\frac{1}{2}\rho n^2 D^2}$. *Source: Noble (2005)*

6.4.3 Viscous Methods

With the increase of available computational power, the possibility of numerically solving the Navier-Stokes equations has opened up. Numerous commercial viscous programs are nowadays available, and many researchers are developing their own specialized codes.

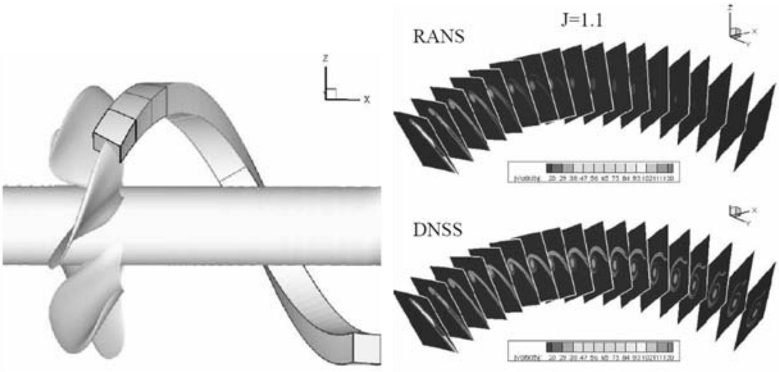
z
x
RANS
J=1.1
DNSS
vorticity 20 29 38 47 56 65 75 84 93 102 111 120
vorticity 20 29 38 47 56 65 75 84 93 102 111 120

Figure 6.14: Left: Reduced computational domain used for the DNS computations. Right: Comparison of vorticity in the reduced domain. Source: Hsiao and Chahine (2008)

Principle differences between the various viscous codes mainly lie in the treatment of the viscous terms in the governing equations of motion. The most complete approach titled Direct Numerical Simulation (DNS), calculates turbulence directly from the Navier-Stokes equations without additional modeling. This approach necessitates very fine grid cells, which result in high computational costs.

In case of Large Eddie Simulation (LES), the larger eddies are resolved numerically but the small scale eddies are modeled heuristically. The mesh that is needed for this method is less demanding, and computational cost are decreased with respect to DNS. However, LES methods are mostly still in a development phase, and are not ready for daily engineering purposes yet.

A viscous method that is becoming feasible for engineering purposes is the Reynolds Averaged Navier-Stokes (RANS)-approach. This approach does not directly calculate the turbulence in both the larger and the smaller eddies, but instead assumes a flow, which is the time average of the fluctuations that occur at a specific position. This obviously results in less computational costs, while for many applications the solutions are still acceptable.

Some illustrative state-of-the-art results from viscous computations are presented by Hsiao and Chahine (2008). There, a tip vortex of a propeller in open water conditions is simulated by means of RANS computations. The mesh is further refined at the location of this tip vortex, and DNS calculations are used to refine the results locally, as shown in Fig 6.14. The DNS method takes into account a specific nuclei distribution, and enables study of cavitation inception at microscopic scale. The mixed RANS/ DNS approach is further used to determine appropriate scaling laws for vortex cavitation inception. Since no validation is carried out, the uncertainty of the method is unknown. High quality validation is believed to be crucial for the path towards high confidence (inception) prediction capabilities. Nevertheless, the work of Hsiao and Chahine is believed to illustrate the limits of our current capabilities in predicting vortex cavitation.

6.5 Experimental Cavitation Inception Prediction Methods

Both kinematic and dynamic similarity of the flow have to be fulfilled when model scale cavitation inception experiments are required to be free of scale effects. Geometric similarity is regarded as a first constraint to get kinematic similarity, and can be obtained if the model scale milling facilities operate within satisfactory tolerances. Kinematic and dynamic similarity are often expressed in relevant non-dimensional numbers such as the advance ratio J, the Froude number F_n, Reynolds number R_n, the cavitation number σ, the gas content number and the Weber number.

As discussed by Carlton (2007), simultaneous identity can only be obtained for few combinations of non-dimensional groups. In other words it is physically impossible to attain complete flow similarity on model scale. In general similarity of σ and J is chosen, extended with the Froude number F_n to assure an identical vertical pressure gradient over the propeller disc. To minimize the effect of a dissimilar Reynolds number, operating speeds are mostly chosen as high as practically possible, thereby increasing the model scale Reynolds number. Furthermore, roughness can be applied on the leading edge of the model propeller and on the model hull to stimulate an identical (turbulent) character of the boundary layer as on full scale.

The dissimilarity of Reynolds number has an effect on inception predictions. First of all the ship wake is Reynolds dependent, and thus suffers from scale effects, leading to a too thick boundary layer on model scale which can affect the velocity field in which the propeller is operating. Secondly the boundary layer of the propeller itself is dependent on the Reynolds number, and although roughness can stimulate turbulence, it does not guarantee complete flow similarity. Kuiper (1981) showed that the presence of a laminar boundary layer can lead to delayed inception. Increase of the propeller Reynolds number is expected to bring the roughness Reynolds number above the critical value, ensuring a turbulent boundary layer and thus inception.

Free stream turbulence levels are also found to play a role (Van Rees et al. (2008)). It has been reported that free stream turbulence can stimulate transition from laminar to a turbulent boundary layer. This in turn might then stimulate inception due to the increasing pressure variations in the turbulent boundary layer.

The presence of sufficient nuclei of appropriate size is also of importance, and should thus be taken into account during cavitation tests. Van Rees et al. (2008) indicate that for a proper application of electrolysis, sufficient measures should be taken to distribute the nuclei throughout the complete propeller disc, as can for instance be done by an electrolysis screen. If the nuclei are not properly distributed over the disc, this can lead to delayed inception for the location where little nuclei are present, while in another location, where there is no lack of nuclei, no delay of inception occurs. If not properly handled, this effect can seriously delay the inception of especially pressure side cavitation, while this type of cavitation typically occurs outside the wake peak. This might for instance well be the case for Fig 6.11b, which demonstrates significantly delayed pressure side inception on model scale.

Validation of a full scale inception prediction by means of model scale tests is reported by Van Terwisga et al. (2007). There, a comparison is made between full scale observed inception conditions on a CPP, and model scale inception predictions that are scaled up

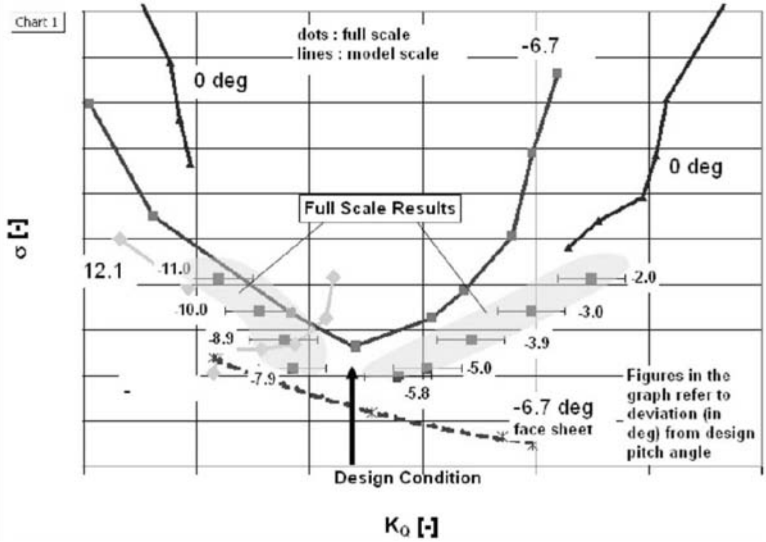

Figure 6.15: Comparison of full scale (visual) cavitation inception with similar results from model tests in the Depressurized Towing Tank (DTT). Source: Van Terwisga et al. (2007)

to full scale. To illustrate the intricacies in such predictions, the reported validation case is discussed in some detail here.

Fig 6.15 shows model scale inception results for three pitch angles, which were obtained in MARIN's Depressurized Towing Tank (DTT). Furthermore it shows full scale inception points, obtained for a range of pitch angles. These full scale inception points show uncertainty bars that correspond with an uncertainty in pitch angle of ±1 deg.

First we consider the full scale observed pressure side inception points, and compare them (by means of visual interpolation) with the predicted inception lines that are expected at the concerned pitch angle. It is reported that on full scale, due to low visual resolution, the distinction between leading edge vortex and sheet cavitation was difficult to discern.

At lower propeller loadings (-11 and -10 degrees) the agreement is relatively good, although due to lack of an operating line and axis labels, the agreement cannot be quantified. Moving towards the -7.9 point, it is observed that the agreement gets worse, resulting in a pessimistic inception speed prediction from this model test.

A possible explanation relates to the applied scaling method of the model scale results. In this case the McCormick scaling rule was applied, probably since at first sight the involved cavitation was of vortex type over the complete range. However, during a further analysis of the experimental observations, at the higher loadings (implying reduced tip load at pressure side), one could observe only low vorticity levels near the inception location. This indicates that no McCormick scaling rule should have been applied, which would result in a downward shift of the model scale inception lines, leading to improved agreement as shown by the dotted line in the figure. The difficulty here thus lies in distinguishing between vortex cavitation and vorticity free cavitation.

Observation on suction side shows a somewhat different picture. Both on full scale and on model scale the first cavitation to occur is found to be local vortex cavitation attached to the aft part of the tip. At the higher loadings an isolated suction side sheet develops near the tip at the leading edge and occurs almost simultaneously with the local tip vortex at inception. Although the character of cavitation agrees for full scale and model scale, Fig 6.15 shows that full scale inception occurs significantly later than predicted.

Because suction side cavitation occurs in the wakepeak, it is suggested that wake scale effects are responsible for the disagreement. Due to a too thick hull boundary layer, the axial velocity deficit in the wakepeak is likely exaggerated, resulting in too pessimistic suction side inception predictions. Correction of these viscous scale effects is likely to improve the predictive value of this type of cavitation. Such corrections can be made by computing both model and full scale wake, and then using the wake deficit at the observed location of inception to correct the inception speed prediction.

Van Terwisga et al. (2007) make a short remark with regard to difficulties in prediction of inception near inner radii. It is suggested that too optimistic predictions might be caused by a laminar boundary layer on model scale. Another possible reason for delayed inception on model scale might be the socalled "bubble screening" effect that prevents nuclei to reach low pressure areas where inception would occur on full scale (Van Rees et al. (2008)).

Based on these validation results, including the given comments, the current author concludes that in order to derive high quality full scale inception predictions from model scale tests, much attention should be given to prevention of, or correction for, scale effects. This requires high quality model scale observations to distinguish between vortex cavitation and vorticity free cavitation. Further gains are suggested by means of wakefield corrections, and should probably become part of inception studies. Mitigation of laminar flow effects and prevention of bubble screening might also help to increase the agreement between prediction and full scale inception.

Despite these (and other) intricacies, a recent expert estimate of current model scale prediction capabilities is that, provided all above mentioned measures are taken, the CIS corresponds with full scale measurements within a ±1 knot interval at a 95% confidence level (Van Terwisga (2009)).

With the exception of above mentioned publication, high quality validation studies on inception predictions are rarely published. Apart from confidentiality reasons, this is likely caused by the difficulties in uncertainty quantification of both model and full scale experiments. Full scale experiments that are necessary to provide validation data have the disadvantage of being a field experiment. This indicates that observations and measurements are made in limited controlled conditions, with limited sensor quality, and in a limited amount of time. In practice it is only possible to gather limited inception data, of which the quality is highly dependent on the weather conditions during the trials. The measurements are often quite uncertain, which directly influences the quality of the validation material and thus of the validation itself. Bias errors easily contaminate full scale torque and thrust measurements, especially those made with sensors that are only temporarily installed. Even electronic pitch measurements have been reported to have a bias of more than 1 degree, due to erroneous sensor calibration or temperature sensitivity of the pitch sensors. The values of these uncertainties are dependent on the installation, water and weather conditions and on the experimental test setup, and should therefore ideally be considered individually per ship.

Inception of vortex cavitation is known to be most sensitive to viscous scale effects, and is therefore treated separately in the next section.

6.5.1 Vortex Cavitation Inception

As discussed in the previous section, model scale cavitation experiments are inherently affected by scale effects. In many cases this is caused by the Reynolds number, that is too low on model scale. Tip vortex cavitation suffers most from this scale effect since its development is related to the (Reynolds related) boundary layer thickness near the propeller tip. The scale effect on vortex cavitation inception led to the development of scaling laws that allow for the prediction of full scale vortex inception, based on model scale observations. Since such a scaling law is in fact an important part of the prediction method, it is dealt with here in some more detail.

McCormick Jr (1962) discusses the semi-empirical analysis of several types of fixed planforms and their tip vortex cavitation. Three types of model scale planforms (elliptic, rectangular and delta) at several aspect ratios AR are analyzed. For reference the aspect ratio is given by $AR = \frac{b^2}{S}$, where b is the span, and S the area of the wing. By means of a semi-empirical analysis McCormick relates the angle of attack, the Reynolds-governed boundary layer thickness on the pressure side near the wing tip, and the aspect ratio to the minimum pressure in the vortex core.

Noordzij (1977) applied the results to rotating propellers, and found that for small angles of attack the inception index can be approximated by:

$$\sigma_i \sim \alpha^{1.48} R_n^{0.35} \frac{AR^{0.89}}{(AR+2)^{1.48}}$$

For α of the order of 1 degree, he found that:

$$\sigma_i \sim \alpha^{1.24} R_n^{0.35} \frac{AR^{0.89}}{(AR+2)^{1.24}}$$

Noordzij further approximated the two equations to $\sigma_i \sim \alpha^{1.4} R_n^{0.35}$, taking the exponent 1.4 as an average value. Assuming equal angle of attack for full scale and model scale, this simplifies to the following scaling rule:

$$\frac{\sigma_{ship}}{\sigma_{model}} = \left(\frac{R_{n,ship}}{R_{n,model}} \right)^{0.35} \tag{6.1}$$

Model scale experiments which are subsequently scaled by Equation 6.1 were validated by Noordzij for three different ships, each at one operating point, which is quite sparse from the viewpoint of Fig 5.2 and Fig 5.4.

The exponent $e = 0.35$ is related to the assumed boundary layer model, and holds the middle between a complete laminar and a complete turbulent turbulent layer. This exponent is taken differently per facility, and is reported to vary between 0.2 and 0.5 (Kuiper et al. (2006)), which gives some indication of the uncertainties that are included in the scaling method.

For a test carried out at equal Froude number, with exponent e, appendix C shows that the McCormick scaling rule can be simplified to:

$$\sigma_{ship} = \sigma_{model} \cdot \lambda^{\frac{3e}{2+e}} \left(\frac{\nu_{model}}{\nu_{ship}} \right)^{\frac{2e}{2+e}} \tag{6.2}$$

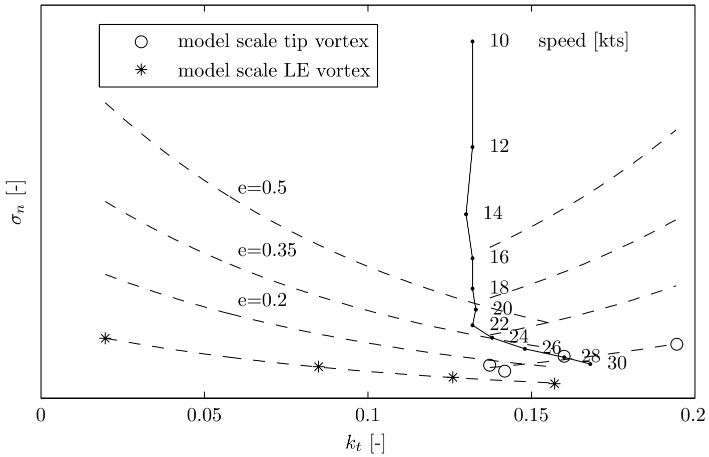

Figure 6.16: Effect of McCormick scaling coefficient on full scale inception prediction

with λ being the geometric model scale factor, and ν the kinematic viscosity (data on viscosity is given by for instance the ITTC recommended procedures and guidelines).

To get a feeling for the dependence of the full scale inception prediction on the value of the exponent e, three scaled up inception buckets are shown in Fig 6.16. The spread in predicted inception speed is quite significant (16-24 kts), and would even increase for off-design conditions.

However, it should be realized that in general the uncertainty in e is much less for a given test facility, since laboratory and procedure effects are included in e. Monitoring the test facility water quality can possibly help to prevent unnoticed temporal drift in e. If no further validation studies are available that indicate otherwise, it seems appropriate to assume an uncertainty of the predicted cavitation inception speed v_{cis} of approximately $\sigma_{v_{cis}} = 1$ kts (σ indicates standard deviation here). Studies such as reported by Van Terwisga et al. (2007) can help to decrease this uncertainty.

The opinion of the author is that the presented validation material by Noordzij (1977) alone does not sufficiently substantiate the validity of the scaling method. All in all it is therefore concluded that no firm conclusions should be drawn from tip vortex inception lines that are derived from model scale experiments, and as such should thus be considered with caution. Once again this does not prove that the method is inadequate, but only says something about the lack of convincing evidence that justifies a certain level of confidence.

6.6 Assessment of Applicability

In the assessment of the adequacy and validity of propeller performance predictions the user should consider the intended application domain in relation to the validation domain. This domain can be seen as a multidimensional space which is partly spanned by geometrical propeller aspects, as well as by the considered operating conditions. Some questions that one should try to answer during the assessment of a candidate propeller analysis program are for instance:

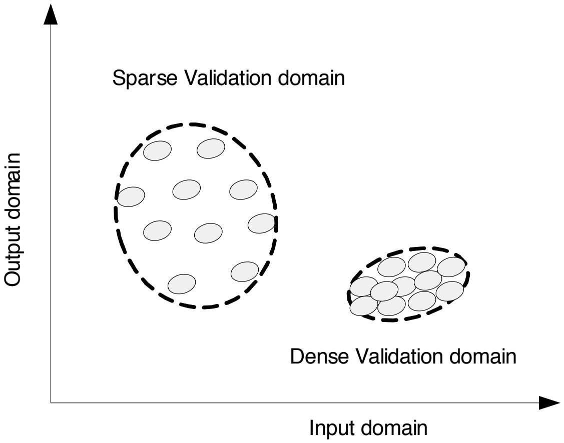

Figure 6.17: Equal validation effort: widespread but sparse, or small but dense

- What is the expected accuracy of the predictions?
- Can the computations be calibrated, if measurements are available?
- To what extent is the considered propeller geometry represented in the validation database?
- To what extent is the considered wakefield represented in the validation database?
- To what extent are the intended operating conditions represented in the validation database?
- Can the type of cavitation that is of interest be predicted by this analysis program?
- Can the considered problem be solved by a steady propeller analysis, or does the nature of the problem require unsteady propeller analysis?

Since these types of questions should be asked by users of a specific prediction methods, the code developers and experimentalists should aim for program verification and validation that helps to answer these questions. This ideally starts with definition of a thorough verification and validation program. The design of specific validation experiments is of great importance, since these experiment determine the validation domain of the code. Too often, due to lack of time and money, non-dedicated experimental data is used as validation material, thereby ignoring the great importance of structured, high quality validation.

The validation effort is related to the validation domain: on the one hand it can be chosen to aim for a widespread sparsely filled domain, while on the other hand a small dense validation domain can be pursued (see Fig 6.17). This trade-off should be driven by issues such as for instance the possible consequences of inaccurate or wrong predictions, and the level of confidence that one has in predictions outside the validation domain.

6.7 Conclusions and Recommendations

This chapter discussed the adequacy of prediction methods for the prediction of propeller cavitation inception. Even though a number of validation cases, covering a small validation domain, are found in literature, there are no sufficiently convincing arguments that propeller inception can be predicted with sufficient accuracy in a large application domain without rigorous further validation work. A more thorough validation of prediction methods can help to increase confidence. On the other hand it can be questioned whether the conceptual models behind the analysis codes capture the physics that are relevant for inception predictions sufficiently well. From the inception prediction results that have been presented in this chapter, the author concludes that the available cavitation inception prediction methods cannot deliver the high fidelity inception predictions for a wide variety of operating conditions that are needed for this project. Taking into account the complex physics that play a role in cavitation inception, it seems essential to improve the physical models.

Improvement of the physical model has already led to the development of viscous codes that are suited for propeller analysis. These programs are under continuous development and validation. A more reliable prediction of cavitation inception from these latter codes is to be expected in the near future.

With regard to model scale inception predictions it is concluded that there are various aspects that need to be taken into account during the tests and analysis. As shown by Van Terwisga et al. (2007), the proper distinction between sheet and vortex cavitation inception is sometimes difficult, but necessary to ensure that the proper scaling law is applied. He also suggest that the detrimental effect of a too thick ship boundary layer on model scale should possibly be corrected for by means of additional CFD computations. Van Rees et al. (2008) suggest that an electrolysis grid should be used to ensure that sufficient nuclei are distributed to all parts in the propeller disc. This should help to prevent the regularly observed delay of pressure side inception on model scale. Furthermore Gindroz (1998) emphasizes the importance of nuclei measurements in cavitation inception tests to prevent, or at least recognize, effects of a deviating nuclei spectrum that is present in the test facility.

Finally, it is emphasized that without extensive high quality verification and validation of both numerical and model scale inception prediction methods, they are not suitable as a tool when high confidence predictions are necessary.

Chapter 7

Controller Development

7.1 Introduction

In this chapter a controller aiming at *increased cavitation free time in operational conditions* is developed. First of all some general considerations on possible control strategies are discussed, after which the principle idea behind the new controller is presented. Then, specific implementation issues that are necessary to bring the idea in practice are dealt with at blockdiagram level.

The behaviour of the developed controller and more importantly, its connected ship propulsion plant, is tested in the simulation environment that was developed and validated in previous chapters. Via a parametric study it is shown how initial full scale parameter settings were chosen.

7.2 General Controller Considerations

Before a start is made with the development, two basic control principles, that might be applied to the system under consideration, are discussed. On a somewhat abstract level there are two types of control: feedforward and feedback. Combinations of the two are of course also possible. An illustrative example of both methods is given here. A modern home-heating system is of the feedback type: The temperature setpoint T_{set} is an input to the thermostat, which continuously measures the actual room temperature T. If there is a difference between the two, the thermostat activates the heating system (or possibly a cooling system), based on a certain control law of some structure, aiming at restoring the room temperature to the desired value. Once the temperature setpoint is reached, the heating switches off and the process starts over again.

One of the advantages of feedback is that it can make the controlled property less sensitive to disturbances that may act on the system. This is a very important property, and has resulted in a widespread use of feedback controllers. But feedback also has its pitfalls: In some circumstances the feedback system can become unstable, which results in unfavourable behaviour and in some cases can have catastrophic results for the plant and its surroundings. Secondly feedback implies measuring the signal that is required to be controlled by means of a sensor. If the property under consideration can be measured at all, the use of a sensor can make the system vulnerable to measurement errors and uncertainty.

Some portable electric home heating systems are of the feedforward type: they have a knob via which the amount of heat that the heater produces is determined. A possible approach might be to let the knob be actuated by a control system that measures the factors that affect the room temperature such as for instance the outside temperature, the neighbors temperature and the wind speed. If the system takes into account the dynamics of the room temperature, as well as the effect of the measured "disturbances", it is possible to control the room temperature T without actually measuring it! However, it is virtually impossible to incorporate all affecting factors, so that in this example case, it is not likely that the room temperature will be controlled satisfactory. However, as will be shown later, if the system property of primary interest (in this case T) is dominantly governed by one single measurable variable, then application of feedforward can be quite successful.

But which type of control is more suited for the current study regarding the increase of cavitation free time? Several aspects of feedforward and feedback related to this project are shortly discussed in the following sections.

7.2.1 Conventional Ship Propulsion Control: Feedforward

As was already briefly shown in Section 2.4.4 and Section 3.3, the conventional ship propulsion control system is in fact a feedforward system. Instead of controlling the true primary goal "ship speed", it is chosen to control a variable called the virtual shaft speed n_{virt}. The virtual shaft speed is a single composed variable that encompasses both shaft speed and pitch, and (in non-transient conditions) has an almost linear relation with ship speed. Its setpoint is defined as

$$n_{set,virt} = \frac{\theta_{set,PPC} - \theta_0}{\theta_{nom} - \theta_0} \cdot \frac{n_{set,gov}}{i_{gb}}$$

where $\theta_{set,PPC}$ is the low level pitch setpoint. $\frac{n_{set,gov}}{i_{gb}}$ is the governor setpoint divided by the gearbox reduction ratio. θ_0 and θ_{nom} are constant and indicate the zero thrust pitch and the nominal pitch respectively. In the same way the actual virtual shaft speed is defined as:

$$n_{virt} = \frac{\theta - \theta_0}{\theta_{nom} - \theta_0} \cdot n$$

Note that the virtual shaft speed only contains variables (shaft speed and pitch) with small time constants when compared to the slow ship speed loop, and are both relatively easily measured.

The relation between virtual shaft speed and ship speed is shown in the contourplot of Fig 7.1. For reference the combinator of the old PCS is also shown. The figure illustrates that the contours of n_{virt} and v_s run approximately parallel, especially if one compares two possible operating points that are not too far apart. n_{virt} is thus a good indicator for (static) ship speed, being more or less independent of the combination of shaft speed and pitch that together constitute the virtual shaft speed.

Although not explicitly shown in the figure, the ship speed that is achieved by a certain virtual shaft speed is dependent on the condition dependent resistance. This means that

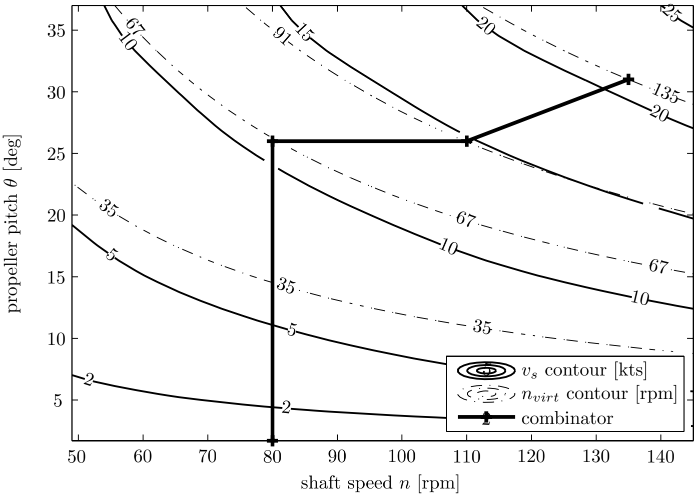

Figure 7.1: Contours of ship speed and virtual shaft speed in the n-θ plane. For increased resistance conditions, the ship speed contours shift towards the northeast. The combinator curve is shown for reference

the watchkeeper in practice makes his own estimate of the conditions, and then chooses a virtual shaft speed setpoint, of which the expectancy is that it will result in the desired ship speed. If after a while (due to the slow ship speed loop) the ship speed proves to be effectuated insufficiently accurate, small manual corrections to the virtual setpoint can be made. Note that this is in fact a feedforward approach, which may be augmented by feedback through a human in the loop. It is noted here that although combinator-based propulsion control systems are in principle feedforward systems, they do include specific feedback loops such as for instance in the engine governor or in the low level propeller pitch controller, but as mentioned before these have small time constants.

The design of a combinator curve in a conventional propulsion control system is a compromise between many performance aspects. One of these aspects is propeller cavitation. If this aspect is considered of importance one could, for instance, design the combinator in such a way that during some operating condition (say nominal or perhaps mean operating condition), the propeller operating points all have maximum margin against cavitation. Such an approach will lead to satisfactory performance as long as no disturbances act on the system. Sailing with one trailing shaft will for instance increase the loading on the other. The propeller operating point is further affected by waves, wind, manoeuvres and ship motions. The impossibility of designing a single combinator curve that meets cavitation requirements in varying weather conditions is explicitly demonstrated in Vrijdag et al. (2008).

The currently applied feedforward approach has the advantage that the plant is not continuously actuated by the controller, which often is beneficial with regards to wear of the installation. Especially the continuous adjustment of the CPP is not common nowadays, and related wear aspects are not fully understood (Godjevac et al. (2006)), which partly explains the common choice for feedforward over feedback.

7.2.2 Experimental Ship Propulsion Control: Noise Feedback

A feedback approach to reduce acoustic underwater signature, involving measurement of underwater noise, has been tested in the past onboard an S-frigate of the RNLN in the 1980's. The project was carried out in cooperation with industry and was titled "VS4". As reported in De Mulder and De Nies (1987) the developed propulsion control system minimized the noise emitted by the propellers by adapting the propeller pitch while ensuring constant average thrust by adjustment of the shaft speed. A blockdiagram of the approach is shown in Fig 7.2. Acceleration sensors were installed near the propellers, which generated input to the optimization program. The optimization program used a steepest descent algorithm to iteratively determine the pitch offset that led to the minimum of measured noise. At the same time, the microcomputer added a correction to the governor setpoint, to ensure that the desired average thrust was maintained. The thrust was measured by means of strain gauges on the shaft.

The optimization program was not active during transients because the applied method needed sufficient time to find the optimal pitch angle with the least noise. It is reported that, in case of twin screw ships such as the S-frigate, the method dealt with each propeller successively to prevent interaction between the propellers.

Noise reductions up to 12 dB are reported at speeds below 12 kts. Between 12 and 18 kts no noise reduction was found, and in the range from 18 to 24 kts a reduction up to 3 dB has been observed. The exact conditions under which these gains have been found are not reported.

It is noteworthy to mention that the "VS4"-approach led to the mounting of propeller noise sensors on the M-frigates. The noise optimization approach was however never applied onboard the M-frigates, although two sensor readouts are still available on the navigation bridge nowadays. As mentioned in De Mulder and De Nies (1987), the M-frigates were also fitted with provisions for a technological spin-off regarding fuel optimization. As far as known to the author these "provisions for" are limited to a sole pushbutton on the bridge console, and no fuel optimization program has ever been applied.

Based on the reported method and results it is concluded that a feedback approach based on measurement of noise is feasible. However, due to the time necessary to find an optimum pitch-shaft speed combination, combined with the fact that the port and starboard shaft have to be optimized sequentially, it is expected that such an approach is not suited for noise reduction during ship speed transients. Wave frequent adjustments of propeller pitch are also not considered possible.

7.2.3 Combined Feedback and Feedforward

In this project a combination of feedback and feedforward is applied, thereby combining desirable characteristics of both. Disturbance rejection due to feedback helps to make the system performance robust against the ever changing environment in which the propeller operates. On the other hand a feedforward approach is applied to operate the propeller in such an operating point that it is least susceptible to cavitation. This "optimal operating point" is based on prior knowledge and understanding of the system. This approach can help to overcome the difficulties in measurement and feedback of underwater noise. Because the proposed feedforward approach does not rely on noise measurements, no interaction effects are to be expected in case of twin shaft ships. A further advantage is that

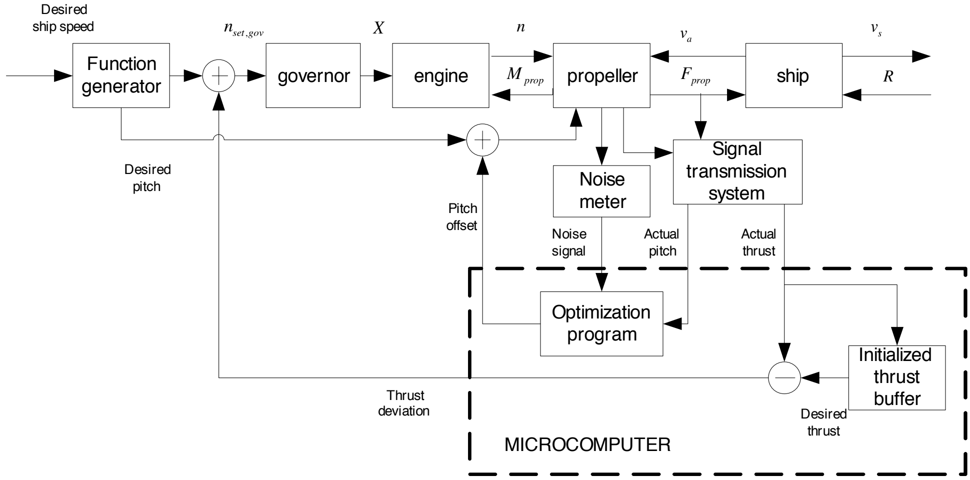
Desired ship speed
$n_{set,gov}$
X
n
v_a
v_s
Function generator
governor
engine
M_{prop}
propeller
F_{prop}
ship
R
Desired pitch
Pitch offset
Noise meter
Signal transmission system
Noise signal
Actual pitch
Actual thrust
Optimization program
Initialized thrust buffer
Thrust deviation
Desired thrust
MICROCOMPUTER

Figure 7.2: Blockdiagram of the "VS4" noise-feedback approach. Reproduced from: De Mulder and De Nies (1987). Note that the command to this system is shown to be "desired ship speed", while the current author believes that this was virtual shaft speed instead

the feedforward approach can react to undesirable propeller inflow before actual noise is generated, while a noise feedback approach reacts when noise has already been generated, which in principle is too late.

On the downside feedforward requires knowledge of the propeller operating points that are least susceptible to cavitation. As was shown in Chapter 6, high confidence predictions of cavitation inception for a big variety of operating conditions are not easily made with the currently available tools.

The structure of the suggested combined approach is shown schematically in Fig 7.3. Analogue to Fig 7.2, corrections to the governor setpoint $\Delta n_{set,gov}$ are generated, but now based on the signals n_{virt} and $n_{set,virt}$ instead of the desired and actual thrust signal as applied in the VS4-project. The noise feedback is replaced by feedback of a derived signal α_{eff}, which can be seen as some derived mean angle of attack of the propeller. Although not part of the control system, noise sensors are used to measure the noise levels (or better the acceleration levels) for reasons of afterward analysis and comparison.

The concept and the content of the PCS+ block is dealt with in the following sections.

7.3 New Controller Concept

There are several requirements on the static operating points that are to be effectuated by the PCS+. First of all there is the ship speed related requirement, that demands that the shaft speed-pitch combination (the solution) that is found, gives approximately the same ship speed as would have been found when the old PCS would have been applied.

Secondly the solution should ensure that the propeller continuously operates in a working point that is least susceptible to propeller cavitation. Furthermore the engine should not be operated outside its envelope, and finally the acceleration and deceleration capability

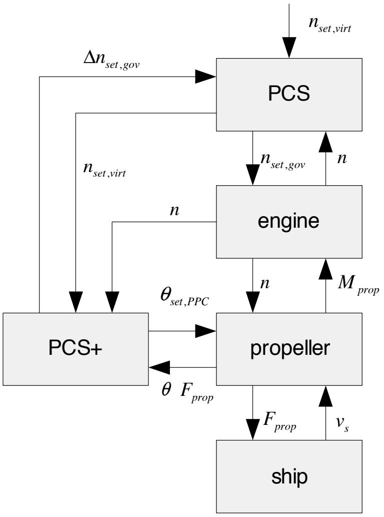
$n_{set,virt}$
$\Delta n_{set,gov}$
PCS
$n_{set,virt}$
$n_{set,gov}$
n
engine
n
n
M_{prop}
$\theta_{set,PPC}$
PCS+
propeller
θ F_{prop}
F_{prop}
v_s
ship

(a) Overall blockdiagram

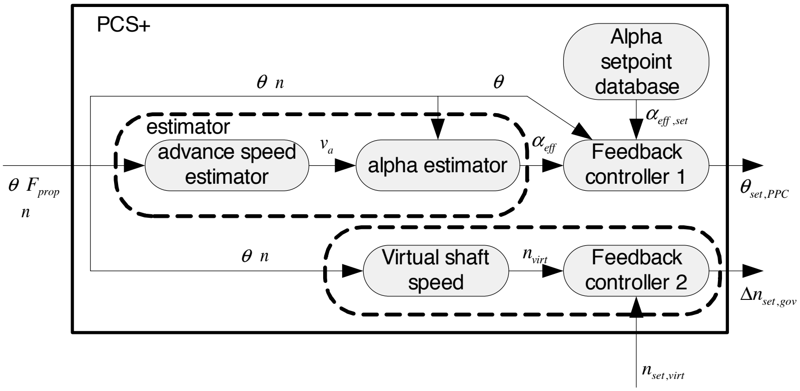
PCS+
Alpha setpoint database
θ n
θ
$\alpha_{eff,set}$
estimator
advance speed estimator
v_a
alpha estimator
α_{eff}
Feedback controller 1
θ F_{prop}
n
$\theta_{set,PPC}$
θ n
Virtual shaft speed
n_{virt}
Feedback controller 2
$\Delta n_{set,gov}$
$n_{set,virt}$

(b) Close up PCS+ blockdiagram

Figure 7.3: Blockdiagram of the proposed approach

of the ship should remain acceptable. In the following the conceptual ideas behind the two main controller loops that are part of the PCS+ are discussed. The actual implementation (on blockdiagram level) is discussed separately.

7.3.1 Control of Ship Speed

In the previous sections two different methods of controlling ship speed were discussed. First of all the (currently applied) feedforward approach that makes use of the virtual shaft speed, and secondly the approach based on thrust, as was shown in Fig 7.2. There are however more variables that could be used to control the ship speed, as is discussed in Stapersma et al. (2004). It is shown there that in principle all ship propulsion related variables that are monotonously rising with ship speed can be used.

Due to its simplicity, its robustness, and its importance in communication with the ship crew, it is decided to let the virtual shaft speed be the high level command that is to be effectuated by the PCS+. Since it is expected that the static operating point (in terms of shaft speed-pitch combination) that will be effectuated by the new PCS will lie close to the "old" combinator curve in most occasions, only small differences in static ship speed are expected. These small differences are not considered of importance during daily operational use.

7.3.2 Control of Effective Angle of Attack: α_{eff}

When considering a specific value of n_{virt} in Fig 7.1, there still is no unambiguously defined operating point in terms of shaft speed and pitch. From a particular contour line, one specific operating point needs to be selected that is least susceptible to cavitation inception. As an example one might question what is the best combination of pitch and shaft speed to realise a virtual shaft speed of 91 rpm ($\approx$ 15 kts) that is least prone to cavitation inception. From the viewpoint of ship speed, a combination of 130 shaft revolutions with 22° pitch is approximately equivalent to 90 rpm with 31° pitch.

For one or more specific operating conditions, computational or experimental prediction methods might be able to give some guidance on the choice for a specific operating point. However, as discussed in Chapter 6, prediction of propeller cavitation inception has not yet reached the required level of accuracy, especially when considering prediction of tip vortex cavitation inception. Furthermore the exact operating conditions in which the propeller is operating are not known beforehand, and are constantly changing in operational conditions, due to for instance extra resistance and waves.

Stimulated by the difficulties in cavitation inception prediction, and the influence of instantaneous operating conditions on inception, it is chosen to follow a robust approach, based on the control of the estimated effective angle of attack of the propeller blades. A definition of that angle of attack, and a method to determine and actively control it, is given in the following sections. But before the effective angle of attack is defined, the effect of waves and wakefield on the propeller inflow is discussed, in order to explain which kind of wakefield disturbances can or cannot be compensated for by pitch or shaft speed adjustments.

Wakefield Disturbances

Without giving an exact definition of angle of attack yet, the approximate relation between angle of attack α, pitch angle θ and flow angle β for a foil section of the propeller blade is given by $\alpha \approx \theta - \beta$. To consider the effect of flow disturbances due to waves and wakefield on local inflow angle β, a short general analysis is made, showing the principle difference between axial and tangential disturbances. For simplicity the variable J is used instead of advance angle β. The two are closely related, but β necessitates use of the tan^{-1} function, which is not desirable at this point because it unnecessarily complicates the analysis.

The (global) advance coefficient J is defined by $J = \frac{\overline{v}_a}{nD}$. In order to incorporate local tangential velocities in a definition of a local advance coefficient J_{local}, we write

$$J = \frac{\overline{v}_a}{nD} = \frac{\overline{v}_a}{2\pi nr} \cdot \frac{2\pi r}{D}$$

Wakefield and waves cause inflow variations in both axial and tangential direction. Wakefield causes blade frequent variations, while waves cause variations that are wave frequent. If we focus on the local axial velocity in the propeller disc, we can write

$$v_{a,local} = \overline{v}_a + \Delta v_{a,wake} + \Delta v_{a,sea}$$

Note that $\overline{v}_a$ is the mean axial velocity, while $\Delta v_{a,wake}$ includes the variations around this mean.

These variations can also be present in tangential direction, including an extra term to account for small shaft speed variations:

$$v_{t,local} = 2\pi(n + \Delta n)r + \Delta v_{t,wake} + \Delta v_{t,sea}$$

If we now define the local advance coefficient by

$$J_{local} = \frac{v_{a,local}}{v_{t,local}} \cdot \frac{2\pi r}{D}$$

then via substitution we find

$$J_{local} = \frac{\overline{v}_a + \Delta v_{a,wake} + \Delta v_{a,sea}}{2\pi(n + \Delta n)r + \Delta v_{t,wake} + \Delta v_{t,sea}} \cdot \frac{2\pi r}{D}$$

This can be written as

$$J_{local} = \frac{\overline{v}_a}{2\pi nr} \cdot \frac{1 + \frac{\Delta v_{a,wake} + \Delta v_{a,sea}}{\overline{v}_a}}{1 + \frac{\Delta n}{n} + \frac{\Delta v_{t,wake} + \Delta v_{t,sea}}{2\pi nr}} \cdot \frac{2\pi r}{D}$$

So that

$$J_{local} = J \cdot \frac{1 + \frac{\Delta v_{a,wake} + \Delta v_{a,sea}}{\overline{v}_a}}{1 + \frac{\Delta n}{n} + \frac{\Delta v_{t,wake} + \Delta v_{t,sea}}{2\pi nr}}$$

The terms $\frac{\Delta n}{n}$ and $\frac{\Delta v_{t,wake} + \Delta v_{t,sea}}{2\pi nr}$ are considered small, and via Taylor series expansion we find that:

$$J_{local} \approx J \cdot \left(1 + \frac{\Delta v_{a,wake} + \Delta v_{a,sea}}{\overline{v}_a}\right) \cdot \left(1 - \frac{\Delta n}{n} - \frac{\Delta v_{t,wake} + \Delta v_{t,sea}}{2\pi n r} + (\ldots)^2 - (\ldots)^3 + \ldots\right)$$

Keeping only zero and first order terms, this can be written as

$$J_{local} \approx J \cdot \left(1 + \frac{\Delta v_{a,wake} + \Delta v_{a,sea}}{\overline{v}_a} - \frac{\Delta v_{t,wake} + \Delta v_{t,sea}}{2\pi n r} - \frac{\Delta n}{n}\right)$$

The latter equation reveals that J_{local} consists of the mean calm water advance ratio J, which might be disturbed by ΔJ as written by:

$$J_{local} = J + \Delta J \approx \underbrace{J}_{calm} + \underbrace{J \cdot \left(\frac{\Delta v_{a,wake} + \Delta v_{a,sea}}{\overline{v}_a} - \frac{\Delta v_{t,wake} + \Delta v_{t,sea}}{2\pi n r} - \frac{\Delta n}{n}\right)}_{\Delta J}$$

which after some manipulation results in

$$J_{local} = J + \Delta J \approx J + \underbrace{\frac{1}{nD} \cdot (\Delta v_{a,wake} + \Delta v_{a,sea}) - \frac{J}{2\pi n r} \cdot (\Delta v_{t,wake} + \Delta v_{t,sea}) - \frac{J}{n} \cdot \Delta n}_{\Delta J}$$

This equations shows how disturbances propagate into the local J. An important property of a tangential disturbance is that its effect on the local advance ratio is dependent on the radial position under consideration. Axial disturbances however have equal effect for all radii. In general the ratio of sensitivities for the two types of disturbances is given by

$$\frac{\Delta J/\Delta v_t}{\Delta J/\Delta v_a} = -\frac{J \cdot D}{2\pi r} = -\frac{J}{\pi \cdot r/R}$$

To investigate the difference in sensitivity into somewhat more detail, a numerical example is elaborated. For the M-frigate $J \approx 1$. This means that the sensitivity-ratio near the hub ($r/R \approx 0.3$) is approximately equal to 1, which means equal sensitivity. Near the tip however, the ratio equals $1/\pi \approx 0.3$, meaning that tangential disturbances only have 1/3 of the effect compared to equal sized axial disturbances. Since inception normally takes place at higher radii, this indicates that inception is more sensitive to axial than to tangential wake disturbances.

The principle difference between axial and tangential disturbances has its effect on the possibility to counteract wave disturbances. Fig 7.4 shows the velocity vector field of a linear undisturbed regular deep water wave, which is traveling to the right, and has no out of plane velocity-component.

The propeller of a ship sailing with head or stern waves, experiences sole axial disturbances in a wave trough or crest, but experiences tangential (and radial) velocity disturbances in between, since the water particle velocity vectors have a vertical component there. The effect of the tangential velocity component is opposite on the upward and the downward moving blade. This is cumbersome for controlling the angle of attack in a seaway, since with conventional CPP systems, it is not possible to vary pitch independently per blade. Therefore it is only considered feasible to compensate axial wave induced wakefield disturbances.

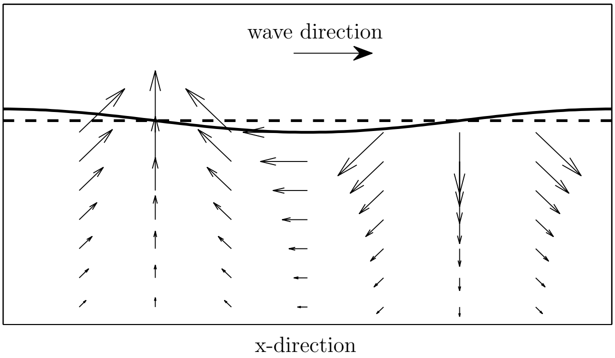

Figure 7.4: Velocity field in an undisturbed linear deep water wave

For a ship sailing with beam waves, the same opposite effect is found for the upper and lower half of the propeller plane. This means that at one side the angle of attack of the propeller blades is increasing, while on the other side it is decreasing. As (undisturbed) beam waves do not cause axial velocities in the propeller plane, these "beam" disturbances cannot be counteracted by pitch adjustments.

These simplified considerations did not take into account the effects of diffracted and radiated waves, nor did they take into account the effect of wave induced ship motions. Nevertheless it demonstrates that mitigation of wave induced inflow disturbances is only partly feasible.

Implicitly, the effect of the calm water wakefield was already included in the above discussion, but is explicitly discussed now. The exact shape of the wakefield is highly dependent on flow and geometry details. The struts as well as the shaft cause an axial velocity deficit in the upper half of the propeller plane, which is called the *wake-peak*. This wake-peak results in a high loading around the 12-o'clock position, around which the first suction side cavitation often appears. Around the 6 o'clock position, the wakefield disturbance is least pronounced. Furthermore, due to shaft inclination and shape of the aft ship, the propeller plane velocity field is directed slightly upward. This upward direction results in opposite tangential velocity for the upward and the downward going blade.

From this crude description of a twin shaft frigate wakefield, it seems that there is no possibility to keep the angle of attack constant during a revolution, without considering individual blade actuation as for instance is applied in helicopter rotors. Individual blade-pitch fluctuations at shaft rate would require a thorough redesign of the propeller-hub-hydraulic system, which is not considered within the scope of this study.

A propeller design method that takes into account the variations in wakefield is described in Kuiper and Jessup (1993). There, the various blade sections are given enough margin against sheet cavitation inception to allow for inflow variations during a revolution due to the calm water wakefield.

Although not part of this research, the effect of (turning circle) manoeuvres on the wakefield has been studied on full scale by Kuiper et al. (2002). Full scale Laser Doppler Velocimetry (LDV) measurements onboard the Australian patrol boat HMAS Townsville revealed that the differences between port side and starboard side inception in a turn were caused by differences in transverse velocities, rather than by differences in axial velocities. This does however not mean that the axial velocities are not important: during a turn the longitudinal ship speed drops, resulting in smaller axial velocity components in the wakefield. Such an axial velocity drop might be compensated for by pitch reduction, while the transverse velocity component has opposite effect in the upper and lower half of the propeller plane, and can therefore not be fully compensated for. Nevertheless, some improvement of inception speed should be possible, through adjustment of the propeller pitch aiming at improvement of the angle of attack of the most critical point (the inception point) in the propeller plane.

Angle of Attack related to Cavitation Inception

Vortex cavitation is usually the first type of cavitation to appear on full scale on naval propellers, and is therefore discussed here in some more detail. Various authors, such as Chandrashekhara (1976), Kuiper (1981) and Holtrop (1997), have derived semi-empirical vortex inception prediction methods, which all include an angle of attack in some form. Kuiper found a rough prediction formula of the (suction side) tip vortex inception index $\sigma_{n,i}$ as follows:

$$\sigma_{n,i} = 0.12\,(P/D - J)_{0.9R}^{1.4}\,R_n^{0.35}$$

with the term $(P/D - J)_{0.9R}$ being a measure of the angle of attack at 0.9R. According to this equation the highest inception speed can be reached if the flow angle matches the pitch angle at r=0.9R. Whether this also holds for strongly unloaded propeller tips is questionable, especially if such a criterion is used for the prediction of pressure side cavitation.

By regression analysis of 95 data points obtained in 32 (mostly model-scale) experiments, Holtrop found that *...local flow parameters as angle of attack were far more significant than the main propeller parameters...* His approximation formulae are different for pressure and suction side vortex cavitation inception, and include as much as 9 numerical coefficients, and around 10 propeller or wakefield related variables.

Note that all empirical data on vortex cavitation inception that was collected on model scale, suffers from scale effects. As discussed in Section 6.5.1, the McCormick scaling rule that is used to make full scale predictions should be considered with caution, and no strong level of confidence is justified. Consequently, any (semi-empirical) prediction method based on extrapolated data should be considered with care.

The concept of a specific angle-of-attack related variable, at which not only an airfoil section, but a whole propeller is least susceptible to inception, is the starting point for the development of the controller. If such an angle does exist, the question arises whether we can find the specific combination of shaft speed and pitch that results in both the desired ship speed *and* the desired angle of attack? Does there exist a single angle of attack that is the least susceptible to inception over a range of pitch angles and shaft speeds? And from a practical point of view: is robust measurement or estimation of the instantaneous angle of attack feasible on full scale? In the following a definition of the effective angle of attack is proposed.

Simplification of the three dimensional hydrodynamic problem of a lifting airfoil has led to lifting line and lifting surface theory. Prandtl's classical lifting line theory showed that the angle of attack varied across the span of a finite wing due to the induced velocities by the trailing vortice system. Lifting line theory relates the sectional lift to the effective angle of attack of a specific spanwise station, from where on the resulting lift can be calculated. For a general geometry this process requires several iterations, since effective angle of attack and sectional lift are mutually dependent. Lifting line theory assumes that all bound vortices are located at the *lifting line*, of which the strength can vary due to trailing vortices.

This concept is refined by lifting surface theory by, instead of lumping all bound vortices to the lifting line, assumption of a system of bound vortices that is distributed over the wing surface. By making use of this theory, resolution is obtained not only in spanwise direction, but also in chord direction, thereby enabling the user to study the effect of foil shape on performance into more detail.

A single angle of attack at which not only an airfoil section, but a whole propeller is least susceptible to inception, can be seen as a further simplification of the lifting line concept. Both chordwise and spanwise resolution is lost, which seems to be an unacceptable simplification of reality. However, the proposed method is not intended for analysis of the propeller performance, but should be seen as an attempt to define an indicator of the instantaneous loading of the complete propeller, with a focus on the leading edge since this is the expected inception location. Note that the term *effective angle of attack* is classically used to indicate the angle of attack that the foil "feels" including the induced velocities, possibly improved by lifting surface corrections. As will be shown, in the present case the term *effective* is used to indicate the angle of attack at the leading edge, since this angle is presumed to be a dominant factor for cavitation inception.

Definition of the Angle of Attack

The effective angle of attack of a propeller should include the propeller geometry, the inflow angle due to wakefield and rotation rate (see Section 7.3.2), and possibly the propeller induced velocities. Since it is assumed that inception takes place close to the leading edge, the local leading edge geometry is also taken into account here by means of the leading edge camber angle.

Based on Fig 7.6, it is found that in general the structure of the angle of attack at a specific radial station $x = r/R$ can be given by:

$$\alpha = \underbrace{\theta_x}_{tan^{-1}\left(\frac{P_x}{\pi x D}\right)} - \underbrace{\theta_{LE,x}}_{\approx tan^{-1}\left(\frac{\partial z_c}{\partial c}\big|_{LE,x}\right)} - \underbrace{\beta_x}_{\approx tan^{-1}\left(\frac{\overline{v}_a + \Delta v_{a,wake} + \Delta v_{a,sea}}{\pi x n D + v_{t,wake} + \Delta v_{t,sea}}\right)} \tag{7.1}$$

where θ_x is the nose-tail pitch angle, $\theta_{LE,x}$ is the shock-free entry angle, of which only the geometric part due to camber is known beforehand, and β_x is the local inflow vector, which is closely related to the local J that was defined earlier.

It seems impossible to monitor and control the angles of attack at all radii during operational conditions, mainly because the wakefield can not be measured in realtime over the complete propeller disc. Furthermore it is of course not possible to control the angle of attack of each section individually.

Therefore only one single angle of attack that is representative for the whole temporally and spatially dependent problem is sought, so that Equation 7.1 is to be narrowed down. Since it is expected that suction side and pressure side inception occur at different locations in the wakefield, it might be considered to introduce two different effective angles of attack for these two types of cavitation inception. As is suggested by Holtrop (1997), the critical inflow angle with respect to suction side inception might be based on w_{max}, while for pressure side inception this flow angle should be based on w_{min} and possibly even on $v_{t,wake,max}$, being the maximum tangential velocity in the same direction as the propeller rotation.

As a starting point it is attempted here to define a single effective angle of attack α_{eff}, with the important property of having the most optimal value from the viewpoint of cavitation inception. This means that the definition of α_{eff} should be such that if the cavitation buckets for various pitch angles would be presented on a basis of α_{eff} (instead of k_t, k_q or J), the middle of these buckets overlap. This will ensure that as long as this angle of attack is kept in the middle of the bucket, the propeller operating point should have maximum margin against inception. A second property of α_{eff} should be that it is measurable or at least estimable. This means that all variables that are necessary to calculate α_{eff} should be available on board. This clearly does not hold for all terms in Equation 7.1 yet, so that simplifications are necessary. A third, but less important, desirable property would imply an overlap of not only the middle of the buckets, but also of the inception lines that form the boundaries of those buckets.

Starting off with Equation 7.1 the first simplification is the neglect of the two tangential velocity terms $\Delta v_{t,sea}$ and $v_{t,wake}$ in the inflow angle β_x since they are hard to estimate, and since they cannot be fully counteracted anyway. The second simplification is made by narrowing down to one specific radius. As a starting point the value of $x = 0.7$ is chosen. Given a certain pitch angle and propeller geometry, the first two terms θ and the correction for camber near the leading edge $\theta_{LE,x}$ are known. The third constituting term $\beta_{0.7R}$ has been simplified to $tan^{-1}\left(\frac{\overline{v}_a+\Delta v_{a,wake}+\Delta v_{a,sea}}{0.7\pi nD}\right)$, where only the nominator, which presents the instantaneous axial velocity in the propeller disc, is not directly known. Before it is explained how this axial velocity component is determined in realtime, based on onboard available measurements, let us for now assume its value is known. As an in-between result the angle of attack at $x = 0.7$ is now estimated by:

$$\alpha_{0.7R} \approx tan^{-1}\left(\frac{P_{0.7R}}{0.7\pi D}\right) - tan^{-1}\left(\left.\frac{\partial z_c}{\partial c}\right|_{LE,0.7R}\right) - tan^{-1}\left(\frac{\overline{v}_a + \Delta v_{a,wake} + \Delta v_{a,sea}}{0.7\pi nD}\right) \quad (7.2)$$

To test if the definition of $\alpha_{0.7R}$ satisfies the required properties, some available full scale cavitation buckets for different pitch angles are used (taken from Kuiper (1996)). These buckets are transformed from a k_q-basis to an α_{eff}-basis, after which they are plotted together as shown in Fig 7.5. The overlap of the middle of the buckets is clearly not as desired, and means that $\alpha_{0.7R}$ is not yet a good indicator for cavitation free operation over a large range of pitch angles. It can be questioned whether the simplified definition of $\alpha_{0.7R}$ should be expected to capture the intricacies that govern (vortex) cavitation inception. On top of that, the quality of the available full scale buckets can be questioned. Nevertheless, as it is expected that there must exist some effective angle of attack definition that (largely) fulfills the required properties, it is attempted to calibrate the definition. Several calibration coefficients have been added and tested, but one that proved to give satisfactory results is noted c_1 and is included in the following definition of α_{eff}:

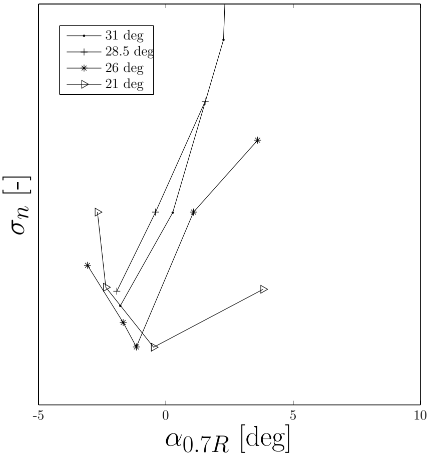

Figure 7.5: Bucket based on $\alpha_{0.7R}$

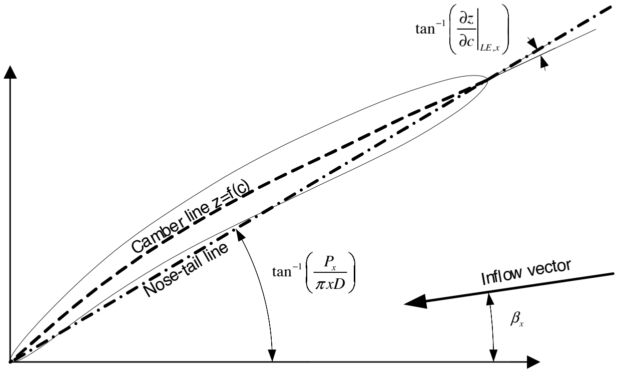
$\tan^{-1}\left(\left.\frac{\partial z}{\partial c}\right|_{LE,x}\right)$
Camber line z=f(c)
Nose-tail line
$\tan^{-1}\left(\frac{P_x}{\pi x D}\right)$
Inflow vector
β_x

Figure 7.6: Propeller section inflow definitions

$$\alpha_{eff} \approx tan^{-1}\left(\frac{P_{0.7R}}{0.7\pi D}\right) - tan^{-1}\left(\left.\frac{\partial z_c}{\partial c}\right|_{LE,0.7R}\right) - tan^{-1}\left(\frac{c_1 \cdot (\overline{v}_a + \Delta v_{a,wake} + \Delta v_{a,sea})}{0.7\pi n D}\right) \tag{7.3}$$

The cavitation buckets based on Eq 7.3 are plotted in Fig 7.7 for four different values of coefficient c_1. The most important desired property (overlapping middle) is largely satisfied by both $c_1 = 0.7$ and $c_1 = 0.8$. For these values the middle of the buckets now seems to be overlapping, so that one single value of α_{eff} guarantees maximum margin against cavitation for all pitch angles. For now a choice for $c_1 = 0.7$ is made, which results in a most desirable effective angle of attack of 4.5 to 5 degrees.

However, the inception lines are not completely overlapping, but this was not a primary desired property anyhow. Deviations are attributed to local flow disturbances, propeller geometry details and inception location, that are not captured by the definition of α_{eff}. Furthermore the quality of the full scale buckets is not known. It is however expected that

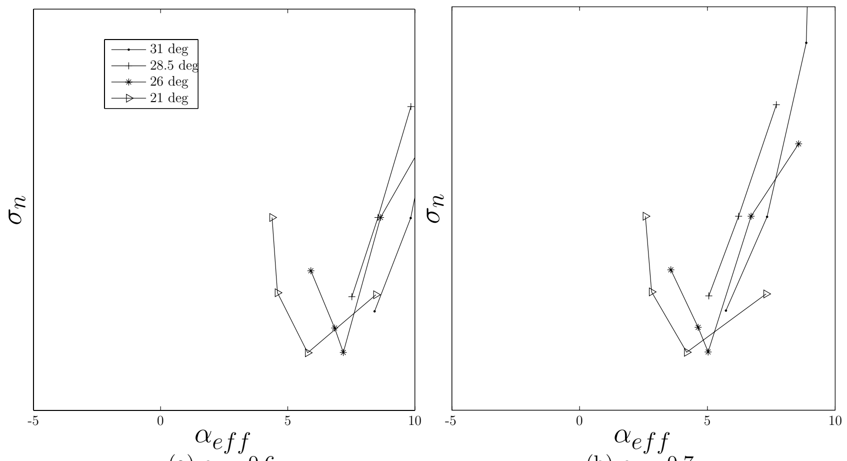

(a) $c_1 = 0.6$ (b) $c_1 = 0.7$

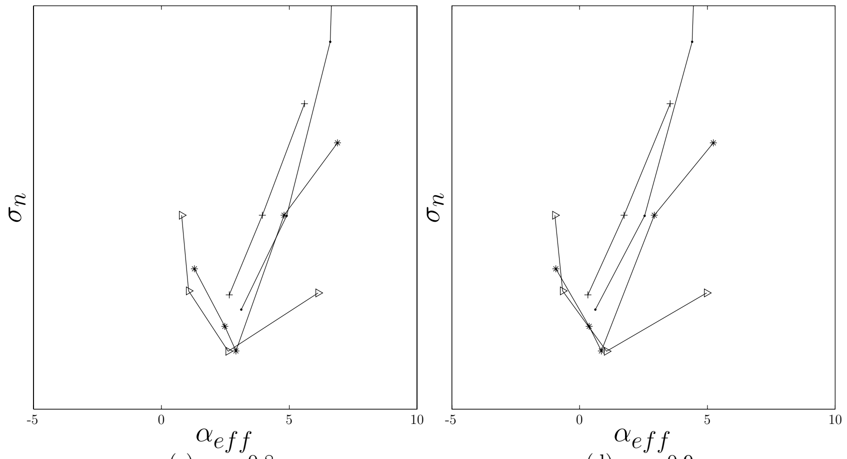

(c) $c_1 = 0.8$ (d) $c_1 = 0.9$

Figure 7.7: Bucket based on α_{eff}, with c_1 ranging from 0.6 to 0.9

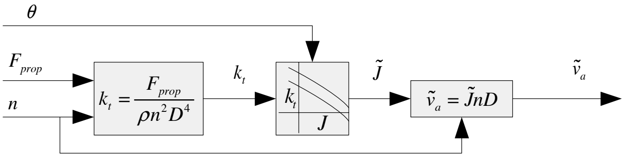
θ
F_{prop}
n
$k_t = \frac{F_{prop}}{\rho n^2 D^4}$
k_t
k_t
J
$\tilde{J}$
$\tilde{v}_a = \tilde{J}nD$
$\tilde{v}_a$

Figure 7.8: Advance velocity estimation process

these buckets are contaminated with relative large uncertainties.

It is concluded that this definition partly satisfies the desired properties. It is acknowledged that a far from perfect overlap has been obtained, which is expected to be caused both by the quality of the full scale observations as by the definition itself. To improve this definition, high confidence predictions of inception lines for various off-design pitch angles would be of great value. As shown in Chapter 6, such predictions are however not easily made. For now an important weak point of this method remains that calibration data (buckets) have to be available before the PCS+ can be put in use.

Estimation of Instantaneous Axial Flow Velocity

Onboard calculation of the flow angle term in Equation 7.3 necessitates knowledge of the instantaneous axial velocity in the propeller plane including a seaway disturbance $\Delta v_{a,sea}$. This speed is however not readily available onboard. Normal speed measuring devices such as a GPS, or a (bottom tracking) Doppler-log deliver the Speed over Ground (SOG), which does not capture the wave induced disturbances of the propeller inflow. Application of a water tracking Doppler log has the same disadvantage of not capturing the disturbances in the propeller plane. One or more Electro Magnetic (EM)-logs, if positioned well, might be able to partially capture the propeller inflow. However, the installed EM log on the M-frigate is positioned around midships, and thus cannot be used for this purpose. Laser Doppler Velocimetry (LDV)-techniques as were used in Kuiper et al. (2002) require sensitive specialized equipment and are not capable of delivering robust realtime data. Development of other robust sensors, possibly combined with sensor fusion techniques might help to improve direct v_a measurement in the future. A possible option might be to fit the hull near the propellers with multiple EM logs in order to measure the inflow velocity field more directly. This might even include measurement of transverse velocities, of which the effect on cavitation might be dominant during beam waves and turning circle manoeuvres.

In this project an axial-flow-velocity estimation method based on reverse use of the open water diagram is employed. Propeller performance is normally presented in the open water diagram, which relates the output (thrust and torque coefficient k_t and k_q) to the input (advance speed v_a, shaft speed n, and pitch angle θ) so that $k_t = f(v_a, n, \theta)$. As long as the open water lines of k_t are descending monotonously, the advance velocity v_a is unambiguously defined for given n and θ so that an inverse operation is possible: $v_a = f^{-1}(n, k_t, \theta)$. Via the same reasoning, v_a can also be reconstructed from k_q: $v_a = g^{-1}(n, k_q, \theta)$. In blockdiagram form the v_a-estimation process is shown in Fig 7.8. An equivalent blockdiagram can be drawn up for estimation via torque coefficient k_q. Likewise reverse use of the open water diagram is reported in Pivano et al. (2007).

Onboard realtime application of the estimation process strongly leans on the assumption that the openwater diagram is valid, even in off design conditions. If the shape of the

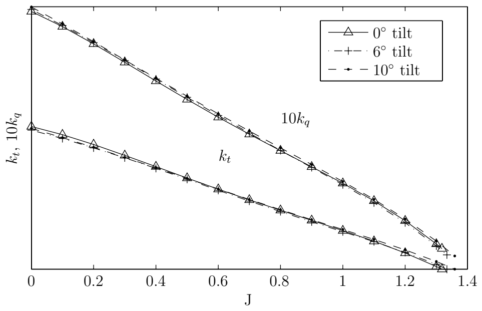

Figure 7.9: Open water propeller performance under tilt angle. Source: Koops (2008)

wakefield changes such that the propeller performance is not accurately described by the open-water diagram anymore, then the estimation of v_a will deviate from the true v_a. To check the effect of drift angle on the open water diagram, a model scale openwater test at tilt angle was carried out, with results shown in Fig 7.9. This indicates that in open water conditions the propeller performance at nominal pitch is not very sensitive to inflow angle. The effect of driftangle on in-behind conditions might be expected to be somewhat more pronounced due to possible asymmetrical tangential velocity disturbances, as is confirmed by Kuiper et al. (2002). However, the current research is limited to straight line manoeuvring, and the effect of non-symmetrical disturbances on the estimated advance velocity is not investigated in detail.

The estimation process is tested by analysis of full scale measured time traces of θ, n, T_{prop} and M_{prop}. The derived estimated advance velocity $\tilde{v}_a$ is compared to the v_s that was measured by means of the EM-log. These two signals should not be expected to be exactly the same, but should show the same trends. The relevant input signals are shown in Fig 7.10, and are taken from calm water measurements. The output signals from the estimation process are compared to the EM-log speed in Fig 7.11. At higher ship speeds both estimations behave well, although they differ up to 0.5 kts at some points. Such differences might be caused by deviations in the actual open water curves, or by a calibration error in the thrust or the torque sensor. At lower speeds the estimation via k_q shows irregular behaviour. This is attributed to the combination of quality of the torque measurement (signal resolution) and the high sensitivity of the estimation process for variations in k_q at low pitch angles, indicated by very low values of $\frac{\partial k_q}{\partial J}$. Combination of the two makes that the estimated v_a behaves highly irregular near low values of J at low pitch angle. The estimation via k_t is therefore preferred over estimation via k_q. This preference is strengthened by the fact that the measured thrust is not affected by shaft losses, while due to the location of measurement the measured torque is. Also due to location of measurement, the torque sensor does not only pick up the undisturbed propeller torque, but in fact measures something between shaft torque and propeller torque. During a shaft acceleration the two clearly are not equal, and the true propeller torque can only be measured at the location where the propeller is attached to the shaft. Another option would be to calculate the true propeller torque from the measured torque via inclusion of the inertia in front of or aft of the torque sensor.

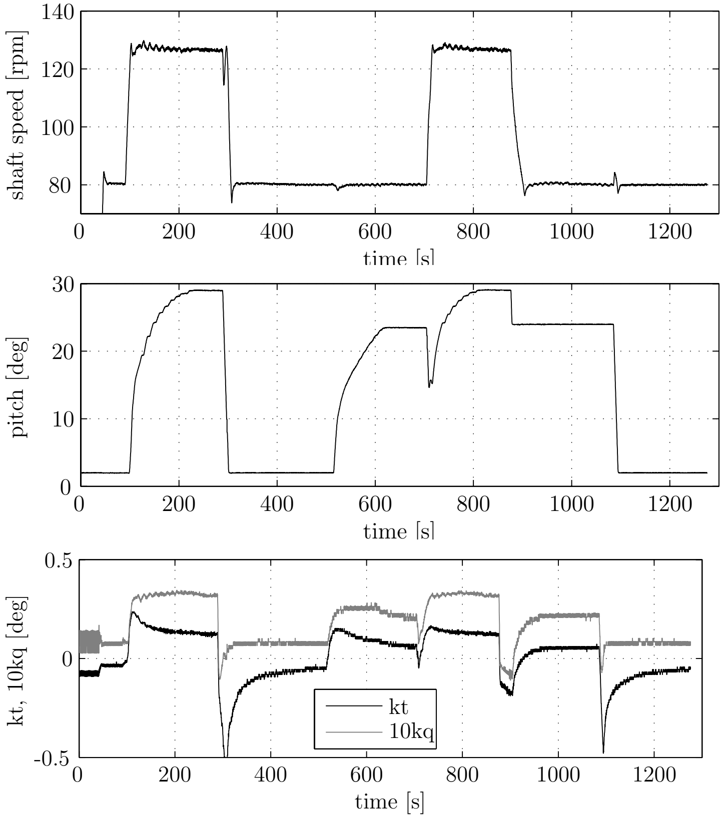

Figure 7.10: Input signals to axial velocity estimation process

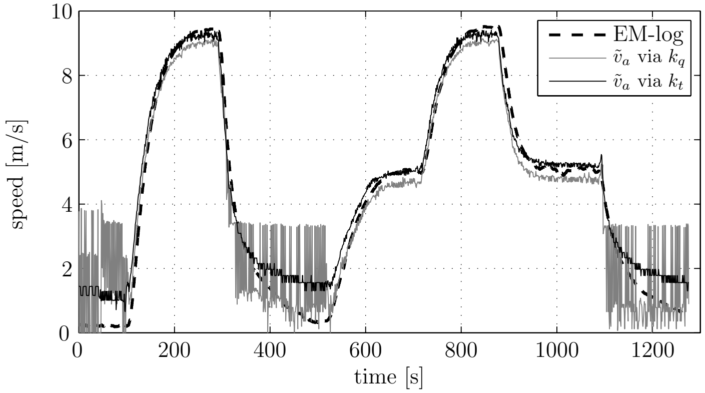

Figure 7.11: Output signals of the axial velocity estimation process

7.4 Relation between α_{eff} and the Engine Diagram

Fig 7.12 shows the calculated static contours of α_{eff} together with the contours of virtual shaft speed in seastate 0 and seastate 4. The intersection between a desired virtual shaft speed contour and the desired angle-of-attack contour line delivers the (static) operating point in terms of pitch and shaft speed that is most desirable. For high resistance conditions this point lies more towards the southeast of the diagram (towards lower pitch and higher shaft speed).

The shaft speed (or better: diesel engine speed) is however limited to both sides. First of all there is the maximum engine speed. If the desired operating point is found at a higher engine speed than is allowed (for instance if $n_{set,virt} = 135$ rpm and $\alpha_{eff,set} = 5$ degrees in seastate 4), it is chosen here to limit the engine speed, while maintaining the pitch angle that leads to the desired angle of attack. As a result the command ($n_{set,virt}$) will not be fully effectuated, resulting in a loss of ship speed. This effect is governed by the involved physics, and it can be argued that if one wants to sail with no or little cavitation in such conditions, one should not sail with such high "commands". Another option that has not been chosen here would be to increase the angle of attack setpoint, after the engine speed has reached the limit. In this way the command can still be effectuated, but this will come at the cost of increased suction side cavitation.

On the left hand side of Fig 7.12, it can also happen that a command is given that finds its operating point on the left hand side of the minimum engine speed (in this case around 400 rpm engine (shaft speed 55 rpm). To prevent the engine to operate below this lower limit, it was decided to fall back to the old controller regime based on the fixed combinator as soon as the operating point exceeded the lower shaft speed limit. In a more advanced PCS+, the available cavitation free space in the bucket (at low shaft speeds) can be further exploited by for instance temporarily lowering $\alpha_{eff,set}$, which will result in combinations of pitch and shaft speed that lie more towards the southeast. In this way the crossing of the lower engine speed limit can be postponed, at the cost of lesser margin against pressure side cavitation.

The engine diagrams in Fig 7.13 show that in both seastate 0 and seastate 4 the shapes of the α_{eff}- contours follow the governor limit. This indicates that independently of the seastate, a specific value of $\alpha_{eff,set}$ will results in a satisfactory locus of operating points in the engine diagram. In this case a value of approximately 6 degrees or lower seems to result in a static operating point with sufficient margin against overloading. Based on Fig 7.7, the effective angle of attack that has been found most desirable from the viewpoint of cavitation inception is $\approx 4.5 - 5$ degrees. Taking into account the more restricting Reduced Time Between Overhaul (RTBO)-lines that are not shown in the engine diagram here to avoid clutter, the choice for $\alpha_{eff,set} \approx 5$ degrees seems to satisfy not only the cavitation-criterion, but also seems to result in favorable behaviour in the engine diagram without explicit (limiting) measures to prevent engine overloading.

7.5 Controller Implementation

In the previous sections the basic principles behind the new PCS have been dealt with. In the following, the actual implementation of the PCS+ is discussed at blockdiagram level.

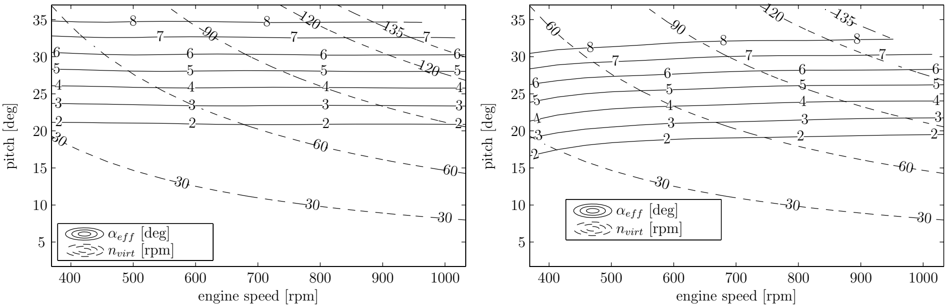

Figure 7.12: Contours of α_{eff} and n_{virt} in the n-θ plane. Seastate 0 and 4

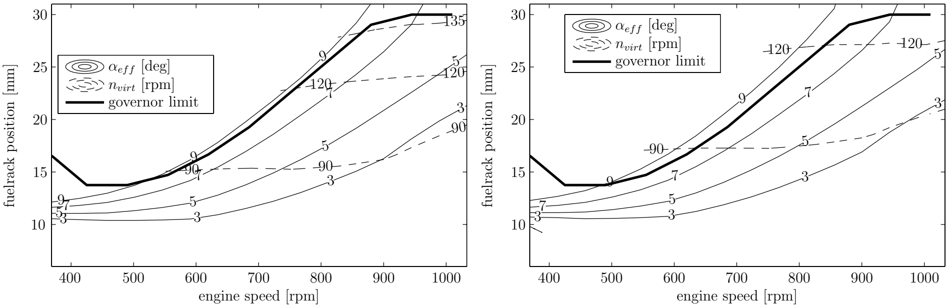

Figure 7.13: Contours of α_{eff} and n_{virt} in the engine diagram. Seastate 0 and 4

The two main controller loops regarding ship speed and α_{eff} are dealt with separately.

7.5.1 Ship Speed Feedback Controller

The ship speed controller that in fact is a virtual shaft speed controller, ensures that independent of the fast corrections that are continuously made to the propeller pitch, the mean requested virtual shaft speed is effectuated. Short temporary deviations from $n_{set,virt}$ may occur as long as they don't last for a longer period since this will result in change of ship speed. Although in principle one might try to control the virtual shaft speed at higher frequencies, this is not of much use: due to the ship mass, high frequency variations in shaft speed (and associated thrust) have no effect on ship speed. Secondly, due to the inertia of the rotating shaft system, constant corrections to the governor setpoint can easily lead to overloading of the engine.

To ensure that only the low frequency disturbances are corrected, and that the steady state error in n_{virt} is zero, a controller of the integral type (I) is chosen, as shown in Fig 7.14. Proportional and derivative action are not included since both will result in a non-smooth and possibly "nervous" governor behaviour. A limiter is applied to prevent too high commanded shaft acceleration. The response of the controller can be influenced with the integral coefficient K_i. Although not explicitly shown, the integrator is enhanced with measures to prevent unnecessary large shaft speed corrections, that result in a total governor setpoint that crosses the maximum or minimum engine speed. Windup of the

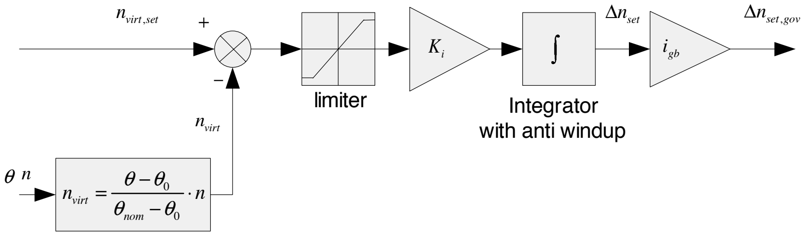

Figure 7.14: Blockdiagram of the virtual shaft speed controller

integrator-state in such a case is also prevented.

7.5.2 Angle of Attack Feedback Controller

With the estimated and the desired effective angle of attack as input as shown in Fig 7.3b, the α_{eff} controller has the function to provide the pitch setpoint to the low level Propeller Pitch Controller (PPC). This PPC subsequently actuates the hydraulic pilot valve that actuates the main hydraulic valve, which ultimately results in a movement of propeller pitch. The (non-linear) dynamic behaviour of the PPC and the connected hydraulic system are therefore of great importance for the dynamic behaviour of the angle-of-attack controller loop.

Because the importance of the PPC and its connected hydraulic system was recognized early in the project, an improved hydraulic system with an improved PPC were designed and implemented onboard, aiming at improved dynamic behaviour, and less dead time after a setpoint change. However, due to practical issues that are not dealt with here, these improved systems were never tested during the final trials. The actual trials were inevitably carried out with the original PPC and the original hydraulic system, which had a negative influence on the dynamic behaviour of the α_{eff}-feedback loop due to relatively large dead times in the hydraulic system, and small proportional gain in the PPC. The time between a change in $\theta_{set,PPC}$, and actual pitch-movement with the current system was found to be approximately $0.6s$, but is expected to be dependent on the exact operating point.

The general structure of the α_{eff} controller is shown in Fig 7.15. The low level PPC requires a setpoint $\theta_{set,PPC}$, so therefore the actual pitch θ is added to the pitch correction $\Delta\theta$. No integral controller action is implemented because the PPC will already ensure (almost) zero steady state error. Although it is attractive to employ derivative action because this might speed up the response, the associated decrease in robustness is not considered desirable. Derivative action combined with the presence of noise in the measurements makes the system less robust for high frequency perturbations. Since the effect of nervous control action by the PPC on the hydraulic system is not well understood, a conservative controller setting of $K_p = 1$ is chosen as a starting point.

7.5.3 Overall Blockdiagram

The overall blockdiagram of the PCS+ consists out of Figs 7.8, 7.14, 7.15 and Eq 7.3, and is shown in Fig 7.16 for reference.

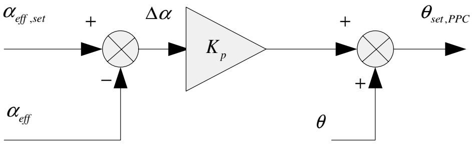
$\alpha_{eff,set}$
+
$\Delta\alpha$
K_p
+
$\theta_{set,PPC}$
−
α_{eff}
+
θ

Figure 7.15: Structure of the α-controller

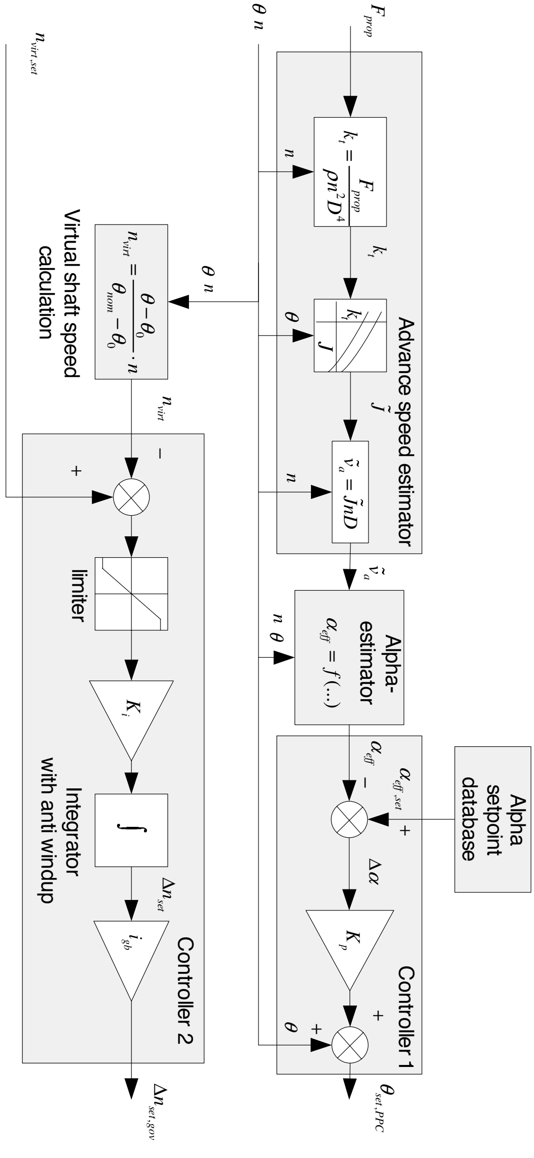
F_{prop}
θ n
$n_{virt,set}$
Advance speed estimator
$k_t = \frac{F_{prop}}{\rho n^2 D^4}$
n
k_t
θ
k_t
J
$\tilde{J}$
n
$\tilde{v}_a = \tilde{J} n D$
$\tilde{v}_a$
Alpha-estimator
$\alpha_{eff} = f(...)$
n θ
Virtual shaft speed calculation
$n_{virt} = \frac{\theta - \theta_0}{\theta_{nom} - \theta_0} \cdot n$
θ n
n_{virt}
−
+
limiter
K_i
Integrator with anti windup
Δn_{set}
i_{gb}
Controller 2
$\Delta n_{set,gov}$
Alpha setpoint database
α_{eff}
−
$\alpha_{eff,set}$
+
$\Delta\alpha$
K_p
+
θ
+
Controller 1
$\theta_{set,PPC}$

Figure 7.16: Overall blockdiagram of the PCS+

parameter set	n_{max} [rpm]	$\dot{n}_{set,gov,max}$ [rpm/s]
A	135	10
B	110	10
C	135	20

Table 7.1: Parameter settings of the reported parameter variation study

7.6 PCS+ Parametric study

The newly developed control system was not immediately tested on full scale, but was thoroughly tested in the simulation model that was validated in Chapter 5. Although most of the tests are not scientifically relevant, they proved to be indispensable for a successful outcome of the project. First of all the tests were necessary to ensure stable and safe behaviour of the PCS+. Secondly the parameters of the PCS+ could be tuned beforehand, which significantly increased the effective full scale testing time due to the minimal necessary full scale tuning time. Finally the test setup allowed for a Factory Acceptance Test (FAT) by RNLN staff, which was a required step before the PCS+ could be installed onboard.

To give an idea of the output of the simulation results with the PCS+, results of a limited controller-parameter-variation study are presented here. The two parameters that are varied are the maximum allowed shaft speed n_{max}, and the maximum shaft acceleration rate $\dot{n}_{set,gov,max}$. These two parameters are part of the PCS and determine the maximum value and the maximum acceleration rate of one of the two main outputs of the propulsion control system: the governor setpoint $n_{set,gov}$. Their exact settings for three parameter sets are listed in Table 7.1.

To enable a comparison with full scale measurements as will later be reported in Chapter 9, an acceleration from 10-14 kts is performed here. Note that this simulation gives results for a ship with both shafts driven by the PCS+.

As shown in Fig 7.17 the simulated command is given at $t = 542s$. Shaft speed immediately reacts as shown in Fig 7.18. Due to the integral term in the shaft speed controller an overshoot occurs for settings A and C, which helps to accelerate the ship faster. Pitch slightly reduces (Fig 7.19) in order to keep the effective angle of attack at the desired value of 5°. For settings A and C pitch shows a second hump, which can be explained by the ship speed time trace.

The ship accelerates as shown in Fig 7.20, and in case of settings A and C also shows an overshoot of approximately 1 kts. The predicted behaviour of the engine is shown in Figs 7.23 and 7.24. As shown, the operating point first moves towards the northeast, and starts to come back again to maintain the desired angle of attack while the ship is accelerating. Setting B has no overshoot because no high shaft speeds are allowed. The difference between A and B lies in the initial shaft acceleration rate, and in the size of the overshoot. Although not shown in this parametric study, the size of the overshoot can also be tuned with the parameters in the virtual shaft speed feedback loop.

The signals α_{eff} and σ_n are shown in Figs 7.25 and 7.26, with the resulting transient in the cavitation bucket shown in Fig 7.27. The effective angle of attack is kept nicely at its desired value of 5°, except for a small deviation at the moment of the command. This is caused by a slight delay before pitch starts to reduce. This delay is also present in reality, and should ideally be removed by making alterations to the hydraulic CPP system, possibly combined with a more advanced propeller pitch controller. The behaviour in the cavitation bucket looks promising, as the operating point is kept nicely in the middle. For settings A and C the temporarily high increase of shaft speed is demonstrated as the small lower loop that occurs before σ_n increases again. Setting B does not show such an overshoot.

Based on these and other parametric studies, parameter setting C was used as an initial starting point for the full scale trials. Due to too high engine loading during acceleration (observed during first full scale run), and due to small shaft speed excursions above the (maximum allowable) value of 135rpm in seaway, these settings were almost immediately changed to $n_{max} = 130$ rpm and $\dot{n}_{set,gov,max} = 10$ rpm/s.

This example clearly illustrates that, if for some reason the initial full scale behaviour turns out to be undesirable, parametric studies such as this one can help to quickly iterate towards a setting that is likely to improve the system behaviour.

The expected accuracy of these predictions is related to the uncertainty intervals that were calculated in Chapter 5. However, although the plant itself has not changed, the extra additions and connections due to the PCS+ do affect the uncertainty propagation throughout the total model. More precisely expressed, additional uncertainty is propagated into the system via $n_{set,gov}$ and $\theta_{set,ppc}$, which are now both controlled dynamically, while in case of the old PCS, they were in principle set at a specific known value. To quantify the uncertainty in the resulting model output, a new uncertainty analysis has to be carried out. From a scientific point of view this is worthwhile since it will give extra insight and understanding. However, in this practical case it is chosen not to carry out a new uncertainty analysis, since the possible gains are expected to be outweighed by the large effort.

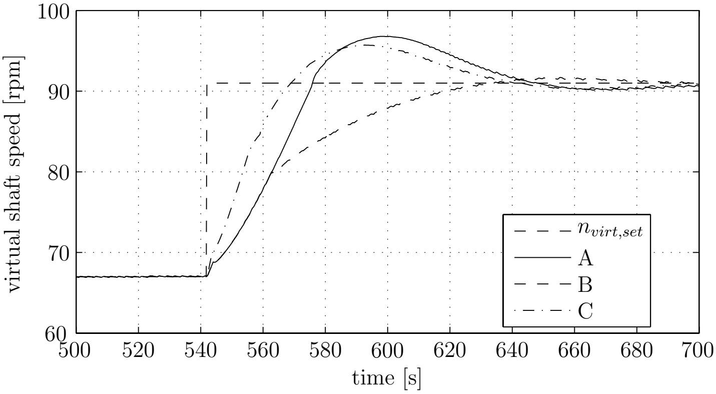

Figure 7.17: Simulated virtual shaft speed

7.7 Possible Controller Extensions

7.7.1 Turning Circles

The developed propulsion controller does not take into account the effects of wakefield changes due to driftangle and yaw rate. In such conditions the transverse velocity field is

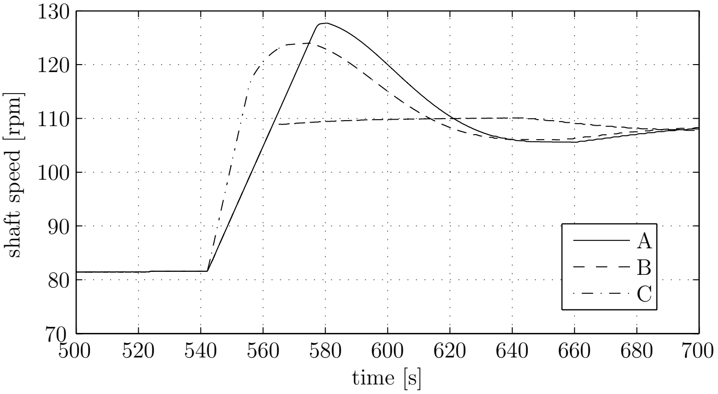

Figure 7.18: Simulated shaft speed

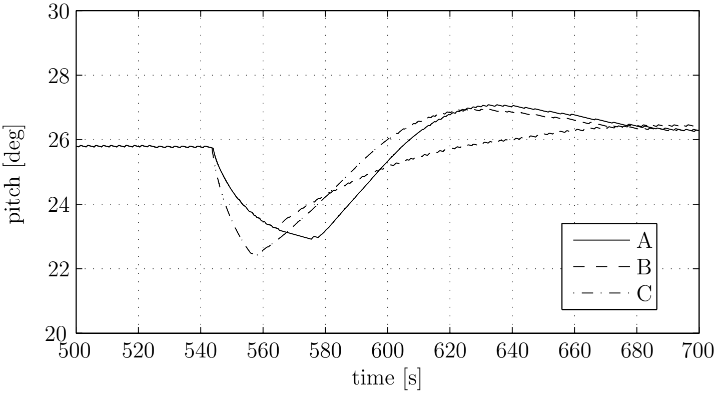

Figure 7.19: Simulated pitch

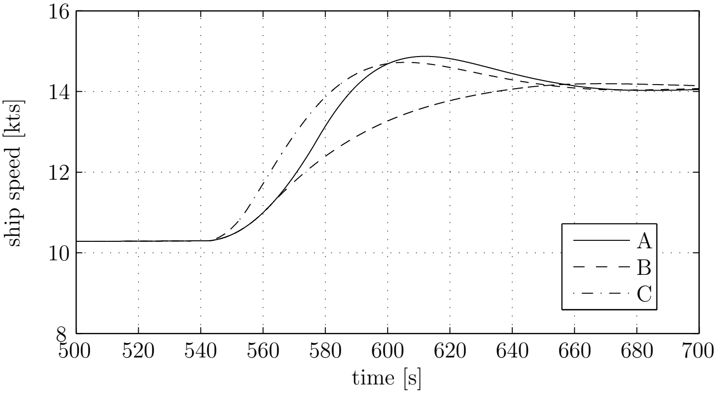

Figure 7.20: Simulated ship speed

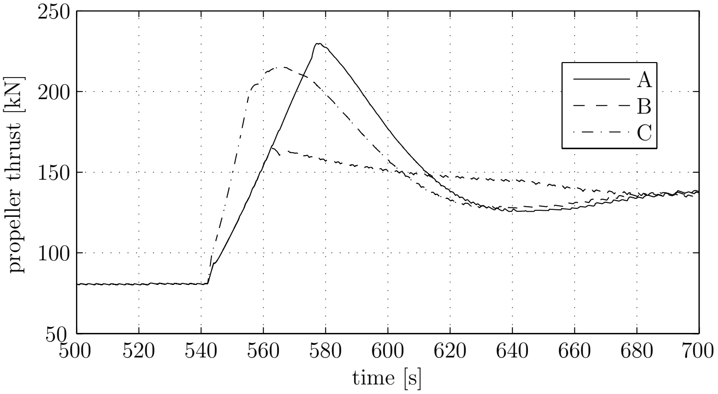

Figure 7.21: Simulated propeller thrust

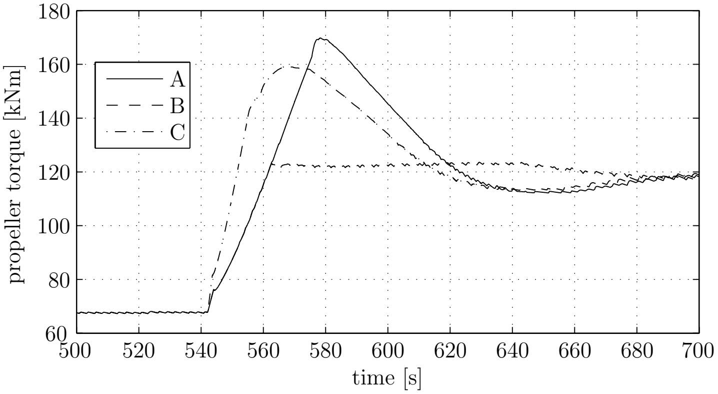

Figure 7.22: Simulated propeller torque

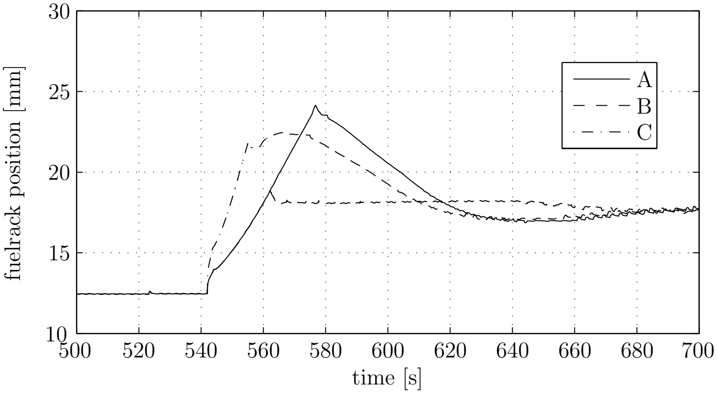

Figure 7.23: Simulated fuelrack

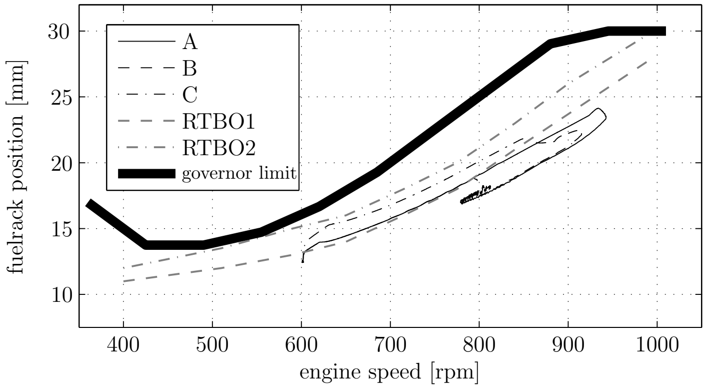

Figure 7.24: Prediction of behaviour in the engine diagram

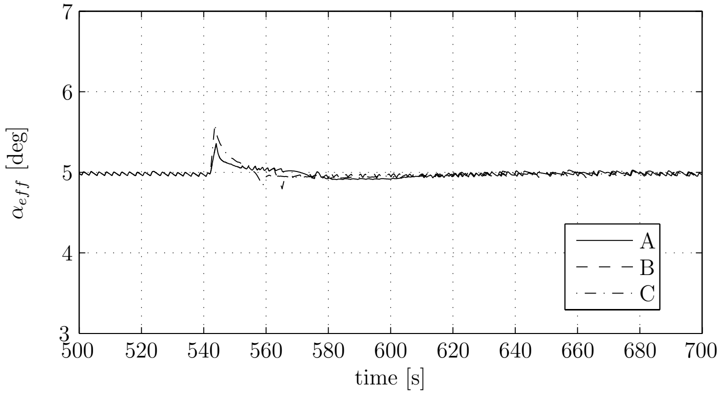

Figure 7.25: Simulated effective angle of attack

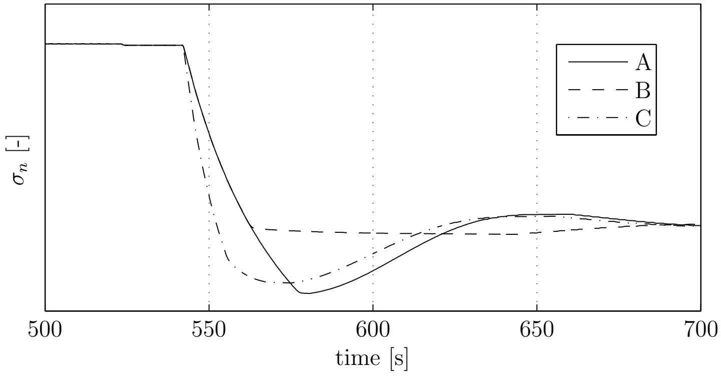

Figure 7.26: Simulated cavitation number

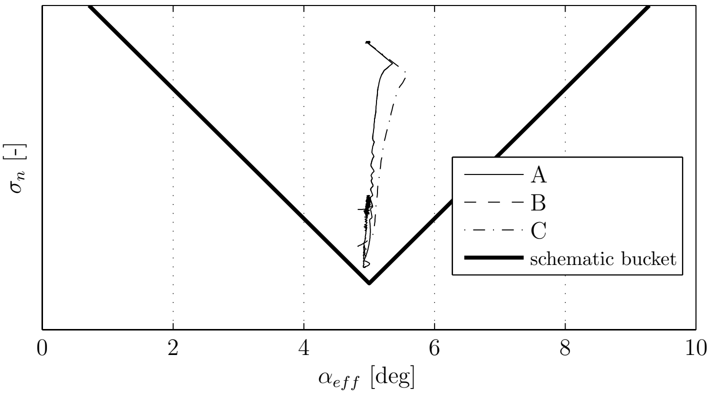

Figure 7.27: Prediction of behaviour in the (schematic) cavitation bucket

disturbed in such a way that the cavitation free operating area can change significantly. Although these wakefield changes can easily result in cavitation, this is not necessarily reflected by a big increase or decrease in propeller thrust and thus in estimated α_{eff}. This means that in a turning circle, the cavitation free operating area (the bucket) is shifted both horizontally and vertically and probably changes shape. If a shift occurs, this means that the original setpoint $\alpha_{eff,set}$ does not guarantee maximum margin against cavitation anymore.

Although the wakefield change is not compensated for in the current version of the PCS+, the effect of decreased ship speed due to additional resistance in a turning circle is (automatically) compensated for by the current version. This can be compared to the effect of increasing resistance when sailing a straight course: the operating point will shift towards higher shaft speed and lower pitch angle. Although additional measures are necessary to prevent cavitation in a turning circle, the current approach does at least prevent overloading of the diesel engine in a turn.

In order to increase the cavitation free time in turning circles, it is proposed to make $\alpha_{eff,set}$ a function of for instance actual drift angle, yaw rate and/or rudder angle. Such a database could then be implemented in the "alpha-setpoint database"-block shown in Fig 7.3b. This "scheduling"-approach is possible, provided that the cavitation free operating area in a big variety of conditions is known beforehand.

Since this knowledge is not easily obtained by means of full scale trials or by predictions methods, it might be considered to log propeller noise sensor data over a long time period to identify the cavitation free operating area in a large variety of operating conditions. By analysis of this dataset, it might be possible to determine the desirable $\alpha_{eff,set}$, dependent on the conditions. A limited attempt to obtain the cavitation free operating area by means of the noise sensors will be demonstrated in Section 9.4.1.

7.7.2 Pressure Variations

As was shown in this chapter, the estimated effective angle of attack is defined in such a way that it says something about the actual operating conditions of the propeller. However, not only the effective angle of attack, but also the pressure field around the propeller determines the operating point in the cavitation bucket. The cavitation number is defined here as the nondimensional pressure at mean shaft immersion:

$$\sigma_n = \frac{p - p_v}{\frac{1}{2}\rho n^2 D^2}$$

with p indicating the ambient pressure at the shaft centerline.

The ambient pressure is approximated by assuming $p = p_0 + \rho g \overline{z}$, with $\overline{z}$ the mean (calm water) immersion. As shown in Van Terwisga et al. (2004), in reality the pressure at the shaft centerline is continuously affected by ship movements and wave induced pressure variations. Since these variations are not included in the current approach, the vertical position of the operating point in the bucket should be seen as a crude estimate. To include the effect of such variations it might be considered to continuously measure or estimate the actual pressure at the shaft centerline. Inclusion of pressure variations is expected to become more important as soon as it is chosen to set $\alpha_{eff,set}$ at a value that differs from the middle of the cavitation bucket, since vertical variations can then easily lead to inception.

7.8 Conclusions

When controlling a ship propulsion system with a CPP, one in principle has the freedom to choose from many shaft speed-pitch combinations that all result in approximately the same ship speed. By choosing one of these possible combinations, a secondary goal (besides ship speed) can be pursued. In this project it is attempted to design a controller aiming at increased cavitation free time in operational conditions. In search of an effective cavitation control variable, it is observed that cavitation inception on airfoil sections is strongly related to the angle of attack. However, in case of a propeller this angle of attack is not unambiguously defined, since each section has its own pitch and inflow angle. Nevertheless, an effective angle of attack with desirable properties is proposed, which is representative for all sectional profiles out of which the propeller is built up.

To estimate this effective angle of attack onboard, it is necessary to continuously measure/ estimate the axial velocity in the propeller disc. For this purpose an axial velocity estimation algorithm, based on measurement of thrust, was developed and tested.

A simple controller, aiming at keeping the angle of attack at the desired value was developed, and thoroughly tested in a simulation environment. The predictions that were shown for various parameter settings give a good idea of initial parameter settings and show how, if necessary, the dynamic behaviour of the plant can quickly be adjusted during the full scale trials.

Chapter 8

Experimental Setup

8.1 Introduction

This chapter discusses the setup that was used during the final trials in the Caribbean Sea in the period from the 26th of February 2008 to the 6th of March 2008, on board the M-frigate HNLMS van Galen. First of all a general overview of the trial setup is given, after which a somewhat more detailed discussion is split up in separate sections on the control computer system and the sensor system.

8.2 General Layout

An overview of the temporarily installed test-setup is given in Fig 8.1. The figure shows a clear separation between the primary system that was necessary to control the plant, and two secondary systems, that were used to gather data for later analysis, and to monitor the condition of the plant during the trials. The secondary system for instance included a high speed video camera and acceleration sensors. It furthermore included the existing ship data-logging system. A synchronization signal between the primary and the secondary system ensured that measurement data was synchronized in time. The figure also shows that the links between the control system and the plant are the diesel engine governor, and the pilot valve of the hydraulic CPP system. The control computer system consist out of a computer with I/O- boards that is connected to the plant via a multitude of electrical conditioning devices and galvanic separators. The CPU that runs the real time controller program is connected to a laptop which is the operator station and has multiple functions:

- Uploading of the controller structure and parameter settings to the CPU.
- Monitoring of plant and controller behaviour during the tests via on screen data.
- Logging of plant measurements and internal variables of the controller.

The power supply to the various part of the installation is taken care of by multiple Uninterruptible Power Supply (UPS) units, which receive their power from the onboard electricity net. Some systems were directly powered by the onboard electricity net.

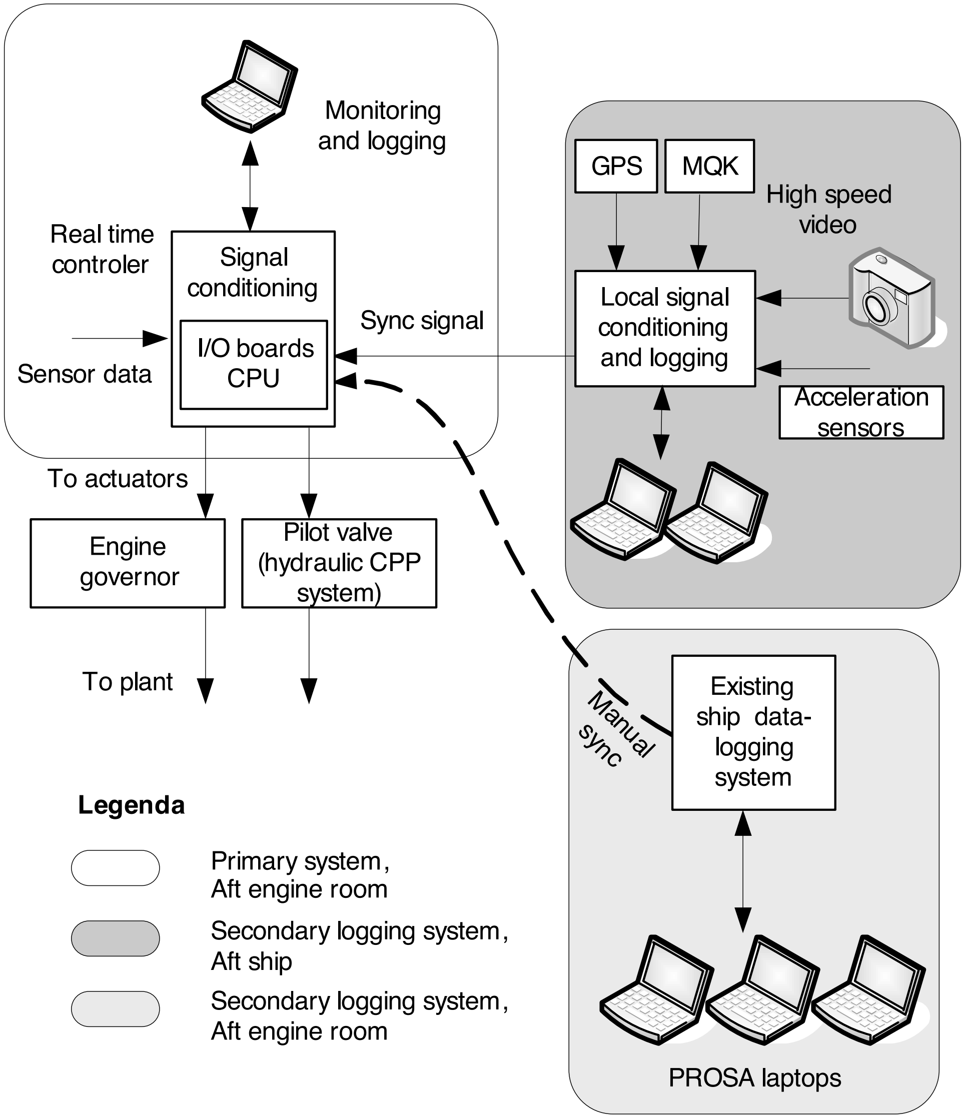
Monitoring
and logging
Real time
controler
Signal
conditioning
I/O boards
CPU
Sensor data
Sync signal
To actuators
Engine
governor
Pilot valve
(hydraulic CPP
system)
To plant
GPS
MQK
High speed
video
Local signal
conditioning
and logging
Acceleration
sensors
Manual
sync
Existing
ship data-
logging
system
PROSA laptops
Legenda
Primary system,
Aft engine room
Secondary logging system,
Aft ship
Secondary logging system,
Aft engine room

Figure 8.1: Schematic overview of trial setup

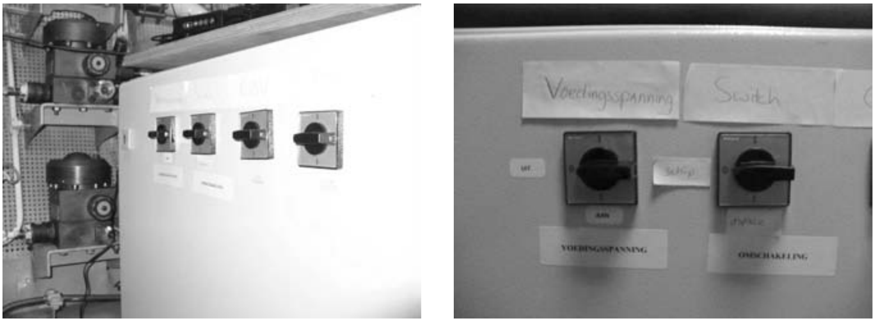

Figure 8.2: Cabinet with switches to electrically disconnect the temporary control system from the plant

As shown in Fig 8.2, a switch was installed that could directly (electrically) disconnect the experimental setup from the plant, and at the same time switch over the control to the normal propulsion control system. This switch and its associated relays and wiring were installed to ensure that the ship could still proceed with its normal operation in case the experimental setup failed, or if more reliable robust propulsion control was deemed necessary.

Note that the temporary control system contained two PCS-versions: first of all the PCS+, that was described in the previous chapter, and secondly a copy of the existing ship propulsion controller. The latter was programmed to ensure that all data-logging capabilities of the temporary setup could also be used for this PCS mode, which would have not been the case if the existing ship control system would have been used. In this way it was ensured that a fair comparison of the two systems could be made, since they both relied on exactly the same sensor and actuator system. In an earlier phase it has been confirmed that the existing ship propulsion system and the copy that was re-programmed were equivalent and resulted in the same system behaviour.

8.3 The Control Computer System

The heart of the temporary installed control computer system is a PowerPC 750GX processor running at 1 GHz. The processor board provides the computing power for the real-time controller program and also functions as an interface to the various connected I/O boards and the laptop.

Three types of I/O boards are used: one for analog input signals, one for analog output signals, and one for combined digital I/O. Table 8.1 lists the exact boards with their main characteristics.

The laptop is connected to the processor board. The user can select a pre-developed controller on this laptop, from where on it can be compiled, downloaded to the processor, and run in real time. Via the same connection the controller-processes and the various I/O signals can be monitored and logged on the laptop. Parameter changes can be made to the real time program (during execution). However, if necessary the real time program can also run without the connected laptop, which is highly beneficial from the viewpoint of reliability.

function	type	main characteristics
processor board	DS1005	IBM PowerPC 750GX, 1 GHz, suited for fast communication with I/O boards
AD converter board	DS2003	32 channels, up to 16 bit resolution
DA converter board	DS2103	32 channels, 14 bit resolution
digital IO board	DS4003	96 TTL lines (three 32-bit ports)
mounting cabinet	PX10	cabinet with mounting space for up to 10 boards

Table 8.1: Main data of processor and I/O board. Extensive performance data is documented by the manufacturer and can be found on: `www.dspace.com`

8.4 The Sensor System

The primary sensor system is interpreted here as the complete system from sensors to the I/O board. Following this interpretation possible electrical signal conversions and hardware filtering thus are part of the sensor system and are treated briefly in this section.

Not all sensors measurements are fed to the I/O boards, simply because they are not necessary for the controller to operate, and are solely logged for the sake of further (afterward) analysis. Such measurement and logging facilities are therefore indicated as the secondary sensor system. Some of the secondary data was logged on different locations, because of practical reasons. The location and connection between the various sensor systems is schematically shown in Fig 8.3.

The existing ship data-logging system named PROSA (Program for Online Signal Acquisition) can for instance be seen as an independent secondary sensor system. Time synchronization between the PROSA system and the primary system was carried out afterwards by using the shaft speed signal, that was measured on both systems, as a manual synchronization signal.

Another more or less individual secondary logging system was positioned in the aft-ship. For reasons of watertightness of the ship no temporary cabling was allowed from the aft part of the ship to the aft engine room were the controller and associated primary data logging system was positioned. Time- synchronization between the primary and this particular secondary logging system was however made possible via an existing spare cable that, via a detour, connected the aft ship to the aft engine room.

Electric conversions were necessary to connect the plant to the I/O boards. For this purpose an industrial cabinet was fitted with necessary conversion units, including galvanic separation to prevent undesired, possibly harmful, electrical currents. Hardware filtering was applied to incoming sensor signals by means of capacitors that were placed just before the I/O boards. Capacitor values were chosen such that the cut-off frequencies lay far beyond the highest frequency of interest. The electrical scheme of the signal conditioning is reported in IMTECH (2007). As shown in Fig 8.1 and Fig 8.4, the industrial cabinet also housed the smaller processor cabinet, that held the components that are listed in Table 8.1.

Further description of the sensor systems is divided by means of their physical location.

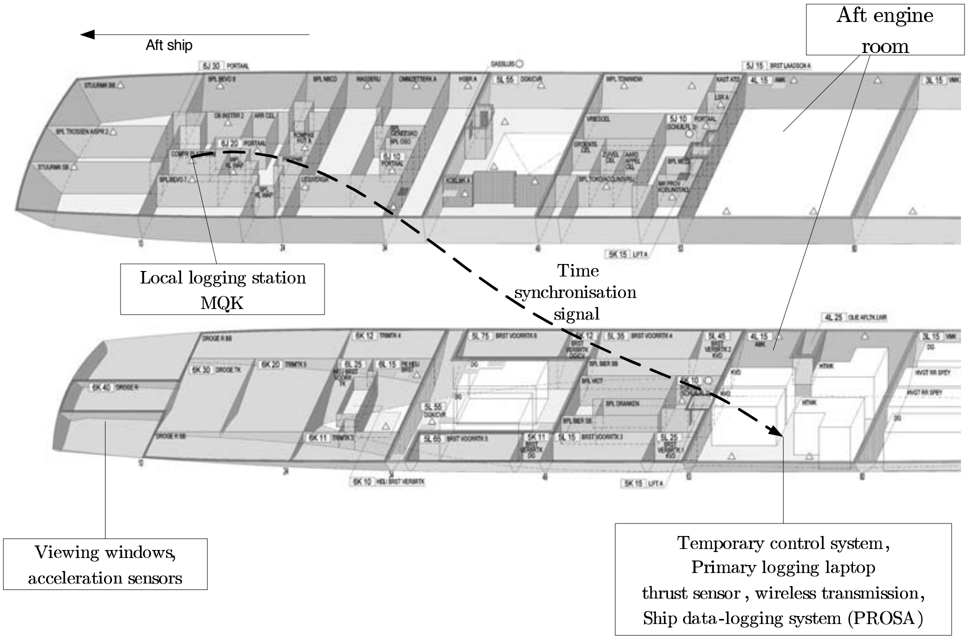
Aft ship
Aft engine room
Local logging station MQK
Time synchronisation signal
Viewing windows, acceleration sensors
Temporary control system, Primary logging laptop thrust sensor , wireless transmission, Ship data-logging system (PROSA)

Figure 8.3: Overview of the sensor system that was used for the trials

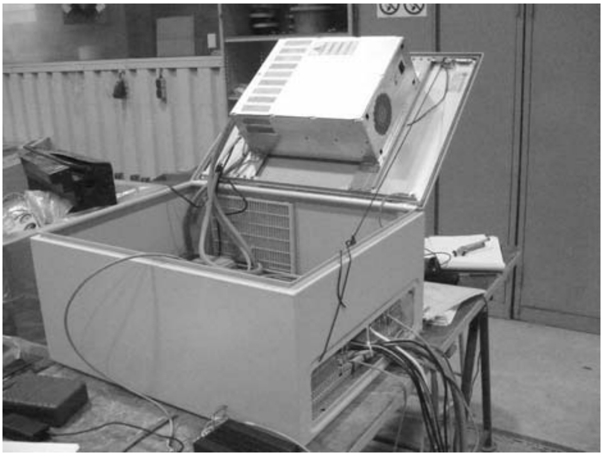

Figure 8.4: Controller cabinet fitted inside the signal-conditioning cabinet. Photograph taken during onshore testing

Propulsion variables	**Steering and roll reduction variables**	**Hydraulic variables**
pitch	rate of turn	excenter position pump
engine speed	roll angle	actual hydraulic pressure
shaft speed	roll rate	
governor setpoint	ship speed (EM log)	
fuelrack position	rudder angle (PS+SB)	
inlet receiver pressure		
thrust		
torque		
main valve position		

Table 8.2: Logged signals by means of PROSA (exclusive internal controller variables)

8.4.1 Engine Room Location

First of all there is the primary system system that provides the temporary controller with all necessary signals. For this purpose mainly already existing sensor cables (that carried sensor signals to the existing controller) were tapped, and conditioned as to be suitable as input to the I/O boards. One of the signals that was used was not simply tapped, but was generated by a temporarily installed specialized thrust sensor, which is dealt with separately. Another feature of the temporary sensor system was the installation of a wireless transmission system to send information from the rotating shaft system to the "fixed" world. Such a system was already present, but only with low data-rate, resulting in a low update frequency of the pitch signal. The new system greatly increased this data-rate, which is highly desirable if continuous pitch movement is to be achieved.

The ship data logging system PROSA was used as a secondary system that collected signals for further afterward analysis. It uses mostly the same sensor data as the primary system, although some useful signals (such as ship speed and rudder angle) could only be collected via this system, and not by the primary system due to practical reasons. The PROSA system is installed on board as a tool for the ship crew in case the installation shows unexpected or undesired behaviour, and can be used to log a big variety of system variables. A restriction of the laptop-system is that is can only show and log the system variables of one specific installation at a time. If for instance the rudder angle is to be related with engine torque data, two laptops (each with their own PROSA-application) have to be used, and time synchronization between the two has to be taken care of manually.

It should be realized that the architecture of this system is such that for most applications only low sampling frequencies are possible (most important signals at 5Hz). Furthermore these signals undergo quite strong analog filtering before they are digitized, which is understandable for reasons of robustness. Nevertheless the system is very useful to capture the main system performance parameters. For reference, the signals that were logged via the PROSA system are listed in Table 8.2. Where possible however, the sensor data that was captured at a higher data rate (by the primary system) is used for the data-analysis.

The Thrust Sensor

As was discussed in Section 7.3.2, the quality of the estimated axial velocity in the propeller disc, and thus the quality of the estimated effective angle of attack, largely depends on the quality of the thrust measurement.

During this project it turned out that a Dutch company was developing a sensor aiming at high quality thrust measurement. This sensor was installed onboard HNLMS van Galen, and has been used during the trials instead of the available strain-gauge thrust measurement. Without going into details, the basic principle of this sensor is shortly described here.

As shown in Fig 8.5, the propeller shaft is fitted with two separate rings which are both fitted with 4 arms that are distributed evenly around the shaft. The arms of one ring are fitted with light sources, while the arms of the other ring are fitted with very sensitive optical sensors. Via this system it is possible to measure displacements up to nanometer precision, which is a measure for the amount of thrust that is exerted on the propeller shaft.

Due to bending moments in the shaft, each source-sensor combination in practice measures an oscillating displacement during a revolution. To compensate for this oscillation, use is made of four arms, so that in theory the shaft-rate oscillations can be canceled out completely. However, during the earlier trials it turned out that a residual oscillatory signal was still present, resulting in an oscillatory thrust signal. An amplitude / phase correction was applied to avoid this effect, leading to a level of less than 0.5% of the maximum thrust. Another phenomenon that was seen in the thrust signal, was the blade frequency. However this oscillation is a true measured thrust, which can be detected due to the high accuracy of the sensor. Since such oscillations ultimately lead to oscillatory actuation of the CPP hydraulics, it was chosen to average the thrust signal over 0.5 to 1 second. Although this choice directly led to performance degradation due to introduction of lag in measured thrust, this signal was still used instead of the strain gauge measurement. This is because the strain gauge measurement had a relatively coarse signal resolution and low update frequency (after wireless transmission from the rotating shaft), so that also this system would lead to oscillatory actuation of the CPP hydraulic system. It is expected that in the near future, shaft rate oscillations due to bending of the shaft can be cancelled out.

Due to the high accuracy and resolution of the optical measurement in comparison with the conventional strain gauge measurement, a thorough analysis and comparison of the signal is necessary to determine which signal conditioning will be the best choice for each application. Due to blade rate thrust variations it might be inescapable to filter the true thrust signal to some extent, if oscillatory signal behaviour is undesirable.

8.4.2 Aft Measurement Location

The more or less independent measurement location in the aft of the ship was primarily used to record the cavitation behaviour of the propellers. Besides cavitation related measurements, ship motions were also recorded, together with various GPS-signals such as position and speed.

For a more detailed description of the test-setup in the aft ship, reference is made to Van Gent et al. (2008).

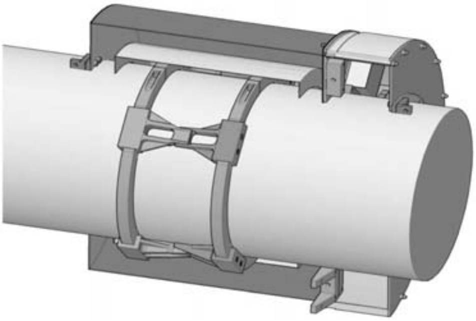

Figure 8.5: Thrust sensor fitted to propeller shaft. Source: VAF Instruments BV

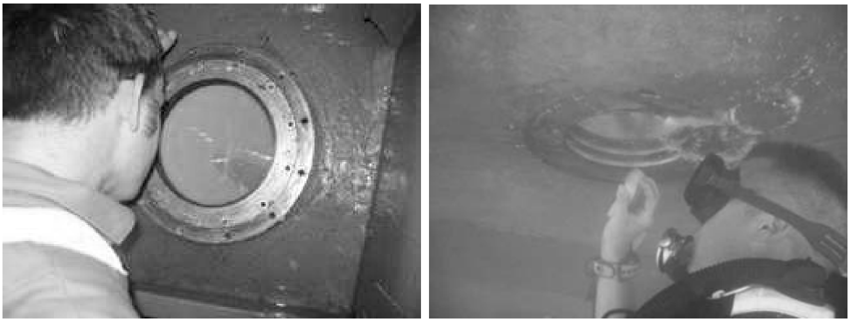

Figure 8.6: Left: viewing window seen from the inside. Right: ship diver cleaning the window before the trials

High Speed Video System

To facilitate visual observation of the propellers, three viewing windows were installed above the starboard propeller when the ship was in dock. Two windows were fitted with high speed video cameras capable of making up to 2000 recordings per second. However, as a compromise between resolution in time and recording interval length, most recordings were made at 250Hz. At the beginning of the trials it turned out that the pressure side viewing window gave the best overview of the complete propeller disc, and the best camera was fitted there.

Although all necessary preparations were made to make boroscope observations, only the high speed video cameras were used during the actual trials. Few small test-observations with the boroscope revealed that the view of the propeller was largely obscured by a large quantity of air bubbles traveling in the line of sight. On the other hand, the light intensification that is possible with the boroscope-setup might be useful when observing in conditions with less (sun) light. The use of the boroscope is illustrated in Fig 8.7.

The Acceleration Sensors

Since the video recordings can not observe cavitation over the complete propeller disc, a secondary supporting system was installed. Two acceleration sensors (type B&K 4368) were fitted on the inside of the hull, above the port and the starboard propeller (Fig 8.8).

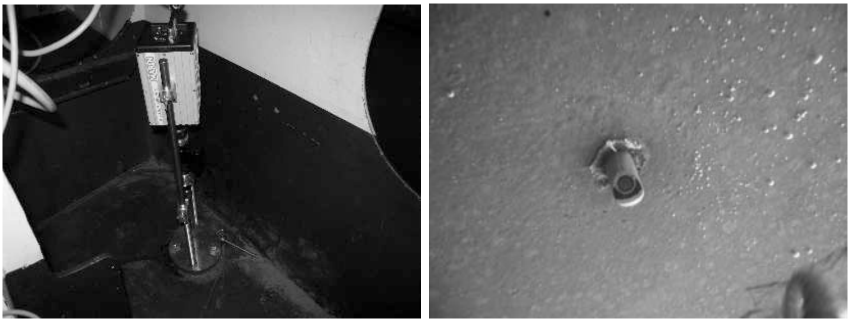

Figure 8.7: Boroscope: inside and outside view. Note that the left figure shows the camera (top), the (dark colored) light intensifier (middle) and the boroscope itself (bottom). The hole diameter is approximately 12 mm, and could be bolted shut after the trials

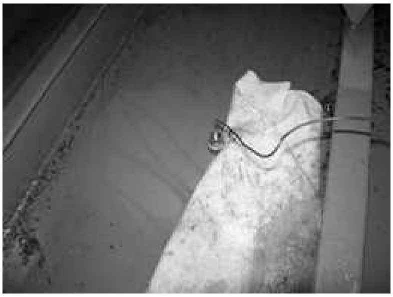

Figure 8.8: Acceleration sensor fitted to the inside of a hull plate

The acceleration signals were amplified, and logged at 20kHz, resulting in data-files of considerable size.

This setup does not isolate cavitation induced vibrations from other sources of vibration. It was for instance observed that a slam in the fore ship was picked up by the acceleration sensors in the aft ship. Furthermore there are various possible propagation paths from noise source to sensor, thereby complicating the differentiation between port and starboard side propeller induced noise. Nevertheless the system proved useful both during the trials and during the analysis of the trial results.

Ship Motion and Position Sensor System

To log the motion of the ship, and of the starboard propeller in particular, a 6 DOF acceleration sensor fitted with accelerometers and angular rate gyros was installed. This device is referred to as the MQK, which stands for *Marine Quality Kit*. It was developed in house by MARIN, and has proven itself over the years.

The GPS position, as well as the course and speed over ground were measured by a DGPS sensor that was mounted on the helicopter deck of the ship. Via a cable the signal was logged in the aft logging location.

Chapter 9

Measurement Analysis

9.1 Introduction

To verify the performance of the newly developed propulsion control system, full scale trials were carried out onboard the M-frigate HNLMS van Galen, in February and March 2008. The operating area was the Caribbean Sea, where the ship was deployed at that time.

In this chapter the measurements of the trials are presented and discussed. The system performance using the new PCS (or PCS+) is compared with the system performance when using the default (or "old") propulsion control system. Where considered useful or necessary, use is made of extra simulation predictions. Such predictions can be used instead of measurements that where not carried out. Furthermore, various simulations can be carried out under exactly the same conditions, so that external disturbances, due to for instance waves, do not contaminate the observations.

In an ongoing research project the full scale measurements could (and should) be used as validation material, thereby further increasing the validation database. With the increasing size of the validation database, the findings from predictions made by the simulation model, are based on an increasing amount of proof. This should lead to a confidence level of the user that corresponds with actual predictive capabilities of the model. In this case however, the project is ended with this dissertation, so that a formal validation of the new cases is not carried out.

9.2 Test Overview

To keep an overview of the tests that have been carried out, this section puts the various experiments in perspective. The experiments that were planned, and communicated with the ships crew were described in a test-protocol (Van Gent et al. (2008)). This protocol contained various types of tests that were designed with the goals of the project, as defined on page 4, in mind. The relevant goals and research questions that led to the test-protocol are repeated here:

- *Use the simulation model to develop a propulsion control system that aims at increased cavitation free time in operational conditions,* ***and test this propulsion control system on full scale.***
- *Investigate the effects of operational conditions on the performance of the propulsion system.*
    - What is the effect of acceleration and deceleration on the system performance?
    - What is the effect of added resistance (due to for instance wind or fouling) on the system performance?
    - What is the effect of waves on the propulsion system performance?

To reach these goals the following dedicated tests were defined:

α-bucket tests: To determine the middle and the approximate shape of the α-bucket, various tests were carried out using the so called hand-electric mode. This means that the PCS is disconnected from the plant, and that the two main plant inputs "governor setpoint $n_{set,gov}$" and "propeller pitch setpoint $\theta_{set,PPC}$" are directly controlled by an operator. In this way it was possible to independently choose the operating point of pitch and shaft speed. The advantage of this approach is that horizontal intersections of the bucket could be made by gradually increasing pitch at a certain shaft speed. By observation of the propeller during the experiment combined with the acceleration sensor signal above the starboard shaft, a cavitation free operating area at that specific shaft speed could be determined. By repeating the same test for multiple shaft speeds, the approximate shape of the bucket could be determined.

Note that the hand-electric mode provides little automatic protection against engine overloading. Therefore RNLN procedures dictate a conservative use of hand electric control of the propulsion system. These conservative procedures combined with the fact that the DE's have little margin against overloading, resulted in the fact that only the pressure-side cavitation inception points could be determined. Determination of suction side cavitation points necessitates a high loading of the propeller and thus of the diesel engine, which is not allowed by the procedures. To determine the suction side inception points it is recommended to drive the shaft by the gas turbine, which has less limitations due to the virtual absence of the risk of overloading.

acceleration/ deceleration test: To investigate the effect of acceleration and deceleration on the system behaviour, a test was defined with a command-cycle similar to the calibration experiment as shown on page 48. The command cycle is chosen such that its setpoints align with the nodes of the combinator curve of the old PCS. This comes down to the following sequence of setpoints: $0 - 67 - 91 - 120 - 91 - 67 - 0 - 120 - 0$ virtual rpm. The 120 rpm setting is chosen because the end-node value of 135 rpm in practice isn't reached anyhow due to pitch reduction ordered by the old PCS.

forced over- and underloading test: To investigate the effect of added resistance on the propulsion system, a test was defined that made use of thrust differences between the port and starboard propeller. By ordering a lower setpoint at the port side than on the starboard shaftline, high resistance conditions could be simulated. By increasing the power on the port shaftline, the starboard side was unloaded to simulate light conditions.

wave test: To investigate the effect perturbations by waves on the system, two tests were defined. The first test was to study the effect of stern waves, with a low encounter frequency. The watch officer was asked to maintain a stern wave course for approximately 20 minutes. The same test was performed in head-waves for a period of approximately 15 minutes.

turning circle test: Investigation of cavitation behaviour during turning circles was not included in the objectives of this thesis. Therefore, no additional features have been implemented in the controller to enhance the cavitation performance during such manoeuvres. As discussed in Chapter 7, such additional measures might include scheduling-measures to decide on the most suitable setpoint for the effective angle of attack $\alpha_{eff,set}$ dependent on the actual (combination of) driftangle, rudder angle or possibly rate of turn. Another possible measure might be to limit the maximum allowed shaft speed during a turning circle.

Although such measures where not included in the tested PCS+, various turning circle tests have been performed. One of these turning circle manoeuvres is discussed in this chapter to show the principle behaviour of the controller and the system during a turn. These results might stimulate necessary future development towards a generally applicable cavitation reducing PCS.

During all tests the helmsman was asked to limit the use of rudder to preferably $< 5°$, and to switch off the roll-damping system. The watch officer was asked to keep a straight course during the run, if possible due to other shipping or mission requirements.

Except for the α-bucket test, which was carried out on hand-electric mode, all tests were carried out by both the existing and the new PCS. To make the comparison as fair as possible, the importance of keeping the same course for a prolonged period (during the comparison tests) was emphasized onboard. During most of the tests this was possible, but as might be expected from a field experiment, in specific cases the conditions necessitated alteration of course, resulting in a less fair comparison between the runs.

A more detailed list of all performed trial runs is given in Appendix D.

9.3 Environmental Conditions

During the test period prevailing easterly winds were encountered, increasing in strength from 4 to 6 Beaufort, resulting in seastate 2 to 4. No calm water conditions where found, so that calm water system behaviour could not be fully separated from the effect of wave perturbations.

9.4 Measurement Analysis

9.4.1 The α-bucket Test

The α-bucket test was designed to determine the approximate shape of the α-bucket. By making use of hand electric propulsion controller mode, the pitch and shaft speed could be chosen independently, within the operating area that is allowed by the procedures. By setting the shaft speed to a specific value and then varying the propeller pitch, a more or less horizontal intersection with the bucket could be made. In this way it was possible to determine a specific point on the inception line. This procedure was repeated for various shaft speeds, so that an inception line could be determined.

Due to the weather conditions the test was largely disturbed by waves and ship motions. Nevertheless the results confirm that the alpha bucket does exist, and gives some guidance on the position of the pressure side limit of the cavitation free operating area. Because of the RNLN procedures, aiming at prevention of engine overloading, higher propeller loadings where largely "forbidden", so that the suction side inception line could not be determined when sailing on DE's.

The operating points that were tested are listed in Table 9.1. Because of the wave disturbances an objective determination of inception conditions was found very difficult (if not impossible). First of all this is a definition question, and secondly the judgment is dependent on the observer. To partly remove subjectivity from the test the acceleration sensor data was used. Based on a comparison between visually observed cavitation and the acceleration sensor signals a helpful derived signal was found: the standard deviation of the acceleration signal over the last τ seconds. By comparison of this running standard deviation with visual observations, it was found that as soon as cavitation was observed, the signal crossed a specific (manually determined) threshold value. Even though the signal also picks up possible cavitation from the portside shaft or from other locations, a good correlation was still found.

Fig 9.1 shows the results of the test, including the derived inception line. The black markers indicate the instances where the running standard deviation did not cross the threshold value, and were no cavitation is assumed. The grey markers indicate the instances were the acceleration signal crossed the limiting value. As expected the trend is that cavitation occurs less often at the right hand side. Unfortunately higher angles of attack were not reached at shaft speed C, so that this operating point does not reveal at which value cavitation can be prevented. A rough inception line indicates an approximate boundary of the cavitation free operating area. The vagueness of this inception line (presumably caused by seastate) reveals that an operating point should preferably be chosen in the middle of the bucket, so that maximum margin against cavitation is present. This middle cannot be estimated from these results, but during the first few days of the trials it turned out that the effective angle of attack with the most margin against cavitation lies around 4.5-5 degrees, which agrees with the expected value, based on Fig 7.7.

Although this test is fairly limited considering the small variety of shaft speeds, pitch angles and resistance conditions, it does demonstrate the possibility of experimental determination of the cavitation free operating area. If a figure like Fig 9.1 would be based on more long term data, it is expected that the true cavitation free area will appear automatically. The middle of this experimentally determined bucket can then rightfully be used as $\alpha_{eff,set}$. As mentioned in Section 7.7, it is expected that this approach can be extended to turning circle manoeuvres.

operating area	shaft speed [rpm]	pitch [deg]
A	80	11-16
B	90	13-19
C	100	17-19

Table 9.1: α-bucket test setpoints

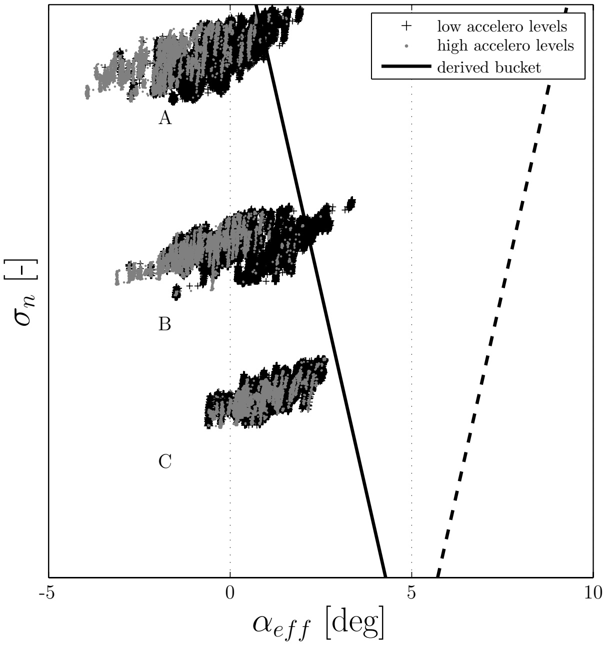

Figure 9.1: Determination of the approximate α-bucket shape

9.4.2 The Acceleration Test

To investigate the effect of acceleration on the system behaviour, an illustrative manoeuvre from $\approx$ 10-14kts is discussed here. This test will reveal possible benefits with regards to cavitation reduction and with regards to acceleration time. The effect on engine loading will also be discussed. Note that the results of the acceleration test are also presented and discussed in Vrijdag et al. (2009).

The test was successively carried out with the existing and the new PCS driving the starboard shaft. The port shaft was continuously driven by the "old" PCS. The most important graphs are shown and discussed, together with various photographs of the starboard propeller, taken with the high speed video camera. To make a comparison possible, the graphs contain measurements of the same manoeuvre, carried out by both the old and the new PCS driving the starboard shaft.

To structure the discussion it is split up into separate sections subsequently covering the aspects *propeller behaviour*, *engine behaviour*, and *manoeuvring behaviour*. The two top level inputs to the system are the virtual setpoint and the rudder angle, as shown in Figs 9.2 and 9.3. The starting point of the transient is $t = 542s$, where the virtual setpoint is changed from 67 rpm to 91 rpm.

Propeller Behaviour

First, the behaviour of the old PCS will be discussed, followed by a discussion of the new PCS.

Old PCS: As can be seen in Fig 9.6 and 9.5, the static propeller pitch operating point at both the beginning and the end of the transient lies at 26 degrees as fixed by the combinator curve. The active pitch reduction that is ordered by the PCS temporarily reduces the pitch to $\approx$ 14 degrees in order to reduce the engine loading. On the other hand the shaft speed increase is quite steep, as shown in Fig 9.4. Fig 9.12 shows that the nett effect of the active pitch reduction and the shaft speed increase results in a steep drop of propeller thrust. Between $t = 542 - 555s$, total thrust drops below the value necessary to maintain the original speed. Between $t = 546 - 551s$ the total thrust even becomes negative, which means that the propellers are effectively braking.

The shaft speed reaches its setpoint around $t = 550s$. The PCS now starts to increase the load by slow increase of the propeller pitch setpoint, followed by the pitch as shown in Fig 9.5. Up to $t = 557s$ this pitch increase is quite fast, until the first Reduced Time Between Overhaul (RTBO)-line of the PCS is crossed (Fig 9.8). The PCS now takes action by decreasing the pitch-rate, in order to prevent an overshoot across the RTBO2-line. From now on the pitch is allowed to increase with a rate that is dependent on the loading of the engine: due to a nett resultant longitudinal force, the ship accelerates, resulting in a decrease of engine loading. Pitch is increased slowly, and the ship speed increases further, and so on. Dependent on the actual conditions, the propeller pitch is increased until the combinator value is reached. If engine loading is too high (due to for instance high ship resistance), pitch remains constant at a reduced value, leaving the operator command only partly effectuated.

The path through the α-bucket is shown in Fig 9.15. The aggressive pitch reduction results in a significant drop of angle of attack, which according to the schematically shown (uncertain) bucket should lead to pressure side cavitation due to under-loading of the propeller. Subsequently, pitch is increased fast, resulting in a quick recovery of angle of attack. After that, pitch increases gradually in such a way that α_{eff} stays approximately constant around 4° as shown in Fig 9.13. The cavitation behaviour of the starboard propeller is shown in Fig 9.19, showing most extreme pressure side vortex cavitation around $t = 550s$. This agrees with the time at which the effective angle of attack is at its lowest as shown in Fig 9.13. Even in the final photograph small traces of cavitation are still visible.

The acceleration signals measured above the port and starboard shaft are shown in Fig 9.16. Both port and starboard sensor are saturated around t=550s, indicating that considerable cavitation is present, which agrees with visual observations of the starboard shaft. It must however be noted that due other noise sources, the limited number of acceleration sensors and due to the variable propagation paths of the pressure waves and hull vibration, the acceleration sensors do not give a clear indication of the source of the sound. In this case however, with the availability of visual observations, it is highly likely that the excitation is caused by propeller cavitation. The acceleration sensors on both sides show a comparable excitation, which indicates that both propellers show comparable cavitation behaviour.

New PCS: From Figs 9.6 and 9.5 it can be seen that active pitch reduction is still applied by the new PCS, albeit a lot less aggressive. As dictated by the new PCS, the pitch is constantly adjusted with the goal of keeping the estimated effective angle of attack α_{eff} at the setpoint $\alpha_{eff,set}$ that is chosen in the middle of the α-bucket. The resulting path in the bucket is presented in Fig 9.15, showing less fluctuations in α_{eff} than in the "old PCS"-case, which is likely to result in increased cavitation free time. On the other hand the new PCS temporarily operates at higher shaft speed, and thus lower in the bucket. This effect helps to accelerate the ship faster, but might possibly lead to unnecessary cavitation. Such effect can easily be prevented by limiting the shaft speed to some maximum value, as was demonstrated by the parameter study in Section 7.6. This will however come at the cost of acceleration-performance degradation.

The cavitation behaviour during the first part of the manoeuvre is shown in Fig 9.20, showing no visual inception, except for a small trace at $t = 552s$. The high shaft speed excursion around $t = 600s$ is however not captured on video, and conclusions have to be drawn based on the acceleration sensors. Fig 9.17 shows considerable excitation around t=549-550s, which was not visible on the video. Since the excitation is much stronger on port side than on starboard side, it is concluded that it is very likely that the noise was caused by the portside shaft that was still controlled by the old PCS. This does however not fully guarantee absence of cavitation on the starboard propeller.

During the rest of the manoeuvre the starboard acceleration sensor shows small irregular spikes, which probably indicate individual cavitation events due to the temporarily increased shaft speed. It is however clear that a considerable gain in cavitation generated noise has been reached.

Engine Behaviour

The trajectory in the engine diagram as shown in Fig 9.8, is quite different for the old and the new PCS. The dip in loading due to active pitch reduction of the old PCS during the acceleration indicates that the engine is overprotected, which is likely to result in decreased acceleration capabilities. The latter is discussed in the next section on manoeuvring behaviour. Around t=560s the old PCS has increased fuelrack up to RTBO1, after which the pitch rate is decreased in order to keep the operating point outside the RTBO2 area. The PCS+ applies only little pitch reduction. Instead, pitch is actively controlled to maintain the angle of attack at its setpoint. During the up-hill transient, except for the short (over)loading hump around t=547s, the operating point follows the RTBO2-line, up to the high shaft speed of $\approx$ 130 rpm. From there on, with increasing ship speed, the balance between pitch and shaft speed gradually shifts towards lower shaft speed and higher pitch.

The amount of fuelrack that is used to accelerate the shaft can easily be influenced by changing the desired shaft- acceleration rate. This will however have its consequence on the acceleration of the ship. The effect of changing the shaft-acceleration-rate parameter was tested by making use of the simulation model, as is shown in Section 7.6.

Manoeuvring Behaviour

Before a comparison of the acceleration capability of the "old" and the "new" PCS is made, possible disturbances that might affect the acceleration performance are considered. Inspection of Fig 9.3 shows that during the "old" test the autopilot was used, resulting in small fluctuations in rudder angle. The mean rudder angle differs approximately 3 degrees between the runs.

Furthermore, as can be seen in for instance the ship speed signal in Fig 9.10, the ship speed fluctuations (or better: the water speed as measured by the EM-log) shows a difference in frequency content during the run. Due to operational circumstances the ship had to change course between the comparison-runs. Based on the encounter frequency as derived from the speed figure, it is concluded that the "new" run was carried out in bow-quartering or bow waves, while the "old" run was most probably carried out in stern-quartering or stern waves. This course change would also explain the difference in total propeller thrust as shown in Fig 9.12. Unfortunately the GPS-log computer failed during the run, and no exact course or heading information is available for these runs.

With the mentioned disturbances in mind, a comparison between the acceleration capabilities of the two systems can only be made in a qualitative sense. Due to the course change the new PCS had a disadvantage due to the extra resistance. In spite of this resistance increase, the measured acceleration time seems to have been shortened by the new controller. This is expected to improve even further if not only the starboard shaft, but also the portside shaft would be controlled by the new PCS.

To enable a fair comparison between the acceleration capabilities of both systems, simulations of this manoeuvre are carried out for various configurations. Predicted ship speed for both double PCS and double PCS+ configuration is shown in Figs 9.18. The comparison between the predicted and measured (PS+SB old) data is in fact a new validation case, giving extra information on the agreement between measurement and simulation. The difference between the measured and simulated double PCS case is attributed to difference in ship resistance due to the wave conditions. No attempt has been made to improve agreement by calibration of resistance.

With this new qualitative validation-information in mind the prediction of the double PCS+ case is trusted to give a correct behaviour, although the absolute acceleration might be on the optimistic side. The new case (PS+SB new) gives an overshoot in ship speed which can be explained by the structure and parameter settings of the PCS+. Due to the absence of disturbing waves a small dip in ship speed at the beginning of the acceleration by the two old PCS's is clearly made visible. This small dip has also been observed on full scale, when sailing in calm water. The possible gain in acceleration capabilities is clearly visible and indicates that the system capabilities are not fully utilized by the old PCS.

This small example of ship acceleration prediction is a demonstration of true symbiosis between measurement and simulation. Such strong symbiosis clearly helps to make high confidence predictions of complex multidisciplinary system behaviour.

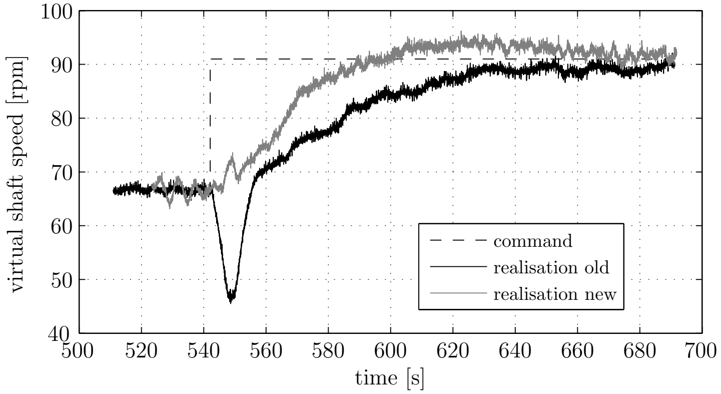

Figure 9.2: Command

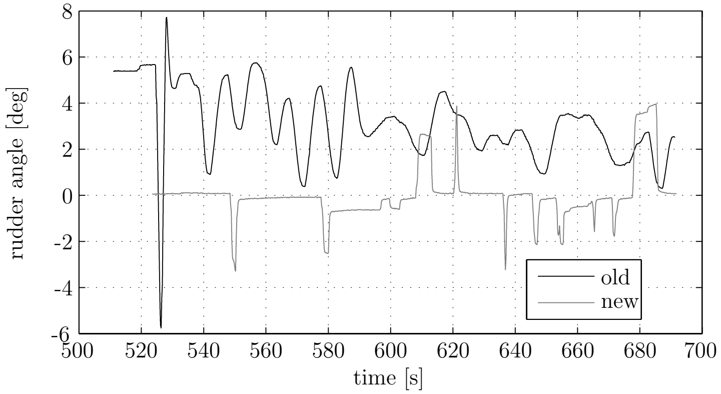

Figure 9.3: Rudder

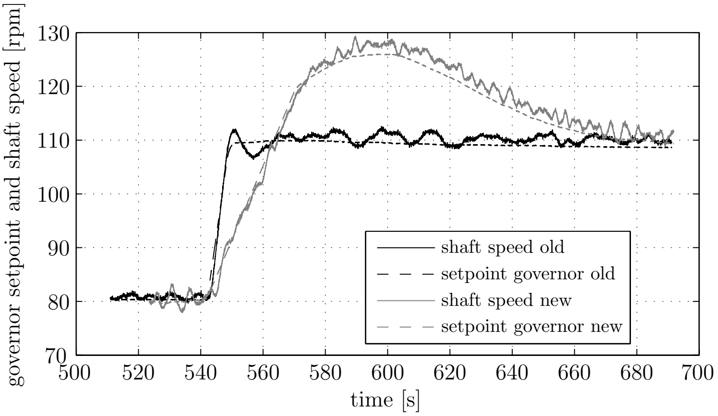

Figure 9.4: Governor setpoint and shaft speed

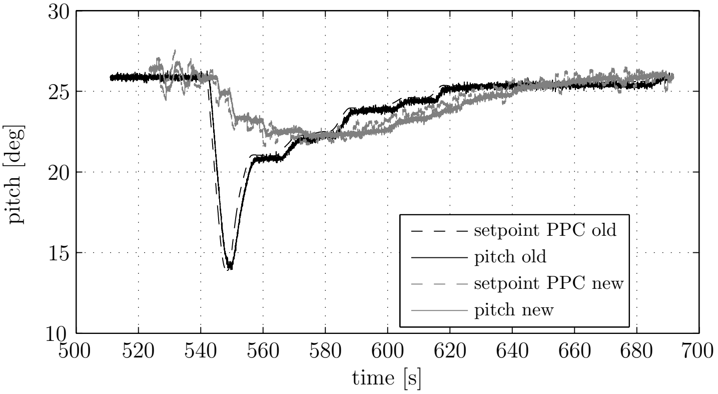

Figure 9.5: Low level pitch setpoint and pitch

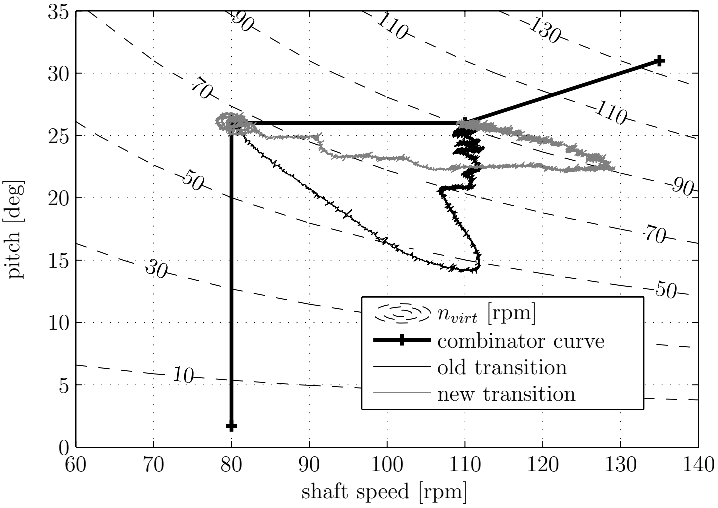

Figure 9.6: Transient in the $n - \theta$ plane

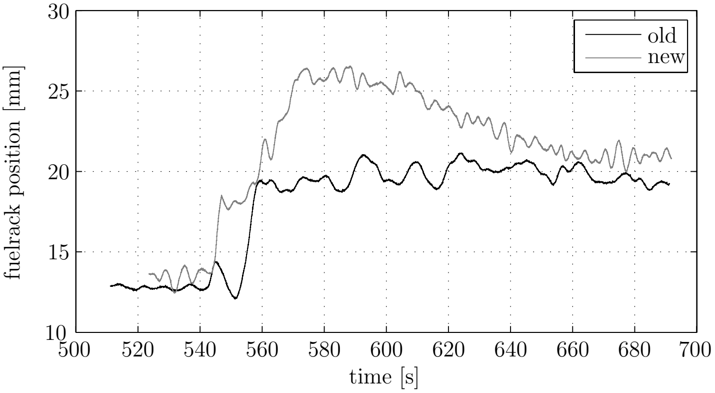

Figure 9.7: Fuelrack position

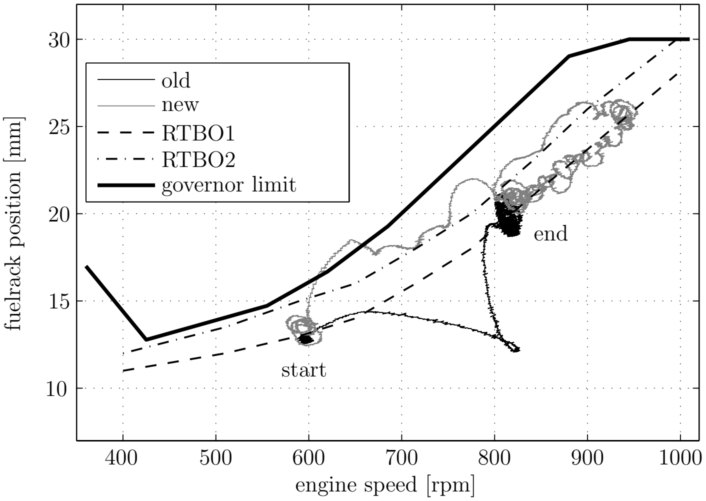

Figure 9.8: Engine diagram

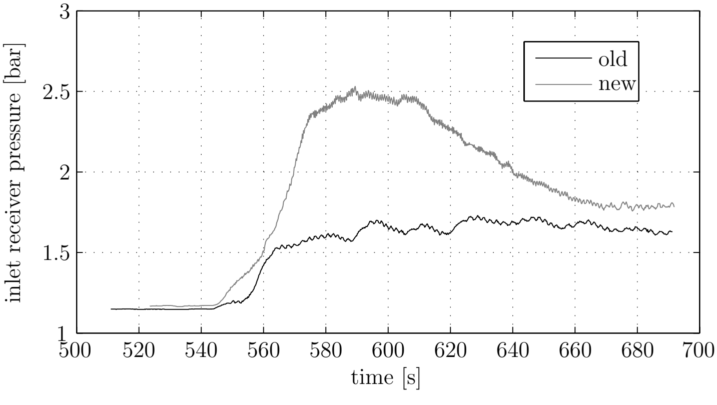

Figure 9.9: Inlet receiver pressure

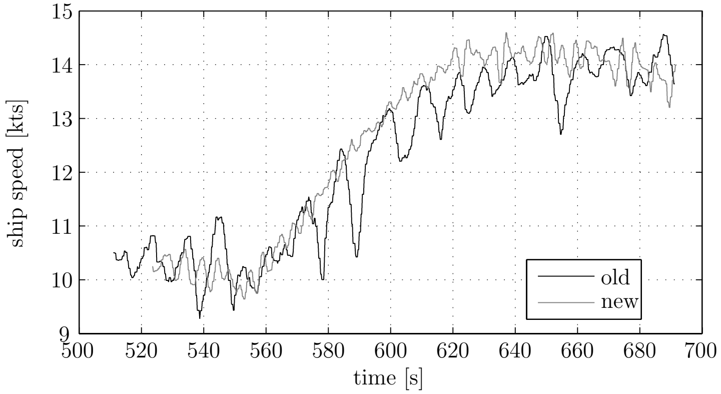

Figure 9.10: Ship speed

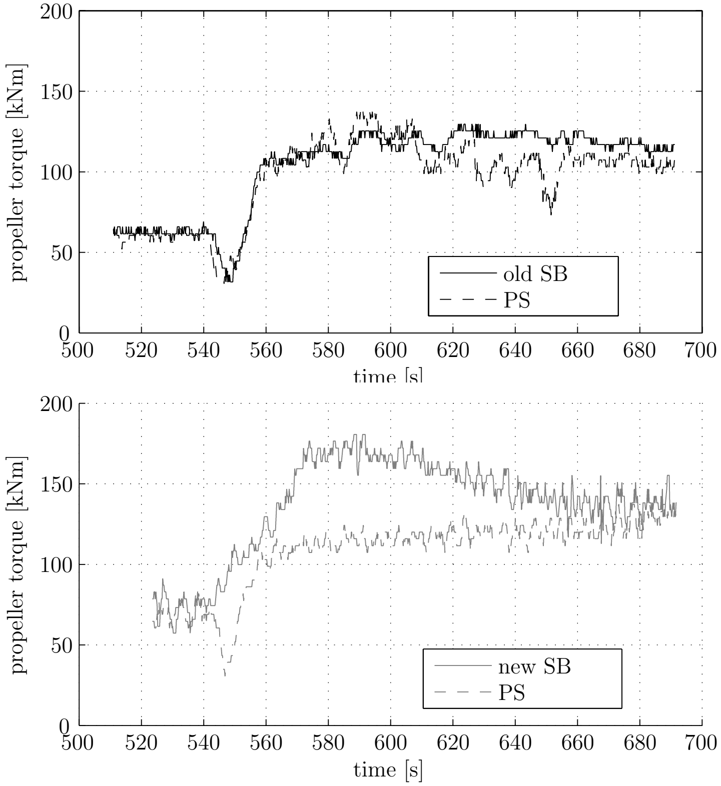

Figure 9.11: Propeller torque (port and starboard) for the old and the new PCS

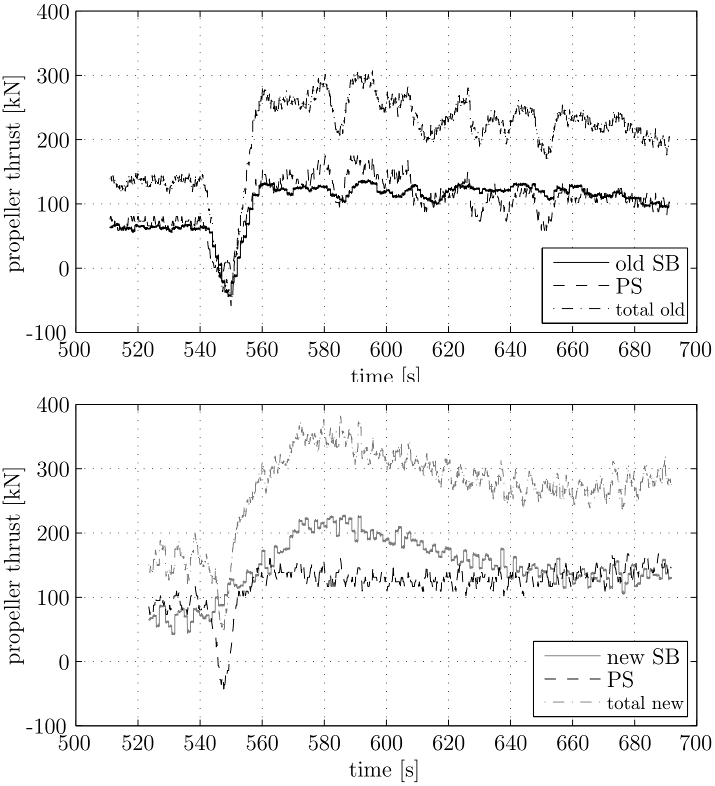

Figure 9.12: Propeller thrust for the old and the new PCS

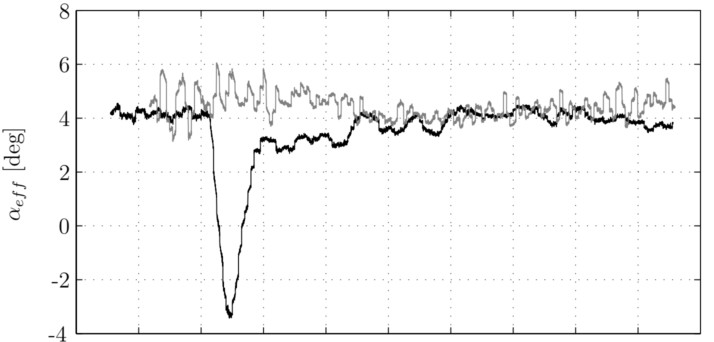

Figure 9.13: Estimated effective angle of attack

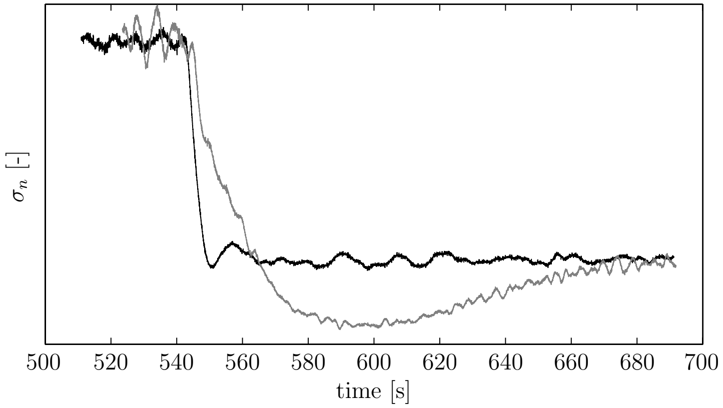

Figure 9.14: Cavitation number

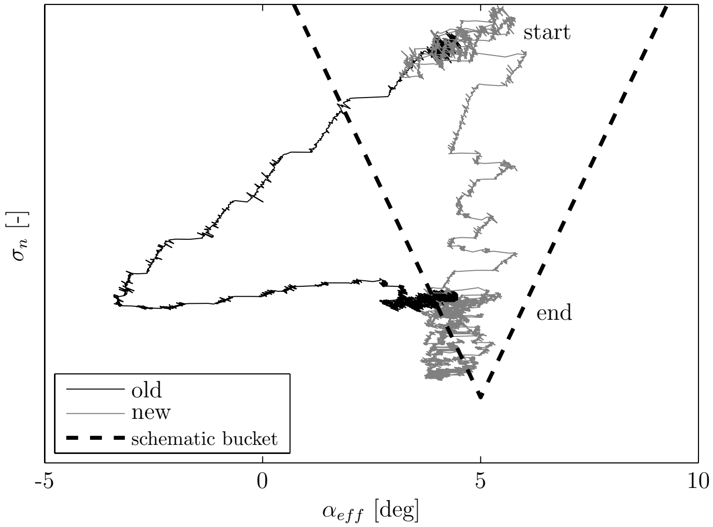

Figure 9.15: α bucket

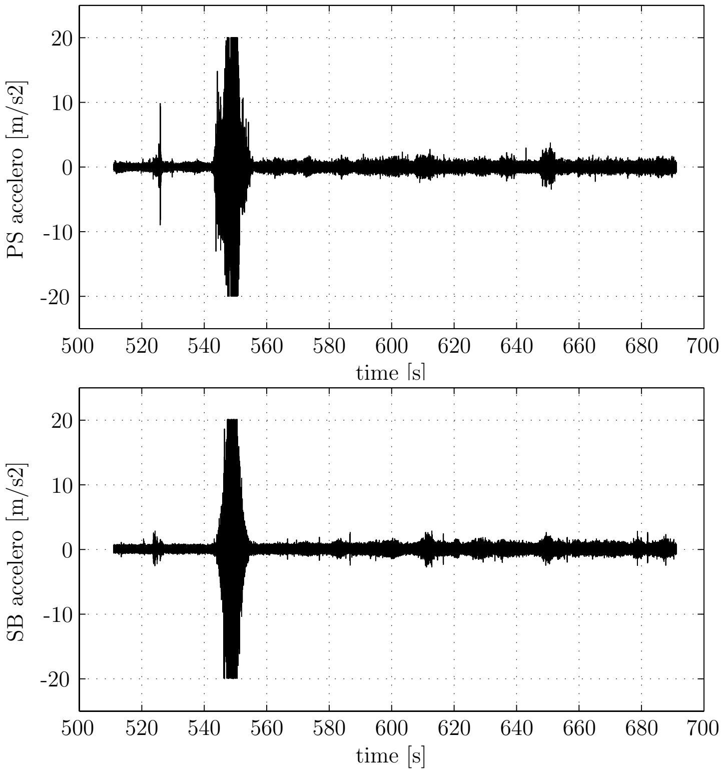

Figure 9.16: Acceleration sensor signals. Acceleration with the ”old PCS”

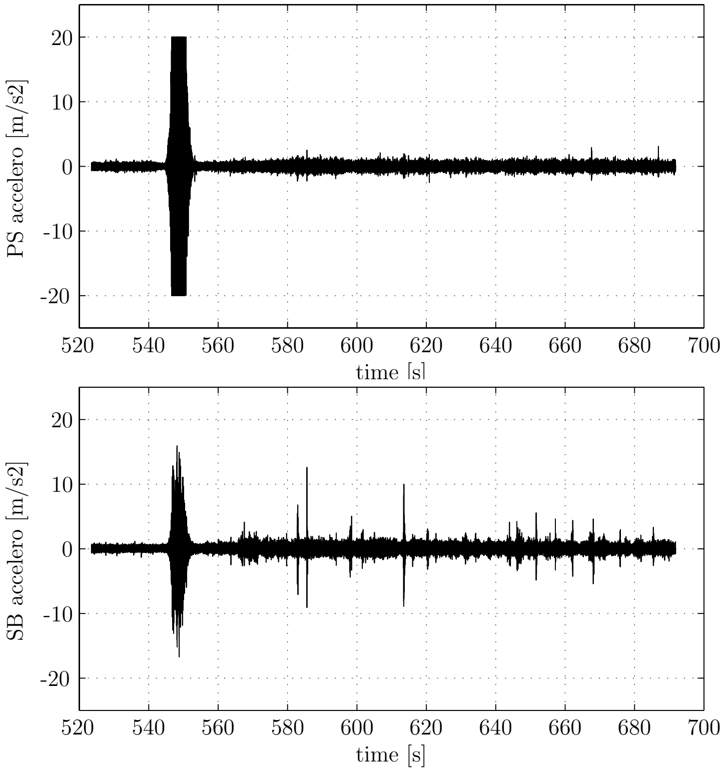

Figure 9.17: Acceleration sensor signals. Acceleration with "new PCS"

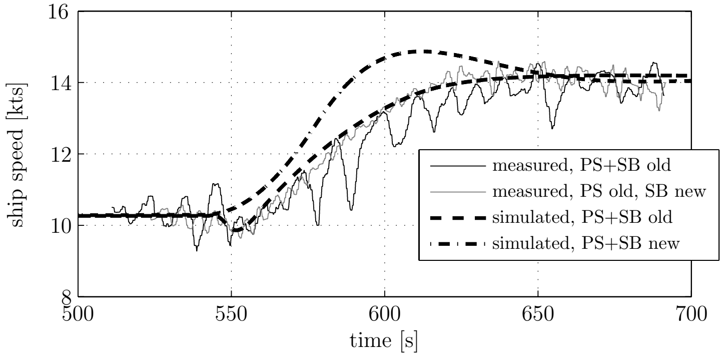

Figure 9.18: Prediction of speed with double PCS+, and double "old PCS"

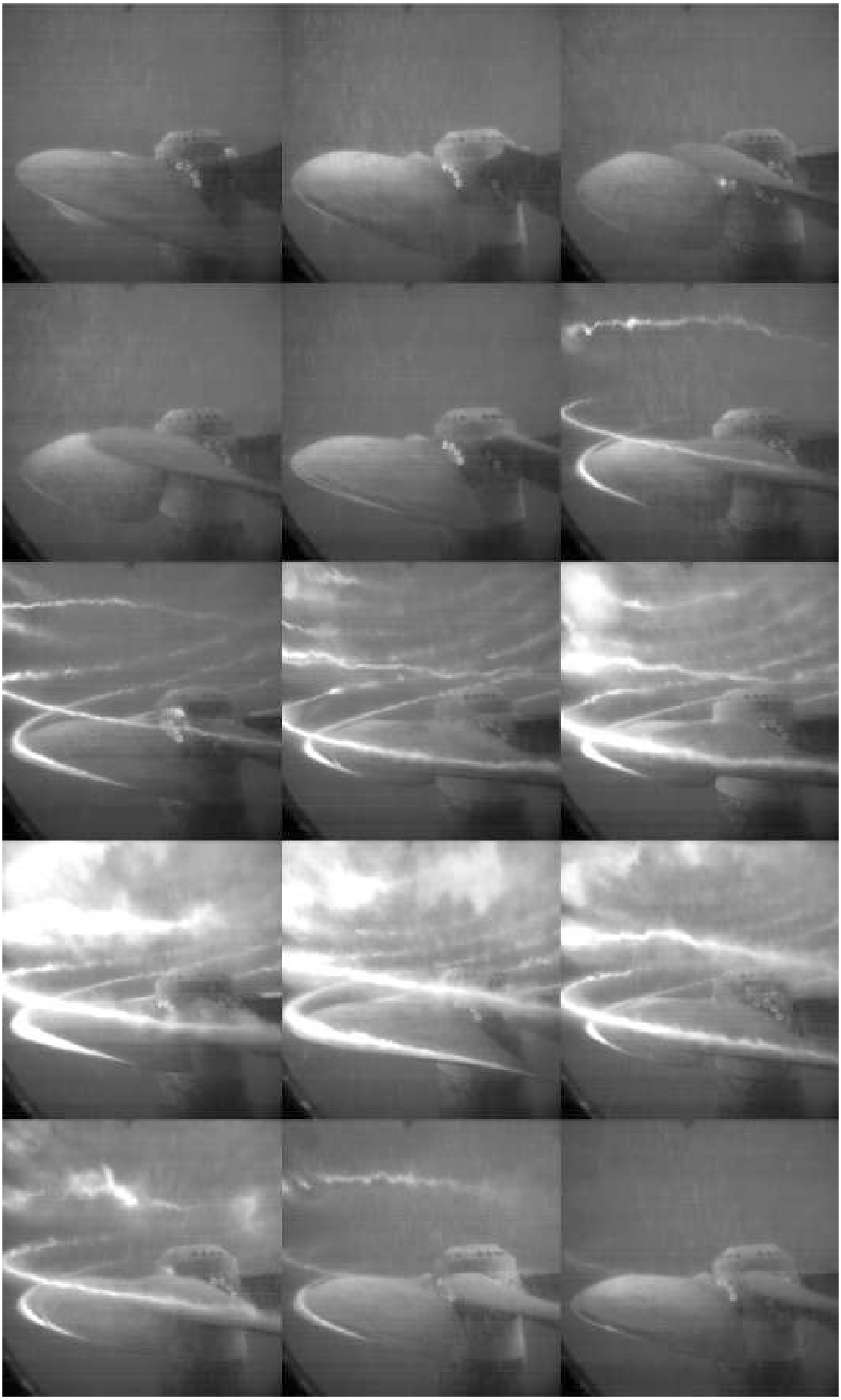

Figure 9.19: Cavitation behaviour of old PCS during acceleration, display interval 1s, start at t=540s. End at t=554s

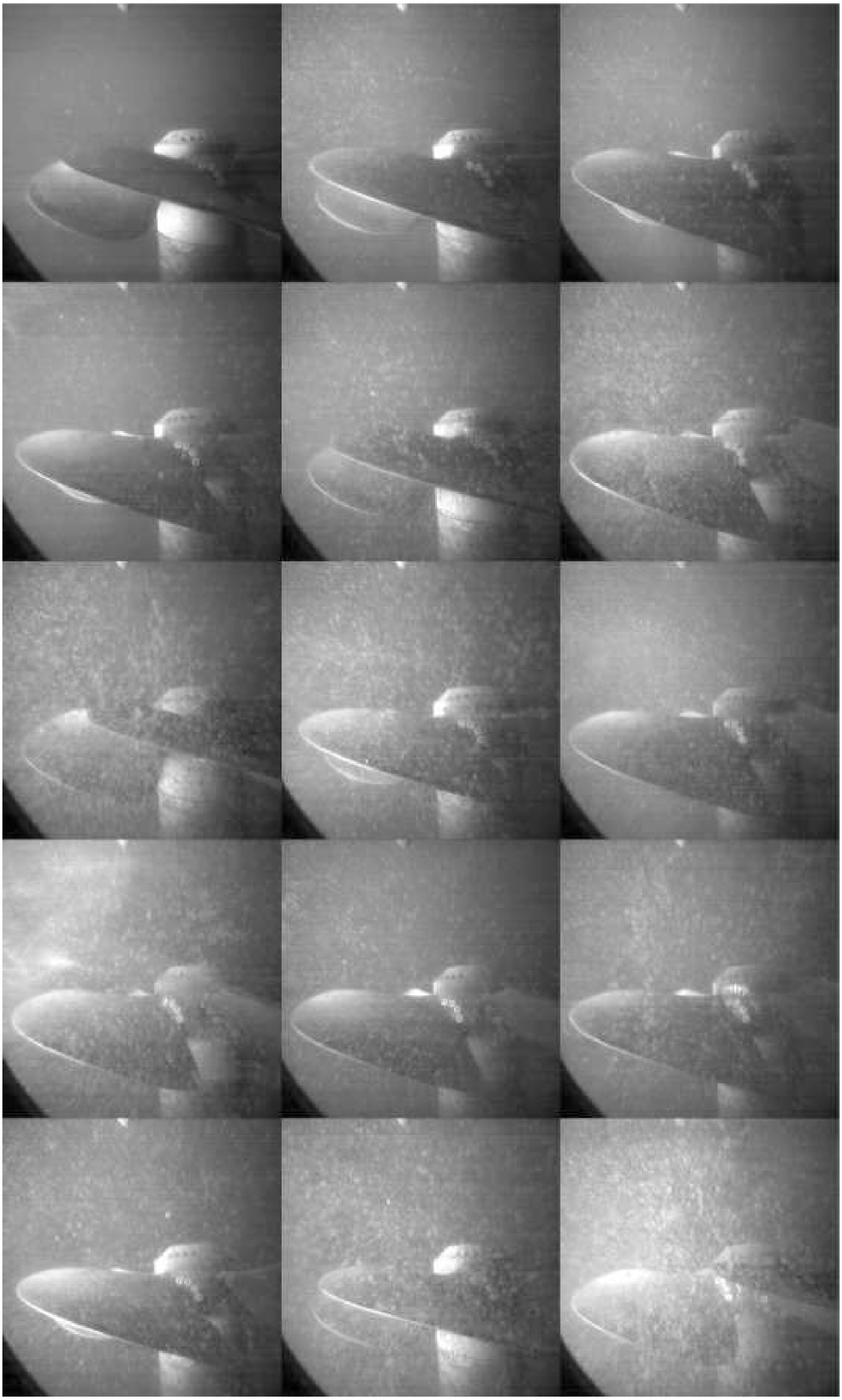

Figure 9.20: Cavitation behaviour of PCS+ during acceleration, display interval 1s, start at t=543s. End at t=557s

9.4.3 The Deceleration Test

To verify the controller performance during deceleration, the manoeuvre from ≈ 14-10 kts is analysed in the same way as the acceleration test. The discussion of the results is again split up into separate sections subsequently covering the aspects *propeller behaviour*, *engine behaviour*, and *manoeuvring behaviour*.

As was the case for the acceleration test, this test was successively carried out with the existing and the new PCS driving the starboard shaft. The port shaft was continuously driven by the "old" PCS.

Results obtained with both the old and the new PCS are shown in Figs 9.21 to 9.37. The command change from 91 to 67 virtual rpm is given at $t = 301.5s$ as shown in Fig 9.21. The rudder was controlled by the autopilot, which as shown in Fig 9.22, gave less than 5 degrees rudder during the manoeuvre.

Propeller Behaviour

First, the behaviour of the old PCS will be discussed, followed by a discussion of the new PCS.

old PCS: As shown in Figs 9.23, 9.24 and Fig 9.25, both shaft speed and pitch follow the combinator curve, which dictates that the deceleration is effectuated by sole reduction of shaft speed. The steep drop in shaft speed immediately results in a drop of effective angle of attack down to ≈ 0.5 degrees, as shown in Fig 9.32. As a result the thrust drops below 0 kN (Fig 9.31) for approximately 15s, which means that both propellers are acting as brakes.

The angle of attack is restored at the rate of the ship deceleration, which is considerably slow due to the ship mass. Only around $t = 360s$, the angle of attack has found its approximate steady value again. In terms of the bucket presented in Fig 9.34, this means that the restoring rightward movement of the operating point takes a long time, during which the propeller is very vulnerable to pressure side cavitation inception. The resulting cavitation behaviour during the manoeuvre is presented in Fig 9.38, showing pictures that were taken with the high speed video camera. Close inspection shows that even the last picture at $t = 319s$ shows small traces of pressure side cavitation. The signals from the acceleration sensors are shown in Fig 9.35. Although the cavitation induced accelerations are clearly visible around $t = 310s$, its amplitude is quite small when compared to the acceleration-test signal that was shown in Fig 9.16. The two small humps around $t = 280s$ and $t = 295s$ are attributed to wave induced cavitation. Note that the highest acceleration amplitude occurs around $t = 310s$, which aligns with the time that the visual cavitation is most pronounced in Fig 9.38.

new PCS: As shown in Fig 9.23 and Fig 9.25, the steady state propeller pitch before and after the manoeuvre lies around 27 degrees. During the manoeuvre the PCS+ orders a pitch increase up to 33 degrees, after which pitch gradually comes back to 27 degrees. This pitch increase might seem strange, but can be explained by the attempt of the PCS+ to maintain the desired angle of attack after a sudden drop in shaft speed, while ship speed initially stays approximately constant due to the inertia of the ship. As shown in Fig 9.32, the drop in angle of attack is corrected by the pitch increase of ≈ 6 degrees. This correction is however not fast enough to prevent the angle of attack from deviating from the middle of the cavitation free area, as shown in Fig 9.34. Ideally the operating point would only shift vertically, which would continuously guarantee maximum margin against inception. Although the propeller operating point stays inside the schematic bucket, it is noted that this is no guarantee for cavitation free operation. Due to for instance the α-estimation errors and local wakefield disturbances, both the location of the operating point and the shape of the bucket are affected by uncertainty. Furthermore the bucket that is shown here is only indicative.

Nevertheless, Fig 9.34, combined with Fig 9.32 and 9.33 does show that the operating point is quickly restored to the desired $\alpha_{eff,set}$, which, despite all uncertainties in both operating point and bucket, is expected to have maximum margin against cavitation inception.

The improved cavitation behaviour of the PCS+ system is demonstrated in Fig 9.36 and 9.39. Although cavitation is present, its timewise extent has decreased significantly when compared to the old PCS. The interval at which cavitation is visible has also decreased significantly.

The acceleration sensor- signals above the port and starboard propeller are shown in Fig 9.36. The hump around $t = 290s$ is attributed to wave induced cavitation. The signal level of especially the starboard sensor has decreased when compared to Fig 9.35. The interval of increased acceleration has also decreased which agrees with the visual observations of the starboard propeller. The portside acceleration signal indicates slightly higher acceleration levels, and if inspected closely, reveals a longer "tail" of slightly increased acceleration levels up to $t = 330s$. This agrees with expectations because the portside shaft was continuously controlled by the old PCS.

Based on the combined photographs and the acceleration signals, it is very likely that the PCS+ has significantly increased the cavitation free time of the starboard propeller during the manoeuvre. Further improvements can be made by faster pitch actuation, or by slower shaft deceleration. More advanced controller techniques might help to take into account the (nonlinear) dynamics of the propulsion plant, including the CPP hydraulics and its limitations.

Engine Behaviour

The behaviour in the engine diagram (Fig 9.27) is quite similar for both control systems. The sudden drop in governor setpoint $n_{set,gov}$ results in a reduction of fuelrack by the engine governor. This drop in fuelrack results in a drop of engine torque so that the engine speed n_{eng} starts to reduce. As shown in Fig 9.26, in case of the old PCS, the fuelrack starts to increase again with the same rate as the ship speed decrease, which is shown in Fig 9.29. Around $t = 380s$ the ship speed and thus the propeller torque and thrust (Fig 9.30 and 9.31) are approximately constant again.

After the initial drop of fuelrack, the PCS+ increases the propeller pitch for reasons of cavitation prevention as shown in Fig 9.25. However, the shaft speed is further reduced to ensure that the (ship speed related) virtual setpoint (the command) is still effectuated regardless of the pitch increase. As shown in Fig 9.21, the command is effectuated around $t = 335s$, from where on the pitch-shaft speed balance is slowly shifted towards higher shaft speed again.

Manoeuvring Behaviour

From the thrust figure (Fig 9.31) and the ship speed figure (Fig 9.29) it can be concluded that the resistance conditions for both manoeuvres were approximately equal. Although a non oscillating rudder angle would have been better, the small oscillations shown in Fig 9.22, are not expected to have a great effect on the manoeuvre.

When closely inspecting the thrust of the new PCS in Fig 9.31, it is clear that after the initial drop in thrust, the pitch increase increases the thrust towards low positive values. This is to be expected since the pitch is used to ensure a positive inflow angle. This should initially lead to a lower ship deceleration rate, but due to wave disturbances this cannot be confirmed by the ship speed signal of Fig 9.29. Due to the reduced shaft speed, after $t \approx 330s$ the thrust is lower than the thrust that was delivered by the old PCS. The latter helps to decelerate the ship speed faster, but again this is not confirmed by the ship speed signal.

To further inspect the effect of the two control systems on the deceleration behaviour, few extra simulation results are shown in Fig 9.37. The absence of disturbances, together with the possibility to simulate a system with both port as starboard side controlled by the PCS+, enables a fair comparison. Due to the pitch increase, the initial deceleration rate is slightly lower compared to the old PCS. The new PCS shows a small undershoot of $\approx$ 0.3 kts, after which the ship speed converges to the static value. If desired, the undershoot can of course be tailored by further tuning of coefficients of the PCS+.

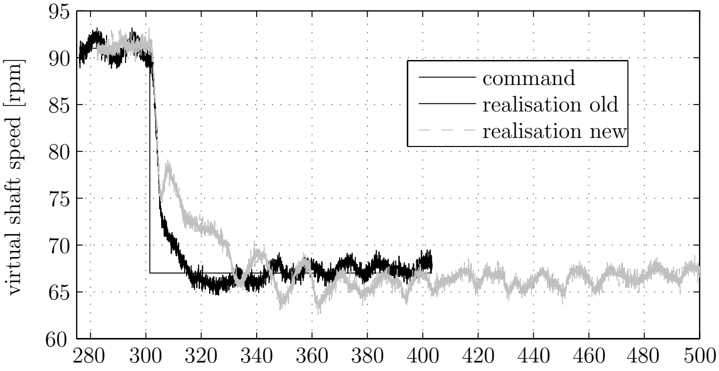

Figure 9.21: Command

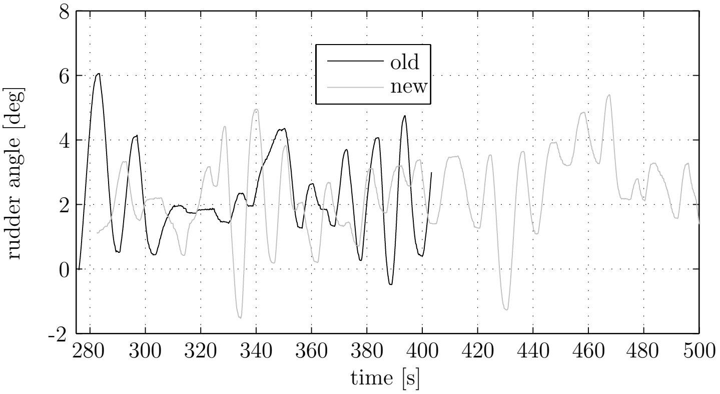

Figure 9.22: Rudder

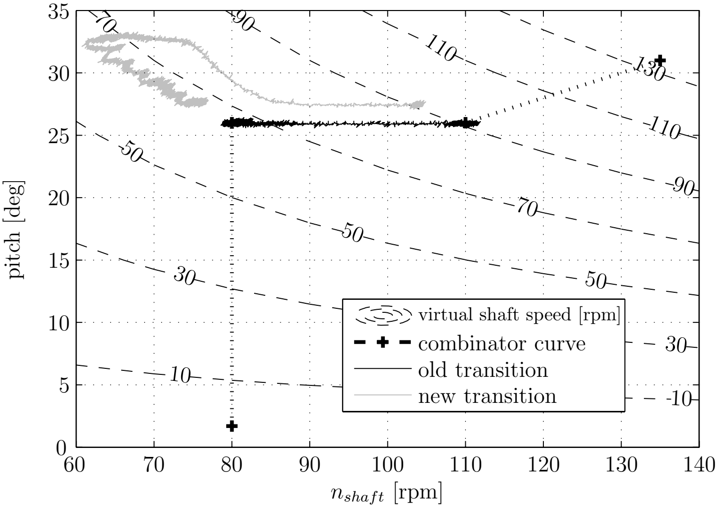

Figure 9.23: Transient in the $n - \theta$ plane

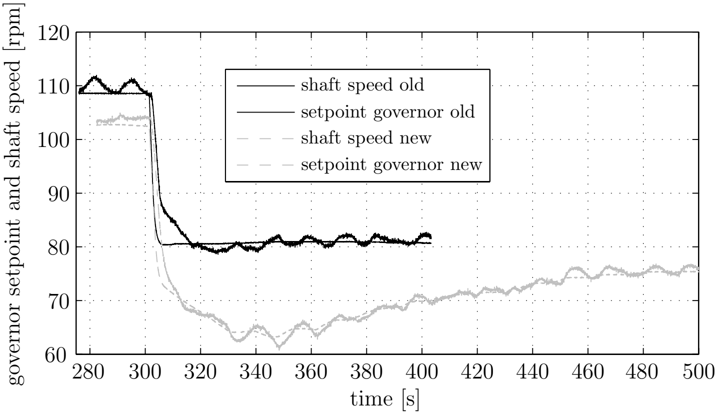

Figure 9.24: Governor setpoint and shaft speed

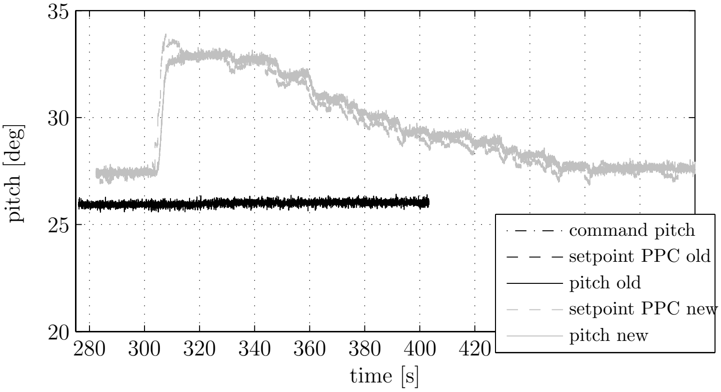

Figure 9.25: Low level pitch setpoint and pitch

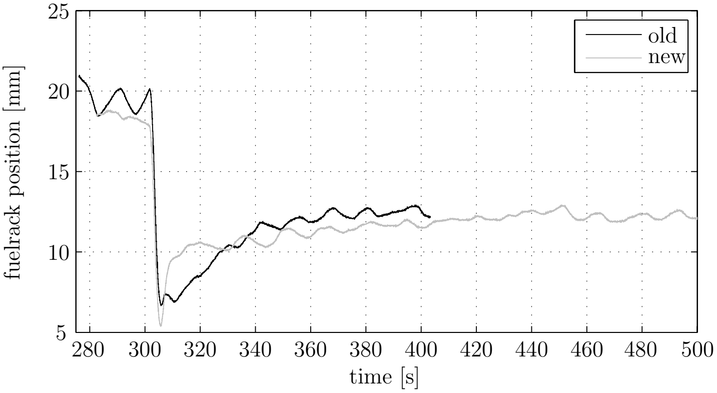

Figure 9.26: Fuelrack position

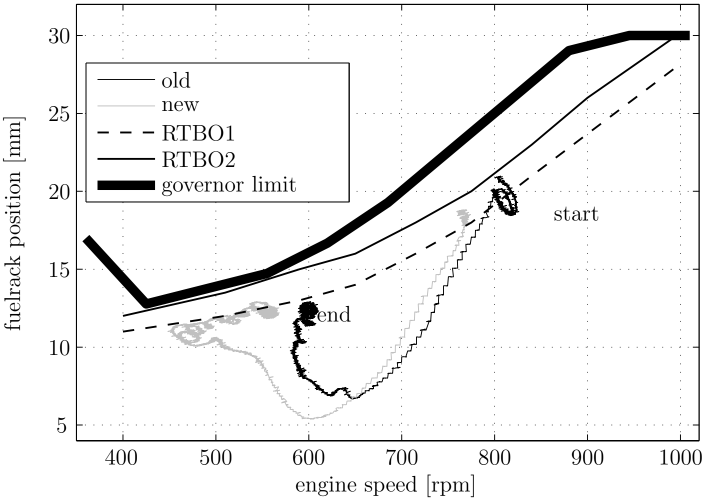

Figure 9.27: Engine diagram

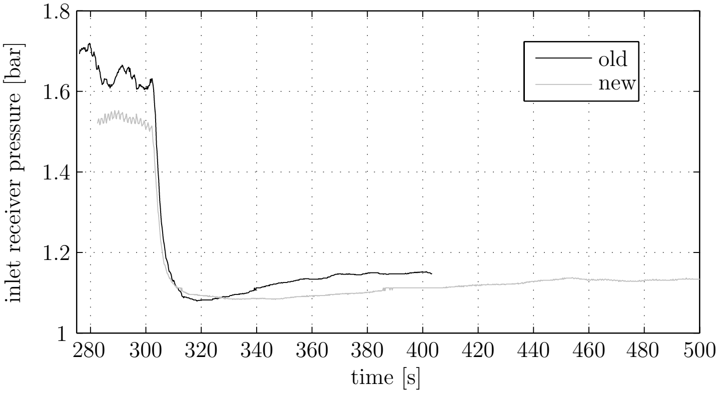

Figure 9.28: Inlet receiver pressure

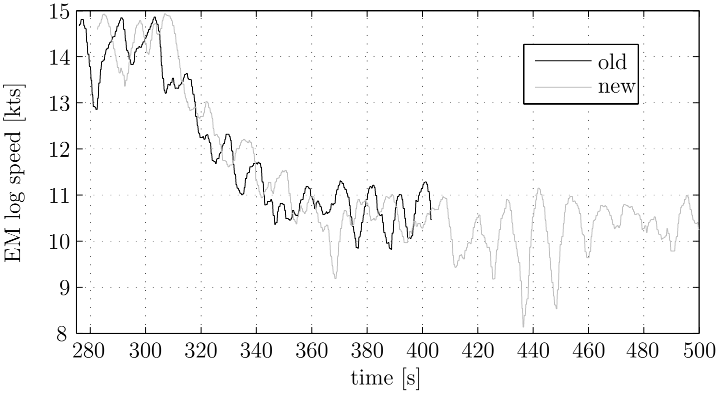

Figure 9.29: Ship speed

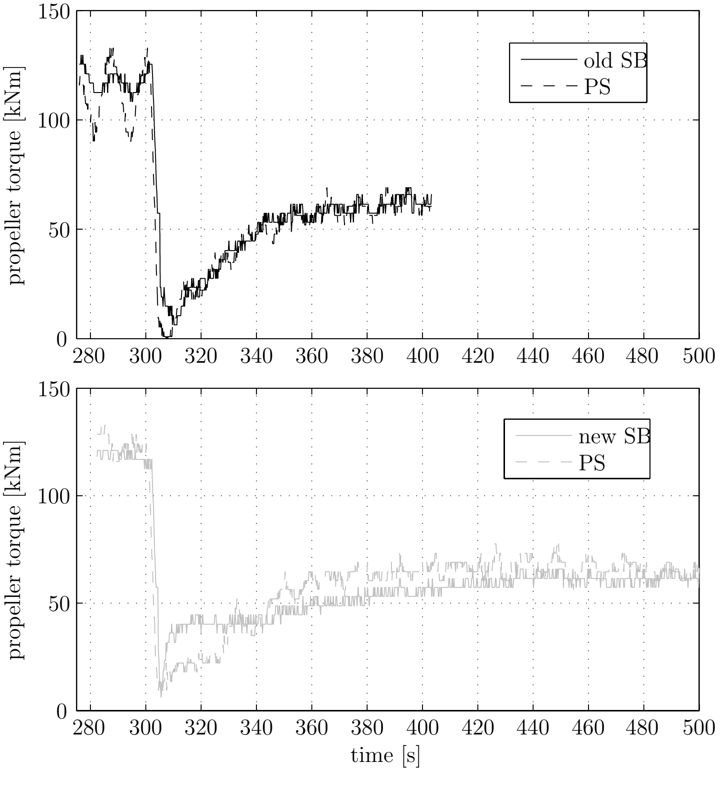

Figure 9.30: Propeller torque (port and starboard) for the old and the new PCS

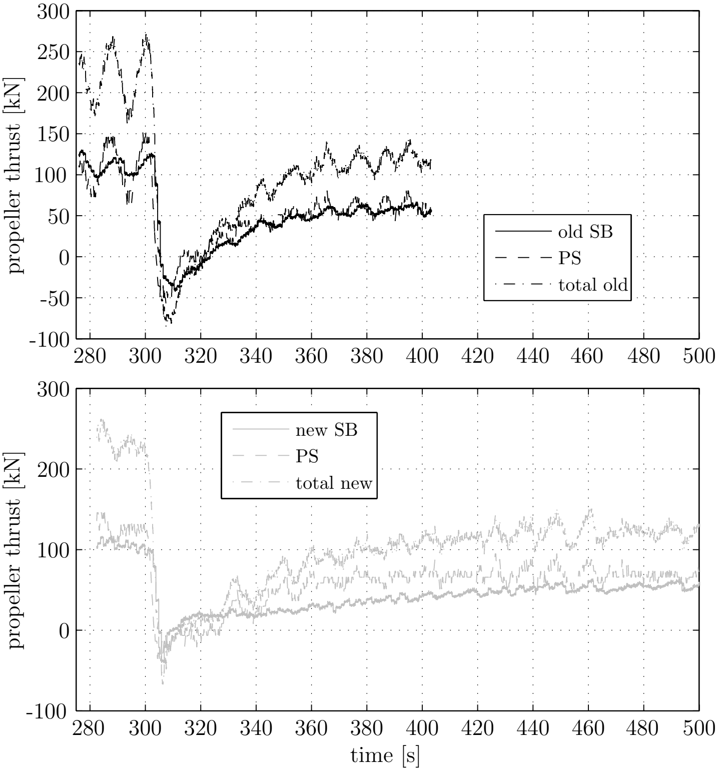

Figure 9.31: Propeller thrust for the old and the new PCS

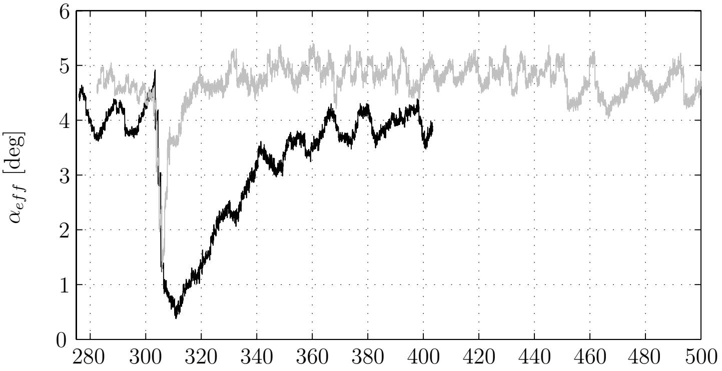

Figure 9.32: Estimated effective angle of attack

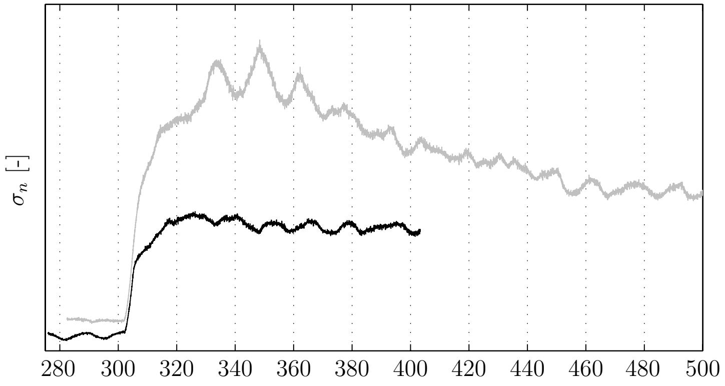

Figure 9.33: Cavitation number

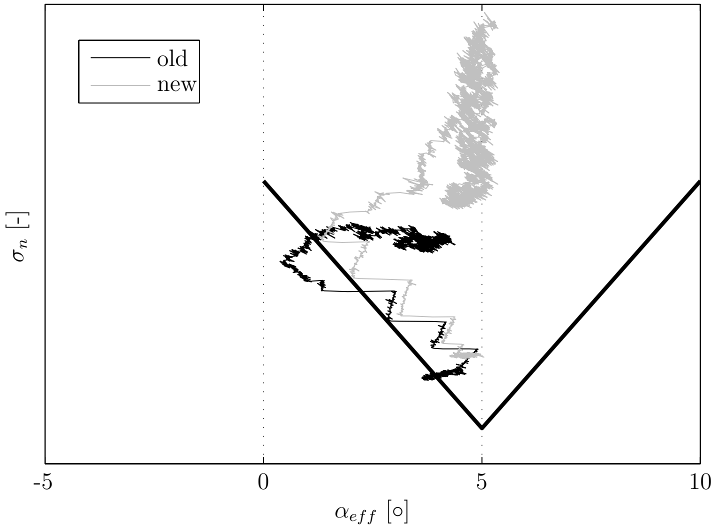

Figure 9.34: Behaviour in the α_{eff} bucket

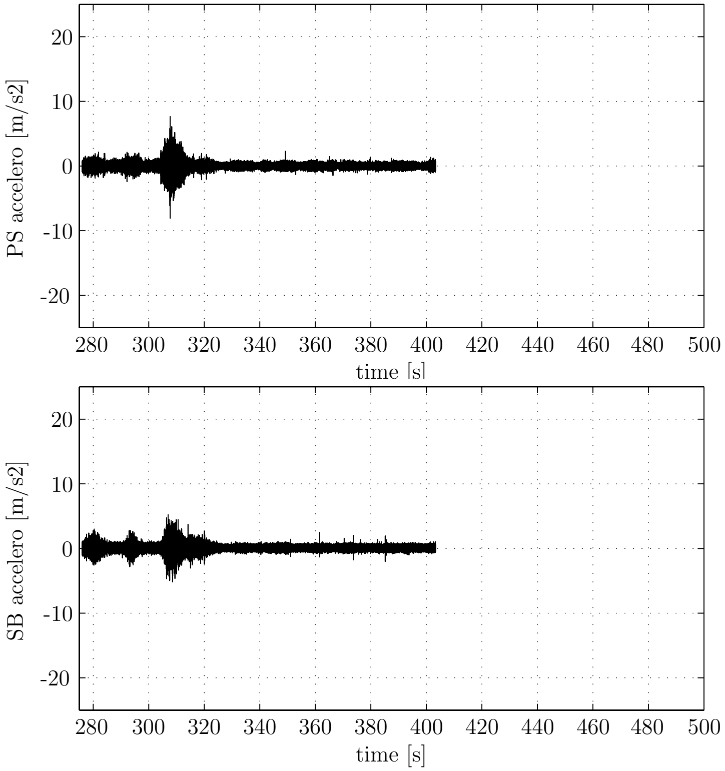

Figure 9.35: Acceleration sensor signals. Deceleration with the old PCS

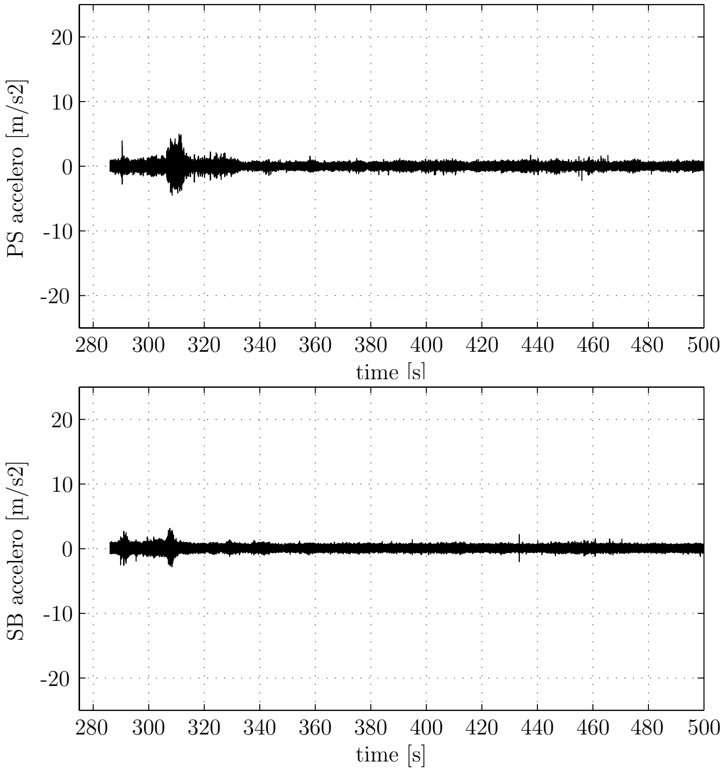

Figure 9.36: Acceleration sensor signals. Deceleration with the new PCS

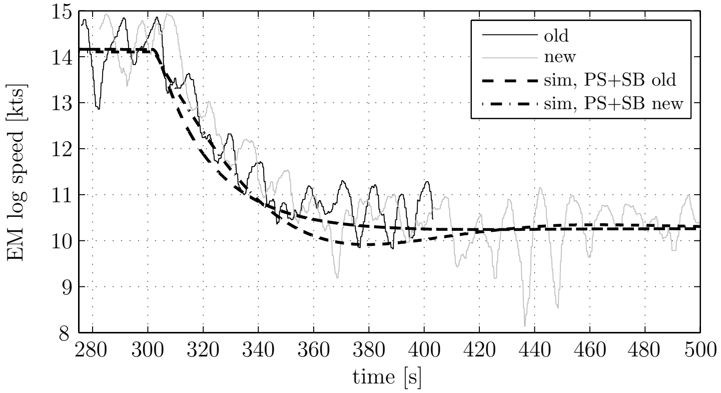

Figure 9.37: Ship speed measurement and simulation

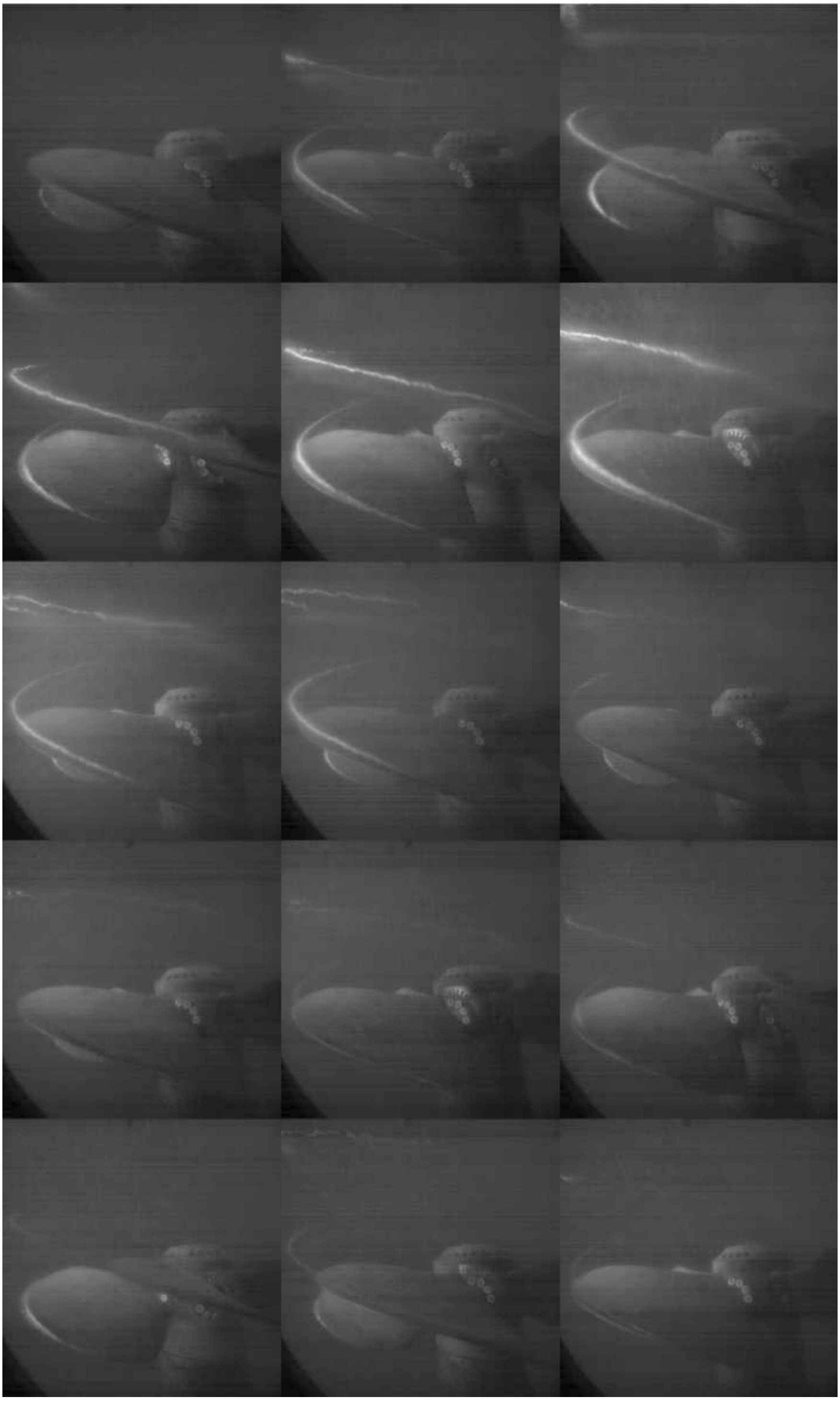

Figure 9.38: Cavitation behaviour of old PCS during deceleration, display interval 1s, start at $t = 305s$

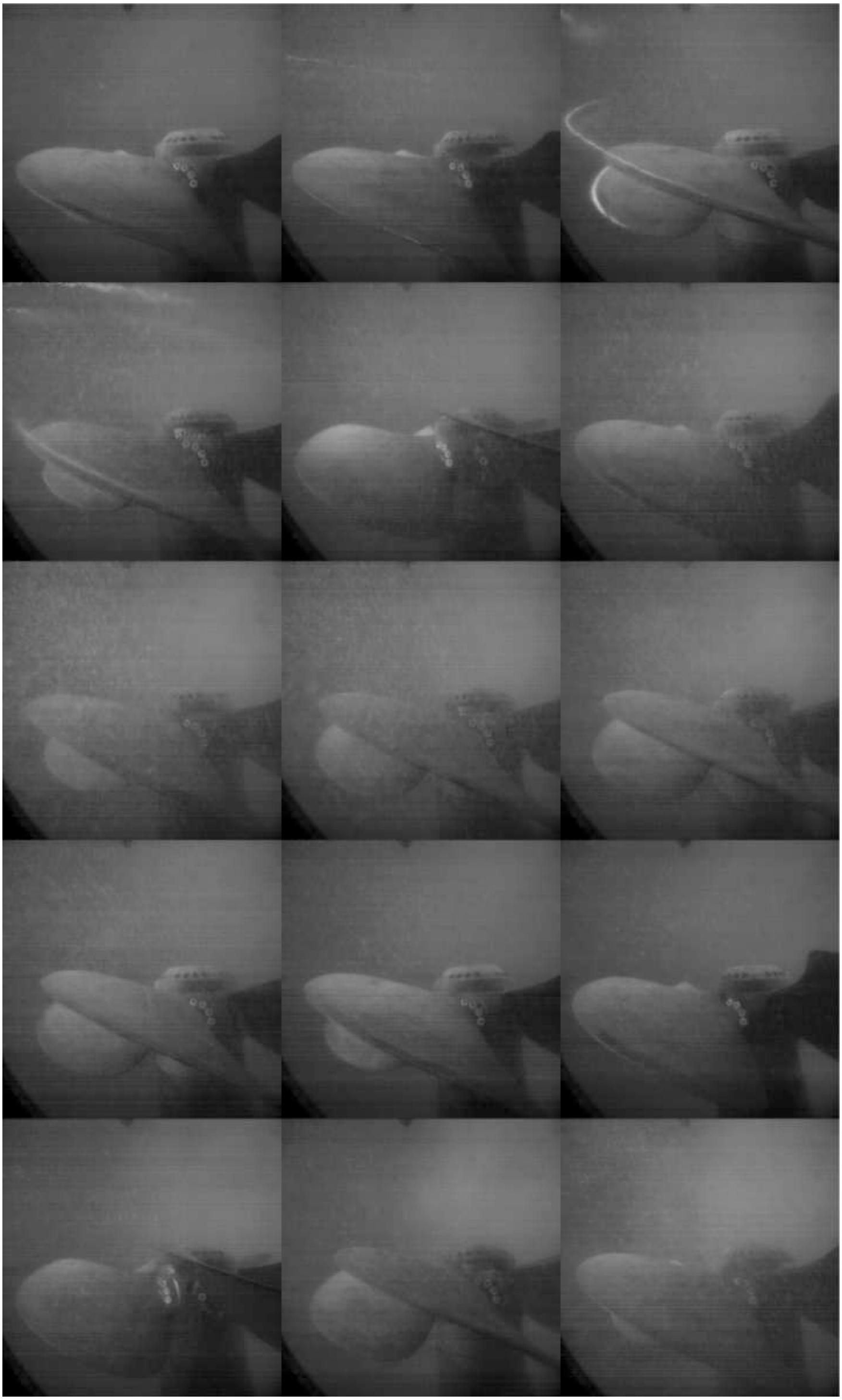

Figure 9.39: Cavitation behaviour of new PCS during deceleration, display interval 1s, start at $t = 305s$

operating point	A	B	C	D	E
port command	70	80	90	100	110
starboard command	95	95	95	95	95

Table 9.2: Commands used for the forced resistance test

9.4.4 The Forced Over-and Underloading Test

The forced resistance test was designed to investigate the effect of increased resistance on the propulsion system without having to wait for different kinds of weather conditions. Besides the effect on engine behaviour, the cavitation behaviour is considered by means of the α -bucket.

new PCS The starboard shaft is driven by the PCS+, while the portside shaft is driven by the old PCS. By fixing the starboard command and stepwise varying the port command, the starboard side can be under- or overloaded relatively easy. Extra advantage of this approach is that all other conditions remain approximately constant during the short duration of the test. The various command-combinations that where tested are listed in Table 9.2, where A indicates the highest load for the starboard shaft, and E indicates the lightest load.

The resulting operating points of both port and starboard side are presented in the $n-\theta$ plane in Fig 9.40. Asterisk-notation is used to indicate the starboard operating point. The starboard shaftline is to stay on the 95 virtual rpm contour, and more specific, in that operating point that has the desired angle of attack. Only the first and last starboard operating point (A* and E*) are annotated in the figure to prevent clutter.

The graph clearly shows that not all desired portside operating points as indicated by the combinator curve are reached: due to protection of the portside engine by the old PCS, the pitch of operating points D and E is limited, so that the command is not effectuated, resulting in a loss of performance (ship speed). This loss of performance is often observed onboard the M-frigate and is caused by the small margin of the combinator curve towards the RTBO-limit of the diesel engines.

On the starboard side, the new PCS does effectuate the command of 95 rpm in all conditions. In the heavy load condition indicated by A*, high shaft speed and low pitch is used, where in the relative low load condition E*, a low shaft speed with high pitch is used. Note that if the load on the starboard side would have been increased more, this side would also have shown performance degradation, simply because the maximum engine speed is the limiting factor then. Pitch increase would then help to improve performance, but this is conflicting with the cavitation-goal.

During the stepwise unloading of the starboard side, the balance between shaft speed and pitch is governed by the new controller that continuously attempts to keep the estimated effective angle of attack constant, while ensuring that the command is still effectuated.

Due to the mentioned protective pitch limiting measures of the portside PCS, strong unloading of the starboard propeller was not possible with the twin DE- configuration in automatically controlled mode. To test such conditions in the future it is recommended to drive the portside shaft with the gas turbine. Based on the observed trend in A*-B*-C*, the author however has no doubt that the starboard operating point at unloaded conditions would lie on the intended 95 rpm- contour, more towards the northwest.

The operating points of both port and starboard are shown in the engine diagram of Fig 9.41. The figure shows that the starboard shaft is not overloaded at any condition. Note that the continuous control of the angle of attack results in an operating point that is well positioned in the engine diagram, independent of the resistance conditions.

The behaviour in the cavitation bucket is shown in Fig 9.42. In this figure it can be seen that the lowest load (E*) has the best margin against cavitation, because it is positioned relatively high in the diagram. The setpoint for the angle of attack was 5 deg for operating point $A*$, but was set to 4.5 deg for operating points B*-E*. This was because earlier during the measurement it was found that 4.5 deg seemed to be the most optimal angle, although 5 degrees was expected and was set as a default. During the first run (A*), the operator (the author) forgot to change the default value to the new setpoint. The effect of this difference of 0.5 deg can also be seen in the engine diagram, where A* is located slightly higher than expected.

While judging the location of the operating point in the bucket it should be realized that this schematic bucket is only drawn for reference, and its inception lines are only indicative. As said before, in reality it seemed that the middle lay more towards 4.5 degrees.

Thanks to the correct angle of attack, engine overloading is highly unlikely if the matching of the propeller-gearbox-engine system is of reasonable quality. The adaptive pitch-shaft speed combination ensures that even at high resistance conditions, the operating point is positioned well inside the engine envelope. This has the advantage that, in low loading conditions, the operating point can lie quite close to the engine-limit, without running the risk of overloading at higher resistance conditions. In general running closer to the engine limit is advantageous from the viewpoint of fuel efficiency, as will be shown in Chapter 10.

old PCS: The same test was repeated with both shafts driven by the old PCS. Attempts to unload the starboard shaft failed since the portside PCS, at which a slightly higher setpoint was given, immediately ordered a pitch reduction on portside, resulting in loss of thrust and thus ship speed.

Attempts to overload the starboard propeller also failed because then, the starboard PCS ordered an active pitch reduction to protect the engine. This reveals that the old PCS is very effective in prevention of overloading. However, this does come at the cost of unnecessary performance degradation.

All in all it is concluded that the current installation has only little margin until the PCS orders pitch reduction. This is confirmed by the fact that loss of performance due to pitch reduction is often observed onboard the M-frigates, even in low seastates. As shown by the PCS+, such loss of performance is unnecessary, and can be prevented by application of condition dependent shaft speed-pitch combinations.

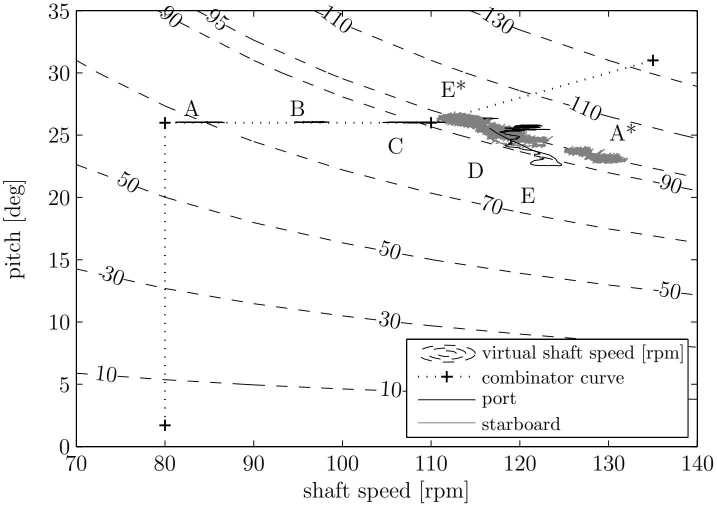

Figure 9.40: Forced Resistance Test: the $n - \theta$-plane. Note that A-E mark the portside operating point, and A-E* mark the starboard side. Annotations B*, C* and D* are not shown to prevent clutter, but lie between A* and E**

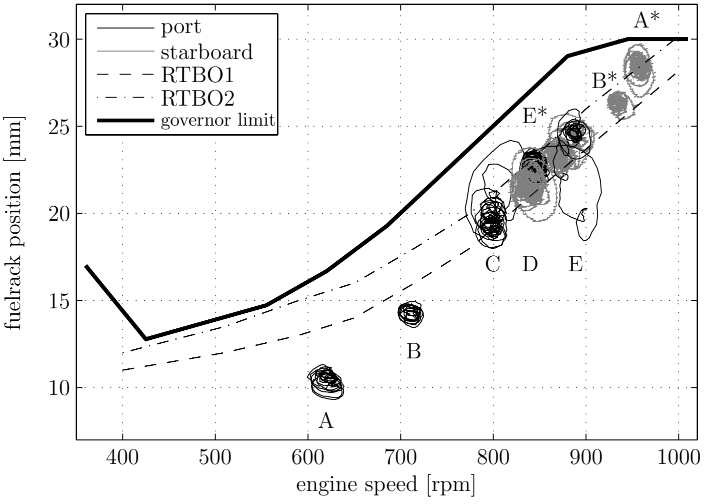

Figure 9.41: Forced Resistance Test: the engine diagram. Annotations C and D* are not shown to prevent clutter*

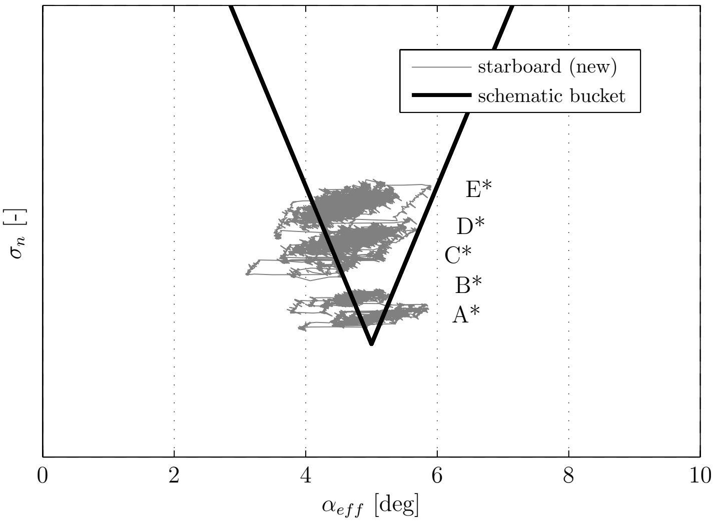

Figure 9.42: Forced Resistance Test: the cavitation bucket.

9.4.5 The Seaway Test

Various runs have been made to investigate the system behaviour in waves, sailing a straight course. Both the old PCS and the PCS+ are tested in head and stern waves, since both conditions have considerable differences in wave encounter frequency. To ensure that enough wave-encounter events were captured, the tests took approximately 20 minutes per run.

The PCS+ run against the waves is the most demanding test for the hydraulic pitch actuating system, and was therefore carried out last. Since the installed hydraulic system is not designed for making wave-frequent pitch adjustments, the PCS+ run against the waves was not successful nor illustrative. Therefore it is chosen to only deal with the stern-wave case here. Some important time traces are presented here, while others are presented in Appendix E for reference. The behaviour in the engine diagram, the shaft speed-pitch plane, and in the cavitation bucket are all presented since they show the most relevant differences between the two systems.

The command was set at 106 virtual rpm, as it was expected that this setting would lead to intermittent occurrence of propeller cavitation. This setpoint is shown in Fig 9.43. However, at this setting the old PCS already applied active pitch reduction, as shown by the actual virtual shaft speed (±104 rpm), and in Fig 9.45 showing the pitch angle. This figure also shows that even with the old PCS, the pitch also is used in a more or less dynamic way. This is because the operating point periodically crosses the RTBO2-line (Fig 9.48), which results in a fast pitch reduction to reduce the engine load.

Around $t = 2900s$ it seems that the pitch angle is reduced with 1 degree, while the shaft speed is increased with approximately 5 rpm in order to sustain the virtual setpoint of 106 rpm. This re-balancing might very well be caused by slow wave-drift forces due to wave groups, or by sudden increase in wind loading. Ultimately this continuous balancing results in a stretched operating area in the shaft speed-pitch diagram shown in Fig 9.46.

Propeller Behaviour

With regards to the propeller behaviour it is clear that the new PCS operates with lower pitch, and consequently with higher shaft speed. The variations in estimated α_{eff} are decreased as shown in Fig 9.50, but the effect on risk of inception is partly mitigated due to the mean increase in shaft speed as shown in Fig 9.51. It was observed earlier during the trials that an effective angle of attack of approximately 4.5 deg resulted in improved cavitation behaviour, so that this value was chosen as a setpoint $\alpha_{eff,set}$.

The horizontal extent of the operating ellipse in the bucket has decreased significantly, but due to the higher shaft speed also has less "room" inside the bucket. This however is an inescapable effect if the performance (virtual shaft speed) is to be effectuated. The other way around it could for instance also be chosen to limit the maximum allowed shaft speed to a specific value, resulting in a lower limit in the bucket. Such constraining measures have not been taken in this research, but might be considered in the future. In fact the old PCS does limit performance, however with the intention to reduce engine loading.

Further reduction of the horizontal extent of the operating ellipse is possible if the pitch would vary in such a way that the axial wave induced variations are completely compensated for. However, as demonstrated in Section 7.3.2, the wave induced tangential variation cannot be fully compensated for since they have opposite effect on the upward and the downward moving blade. Therefore, even if the operating point in the bucket could be reduced to 1 single dot, the cavitation behaviour in waves will still be worse than indicated by the bucket.

The acceleration sensor signals are shown in Figs 9.52 and 9.53. Note that not the complete time traces are shown, but only the first 600 seconds of both the old and the new run. This deviating time-base is because the time-synchronization with the other system variables failed because of a temporary lost synchronization signal between the aft ship and the aft-engine room. In this case this does not matter too much since the longer term trends are of greater importance than specific events.

Comparison of the port and the starboard signal of the old PCS in Fig 9.52 shows that in general the starboard signal shows slightly more peaked behaviour than the portside signal. The same is observed in the new PCS run as shown in Fig 9.53. This difference cannot be explained, since it is not clear whether it stems from cavitation differences between the port and the starboard propeller or from other sources such as the sensor itself, its connection to the hull or in the interface with the logging computer. Nevertheless, for each sensor a comparison between the old and new case can be made. Although a difference in peakedness for the starboard sensor is present, the difference is not convincing. However, when playing these signals as audio, a distinct "ticking" cavitation noise is observed at these peaks.

Based on these observations in it concluded that a small reduction in audible acoustic underwater signature is achieved. This conclusion is strengthened by the fact that at the same time there even is a slight increase in performance when driven by the new PCS.

Engine Behaviour

Fig 9.48, together with Fig 9.47, shows the decrease in fuelrack variations, combined with the more desirable orientation of the operating area in the engine diagram.

The vertical orientation of the operating ellipse of the old PCS is the result of the choice for a specific shaft speed-pitch combination that is (more or less) independent of the actual conditions. This fixed combination causes that wave loading induced shaft speed variations immediately are compensated for by the engine governor. In other words: the governor keeps the shaft speed at its desired value, at the cost of sometimes undesirably high fuelrack variations.

The new PCS attempt to keep the angle of attack constant, which directly damps the propeller torque variations, and thus the shaft speed variations. Therefore the propeller partly takes over the role of the governor, so that the necessary fuelrack variations decrease.

Manoeuvring Behaviour

The difference between the two control systems with regards to ship speed is the (unnecessary) loss of performance of the old PCS. Since in this case the mean pitch reduction is only small, the difference in ship speed as shown in Fig 9.49 is found to be 0.25 kts. This speed loss is approximately what can be expected for a loss of virtual shaft speed of 2 rpm (104 vs 106 virtual rpm).

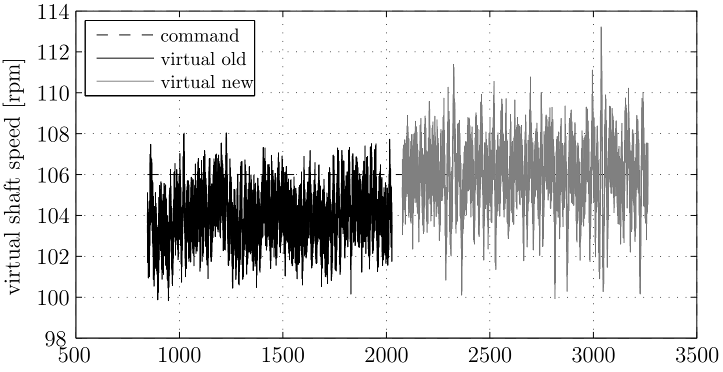

Figure 9.43: Command

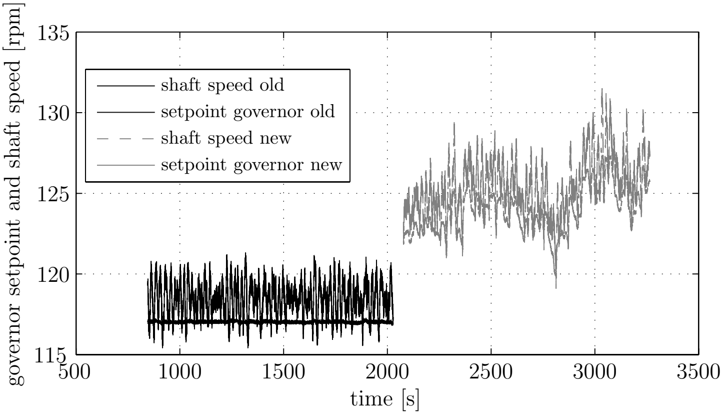

Figure 9.44: Governor setpoint and shaft speed

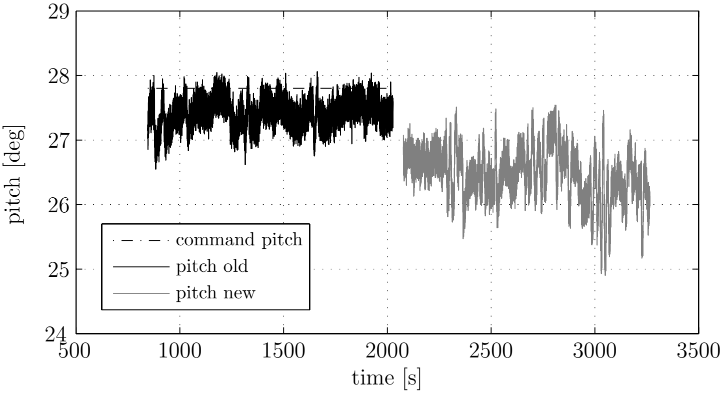

Figure 9.45: Low level pitch setpoint and pitch

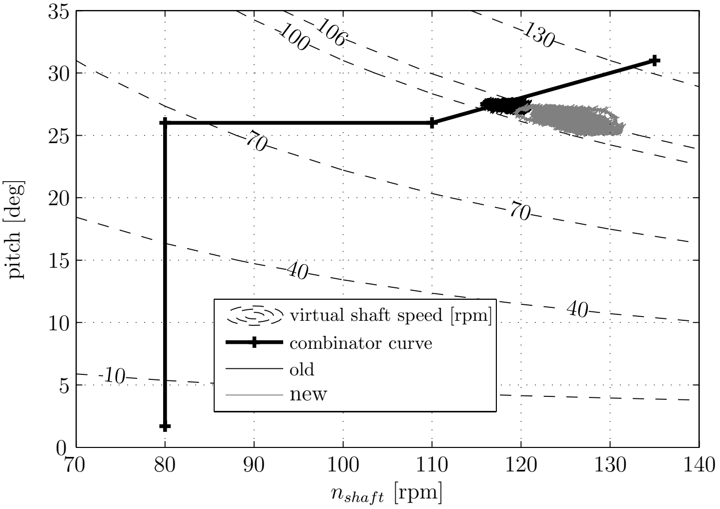

Figure 9.46: Operating ellipse the $n - \theta$ plane

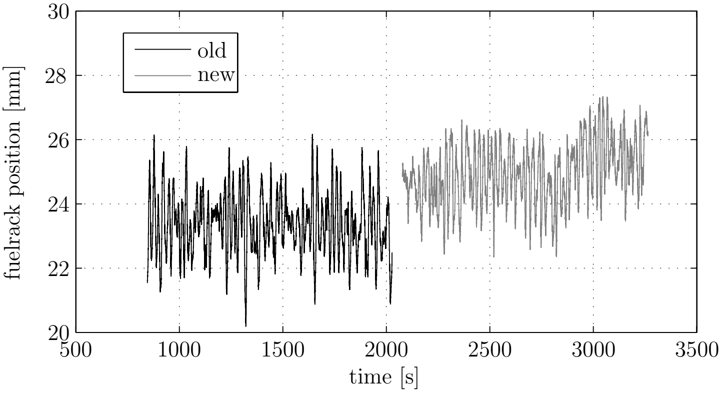

Figure 9.47: Fuelrack position

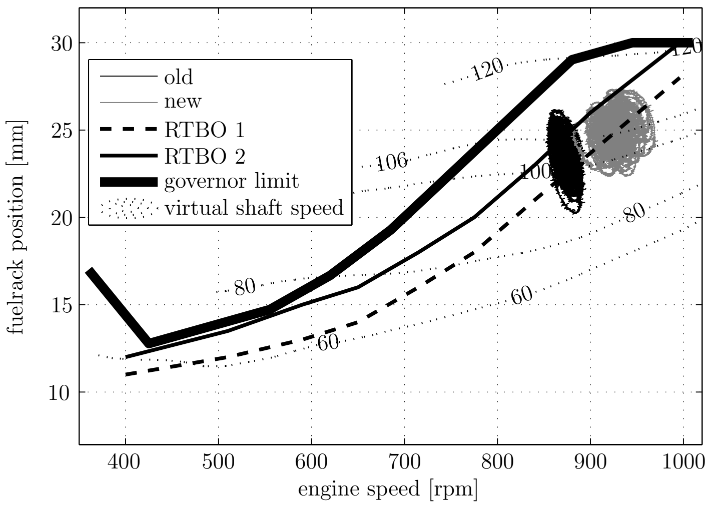

Figure 9.48: Engine diagram. Note that the virtual shaft speed contours are indicative, and are in fact condition dependent

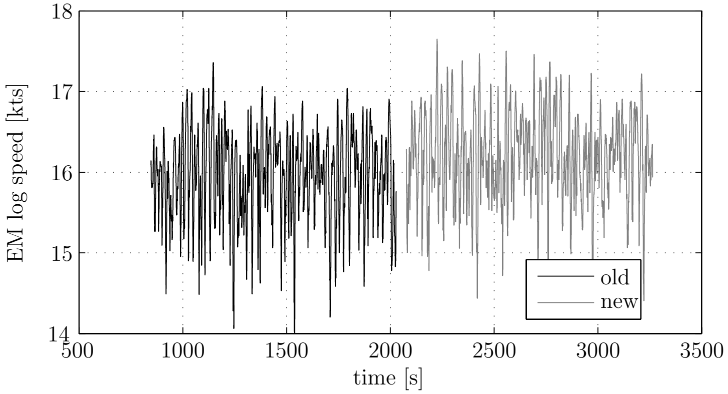

Figure 9.49: Ship speed

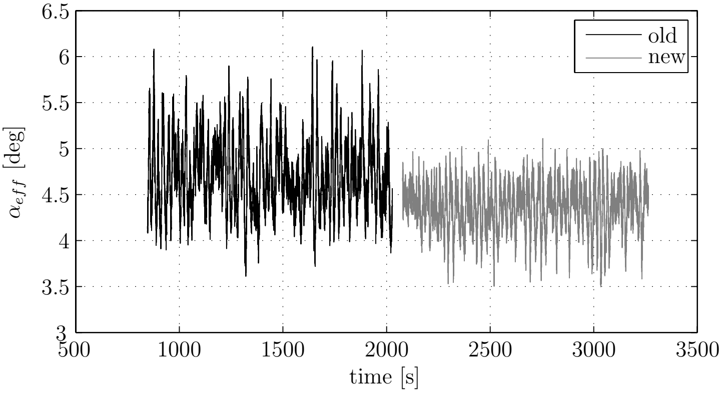

Figure 9.50: Estimated effective angle of attack

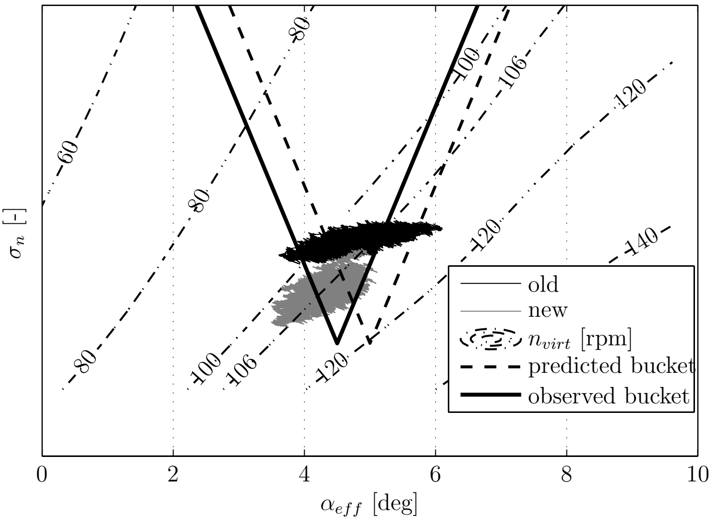

Figure 9.51: α bucket. Note that the virtual shaft speed contours are indicative, and are in fact condition dependent

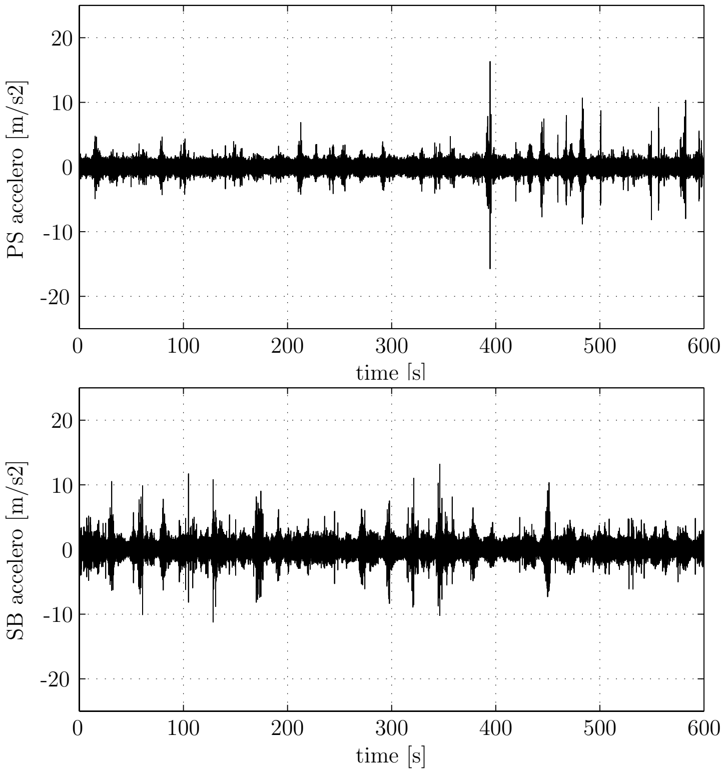

Figure 9.52: Acceleration sensor signals old PCS

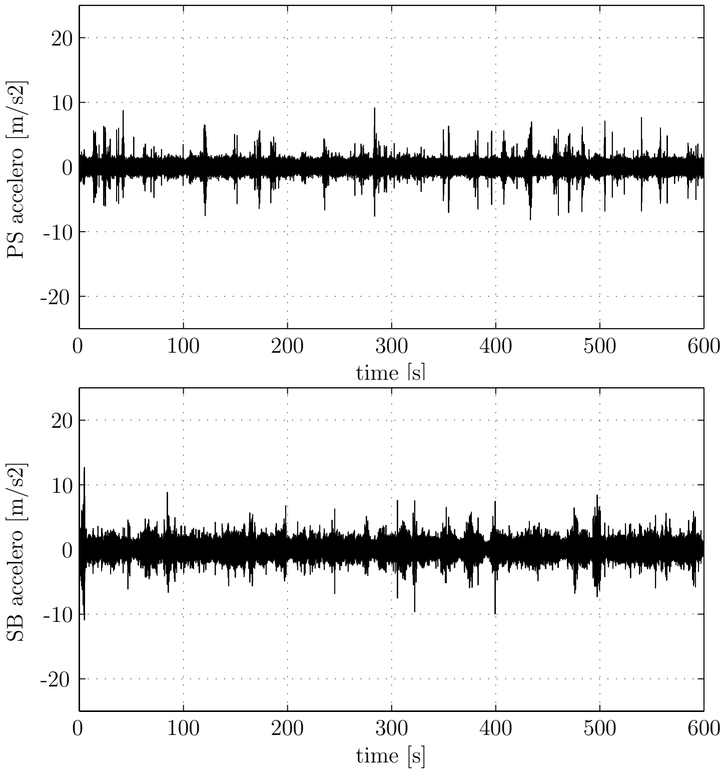

Figure 9.53: Acceleration sensor signals new PCS

9.4.6 The Turning Circle Test

Various runs have been made to investigate the system behaviour in turning circles. Both the old PCS and the PCS+ were tested at various speeds, mainly at a rudder angle of 10 degrees to port and to starboard. Only one of the turning circle manoeuvres is shown here, to demonstrate the principle behaviour of the PCS+ and the plant in a turning circle. The manoeuvre started in stern waves, and after a 360° turn ended with stern waves. Due to significant seastate (≥ 4) the manoeuvre induced behaviour was strongly disturbed by waves.

The virtual shaft speed setting for this run was 90 rpm (Fig 9.54), and 10 degrees port-side rudder was applied (Fig 9.55), meaning that the starboard propeller was the outside propeller.

Shaft speed and pitch behaviour are shown in Figs 9.56 and 9.57. The behaviour in the n-θ plane is shown in Fig 9.58. Engine related variables are shown in Fig 9.59 and Fig 9.60.

Due to the increased loading in the turning circle (due to increased resistance and change in wakefield shape), the old PCS applies ≈ 3 degrees of active pitch reduction, so that the mean operating point stays approximately on the RTBO1-line in the engine diagram. Although this is effective in reducing the risk of overloading the engine, it means a direct loss of propulsive performance, as shown by the actual virtual shaft speed (Fig 9.54), and by the drop in ship speed (Fig 9.63). The nett effect of pitch reduction and drop in ship speed on the propeller thrust is shown in Fig 9.61.

The PCS+ however attempts to find an operating point that effectuates both the command and the effective angle of attack at the same time. As mentioned before, due to the change in wakefield shape, the most optimal $\alpha_{eff,set}$ from the viewpoint of cavitation most probably shifts to another value. This effect was however not included in this PCS+ version, and the previously found value of $\alpha_{eff,set}$ of 4.5 degrees was kept during this manoeuvre as shown in Fig 9.66. Just as in the forced overloading test, the balance between shaft speed and pitch is found to lie more towards lower pitch and higher shaft speed with decreasing ship speed (Fig 9.58). Most likely due to wind and wave direction the ship speed picks up around 350s, resulting in lower engine loading, and thus a restoring operating point in terms of shaft speed and pitch.

Since the maximum allowed shaft speed was not limited during this manoeuvre, the PCS+ increases the shaft speed significantly in order to effectuate the command while the pitch is reduced. This means a decrease in σ_n as shown in Fig 9.64, resulting in a downward shift of the operating point in the bucket (Fig 9.66). This higher shaft speed is likely to result in deteriorated cavitation behaviour of the PCS+, although firm conclusions can only be drawn if the shift in bucket would be known, and would be taken into account. The behaviour of the PCS+ case in the engine diagram is acceptable, as the operating point shifts along the RTBO1-line during the manoeuvre, as shown in Fig 9.60.

It is concluded that with regard to propulsive performance the PCS+ behaves well, since it is able to effectuate the command during the complete manoeuvre, while the existing PCS shows degraded performance due to active pitch reduction. With regard to engine behaviour both systems performed well. In hindsight it seems that all turning circles were carried out at a too high ship speed, since cavitation was visible during great parts of the manoeuvre. This is even worsened by the seaway induced disturbances that were present during the runs.

Based on the performance in the cavitation bucket, it is concluded that it is likely that the increase in shaft speed, as ordered by the PCS+, has a negative influence on the cavitation behaviour. Additional measures to limit this shaft speed increase, and to incorporate knowledge of the true (middle of the) bucket in the controller, are expected to improve the cavitation behaviour in a turning circle. The effect of such measures may however result in performance degradation in terms of ship speed during a turning circle. Whether this is acceptable should be decided by the user.

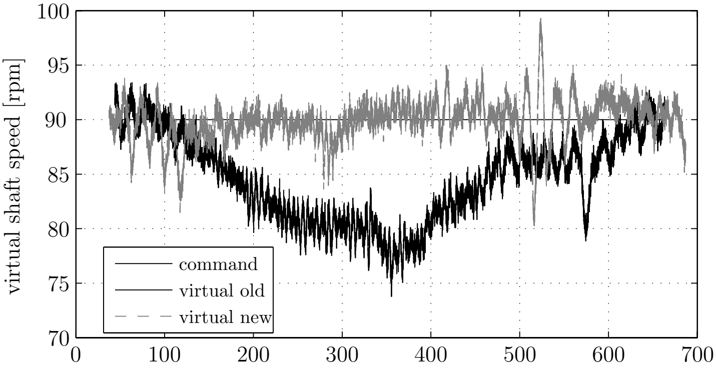

Figure 9.54: Command

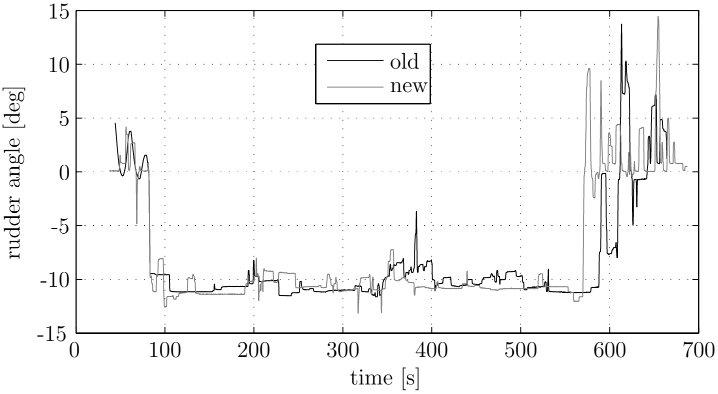

Figure 9.55: Rudder angle

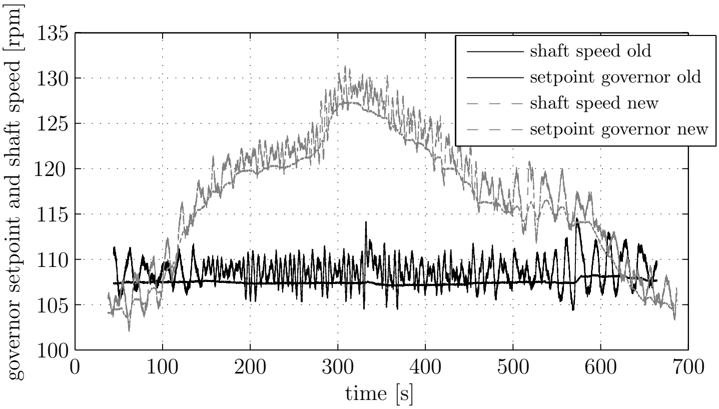

Figure 9.56: Shaft speed and governor setpoint

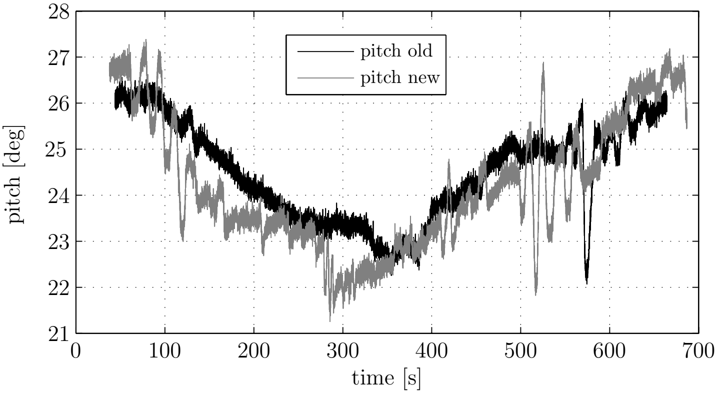

Figure 9.57: Pitch angle

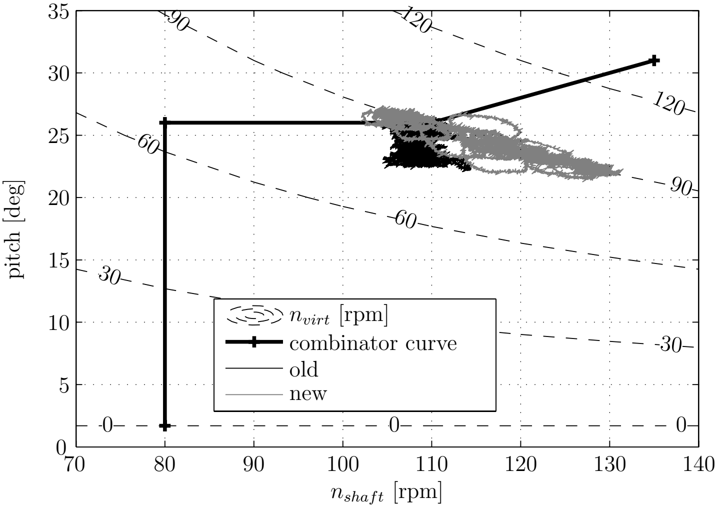

Figure 9.58: Behaviour in the $n - \theta$ plane

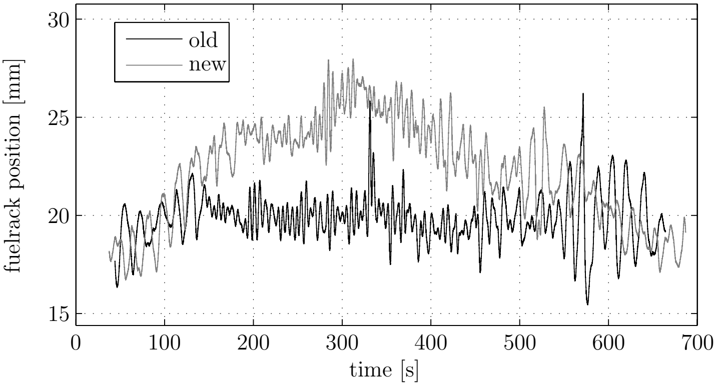

Figure 9.59: Fuelrack position

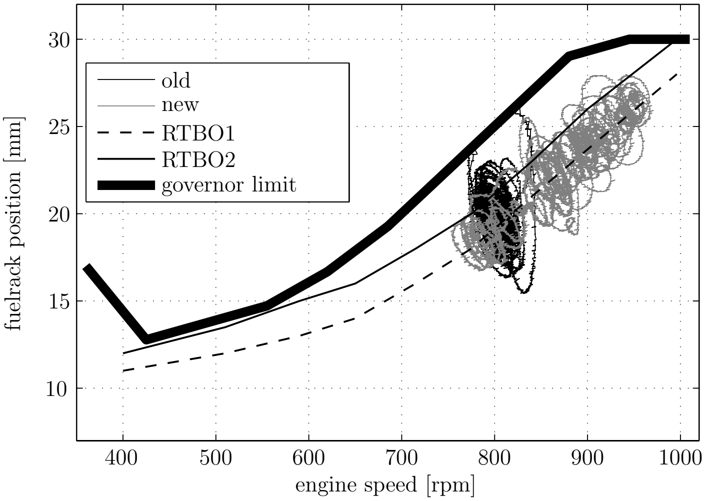

Figure 9.60: Behaviour in the engine diagram

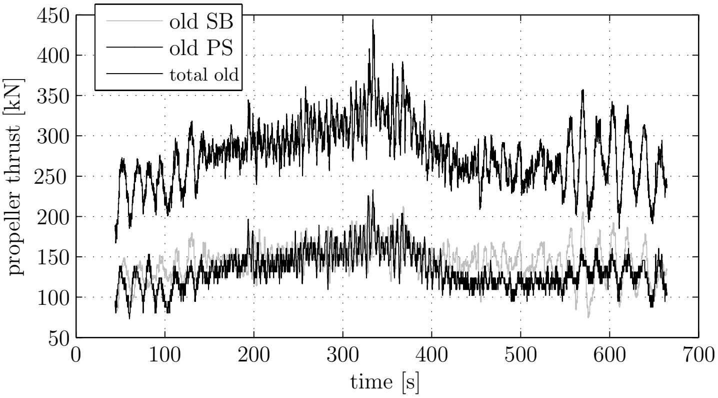

Figure 9.61: Thrust old PCS

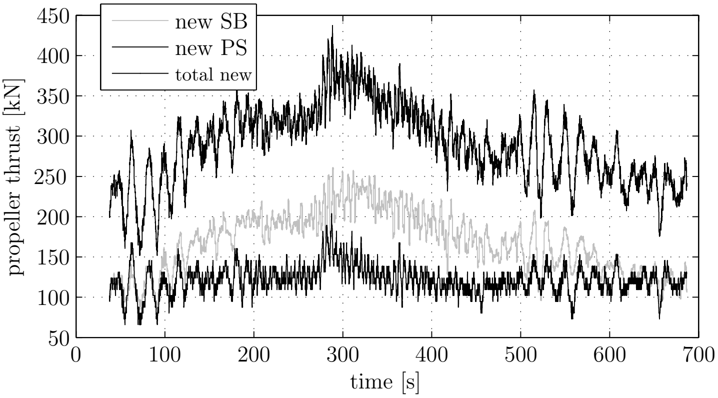

Figure 9.62: Thrust PCS+

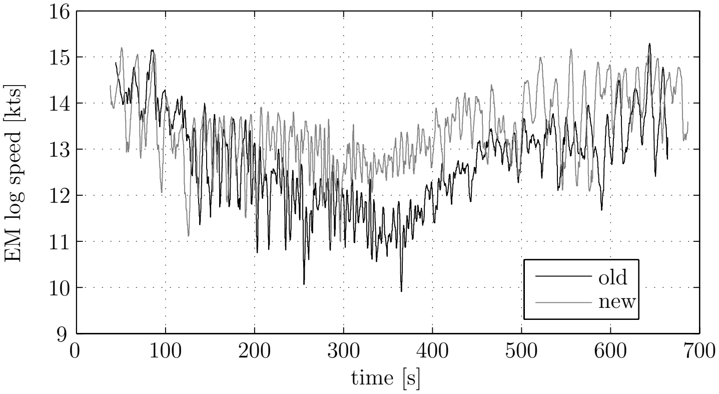

Figure 9.63: Ship speed

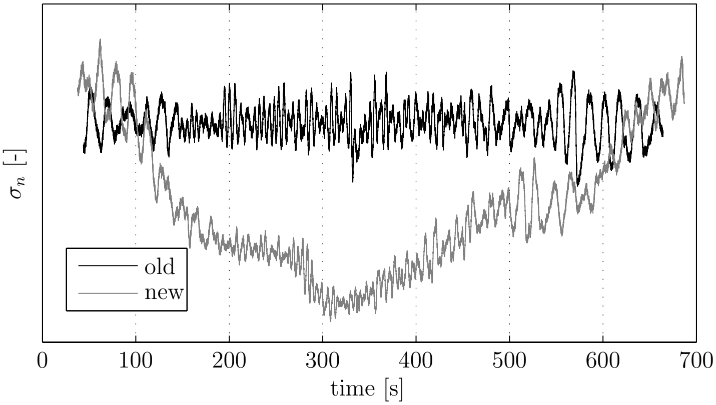

Figure 9.64: Cavitation number

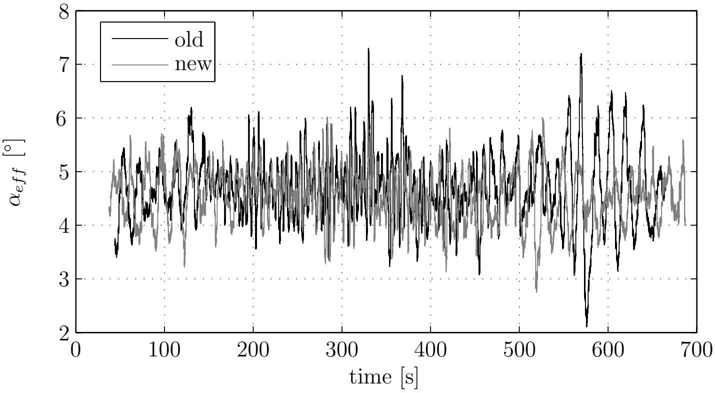

Figure 9.65: Effective angle of attack α_{eff}

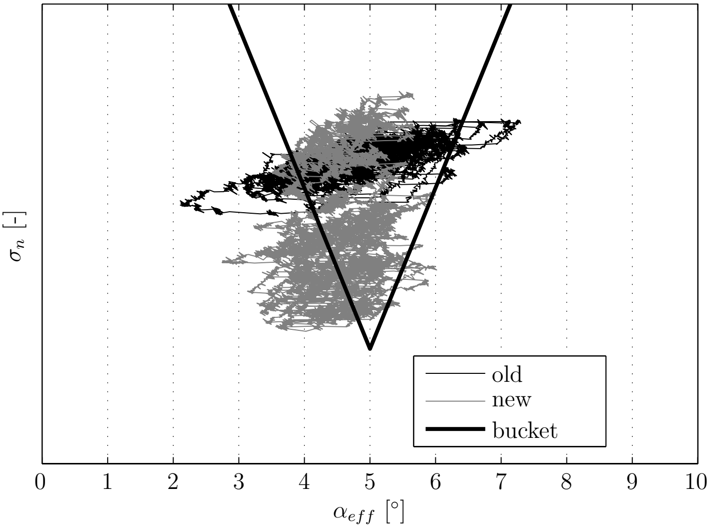

Figure 9.66: Behaviour in the cavitation bucket. Note that the schematic bucket is only indicative, as the real bucket in a turning circle can shift and change shape

9.5 Trial Conclusions and Recommendations

The main conclusions based on the presented results are listed in Table 9.3. The main improvement of cavitation free time was obtained during the acceleration and deceleration test. The forced overloading test showed that engine-overloading can be prevented without loss of propulsive power. The seaway test revealed a very small gain in cavitation behaviour, but further improvements are considered possible. It is therefore recommended to investigate the effect of the various components in the α_{eff}-feedback loop on the lag in the pitch actuation system. This involves lags that are related to measurement/ filtering, hydraulic hardware, and controller software. By removing or decreasing these lags where possible, it is expected that the α_{eff}-excursions can further be decreased, which should have a positive effect on the cavitation behaviour.

The quality of the turning circle measurements is strongly affected by seaway, and by a too high ship speed. This complicates the comparison of the two systems with regards to the cavitation behaviour. Based on the behaviour in the cavitation bucket it is however expected that the cavitation behaviour has deteriorated with the PCS+. The behaviour in the engine diagram remains acceptable with the PCS+, and a significant improvement in ship speed is found.

It is recommended to further investigate the possibility of increasing the cavitation free time in a turning circle manoeuvre. As the effect of wakefield changes on cavitation inception cannot fully be captured by the simplified α_{eff} approach, it is expected that a scheduled shift in $\alpha_{eff,set}$ during turning circles, based on additional input such as rudder angle, drift angle or rate of turn, is necessary. Note that such extensions still fall within the controller structure as was sketched in Fig 7.3, and simply indicate that more knowledge has to be put into the feedforward-database. Furthermore it is recommended to consider shaft speed limitation as to prevent cavitation during high shaft speed excursions. As was demonstrated by the parametric study in Section 7.6, this does however directly affect the system performance (ship speed).

Expected difficulties with above mentioned improvements mainly lie in the automatic recognition of a turning circle manoeuvre and its associated drift angle, and in the off-line prediction of the most desirable effective angle of attack during such manoeuvres. Possibly this off-line prediction can be replaced by means of continuous long term data gathering, aiming to reveal the optimal propeller operating points for a large variety of conditions. After processing, this data might then be used as input for the database. A limited example of this process is given in the α_{eff}-bucket test, which was shown in the beginning of this chapter.

test description	**cavitation behaviour**	**engine behaviour**	**manoeuvring behaviour**
accel/ decel	improved	higher engine load still acceptable	improved
forced loading	no comparison possible	improved	improved
stern waves	small improvement	improved	small improvement
turning circle	likely deteriorated	comparable	improved

Table 9.3: Summary of full scale trial results

Chapter 10

Alternative Use of the Ship Propulsion Simulation Model

10.1 Introduction

Up to here the focus of this thesis was on the increase of cavitation free time in operational conditions. The validated simulation model can however be used for many other studies. On the one hand other propulsion controllers aiming at various goals might be developed with the help of the simulation model. On the other hand, even without making modifications to the simulation model, the understanding of the system behaviour can be increased, especially due to the virtually unlimited amount of test-cases that can be run in a simulation environment.

This chapter gives some introductory examples of such applications. First of all some exploratory investigations on the optimum operating point when considering fuel efficiency are made. Secondly an improved thermal overloading criterion of a diesel engine is considered, since the currently applied overloading criterion is only valid for stationary operating conditions.

After these explorations it is shown how the simulation model can help to predict manoeuvring behaviour. This may help to reduce the testing time necessary for the construction or updating of the manoeuvring booklet. This booklet is of importance because it is used on board for the planning of ship manoeuvres during for instance Replenishment at Sea (RAS) operations or manoeuvring in confined waters. Furthermore simulations can give an idea of the manoeuvring characteristics of a ship, even before actual (parameter) changes are made to the PCS. Although manoeuvring predictions by means of simulation are nowadays common during the design phase of a ship, it is emphasized here that also after the commissioning, the use of simulation models can be of value.

Finally it is discussed how structured modeling, verification, calibration and validation can help to actively monitor the (naval) ship propulsion plant during the ship life cycle from the very design to the final decommissioning. By keeping a simulation model "alive" during the life cycle by for instance carrying out scheduled standard propulsion tests, possible performance degradation can be discovered timely, and can more easily be attributed to specific subsystems.

10.2 Fuel Efficiency

Due to increasing fuel prices as well as environmental issues there is a constant demand for more energy efficient propulsion systems. Therefore, marine engine manufacturers have to comply with increasingly strict norms on efficiency and exhaust gas quality. The total efficiency of the ship propulsion plant is however not solely dependent on the engine efficiency. Other contributors are for instance the transmission efficiency and the propeller efficiency. Only when all involved efficiencies are combined and considered as a whole, well founded statements about the total efficiency can be made.

In this section the total efficiency of the propulsion plant is determined by means of the developed simulation model. The trends of relevant variables are verified for many combinations of shaft speed and propeller pitch, just as was done for other system variables in Chapter 3. Validation is carried out where possible, but is fairly limited due to the absence of suitable measurements.

10.2.1 Efficiency Definitions

The total efficiency of a ship propulsion plant is the ratio between the heat input $\dot{Q}_f$ (fuel), and the effective power $P_e = R \cdot v_s$. The total efficiency is thus defined as:

$$\eta_t = \frac{P_e}{\dot{Q}_f}$$

To increase insight in the development of the total efficiency, the contributing efficiencies that are present in the propulsive train, need to be defined. A clear figure showing the various contributors to the total efficiency is found in Klein Woud and Stapersma (2002), and is shown in Fig 10.1. Starting at the fuel side, the effective engine efficiency η_e relates heat input $\dot{Q}_f$ to brake power P_b. The transmission efficiency η_{trm} relates the engine brake power P_b to in behind propeller power P_p. Finally the propulsive efficiency η_d comprises the losses from total in behind propeller power $k_p \cdot P_p$ to effective power P_e, where k_p is the number of operating propellers.

Further subdivision can be made with regards to the propulsive efficiency η_d, which comprises the hull efficiency η_h, the open water efficiency η_0, and the relative rotative efficiency η_r to correct open water propeller torque for the wakefield. The transmission efficiency η_{trm} can also be subdivided in a gearbox efficiency η_{gb} and shaft efficiency η_s, as is shown in the figure. Ultimately the total efficiency is given by $\eta_t = \eta_e \eta_{trm} \eta_d$.

A ship sailing in operational conditions is affected by wind and waves. Disturbances act on the wakefield and the resistance of the ship, resulting in oscillations and offset of the nominal calm water operating point of the propulsion plant. In the following no transient behaviour is considered, and only the offset of the disturbances is taken into account. In the next section the constituting efficiencies η_d, η_e as well as the resulting total efficiency η_t are presented in the $n - \theta$ plane. Since only few of the variables that are used in the definition of the various efficiencies have been verified and validated in Chapter 3 and 5, the quantitative output should be considered with care. Limited validation material of engine efficiencies is available from the following engine-test reports: SW Diesel B.V. (1987), SW Diesel B.V. (1990a) and SW Diesel B.V. (1990b). These reports are however around 20 years old, and the quality and conditions of the measurements are largely unknown.

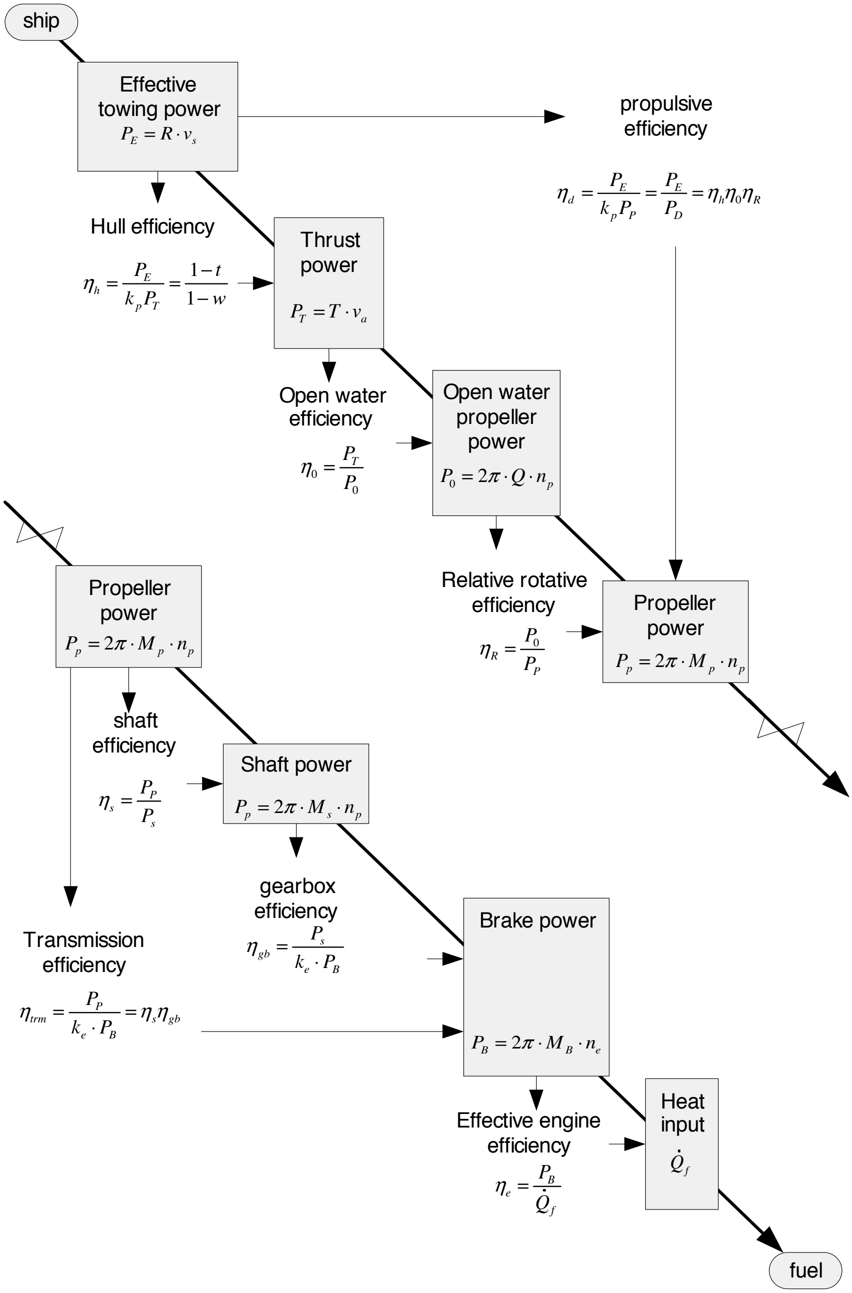
ship
Effective towing power
$P_E = R \cdot v_s$
propulsive efficiency
$\eta_d = \frac{P_E}{k_p P_P} = \frac{P_E}{P_D} = \eta_h \eta_0 \eta_R$
Hull efficiency
$\eta_h = \frac{P_E}{k_p P_T} = \frac{1-t}{1-w}$
Thrust power
$P_T = T \cdot v_a$
Open water efficiency
$\eta_0 = \frac{P_T}{P_0}$
Open water propeller power
$P_0 = 2\pi \cdot Q \cdot n_p$
Relative rotative efficiency
$\eta_R = \frac{P_0}{P_P}$
Propeller power
$P_p = 2\pi \cdot M_p \cdot n_p$
Propeller power
$P_p = 2\pi \cdot M_p \cdot n_p$
shaft efficiency
$\eta_s = \frac{P_P}{P_s}$
Shaft power
$P_p = 2\pi \cdot M_s \cdot n_p$
gearbox efficiency
$\eta_{gb} = \frac{P_s}{k_e \cdot P_B}$
Transmission efficiency
$\eta_{trm} = \frac{P_P}{k_e \cdot P_B} = \eta_s \eta_{gb}$
Brake power
$P_B = 2\pi \cdot M_B \cdot n_e$
Effective engine efficiency
$\eta_e = \frac{P_B}{\dot{Q}_f}$
Heat input
$\dot{Q}_f$
fuel

Figure 10.1: Efficiency train of a ship propulsion plant. Reproduced from: Klein Woud and Stapersma (2002)

Although the author does believe that the results show the correct trend, no firm conclusions should be drawn before a proper validation study has been conducted.

10.2.2 Verification and Validation of efficiency related variables

To examine the efficiency of the system in the various operating points, as well as the effect of high resistance conditions, the static contour plots of the propulsive efficiency η_d, the engine efficiency η_e, the specific fuel consumption SFC and the total efficiency η_t, are presented in the $n - \theta$ plane in Figs 10.2 to 10.5. To enable otherwise "prohibited" shaft speed- pitch combinations, the fuelrack limitation in the modeled engine governor was relaxed. For reference the fuel-characteristics that were used are listed in Table 10.1.

To study the effect of resistance change on the constituting efficiencies, the simulation results are presented both for seastate 0 and seastate 4. These results are presented side by side for comparison reasons. As shown in Fig 10.2, the engine efficiency η_e in general increases towards the northeast, with contour lines approximately parallel to the shown ship speed contours. This behaviour of η_e indicates that the engine efficiency does have influence on the overall efficiency, but its influence on the choice for one specific operating point in terms of shaft speed and pitch is limited.

The engine efficiency is often expressed as the Specific Fuel Consumption (SFC), which is defined as:

$$SFC = \frac{\dot{m}_f}{P_b} = \frac{1}{\eta_e \cdot H_0}$$

where H_0 is the lower calorific value in J/kg. The SFC is shown together with SFC measurements from various engine tests in Fig 10.3. This low quality validation shows that the trend in SFC is captured well, although at higher loading no validation is possible due to the limited domain of the lookup tables that are used to model the diesel engine. This lack of data should however be seen in perspective: in reality these high loadings are limited/ prohibited by the electronic engine governor.

The transmission efficiency is not shown since it only shows a constant value of 0.93, which is exactly the value that was put into the model in the calibration phase. Because the modeled gearbox is quite simple (it was not deemed necessary to improve its conceptual model for the main modeling goals of this research), the gearbox efficiency is not believed to give the correct trend. To make high confidence efficiency-predictions with the simulation model it is recommended to improve the conceptual gearbox model. Validation and calibration of this model is similarly important, and necessitates validation experiments that accurately capture the loss of power to the gearbox and shaft over a large range of operating points.

The propulsive efficiency as shown in Fig 10.4 is dominated by the open water efficiency, which increases with increasing pitch angle. It is shown that over the complete shaft speed range, the highest efficiency can be obtained with higher pitch angles. This fully agrees with the trend of efficiency curves in open water diagrams. It is however impossible to drive a high pitch propeller at very low shaft speed with a diesel engine, due to the shape of the engine's operating envelope.

The end result in terms of total efficiency η_t is shown in Fig 10.5. Overall the contours follow the propulsive efficiency (and thus openwater propeller efficiency), while for the lower

parameter	value	unit
H_0	42700	kJ/kg
ρ_{fuel}	850	kg/m^3

Table 10.1: Fuel properties

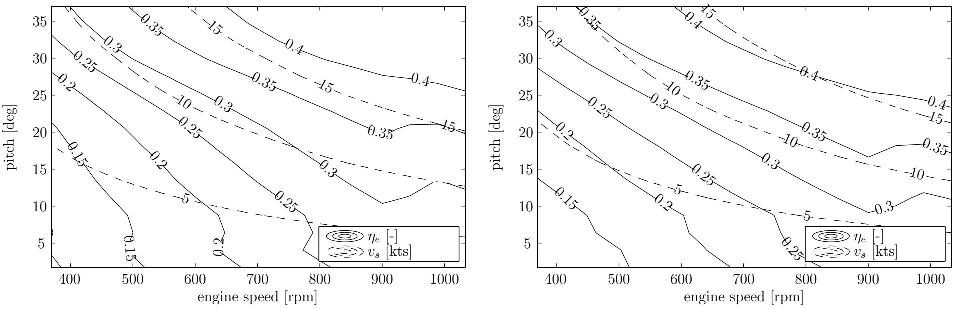

(a) Seastate 0

(b) Seastate 4

Figure 10.2: Engine efficiency η_e in ss 0 and ss 4.

engine speeds, the engine efficiency η_e causes a decrease of efficiency at equal pitch angle. Contours of ship speed are also shown, which reveals that from a viewpoint of efficiency, low shaft speed combined with high pitch is the best choice. A ship speed of 10 kts can for instance be obtained at all efficiencies between 0.06 and 0.23 (in calm water).

However, the chosen operating point also has to satisfy diesel engine loading criteria. These criteria are shown in Fig 10.6, where the engine governor limit is shown in the plane spanned by engine speed and fuelrack position. The figure for instance shows that, in seastate 4, a ship speed of 15 kts can be reached at various operating points with a range of total efficiencies from 21.5% at 1000 rpm to 28% on the governor limit. The currently applied combinator is designed with a certain margin to the governor limit, even in seastate 4. This margin is considered necessary to compensate for adverse operational conditions. However, at low loading in seastate 0, this leads to unnecessary loss of total efficiency. This unnecesary loss of efficiency could be prevented by making use of condition dependent shaft speed-pitch combinations.

Another aspect that is made clear by this figure, but which is not related to fuel efficiency, is the fact that the combinator runs outside the engine envelope at high loading. In practice this is compensated for by means of active pitch reduction (and thus loss of ship speed).

10.2.3 Conclusions and Recommendations

To improve insight in the total efficiency of ship propulsion plants, high quality full scale measurements aiming at validation of massflow of fuel $\dot{m}_f$ and the transmission efficiency η_{trm} are recommended. The measurements should preferably span a vast validation domain, so that high confidence conclusions can be drawn for a large range of possible operating points.

From the analysis that was carried out here, it is concluded that (for the M-frigate) it is most efficient to sail at highest possible pitch, combined with the (low) shaft speed that

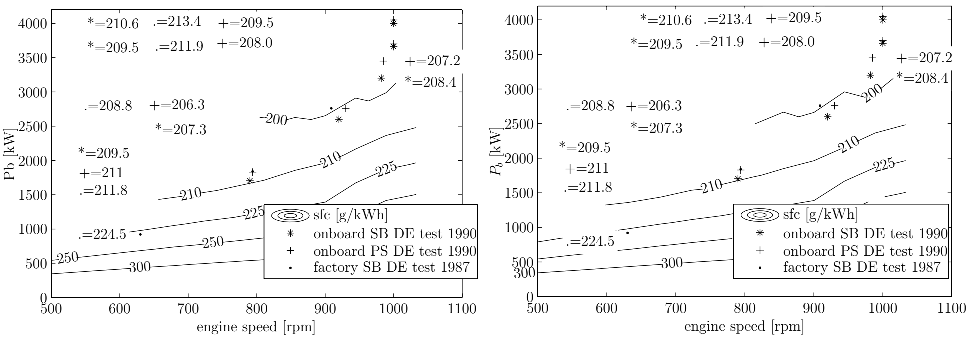

(a) Seastate 0

(b) Seastate 4

Figure 10.3: Validation of SFC in ss 0 and ss 4. To avoid clutter the validation points are only marked. Their respective values are shifted to the left hand side of the figures

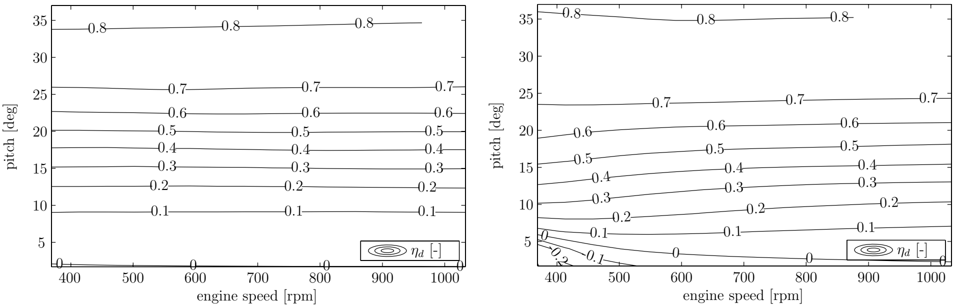

(a) Seastate 0

(b) Seastate 4

Figure 10.4: Propulsive efficiency η_d in ss 0 and ss 4

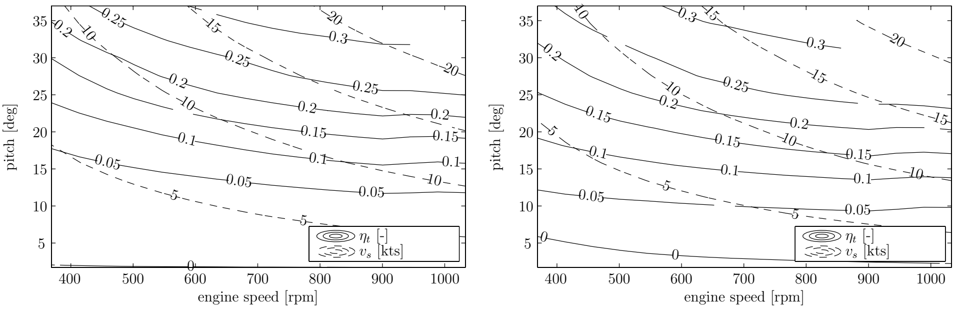

(a) Seastate 0

(b) Seastate 4

Figure 10.5: Total efficiency η_t in ss 0 and ss 4

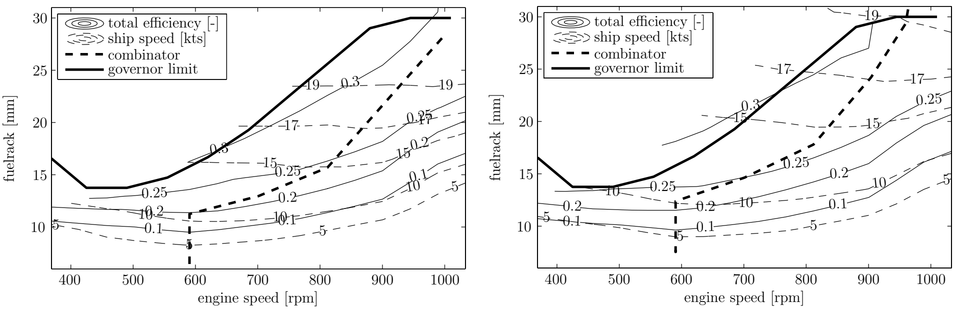

(a) Seastate 0

(b) Seastate 4

Figure 10.6: Total efficiency and ship speed contours in the engine diagram

is necessary to sustain the desired ship speed. This is however conflicting with the engine loading criteria, and a compromise needs to be found. The behaviour of total efficiency is largely dominated by openwater propeller efficiency and the engine efficiency. The trends of these two efficiencies are expected to be the same for most other diesel engine driven ships, so that similar conclusions are expected there. All in all, these conclusions are not new, and the only addition by this thesis is the structured representation of the various contributions to the total efficiency.

A fixed combinator curve often is designed with sufficient margin against overloading of the engine. This will ensure that during medium/high resistance conditions, the operating point will still lie inside the engine overloading limits. On the downside this results in unnecessary loss of total efficiency in low resistance conditions. Condition dependent combinations of shaft speed and pitch are therefore recommended if high efficiency is of importance. Such condition dependent combinator curves are not new, and were for instance already proposed by Morvillo (1996).

Based on the simulation results that are presented here, it is expected that the gain in efficiency can be up to 5% if the original combinator curve was chosen very conservative. It is noted that an adaptive combinator may require that, in light running conditions, it is necessary to exceed the nominal pitch angle, which might have its consequenses for CPP design.

A more fundamental understanding of engine overloading, and its associated indicators can help to determine the true engine limits instead of the static curves that are often used. An inventory of possible overloading indicators can be found in for instance Grimmelius and Stapersma (2000). Real time onboard measurement or estimation of such thermal overloading indicators can possibly be used as input to a propulsion control system that automatically decides on the most desirable operating point considering the compromise between efficiency and engine loading.

10.3 Thermal Overloading

Prolonged thermal overloading of the diesel engine can significantly reduce the time between necessary overhaul. Therefore its prevention should receive sufficient attention during the design and operation of a ship propulsion plant. From the viewpoint of overloading prevention it is desirable to choose as engine-gearbox-propeller-PCS combination with enough margin against overloading. This will ensure that disturbances in the nominal operating point due to for instance waves, wind and manoeuvres can be coped with without overloading the engine. On the other hand, as was shown in Fig 10.6, more margin means less total efficiency for a given installation.

Once a specific installation has been chosen, the main way of preventing thermal overloading is via the Propulsion Control System (PCS) and via the settings of the engine governor. Many settings in the PCS play a role, such as for instance the shape of the combinator curve, the pitch rate $\dot{\theta}_{set,PPC}$ and the governor-setpoint-rate $\dot{n}_{set,gov}$. To choose a right combination of engine-gearbox-propeller-PCS, it is important to have knowledge of engine overloading criteria.

The currently applied thermal overloading criterion of the diesel engines of the M-frigate is a static line in the engine diagram that was already shown in many of the presented engine diagrams (noted as governor limit). This line is programmed in the electronic governor, resulting in a maximum allowable fuelrack position that is dependent on actual engine speed. Many (electronic) governors have the possibility to limit the fuelrack rate not only on basis of fuelrack, but also on for instance inlet receiver pressure. Both aspects have an indirect relation with overloading, which makes it difficult to define limiting values for their respective limiters. As discussed by Grimmelius and Stapersma (2000) and Grimmelius and Stapersma (2001), a good understanding of the principles of thermal overloading might help to define more direct overloading criteria.

Schulten (2005) showed that, with his simulation model, it is possible to calculate an overloading-indicator based on various temperatures that occur during the combustion and scavenge cycle. However, the diesel engine model that is used in the current project does not deliver such temperatures. Nevertheless, another overloading indicator that is mentioned in Grimmelius and Stapersma (2000) can be estimated, based on available model output. This variable is known as the air excess ratio λ, and is introduced hereafter. The available mass of combustion air in the cylinder is proportional to the charge air pressure, and according to the gas law can be approximated by:

$$m_{ca} = \eta_{trap} \cdot \frac{p_{ir} \cdot V_s}{R_a \cdot T_{ir}}$$

where V_s is the swept volume of the cylinder, R_a is the gas constant of air and T_{ir} is the inlet receiver temperature. Note that the current simulation model gives the dynamic inlet receiver pressure p_{ir} as an output, which includes the effect of turbocharger inertia. η_{trap} is the trapped air efficiency and corrects for differences in pressure and temperature between inlet receiver and cylinder. It furthermore corrects for a small amount of unrefreshed residual gas that is left in the cylinder.

An increase in inlet receiver pressure logically results in more airmass available for combustion. The air excess factor λ is defined as the ratio between the available mass of combustion air m_{ca} and the air mass that is necessary for complete combustion of the fuel mass m_f. The required airmass is equal to the stoichiometric value of fuel σ times the fuel mass m_f so that:

$$\lambda = \frac{m_{ca}}{\sigma \cdot m_f}$$

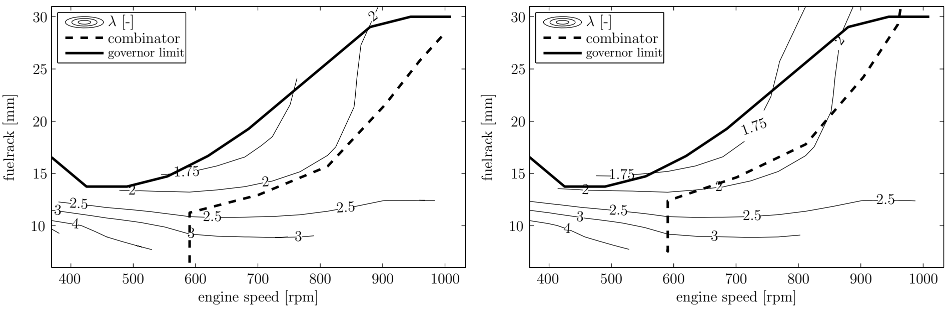

(a) Seastate 0

(b) Seastate 4

Figure 10.7: Static map of (estimated) air excess ratio λ in ss 0 and ss 4

Since the developed simulation model does not deliver the inlet receiver temperature T_{ir} which is necessary to calculate λ, no direct assessment of the air excess ratio is possible. It is however possible to estimate T_{ir}, and then inspect the qualitative behaviour of λ by means of contours in the n-θ plane, which should give some idea of the loading level at a specific operating point.

Based on expert opinion the following estimates are made: $\eta_{trap} = 0.9$ [-], $R_a = 287$ [kJ/kg], $T_{ir} = 323$ [K] and $\sigma = 14.5$ [-]. The assumption of constant temperature is based on (transient) measurements of the inlet receiver temperature, reported by Schulten (2005), page 103. With these assumptions it is possible to make static maps of λ, and to investigate its behaviour during transient operation. As an example the acceleration manoeuvre, as was reported on page 150 will be analyzed for its value of λ. This might reveal the loading difference between the old and the new PCS.

10.3.1 λ in Static Conditions

The static λ-map has been determined for both seastate 0 and seastate 4, and the results are presented in the engine diagram in Fig 10.7. These figures reveal that the static air excess ratio is particularly low in the middle engine speed region, which shows a local decrease of λ down to approximately 1.75. This is approximately the smoke limit, beyond which longer term operation should be prevented. Although in both seastates the combinator curve stays well away from the $\lambda = 1.75$ contour, the risk of smoke and overloading increases with increasing ship resistance, especially around this middle engine speed region.

However, as argued by Schulten, the air excess ratio in itself is not a sufficient indicator for thermal (over) loading. Absolute temperatures of engine components seem to be the reason for increased wear, so that these should also be incorporated in an engine overloading criterion. Contours of such temperatures are in general increasing towards the northeast, so that no strict conclusion with regards to overloading should be drawn from Fig 10.7. On the other hand it might be argued that the shape of the governor limit should at least follow the shape of λ in the middle engine speed region.

10.3.2 λ during Acceleration

Determination of the transient behaviour of λ during the full-scale acceleration test necessitates various assumptions. First of all the inlet receiver temperature T_{ir} has not been measured during the trials. This variable can however be estimated, since it stays approximately constant due to intercooler action as is illustrated by measurements carried out by Schulten. In the following the inlet receiver temperature is again assumed to be constant at $T_{ir} = 323$ [K].

Secondly the fuel massflow $\dot{m}_f$ has not been measured. The closest related variable that is measured is the fuelrack setting. By making use of the fuelpump model, and by assuming a specific ρ_{fuel}, the fuel massflow $\dot{m}_f$ can be derived, so that an estimate of λ can be made. Although no firm conclusions should be drawn based on the quantitative output, this analysis does allow for a comparison between various control strategies.

The estimated λ has been determined for the acceleration manoeuvre that was extensively discussed in Chapter 9.4.2. During that discussion the only means of assessing the engine loading was by looking at the position of the operating point in the engine diagram with respect to the governor limit, or possibly the Reduced Time Between Overhaul (RTBO)-lines. With the estimated air excess ratio this aspect can be studied in somewhat more detail. The results obtained for both propulsion control systems are shown in Fig 10.8. This figure shows that the air excess ratio of the old PCS initially drops due to lagging inlet receiver pressure compared to fuelrack (due to turbocharger inertia), but then increases again (due to the drop in pitch around $t = 543s$). Around $t = 550s$ the pitch is increased again, thereby increasing the load and the amount of injected fuel. This results in a quick drop of λ down to approximately 1.5. After this the air excess ratio stabilizes around 1.75.

The new controller initially experiences a steep drop in λ due to the increased fuelrack in combination with only slight pitch reduction for reasons of cavitation prevention. However, around $t = 560s$ the balance between injected fuel and available combustion air is restored, and due to the higher shaft speed even experiences a temporary maximum of $\lambda = 2$. Since the final operating points of both systems are approximately the same, the values of λ slowly converge to 1.75.

The question now is which system is preferred with regard to engine loading. To answer this question the overhaul-related consequences of temporary overloading should be known. However, the link between the loading profile and overhaul is far from fully understood.

10.3.3 Conclusions and Recommendation

The static air excess map revealed the "hollow" air excess ratio in the engine diagram (Fig 10.7). This hollow map should possibly be taken into account during the design of the combinator and during the determination of limiters in the engine governor. However, a true thermal (over)loading indicator based on other loading-related variables such as cylinder or valve temperatures may well show different contour lines. Such an indicator has been proposed in literature, but could not be determined with the relatively simple engine model that is used in this study.

With regards to the dynamic behaviour of λ in relation to wear, no firm conclusions can be drawn as long as the relation between loading profile and engine wear is not well understood. It is however expected that a strong increase of engine loading for a few seconds is less harmful than a prolonged operation with only slight overloading.

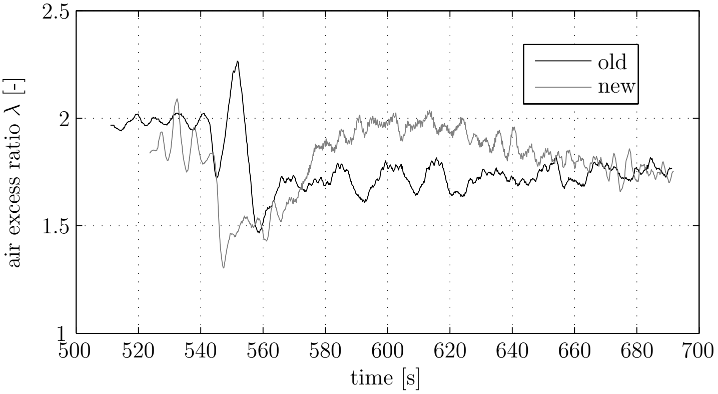

Figure 10.8: Air excess ratio λ during an acceleration. Estimation based on full scale measurements

10.4 Manoeuvring Behavior

IMO resolution A601(15) titled *"provision and display of manoeuvring information on board ships"* was accepted in 1987. It deals with presentation of manoeuvring information aboard ships, by means of:

- a Pilot Card, which should present the basic ship information on loading and steering/ propulsion machinery that is relevant to the pilot.
- a Wheelhouse Poster that is to be permanently displayed on the bridge. It should present general particulars and detailed information of the manoeuvring characteristics of the ship.
- a Manoeuvring Booklet that should contain comprehensive details of the ship manoeuvring characteristics. Most of the manoeuvring booklet can be estimated but some should be obtained from trials. This information may be supplemented during the ship's life. The IMO presents a list of recommended information that is to be included in the manoeuvring booklet. Acceleration and deceleration capabilities are of course part of this list.

For all three documents IMO indicates that the manoeuvring information should be updated after modifications are made to the ship, that have an effect on the manoeuvring characteristics. Clearly, modifications to the Propulsion Control System (PCS) are likely to have effect on the manoeuvring characteristics. Therefore, it is recommended here that after modifications of this system, it should be considered whether the manoeuvring information is still representative for the actual ship behaviour. If not, new information should be gathered and presented to the ship crew. However, the gathering of manoeuvring data by means of full scale trials is time consuming and expensive. To prevent this costly operation it is argued here that, by use of a validated ship propulsion simulation model, a big part of the necessary full scale trials can be substituted by simulations.

To demonstrate the possible use of such simulations, a small case study regarding the acceleration capabilities of the M-frigate is carried out here. During the lifetime of the M-frigate, mostly to prevent engine overloading, considerable modifications have been made to the PCS. In the following sections few PCS-versions are shortly reviewed. Furthermore some information from the (presumably outdated) manoeuvring booklet is presented. This information is based on full scale trials with an old PCS version as is reported in KM (1991). A comparison is made with recent measurements, which will reveal differences in manoeuvring behaviour. Finally, it is demonstrated how simulations can assist in updating the manoeuvring information.

10.4.1 PCS Modifications

As mentioned before, because of continuous problems with diesel engine overloading in the past, the PCS of the M-frigate has often been modified. Not only simple parameter changes have been made, but also big changes in controller philosophy and structure have been applied. Few relevant PCS-versions are selected and shortly discussed here:

PCS V4.0: indicates one of the first initial versions that was installed onboard. Operation with this PCS resulted in serious thermal overloading of the diesel engines and therefore was replaced by another version. (Brouwer et al. (1992)). This version is assumed to have been in operation onboard when the manoeuvring characteristics were collected. This assumption is supported by the good agreement between the manoeuvring booklet and simulations with this version, as will be shown. It could however not be confirmed with full certainty that this is the version (including parameters) that was installed when the manoeuvring trials were carried out.

PCS V6.3: indicates the version that was installed after various interim versions that superseded V4.0. This version is modeled in this thesis, where it is often indicated as the ”old” PCS. This version makes use of active pitch reduction, thereby seriously unloading the diesel engines when deemed necessary. Most recent parameter settings were obtained to model the actual onboard PCS in this thesis. A difference with V4.0 is that since then an electronic governor with engine speed dependent fuelrack limitation was installed. (Brouwer and Dupré (2004))

Version PCS+ is the temporary version that was developed in this research project to study the possibility of increasing the cavitation free time in operational conditions. It is not further considered in this section on manoeuvring prediction.

10.4.2 Application of Manoeuvring Predictions

The manoeuvring information that is dealt with here is limited to acceleration data. As said, the onboard available acceleration data still dates from the time that the ship propulsion plant was controlled by PCS V4.0. For the sake of this example the PCS V4.0 was programmed, and connected to the validated ship propulsion model. The acceleration manoeuvre that is listed in the manoeuvring booklet is simulated, and the results are compared in Fig 10.9. This in fact is a qualitative validation, and indicates the validity of the model. Although there are differences between the two it is concluded that the model gives predictions with sufficient accuracy for the intended use. Note that both the governor settings and the resistance factors α_R and R_0 (see Section 2.4.3) were changed to match conditions as were present during the full scale trials.

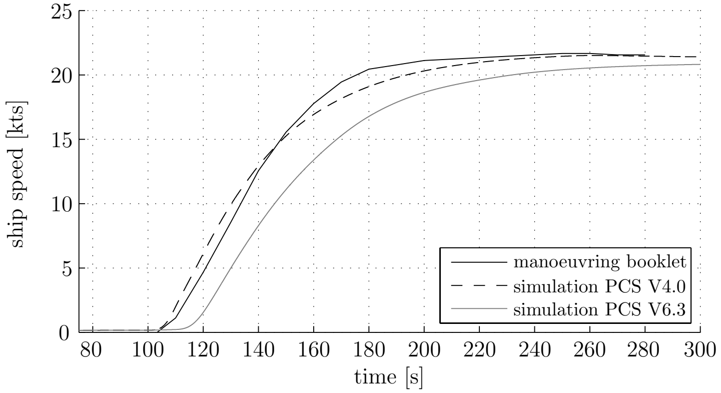

Figure 10.9: Comparison of calm water acceleration curve. Virtual setpoint 0-135 rpm at $t = 100s$

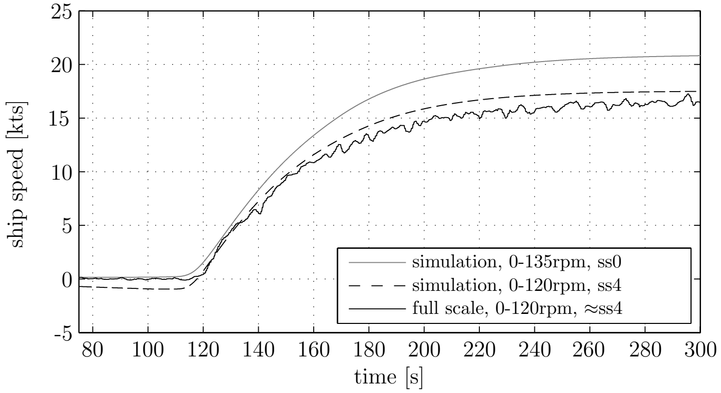

Figure 10.10: Comparison of predicted and measured acceleration capabilities of PCS V6.3. For reference the simulated full acceleration (0-135 rpm, V6.3) in calm water is also shown. The command is given at $t = 100s$.

To demonstrate the relevance of keeping the manoeuvring information up-to-date, Fig 10.9 also shows the predicted acceleration behaviour of the ship driven by PCS V6.3, sailing in the same conditions. The difference in acceleration time is significant, showing a deteriorated acceleration behaviour, as might be expected due to the engine-protective measures that are taken by the PCS. The most striking difference is the 10-second interval between command and actual acceleration, which is caused by the delay in pitch increase, while the shaft speed is accelerating.

Disregarding the possible negative effects of the reduced acceleration capabilities, it is at least important that the ship crew is provided with the updated manoeuvring information. By means of further simulation with PCS V6.3 the data as shown in Fig 10.10 is obtained. A check of the validity is made by using limited acceleration data as was measured in recent trials. Since this recent data was obtained in a considerable seastate, it shows a somewhat pessimistic behaviour. However, taking into account the uncertainties in conditions and measurements, the presented results give a good idea of the actual acceleration capabilities of the (diesel driven) M-frigate.

10.4.3 Conclusions and Recommendation

It is concluded that partial substitution of full scale manoeuvring trials by simulations is sufficiently reliable and can help to decrease testing time and costs. More importantly the ship crew can be provided with valid manoeuvring data earlier in time, thereby improving safety at sea. The demonstrated predictions can help to compare manoeuvring characteristics of various PCS versions that are under development, and can indicate strong/weak points at an early stage. An example of a manoeuvring related weak point that was uncovered by the simulation model that was developed in this thesis, is the unsuitability of the PCS V6.3 for Replenishment at Sea (RAS) operations alongside a tanker: a commanded acceleration to stay alongside a tanker can easily result in loss of thrust due to active pitch reduction, which is not considered safe during such operations.

Improvement of the conceptual manoeuvring model might be able to increase the prediction capabilities towards turning circles or zig-zag manoeuvres. Obviously such a manoeuvring model should be thoroughly validated before it can rightfully be used to substitute actual full scale trials.

The other way around it should also be realized that stand-alone ship manoeuvring simulation models should include a representative propulsion plant and PCS to make high quality predictions of dynamic system behaviour (such as accelerations).

10.5 Life Cycle Applications

The design of the propulsion plant of a new-to-build ship starts with conceptual studies, comparing different propulsion concepts from the viewpoint of performance, purchase costs and life-time maintenance and operation costs. By comparing the various concepts against each other and against the required capabilities of the ship, the concepts are narrowed down to one or two options that are considered most suited.

The comparisons are often made based on global data obtained from comparable ships, and comparable propulsion components. The further the design process proceeds, the more data becomes available, and the more detailed and accurate the performance predictions can be. In the selection and matching phase of the various components such as engine, gearbox and propeller or waterjet, it is often chosen to make use of time domain simulation models of certain degree of complexity. These models are for instance used to identify possible problems in the design, to study the effect of off-design conditions on the installation, and to design the increasingly complex Propulsion Control System (PCS).

As was repeatedly emphasized in this thesis, the merit of a simulation model can only be assessed if it is properly validated at the necessary quality level. However, it is not possible to calibrate and validate a simulation model of a (first of class) ship that is not built in reality yet! In this section a structured approach to the modeling during the design, construction, acceptance tests, maintenance and operation is proposed. By keeping the model alive during these phases, it is readily available whenever necessary, and up to date with the latest modifications. The biggest modeling effort is only necessary once, after which only small model-maintenance is necessary. The costs related to development and maintenance of the model are expected only small when compared to possible costs of reduced time between overhaul because of overloading (Section 10.3), and cost savings due to decreased need for full scale testing time (Section 10.4).

10.5.1 Design Phase

In the design phase, at some point the propulsion concept is narrowed down to one or more feasible options. To make well founded decisions, there is a need to compare performance of possible component choices/ combinations in a simulation environment. By use of well defined subsystems with clear boundaries, and general component data available from the manufacturers project guides and from sound estimations, a first conceptual model can be verified for credibility of its output. Verification can first be carried out at subsystem level, after which the total system can be verified.

If it is assumed that the manufacturers data represents reality well enough, this model can be a supportive tool in decision making on exact type of the components. In this phase a start can be made with the design of a PCS. Although this PCS design is very useful for predictions of steady system behaviour, the dynamic system behaviour as predicted by this model most probably does not sufficiently agree with reality, due to the lack of detailed system data.

10.5.2 Engineering Phase and Component Acceptance Tests

Once the main components have been chosen, the model should be updated with the most recent subsystem information from the manufacturers. Pre-calibration and pre-validation simulations can be carried out, to identify the parts and operating points of the model that need extra attention during the calibration and validation phase.

The Factory Acceptance Test (FAT) protocols and model tests can now be defined in such a way that the measurement data, together with the simulations, can provide valuable information for model-calibration and validation. These measurements largely overlap with the primary goal of the FAT: to show that a specific subsystem is functioning as expected.

The validation can for instance reveal differences between project guide manufacturer data and reality, or can reveal modeling flaws. By being involved with the definition of the test protocols and the comparison with simulation results, possible problems are identified in an early stage, so that proper action can be taken. This involvement further helps to be able to ask the right questions related to the acceptance of the specific subsystem.

After the FATs and the model tests have been carried out, and the subsystem simulation models have been validated, the submodels are ready to be combined altogether. The total model now is updated with the best available information, and can be used for further propulsion controller development. It should however be realized that even now the predictive value of the simulation model has not been validated as a whole, and output should thus be considered with care. Therefore the PCS that is (further) developed at this phase should still be flexible enough to be tuned if one or more specific subsystems turn out to perform differently on full scale than expected.

10.5.3 Sea Trials

The first opportunity to test the total ship propulsion system throughout its operating envelope is during the sea trials. These trials generally aim at testing if the total system (and subsystem) performance is as requested by the customer. The value of the sea trials can be increased by defining the test-protocol in such a way that high quality total system validation material is collected. Pre-sea trial simulations can help to define the measurement protocol, and help to give an idea of critical manoeuvres/ conditions beforehand.

With the acquired performance data the total model can be validated. Furthermore the performance of specific subsystems can be checked, and in the case of disappointing performance, this can possibly be attributed to specific subsystems (provided that adequate measurements have been made on the subsystem boundaries).

At this stage the simulation model is expected to be able to give high confidence predictions in a large application domain. The propulsion control system can now be tuned further with help of the simulation model, which helps to iterate relatively fast towards a PCS that results in desirable performance over a large range of operating conditions.

10.5.4 Pre- and Post Maintenance Performance Tests

By definition of standard performance tests that cover a large application domain, some sort of performance ”fingerprint” can be obtained per class of ships, or possibly per ship. This fingerprint is likely to change over time, due to for instance fouling or (component) wear. By performing periodical performance tests, and comparing the results both against each other and against simulation results, possible degradation of specific subsystems might be discovered timely, so that pro-active maintenance can take place. In the same way, the performance can be checked directly after small- or large scale maintenance, in order to update the recent ”fingerprint”.

10.5.5 Conclusions and Recommendation

Sections 10.3 and 10.4 demonstrated that simulations can help to monitor and increase the performance of the propulsion plant during the life-cycle of a ship. This does require considerable effort, especially in the modeling phase, but the author expects that the related costs are outweighed by the possible gains. Often simulation models are built during the design phase, but are forgotten soon after that, to be never used again. By keeping the model alive and up-to-date, the shore based engineering staff can immediately make use of the simulation model results in the decision making process regarding for instance maintenance planning, ship modifications or performance predictions.

Chapter 11

Conclusions and Recommendations

In the first place this thesis aims at answering the research questions as were posed in Chapter 1. These questions relate to the development of a simulation model, and determination of its validity. Subsequently the validated simulation model is used to develop and test a Propulsion Control System (PCS) that aims at increased cavitation free time in operational conditions. This newly developed propulsion controller has been installed on full scale, and its performance has been assessed and compared to the performance of the "old" PCS. The various aspects that were investigated include the acceleration/ deceleration behaviour, the effect of off-design resistance, and the effect of waves.

Although not directly driven by the research objectives, some other applications of a ship propulsion simulation model have been discussed in Chapter 10. In this chapter it is also discussed how a ship propulsion simulation model can be kept "alive" and useful during the life cycle of a ship.

The latter is related to the first objective of this thesis: to demonstrate how a ship propulsion simulation model is developed, verified and validated systematically, so that it can rightfully be used to support decision making during the ship life cycle, based on high confidence predictions.

In the following the main conclusions and recommendations from the various phases are summarized.

11.1 Modeling, Verification, Calibration and Validation

11.1.1 Conclusions

The basis of the modeling phase was given by the *modeling goals*, that determine which variables need to be predicted by the model, and in what conditions. The level of complexity that is necessary for a specific subsystem-model is not easily determined beforehand, because it is dependent on the surrounding submodels, and its resulting operating point. This is reflected in the validation phase, which reveals that the uncertainty of a specific submodel output is dependent on its operating point, and on the uncertainties in the linking variables that are input to this submodel. The suitability of a submodel can therefore not be determined without having knowledge of its operating point that is influenced by the connections with the other submodels.

If a model is found unsound at some point during the development cycle, its conceptual model should be reviewed or improved, and the next iteration in the cycle should be made until a suitable model is found, or until the model goals or requirements are relaxed. Experience can help to reduce the burden of iterative model development.

With respect to the model that was developed here, the validation shows that, in terms of static model behaviour, the variables shaft speed n, inlet receiver pressure p_{ir}, fuelrack position X, propeller thrust F_{prop}, propeller torque M_{prop}, pitch θ and ship speed v_s, in general are in sufficient agreement with reality, as indicated by the introduced "static" metric. However, especially at low ship speeds, where the virtual shaft speed is set to zero ($n_{virt,set}$=0 rpm), the validity is less, which is attributed to the large effect of environmental disturbances on the static operating point.

The validity of the dynamic behaviour has partly been determined by making use of two validation metrics that were found in literature. Although these metrics do not take the involved uncertainties into account, they at least objectively quantify the agreement between simulated and measured transients. It was found that the transient behaviour of variables that are directly affected by waves (such as propeller thrust F_{prop} and torque M_{prop}) have less agreement than for instance other variables such as θ and n.

11.1.2 Recommendations

The author believes that the current research demonstrates that the art of modeling and prediction of ship propulsion systems has grown to a level where it can be used as a valuable supporting tool. This does however necessitate a structured approach and a clear understanding of the various phases during the development of a simulation model. To improve the validity of a simulation model it is recommended to incorporate the collection of high quality calibration and validation data in the acceptance tests during the new building of (parts of) a ship.

This overall recommendation can be stated more precisely by considering the parts of the current simulation model that could benefit from such high quality data. Such a list is never finished because it depends on the variables that the user would like to predict with the simulation model. Nevertheless an attempt is made here, thereby assuming that the goals of the user are the same as in the current project.

If true dynamic use of the CPP is set as a goal, it is recommended to model the dynamics of the CPP system and the Propeller Pitch Controller (PPC) in more detail. The long oil lines, oil leakage, and the difficulties in measuring the oil pressure inside the shaft and in the hub, make this a difficult task. This is further complicated by a lack of knowledge about the hydrodynamic and frictional forces that act on the blades. Work in this direction has been done by Bakker (2005) and Huijbers (2008), but further improvements are necessary.

Other issues that should receive more attention in the modeling phase are the transmission losses and the shaft losses. Related to this, it is recommended to investigate the possible gains of a multi-mass shaft model, which will allow for better understanding of the effect of torque measurement location. Such a model will also give torsional vibrations. Note that valuable data can be obtained by simultaneously measuring propeller, engine and possibly gearbox torque on full scale.

Furthermore it is recommended to develop and use improved "dynamic" validation metrics that possibly include uncertainties in the model and in the measurements. Possibly, such metrics can be used to quantify the agreement of dynamic system behaviour in the relevant part of the frequency domain, as to ensure that the system behaviour in waves is well predicted. Difficulty is however the collection of high quality full scale validation data that includes measurements of the exact wave-induced excitation of the system. A way to gather validation data with known measurable disturbance is to superimpose a sinusoidal variation of pitch setpoint and governor setpoint on a mean operating point. By variation of frequency and amplitude, a full scale data set can be generated, which will help to uncover whether the model behaviour in the frequency domain is valid.

It is further recommended to keep up a validation-portfolio belonging to a specific simulation model, showing the results from validation studies. This will ensure that new users have realistic expectation levels, thereby decreasing the risk of erroneous decision making, based on simulation model output.

11.2 Cavitation Inception Predictions

With respect to cavitation inception predictions the current study showed that the numerical prediction capabilities in that field are not fully mature yet. To increase the prediction quality, quantification of the uncertainties in predictions and (full scale) measurements is necessary. Current developments towards viscous inception prediction codes, including necessary rigorous validation studies might be able to deliver high quality inception predictions in the future.

Model scale inception prediction methods might have the potential of delivering high quality predictions, provided that thorough attention is given to the prevention or correction of scale effects. Various ways to prevent or correct for scale effects are reported in literature. However, simultaneous application of these measures, including a thorough high quality validation study has not been found in open literature.

11.3 Newly Developed Propulsion Controller

11.3.1 Conclusions

When controlling a ship propulsion system with a CPP, one in principle has the freedom to choose from many shaft speed-pitch combinations that all result in the same ship speed. Dependent on the goal that is pursued, one can aim at sailing at one specific shaft speed-pitch combination that is most desirable from the viewpoint of that specific goal. In this thesis the secondary goal (next to ship speed) was to increase the cavitation free time in operational conditions. Since propeller cavitation inception is related to local inflow angles of the propeller blade sections, it is attempted to continuously estimate an effective angle of attack. This effective angle of attack is however not unambiguously defined, since each section has its own pitch and inflow angle. Nevertheless, an effective angle of attack is proposed, which is representative for all sectional profiles out of which the propeller is built up.

To enable continuous estimation of the effective angle of attack of the propeller, it is necessary to continuously measure or estimate the axial velocity in the propeller disc.

Since no suitable sensors were available, an axial velocity estimation algorithm, based on thrust measurement was developed and applied.

A simple control loop, aiming at keeping the estimated effective angle of attack at a desirable value, was then developed. To compensate for loss or increase of ship speed due to prolonged pitch reduction or increase, a secondary feedback loop ensured that the ship speed related "virtual shaft speed" signal was kept at the desired value, as set by the watch keeper. From thorough testing in a simulation environment is was concluded that the system was ready and safe for full scale testing.

The proposed effective angle of attack, in combination with active control via a feedback system, is considered original, and can be seen as the most important novelty of this work.

11.3.2 Recommendations

In this thesis a possible way of improving cavitation behaviour via active control of the effective angle of attack α_{eff} has been developed and tested. To improve the behaviour of the controller the following steps are recommended:

- Improve the definition of α_{eff}. This can be done by systematic analysis of cavitation buckets of off-design pitch angles and operating conditions. However, as was shown in Chapter 6, numerical predictions suffer from high uncertainties, which also holds for full scale observations. Despite these uncertainties it remains necessary to have knowledge of the cavitation free operating area in a wide variety of conditions.

- Related to the foregoing, it is recommended to further investigate the possibility of monitoring the cavitation inception conditions by means of noise sensors. Especially the possibility to automatically distinguish between various noise sources (rudder, strut, port side or starboard propeller) might help to determine those operating points that are least susceptible to cavitation inception. This approach can possibly be extended to turning circles, so that even during such manoeuvres the most silent operating point can be determined. It is however expected that developments in that direction require a strong signal processing component, in order to prevent cross-talk between the two propellers.

- Improve the angle-of-attack-estimation process by means of better advance speed measurement or estimation (in terms of signal resolution as well as resolution in time). Such estimation does not necessarily make use of a thrust sensor as is applied in this project. Possibilities may lie in the direction of water speed measurement by means of one or more logs near the propeller. Another option might be to make use of more advanced estimation techniques, instead of straightforward reverse use of the open water diagram.

- Improve the controller by using more advanced (non-linear) controller techniques that take into account the dynamic characteristics and limitations of the plant. Such improvements should probably be sought in cooperation with system-and-control engineers.

11.4 Full Scale Measurement Results

Various types of full scale tests have been carried out, each aiming to isolate a different aspect of the system behaviour. Most tests were subsequently carried out by both the existing control system and the newly developed PCS, so that a fair comparison could be made.

α-bucket test: The α-bucket test revealed that the approximate shape of the α-bucket can be determined experimentally by making use of acceleration sensors. The possibilities of such an approach should be investigated further, including the behaviour during turning circles. Recommendations in this direction were already given in the previous paragraph.

acceleration test: The acceleration test revealed that the cavitation behaviour of the existing system is particularly bad because of the aggressive pitch reduction. This pitch reduction successfully prevents engine overloading, but results in unnecessary performance reduction. From the viewpoint of acceleration capability and cavitation behaviour the newly developed PCS shows significant improvements. From the viewpoint of engine loading the new PCS results in a higher loading than before, but still appears acceptable, especially when the short duration of the increased loading is taken into account.

deceleration test: The deceleration test partly re-enforced the conclusions that were drawn from the acceleration test with regard to the cavitation behaviour. The ship deceleration capability and the engine loading remained approximately unchanged. This test revealed that pitch increase during deceleration can help to decrease or even prevent pressure side cavitation.

forced over/under loading: The forced over/under loading test isolated the behaviour in off-design loading conditions due to for instance heavy weather. It is concluded that the adaptive behaviour of the new PCS is highly desirable from the viewpoint of engine loading. Where in the current installation high engine load is limited by pitch reduction and thus loss of performance, the new PCS succeeds in finding a shaft speed-pitch combination that lies within the engine envelope, without resulting in loss of ship speed. This feature is highly beneficial since it ensures desirable behaviour in all kinds of weather, while a conventional combinator curve in general is designed for one weather condition.

wave test: The seaway test revealed only very small gains in cavitation behaviour. It is therefore recommended to investigate the effect of the various components in the α_{eff}-feedback loop on the lag in the pitch actuation system. This involves lags that are related to measurement/ filtering, hydraulic hardware, and controller software. By removing or decreasing these lags wherever possible, it is expected that the α_{eff}-excursions can further be decreased, which should have its positive consequences on the cavitation behaviour .

turning circle test: When the buckets (or their middles) are known in a large variety of operating conditions, this knowledge should be implemented in the controller, in a way that the setpoint for the angle of attack is dependent on the actual rudder angle,

drift angle or possibly rate of turn.
As was illustrated by the full scale turning circle test, it is probably necessary to implement a limitation on the maximum allowable shaft speed during a turning circle, to prevent operation below the bottom of the cavitation bucket. This will however come at the cost of reduced ship speed in a turn.

11.5 Alternative Use of the Simulation Model

In Chapter 10 some alternative application of a ship propulsion simulation model were discussed. The conclusions and recommendations are presented in the following.

fuel efficiency: As already known, from the viewpoint of fuel efficiency it is wise to operate the installation in an operating point with low shaft speed and high pitch. This is however conflicting with engine loading criteria, so that a compromise needs to be found. Use of a combinator curve that leads to desirable behaviour in a certain seastate will lead to unnecessary loss of efficiency in calm water conditions. An adaptive PCS is expected to be able to effectuate an efficient operating point independent of the environmental conditions, taking into account the limits of the diesel engine. Approximate fuel savings up to 5% might be achieved.

engine loading: Although the investigated air excess ratio λ does not capture all effects that contribute to thermal engine loading, it can help to identify the static operating points that should be avoided, especially for long term operation. Secondly this variable can help to compare the dynamic loading differences for various propulsion controllers. An overloading criterion that acknowledges the importance of dynamic loading variations is therefore preferred over the currently applied shaft speed dependent fuelrack limitation (RTBO line).
In this thesis an acceleration manoeuvre was investigated, revealing clear differences in dynamic λ. Assessment of these dynamic air excess ratios remains a difficult task since the relation between thermal loading profile and reduced time between overhaul is not well understood. To develop a controller that leads to reduced maintenance costs, it is recommended to further develop a "loading"-variable, and to investigate the relation between engine loading profile and engine wear.

manoeuvring behaviour: An alternative use of the simulation model is to use it to make predictions of manoeuvring behaviour, before or after changes are made to the ship or the PCS. From a limited amount of simulations it is concluded that such (straight line) predictions are very well possible, with a quality that is deemed good enough for onboard presentation of manoeuvring data in for instance the manoeuvring booklet.

To further extend the application domain of the simulation model it is recommended to include a multiple-degree of freedom manoeuvring model. However, such a model should be validated extensively (both statically and dynamically) before high confidence full scale predictions can be made. The two introduced "dynamic" validation metrics might prove useful during such validation.

life cycle monitoring: The development of an appropriate ship propulsion simulation model takes considerable time and effort. Ad hoc development of such a model, whenever there is need for it, is highly undesirable, and easily leads to unstructured low confidence simulation results. It is concluded that a structured, well organized modeling approach, as applied in this thesis, can help to keep simulation models "alive" during the life cycle of a ship. Such an approach would ensure that, whenever simulations can help to support decision making regarding maintenance, modification, or performance, a model with proven capabilities is available.

Appendix A

Engine Lookup Tables

This appendix visualizes the engine lookup tables, that are discussed in Section 2.4.2. Table 1 is the static map given by $p_{me,s} = f(Q_f, n_{eng})$, and is shown in Fig A.1. Table 2A and 2B are visualized in Fig A.2: $p_{ir} = g(p_{me}, n_{eng})$. Table 3 is shown in Fig A.3: $p_{me,d} = h(n_{tc}, n_{eng})$. Finally table 4 is shown in Fig A.4: $p_{me,d2} = k(p_{ir,d})$.

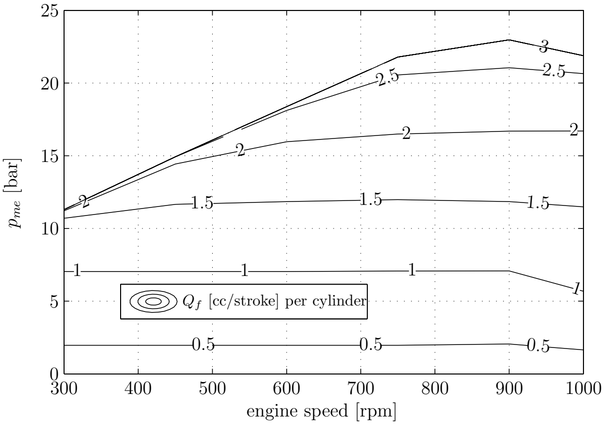

Figure A.1: Engine lookup table 1

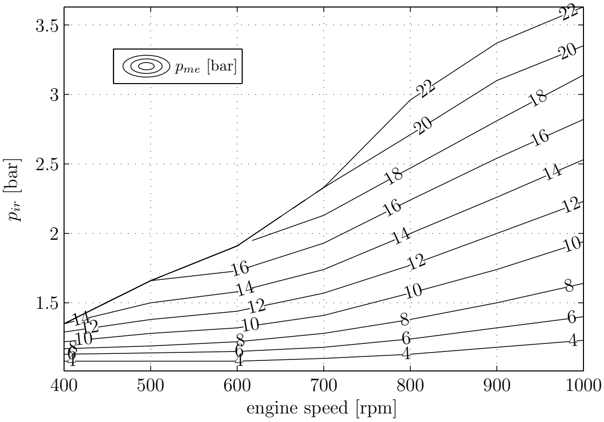

Figure A.2: Engine lookup table 2

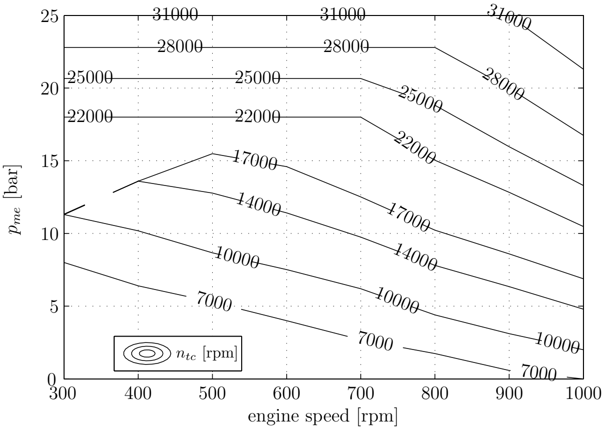

Figure A.3: Engine lookup table 3

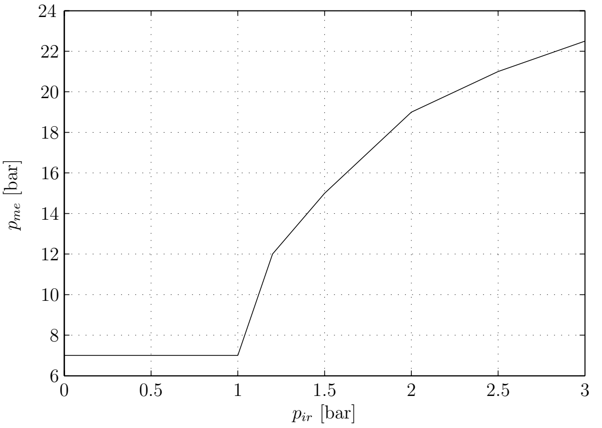

Figure A.4: Engine lookup table 4

Appendix B

Validation Data

This appendix contains the input parameter uncertainty data and the end results of the validation process that were visually presented in Section 5.2.4. The relevant data for operating point II is not listed here because it is already listed in Tables B.1 and 5.3. Parameter uncertainty and measurement uncertainty have been determined by means of expert opinion.
A short description is given of the uncertain parameters that are listed in Table B.1.

$n_{set,gov}$ is the governor setpoint that is generated by the PCS

$\eta_{fuelpump}$ is a multiplicative factor applied to the output of the fuelpump model

η_p is a multiplicative factor directly after engine lookup table 1 (which generates p_{me}

$C_{p_{ir}}$ is a multiplicative factor directly after engine lookup table 2B

V_s is the swept cylinder volume

η_{gb} is the gearbox efficiency

$\theta_{set,PPC}$ is the pitch setpoint to the PPC from the PCS

α_w is a parameter in the wakemodel that was introduced in the calibration chapter

C_{k_t} is a multiplicative factor on the open water k_t value

C_{k_q} is a multiplicative factor on the open water k_q value

η_r is the relative rotative efficiency

R_0 is an additive constant in the resistance model

α_R is a multiplicative constant in the resistance model

α_t is a multiplicative factor on the thrust deduction factor t

The Steady State validation results of operating point I, III and IV are listed in Tables B.2 to B.4.

input parameters $\boldsymbol{x}_s$		$\boldsymbol{x}_{s,0}$	$\boldsymbol{\sigma}_{\boldsymbol{x_s}}/\boldsymbol{x}_{s,0}$ [%]	σ_{x_s}
$n_{set,gov}$	rpm	593.25	1.0	5.93
$\eta_{fuelpump}$	[-]	0.90	2.5	0.02
η_P	[-]	1.00	1.0	0.01
$C_{p_{ir}}$	[-]	1.00	5.0	0.05
V_h	m^3	0.02	0.0	0.00
η_{gb}	[-]	0.93	2.5	0.02
$\theta_{set,PPC}$	deg	26.00	0.5	0.13
α_w	[-]	1.20	1.0	0.01
C_{k_t}	[-]	1.00	2.0	0.02
C_{k_q}	[-]	1.00	2.0	0.02
η_r	[-]	0.99	1.0	0.01
R_0	[N]	30000	10	3000
α_R	[-]	1.35	5.0	0.07
α_t	[-]	1.00	1.0	0.01

Table B.1: Input parameter uncertainty determined by expert opinion (for operating point II). The same percentages were kept for the other operating points

I	**unit**	**computation**		**measured**		ψ
		mean	sigma	mean	sigma	
n	[rpm]	80.75	0.96	80.20	0.50	0.61
p_{ir}	[bar]	1.11	0.00	1.08	0.10	0.00
X	[mm]	7.61	0.25	7.90	0.15	0.45
M_{prop}	[Nm]	18900.57	607	15333.10	1533.31	0.09
F_{prop}	[N]	-3495.08	1227	16115.17	2417.28	0.00
θ	[deg]	1.67	0.00	1.96	0.10	0.00
x_m	[mm]	0.16	0.10	-0.05	0.75	0.24
v_s	[m/s]	0.30	0.48	0.32	0.15	0.49

Table B.2: Steady State validation results of operating point I: command 0

III	**unit**	**computation**		**measured**		ψ
		mean	sigma	mean	sigma	
n	[rpm]	110.11	1.10	109.89	0.50	0.63
p_{ir}	[bar]	1.77	0.10	1.68	0.10	0.65
X	[mm]	18.20	0.70	18.21	0.15	0.37
M_{prop}	[Nm]	123155.23	4833.74	119753.51	5987.68	0.62
F_{prop}	[N]	145220.17	5510.39	143795.00	10784.63	0.86
θ	[deg]	25.97	0.13	25.88	0.10	0.68
x_m	[mm]	0.10	0.00	0.01	0.75	0.00
v_s	[m/s]	7.22	0.10	7.33	0.15	0.62

Table B.3: Steady State validation results of operating point III: command 91

IV	**unit**	**computation**		**measured**		ψ
		mean	sigma	mean	sigma	
n	[rpm]	126.78	1.27	126.20	0.50	0.53
p_{ir}	[bar]	2.85	0.18	2.67	0.10	0.49
X	[mm]	25.17	0.99	24.45	0.15	0.23
M_{prop}	[Nm]	189275.10	7500	179711.74	8985.59	0.56
F_{prop}	[N]	215683.52	8053	199324.23	14949.32	0.44
θ	[deg]	27.76	0.14	27.37	0.10	0.10
x_m	[mm]	0.11	0.00	0.26	0.75	0.00
v_s	[m/s]	8.77	0.13	8.74	0.15	0.89

Table B.4: Steady State validation results of operating point IV: command 120

Appendix C

Scaling of Vortex Cavitation Inception

This appendix shows how the vortex cavitation inception rule that was developed by McCormick Jr (1962) can be applied to rotating model scale propellers.

Based on McCormick the ratio of inception indices is related to the ratio of Reynolds numbers to a specific power e:

$$\frac{\sigma_{i,ship}}{\sigma_{i,model}} = \left(\frac{R_{n,ship}}{R_{n,model}}\right)^{e} \tag{C.1}$$

Note that σ_i is used here where in fact we mean $\sigma_{n,i}$. This short notation is kept throughout this appendix. The Reynolds number is defined as

$$R_n = \frac{nD^2}{\nu} \tag{C.2}$$

with n the propeller rotation rate, D the propeller diameter, and ν the kinematic viscosity. Substitution of equation C.2 in C.1 gives:

$$\frac{\sigma_{i,ship}}{\sigma_{i,model}} = \left(\frac{n_{i,ship}}{n_{i,model}} \cdot \left(\frac{D_{ship}}{D_{model}}\right)^2 \cdot \frac{\nu_{model}}{\nu_{ship}}\right)^{e} \tag{C.3}$$

The inception index is defined by:

$$\sigma_i = \frac{p_0 - p_v + \rho g h}{1/2 \rho n_i^2 D^2} \tag{C.4}$$

with p_0 the atmospheric pressure, p_v the vapour pressure, h the immersion depth of the shaft centerline, and n_i the rotation rate at inception.

From this, the rotation rate at inception can be written as:

$$n_i = \sqrt{\frac{p_0 - p_v + \rho g h}{0.5 \rho \sigma_i D^2}} \tag{C.5}$$

Further simplification is possible by use of:

$$\frac{(p_0 - p_v + \rho g h)_{model}}{(p_0 - p_v + \rho g h)_{ship}} = \frac{\rho_{model}}{\rho_{ship}} \cdot \frac{1}{\lambda} \tag{C.6}$$

which guarantees an equal vertical pressure gradient over the propeller disc, and where $\lambda = \frac{h_{ship}}{h_{model}}$ is the geometric scale factor.

Combination of equation C.6 and C.5 gives:

$$\frac{n_{i,ship}}{n_{i,model}} = \left(\lambda \cdot \frac{\sigma_{i,model}}{\sigma_{i,ship}} \cdot \left(\frac{D_{model}}{D_{ship}} \right)^2 \right)^{1/2} \tag{C.7}$$

Substitution of C.7 in C.3 gives:

$$\frac{\sigma_{i,ship}}{\sigma_{i,model}} = \left(\left(\lambda \cdot \frac{D^2_{model} \sigma_{i,model}}{D^2_{ship} \sigma_{i,ship}} \right)^{1/2} \cdot \left(\frac{D_{ship}}{D_{model}} \right)^2 \cdot \frac{\nu_{model}}{\nu_{ship}} \right)^e \tag{C.8}$$

By making use of $\lambda = \frac{D_{ship}}{D_{model}}$, this simplifies to:

$$\frac{\sigma_{i,ship}}{\sigma_{i,model}} = \left(\lambda^{1/2} \cdot \lambda^{-1} \cdot \left(\frac{\sigma_{i,model}}{\sigma_{i,ship}} \right)^{1/2} \cdot \lambda^2 \cdot \frac{\nu_{model}}{\nu_{ship}} \right)^e \tag{C.9}$$

so that via:

$$\frac{\sigma_{i,ship}}{\sigma_{i,model}} = \lambda^{3e/2} \cdot \left(\frac{\sigma_{i,model}}{\sigma_{i,ship}} \right)^{e/2} \cdot \left(\frac{\nu_{model}}{\nu_{ship}} \right)^e \tag{C.10}$$

eventually

$$\frac{\sigma_{i,ship}}{\sigma_{i,model}} = \lambda^{\frac{3e}{2+e}} \cdot \left(\frac{\nu_{model}}{\nu_{ship}} \right)^{\frac{2e}{2+e}} \tag{C.11}$$

For a value of $e = 0.35$, this equals:

$$\frac{\sigma_{i,ship}}{\sigma_{i,model}} = \lambda^{0.447} \cdot \left(\frac{\nu_{model}}{\nu_{ship}} \right)^{0.298}$$

Appendix D

Trial List

test-description	virtual setpoint [rpm]	shaft speed [rpm]	pitch [deg]	description	mode
alpha bucket test		80	5-10-15-20-25-20-15-10-5	variation of pitch at fixed shaft speed	hand- electric
		90	13-15-16		
		100	17-18-19		
		120	5-10-15-20-25-20		
static test	0-30-60-90-120-90-60-30-0			determination of static operating points	auto, PCS V6.3
	0-30-60-90-120-90-60-30-0				auto, PCS+
acceleration/ deceleration	0-67-91-110-91-67-0-110-0			determination acceleration/ deceleration behaviour	auto, PCS V6.3
	0-67-91-110-91-67-0-110-0				auto, PCS+
forced over/ under loading	SB: 95			forced high/low resistance conditions by using differential thrust	SB:PCS+ PS:PCS V6.3
	PS: 70-80-90-100-110				SB:PCS+ PS:PCS V6.3
seaway test- stern waves	106 (realised 104)				auto, PCS V6.3
	106				auto, PCS+
seaway test- head waves	120 (realised 107)				auto, PCS V6.3
	116 (realised 108/109)				auto, PCS+
turning circle tests	90-100-110 rudder 10 deg ps/sb			low quality due to seastate and probably too high virtual setpoint	auto, PCS V6.3
	90-100-110 rudder 10 deg ps/sb			low quality due to seastate and probably too high virtual setpoint	auto, PCS+

Table D.1: Overview of full scale test runs

Appendix E

Seaway Test time traces

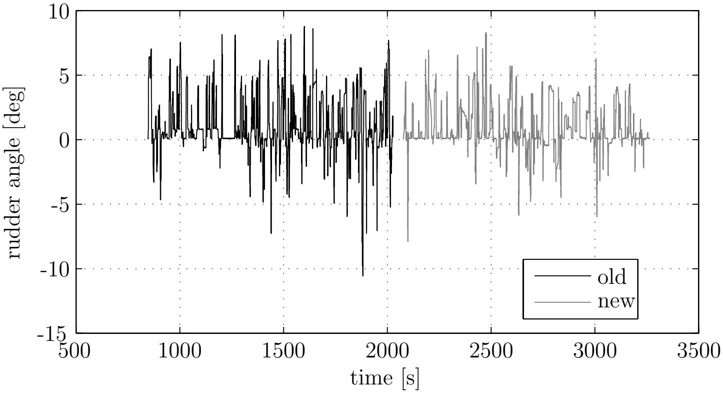

Figure E.1: Rudder

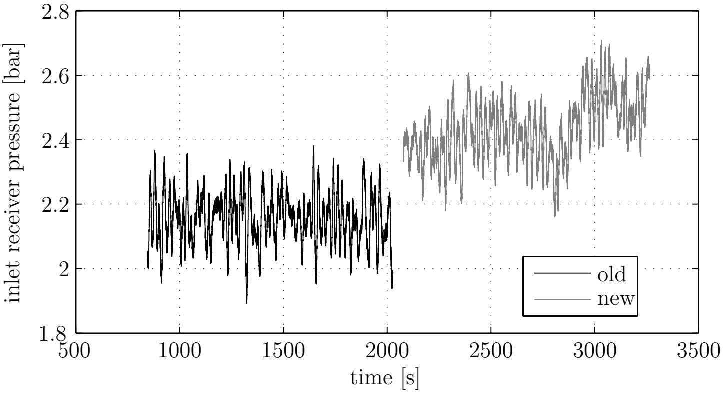

Figure E.2: Inlet receiver pressure

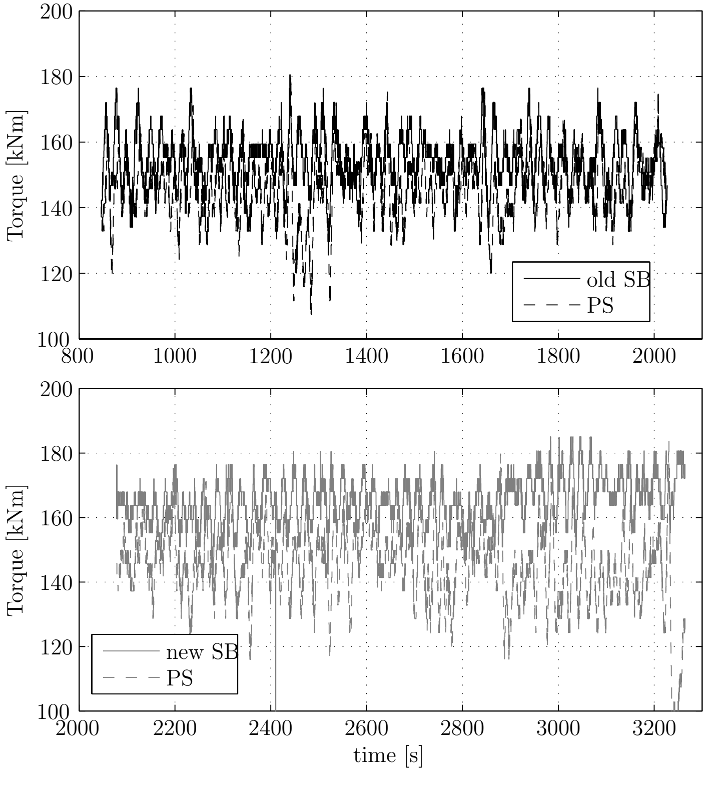

Figure E.3: Propeller torque (port and starboard) for the old and the new PCS

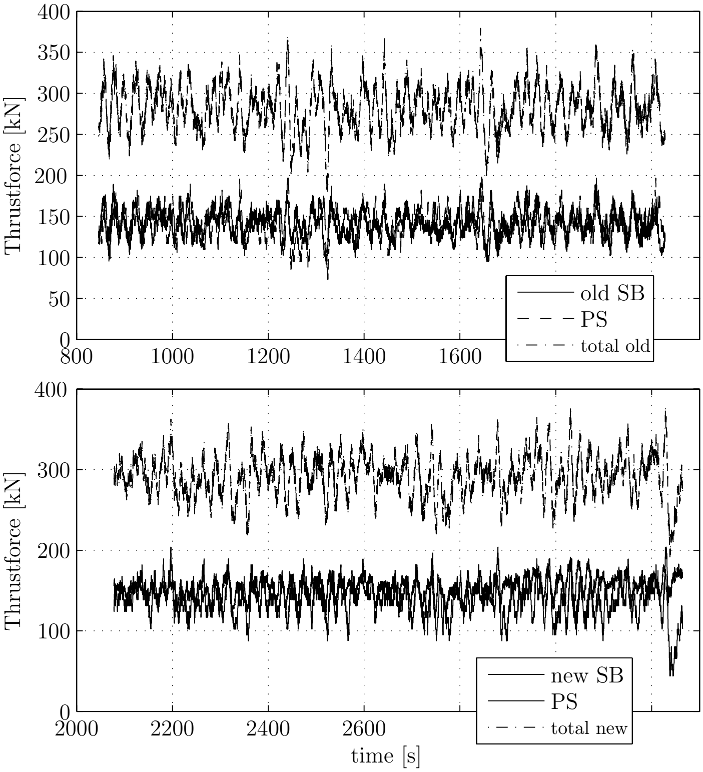

Figure E.4: Propeller thrust for the old and the new PCS

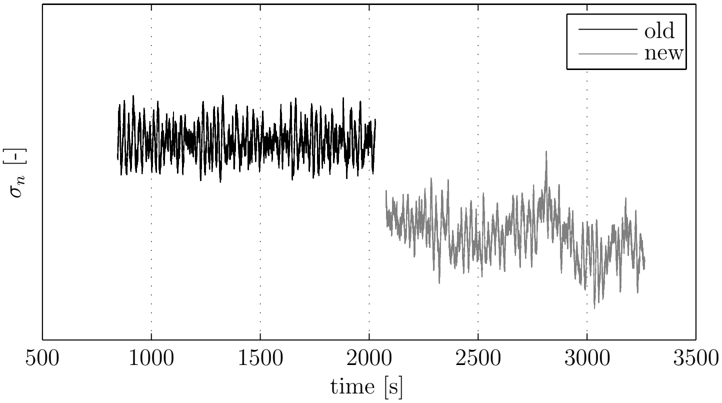

Figure E.5: Cavitation number

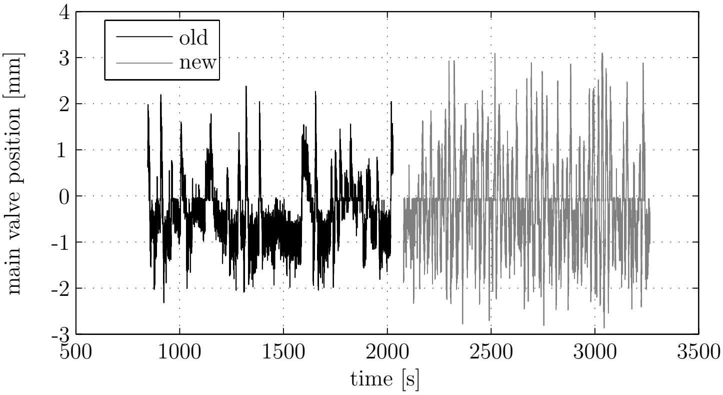

Figure E.6: Main valve position of the CPP hydraulic system

Bibliography

Aalbers, A. B. and Van Gent, W. (1984). Unsteady wake velocities due to waves and motions measured on a ship model in head waves. In *Proceedings of the 15th symposium on Naval Hydrodynamics*.

Altosole, M., Benvenuto, G., Figari, M., and Campora, U. (2009). Real-time simulation of a COGAG naval ship propulsion system. *J. Engineering for the Maritime Environment, Part M*, 223:47–61.

Altosole, M. et al. (2008). Real Time Simulation of the Propulsion Plant Dynamic Behaviour of the Aircraft Carrier "Cavour". In *Proceedings of the 9th International Naval Engineering Conference and Exhibition (INEC2008)*, pages 123–130.

ASME (2006). Guide for verification and validation in computational solid mechanics. Technical report, the American Society of Mechanical Engineers.

Bakker, J., Grimmelius, H., and Wesselink, A. (2006). The use of non linear models in the analysis of cpp actuator behaviour. In *Proceedings of the 2nd World Maritime Technology Conference (WMTC 2006)*. ISBN 1-902536-54-1.

Bakker, J. C. (2005). Dynamic behaviour and nonlinear aspects of the controllable pitch propeller. Master's thesis, Delft University of Technology.

Boswell, R. J. (1971). Design, cavitation performance and open-water performance of a series of research skewed propellers. Technical Report 3339, Naval Ship Research and Development Center.

Brennen, C. E. (1995). *Cavitation and bubble dynamics*. Oxford University Press.

Brouwer, A. B. M. and Dupré, J. (2004). Functioneel ontwerp voortstuwingsregelautomatiek V6.3. Technical Report 3063 MCS D/085, van Rietschoten & Houwens. in Dutch.

Brouwer, A. B. M., Dupré, J., and Kalkhoven, W. J. H. (1992). Functioneel ontwerp voortstuwingsregelautomatiek V4.0. Technical Report 3063 MCS D/085, van Rietschoten & Houwens. in Dutch.

Campora, U. and Figari, M. (2003). Numerical simulation of ship propulsion transients and full-scale validation. In *Proceedings of the Institution of Mechanical Engineers*, volume 217.

Carlton, J. S. (2007). *Marine Propellers and Propulsion*. Buttersworth-Heineman Ltd, ISBN 978-07506-8150-6.

Chandrashekhara, N. (1976). Analysis of tip vortex cavitation inception at hydrofoils and propellers. *Schiffstechnik*, 23(112):47–62.

De Mulder, E. P. H. M. and De Nies, J. P. M. (1987). Experience with an exploratory noise optimization control and an electrical pitch measurement system. In *Proceedings of the 8th Ship Control Systems Symposium.* the Hague, the Netherlands.

Deleroi, K. H. E. (1995). Simulation study of acceleration and crash-stop manoeuvres for ship machinery systems. Master's thesis, Technical University Delft, Section of Marine Engineering. OEMO report no. 95/09.

Du, X. and Chen, W. (2002). Efficient uncertainty analysis methods for multidisciplinary robust design. *AIAA Journal*, 40(3):545–552.

Easterling, R. G. (2001). Measuring the predictive capability of computational methods: Principles and methods, issues and illustrations. Technical report, Sandia National Laboratories.

Fossen, T. I. (2002). *Marine Control Systems.* Marine Cybernetics.

Garfinkel, D., Marbach, C. B., and Shapiro, N. Z. (1977). Stiff differential equations. *Annual Review Biophys Bioeng*, 6:525–542.

Geers, T. L. (1984). An objective error measure for the comparison of calculated and measured transient response histories. *Shock and Vibration bulletin*, 54:99–107.

Gindroz, B. (1998). Cavitation nuclei and cavitation inception of marine propellers: State of the art at the dawn of the 21st century. *JSME International Journal*, 41(2):464–471. series B.

Gindroz, B., Hoshino, T., and Pylkkanen, J. V. (1998). ITTC propulsion committee propeller RANS/ panel method workshop. In *Proceedings of the 22nd ITTC.*

Godjevac, M., Grimmelius, H., Stapersma, D., and Van Beek, T. (2006). Wear mechanisms of a blade foot bearing on a controllable pitch propeller. In *Proceedings of the 2nd World Maritime Technology Conference (WMTC2006).*

Grimmelius, H. and Stapersma, D. (2000). Control optimisation and load prediction for marine diesel engines using a mean value simulation model. In *Proceedings of the Ensus 2000 Conference*, Newcastle-upon-Tyne.

Grimmelius, H. and Stapersma, D. (2001). The impact of propulsion plant control on diesel engine thermal loading. In *Proceedings of the CIMAC conference 2001*, Hamburg. CIMAC.

Holtrop, J. (1997). Tip-vortex cavitation inception in relation to propeller and wake parameters. Technical report, MARIN report no. 13509-1-SR.

Hoppe, F. (2008). Naval gear systems and their future demands. In *Proceedings of the 9th International Naval Engineering Conference and Exhibition (INEC2008)*, pages 143–153.

Hsiao, C. T. and Chahine, G. L. (2008). Scaling of tip vortex cavitation inception for a marine open propeller. In *Proceedings of the 27th Symposium on Naval Hydrodynamics.*

Huijbers, J. H. H. (2008). Non-linear propeller pitch control. Master's thesis, Technische Universiteit Eindhoven Department Mechanical Engineering Dynamics and Control Group.

IMTECH (2007). Unit connection diagram. Technical Report 910227-RZ1000-BDS, IMTECH.

Jessup, S. D. and Wang, H.-C. (1996). Propeller cavitation prediction for a ship in a seaway. Technical report, Carderock Division, Naval Surface Warfare Center, United States Navy.

Klein Woud, H. and Stapersma, D. (2002). *Design of propulsion and electric power generation systems*. Institute of Marine Engineering, Science and Technology. ISBN 1-902536-47-9.

KM (1991). *Manoeuvreergegevens t.b.v. de navigatie behorende bij het devies van Hr. Ms. "Karel Doorman"*. Koninklijke Marine. in Dutch.

Koops, A. (2008). Cavitation experiments m-class frigate for various drift angles. Technical Report 20446-4-DT-VT, MARIN.

Kuiper, G. (1981). *Cavitation Inception on Ship Propeller Models*. PhD thesis, Technische Hogeschool Delft. ISBN 0-19-509409-3.

Kuiper, G. (1996). Cavitation observations on Hr. Ms. Karel Doorman. Technical Report 13522-1-ST, MARIN.

Kuiper, G., Grimm, M., McNeice, B., Noble, D., and Krikke, M. (2002). Propeller inflow at full scale during a manoeuvre. In *Proceedings of the 24th Symposium on Naval Hydrodynamics*. Fukuoka, Japan. July 8–13.

Kuiper, G. and Jessup, S. D. (1993). A propeller design method for unsteady conditions. *SNAME transactions*, 101:247–273.

Kuiper, G., Van Terwisga, T., Zondervan, G.-J., Jessup, S., and Krikke, E. (2006). Cavitation inception tests on a systematic series of two-bladed propellers. In *Proceedings of the 26th Symposium on Naval Hydrodynamics*, Rome, Italy.

McCormick Jr, B. W. (1962). On cavitation produced by a vortex trailing from a lifting surface. *ASME Journal of Basic Engineering*, 84:369–379.

Morvillo, R. A. (1996). Application of modern digital controls to improve the operational efficiency of controllable pitch propellers. *SNAME transactions*, 104:115–136.

Noble, D. J. (1997). Evaluation of the cavitation inception prediction capabilities of the propeller surface panel code ASP-2. In *Proceedings of the 4th Canadian Marine Hydromechanics and Structures Conference*.

Noble, D. J. (2005). Validation of procal prediction of the cavitation inception performance of the NSRDC skewed propeller series in open water. Draft DRDC Atlantic ECR 2005-096, Defence R&D Canada-Atlantic.

Noordzij, L. (1977). A note on the scaling of tip vortex cavitation inception. *International Shipbuilding Progress*, 24:233–236.

Oberkampf, W. L. and Barone, M. F. (2006). Measures of agreement between computation and experiment: Validation metrics. *Journal of Computational Physics*, 217:5–36.

Oberkampf, W. L. and Trucano, T. G. (2002). Verification and validation in computational fluid dynamics. *Progress in Aerospace Sciences*, 38:209–272.

Oberkampf, W. L., Trucano, T. G., and Hirsch, C. (2003). Verification, validation and predictive capability in computational engineering and physics. Technical Report SAND2003-3769, Sandia National Laboratories.

Pivano, L., Smogeli, O. N., Johansen, T. A., and Fossen, T. I. (2007). Experimental validation of a marine propeller thrust estimation scheme. *Modeling, Identification and Control*, 28(4):105–112.

Ray, M. H., Anghileri, M., and Mongiardini, M. (2008). Comparison of validation metrics using repeated full-scale automobile crash tests. In *Proceedings of the 5th European congress on computational methods in applied Sciences and Engineering.*

Routhier, M. and Horning, S. (2006). Machinery control system design using dynamic modelling and simulation -lessons learned. In *Proceedings of the World Maritime Technology Conference 2006 (WMTC 2006).*

Russel, D. M. (1997a). Error measures for comparing transient data: part i:development of a comprehensive error measure. In *Proceedings of the 68th shock and vibration symposium*, pages 175–184.

Russel, D. M. (1997b). Error measures for comparing transient data: part ii: error measure case study. In *Proceedings of the 68th shock and vibration symposium*, pages 175–184.

Schlesinger, S. (1979). Terminology for model credibility. *Simulation*, 32(3):103–104.

Schulten, P. J. M. (2005). *The interaction between diesel engines, ship and propellers during manoeuvring.* PhD thesis, Delft University of Technology. ISBN 90-407-2579-9.

Schulten, P. J. M. and Stapersma, D. (2007). A study of the validity of a complex simulation model. *Journal of Marine Engineering and Technology*, A10:67–77.

Schwer, L. E. (2007). Validation metrics for response histories: perspectives and case studies. *Engineering with Computers*, 23:295–309.

Sinnema, M. F. (1986). Report no. 45955-3-vt, m-frigate; model tests with final propellers in still water. Technical report, MARIN.

Spraque, M. A. and Geers, T. L. (2003). Spectral elements and field separation for an acoustic fluid subject to cavitation. *Journal of Computational Physics*, 184:149–162.

Stapersma, D. (2000). Interaction between propulsor and engine. In *Proceedings of the 34th WEGEMT School.*

Stapersma, D., Grimmelius, H., and Schulten, P. (2004). A fresh view on propulsion control. In *Proceedings of the 2004 INEC conference.* Amsterdam, the Netherlands.

SW Diesel B.V. (1987). Beproevingsprotokol (motornummer 80054-1 (s.b. motor) dd. 3-12-1987. Technical report, Stork Werkspoor Diesel B.V. in Dutch.

SW Diesel B.V. (1990a). Proefvaartprotokol (motornummer 80054-1 (s.b. motor m-fregat karel doorman) dd. 5-10-1990. Technical report, Stork Werkspoor Diesel B.V. in Dutch.

SW Diesel B.V. (1990b). Proefvaartprotokol (motornummer 80054-2 (b.b. motor m-fregat karel doorman) dd. 5-10-1990. Technical report, Stork Werkspoor Diesel B.V. in Dutch.

Thacker, B. H. (2004). Concepts of model verification and validation. Technical report, Los Alamos National Laboratory.

Trucano, T. G., Swiler, L. P., Igusa, T., Oberkampf, W. L., and Pilch, M. (2006). Calibration, validation, and sensitivity analysis: Whats what. *Reliability Engineering and System Safety*, 91:1331–1357.

Urick, R. J. (1983). *Principles of Underwater Sound*. Peninsula Publishing. ISBN 0-932146-62-7.

Van Amerongen, J. (1982). *Adaptive Steering of Ships*. PhD thesis, Delft University of Technology.

Van Der Klugt, P. M. (1987). *Rudder, Roll, Stabilization*. PhD thesis, Delft University of Technology.

Van Gent, A., Van Der Hout, I. E., and Koops, A. (2008). M-fregat trial installation and measuring equipment. Technical Report 20446-5-TM/POW, MARIN.

Van Rees, W. M., Van Rijsbergen, M. X., Kuiper, G., and Van Terwisga, T. J. C. (2008). An exploratory investigation of cavitation inception on the pressure side of propellers. In *Proceedings of FEDSM2008*, Jacksonville, Florida USA.

Van Terwisga, P. F. (2000). Hydrodynamic aspects of the application of a dynamic simulation model in frigate propulsion system design and operation. In *Proceedings of the 34th WEGEMT School*.

Van Terwisga, T. (2009). Personal communication, March 2009.

Van Terwisga, T., Van Wijngaarden, E., Bosschers, J., and Kuiper, G. (2007). Achievements and challenges in cavitation research on ship propellers. *International Shipbuilding Progress*, 54:165–187.

Van Terwisga, T. J. C. et al. (2006). Cavitation research on ship propellers. In *Proceedings of the 6th International Symposium on Cavitation (CAV 2006)*.

Van Terwisga, T. J. C., Noble, D. J., Van 't Veer, R., Assenberg, F., McNeice, B., and Van Terwisga, P. F. (2004). Effect of operational conditions in the cavitation inception speed of naval propellers. In *Proceedings of the 25th Symposium on Naval Hydrodynamics*, St. John's, Newfoundland and Labrador.

Vaz, G. (2005). *Modelling of Sheet Cavitation on Hydrofoils and Marine Propellers using Boundary Element Methods*. PhD thesis, IST, UTL, Lisbon, Portugal. ISBN 10 90-90920325-7.

Verkuyl, J. B. and Van Terwisga, P. F. (2000). Testing a new fullscale cavitation observation system on board of Hr. Ms. Tydeman. In *Proceedings of the 34th WEGEMT School*.

Visser, E. W. and Pol, J. W. (1996). Functioneel ontwerp schroefspoed automatiek, versie 4.0. Technical Report 3063 MCS D/028, IMTECH. in Dutch.

Vrijdag, A., Schulten, P., Stapersma, D., and Van Terwisga, T. J. C. (2007). Efficient uncertainty analysis of a complex multidisciplinary simulation model. *Journal of Marine Engineering and Technology*, A10:79–88.

Vrijdag, A., Stapersma, D., and Van Terwisga, T. J. C. (2008). Tradeoffs in ship propulsion control: engine overloading and cavitation inception in operational conditions. In *Proceedings of the 9th International Naval Engineering Conference and Exhibition (INEC'08).* Hamburg, Germany.

Vrijdag, A., Stapersma, D., and Van Terwisga, T. J. C. (2009). Control of propeller cavitation in operational conditions. In *Proceedings of the third World Maritime Technology Conference (WMTC 2009)*, Mumbai, India. Institute of Marine Engineers India.

Nomenclature

Roman variables

AR	aspect ratio	[-]
C	combined, constant, coefficient	[-], [-], [-]
c	calculation, chord length	[-], [-]
D	diameter	[m]
e	scaling rule exponent	[-]
F	force	[N]
F_n	Froude number	[-]
h	submersion depth	[m]
H_0	lower calorific value	[J/Kg]
I	current	[A]
i	number of cylinders, ratio	[-], [-]
I_p	polar moment of inertia	[kgm^2]
J	advance ratio	[-]
k	number of revolutions per cycle	[-]
k_p	number of propellers	[-]
k_t	thrust coefficient	[-]
k_q	torque coefficient	[-]
M	torque, metric	[Nm],[-]
m	mass, measurement	[kg], [-]
n	rotational speed	[1/s]
P	power, phase metric, pitch	[W], [-],[m]
p	pressure	[Pa]
Q	openwater torque, volume flow, weight factor	[Nm], [m^3/s], [-]
	energy	[J]
QS	normalisation factor	[-]
R	resistance,radius, gas constant	[N],[m], [J/kg]
r	radial position	[m]
R_n	Reynolds number	[-]
T	thrust, temperature	[N],[K]
t	thrust deduction factor, time	[-], [s]
V	volume, speed	[m^3], [m/s]
V_s	swept volume	[m^3]
v	speed	[m/s]
W_n	Weber number	[-]
w	wakefraction	[-]
X	fuelrack position	[mm]

x	(nondimensional) position	[-], [m]

Greek variables

α	multiplication factor, angle	[-], [deg]
β	inflow angle	[deg]
ϕ	angular position	[deg]
η	efficiency	[-]
λ	geometric scaling factor, air excess ratio	[-], [-]
μ	mean (normal distribution)	[-]
ν	kinematic viscosity	$[m^2/s]$
θ	propeller pitch	[deg]
ρ	density	$[kg/m^3]$
σ	standard deviation, cavitation number, stoichiometric value	[-], [-], [-]
τ	time constant, time difference	[s], [s]
ψ	validation metric, gas content number	[-], [-]

Subscripts

0	nominal/ calm
a	advance, air
c	calculation
ca	combustion air
cis	cavitation inception speed
$crit$	critical
d	drive, dynamic
e	effective, engine
eff	effective
eng	engine
f	fuel
$fuel$	fuel
gb	gearbox
gov	governor
h	hull
i	index, counter, inception
ir	inlet receiver
KG	Knowles and Gear
LE	leading edge
m	main valve, measurement
me	mean effective
$model$	model
n	shaft speed
nom	nominal
p	pressure, propeller
PPC	propeller pitch controller
$prop$	propeller
r	relative rotative

s	ship, swept, shaft, static
set	setpoint
$shaft$	shaft
$ship$	ship
SG	Sprague and Geers
t	total
tc	turbocharger
$trap$	trapped
trm	transmission
v	vapour
$virt$	virtual
w	wake

Acronyms

CBV Counter Balance Valve

CSSUA Concurrent Sub-System Uncertainty Analysis

CFD Computational Fluid Dynamics

CIS Cavitation Inception Speed

CODAG Combined Diesel and Gas

CODOG Combined Diesel or Gas

CPP Controllable Pitch Propeller

DE Diesel Engine

DGPS Differential Global Positioning System

DNS Direct Numerical Simulation

DRDC Defence Research and Development Canada

DTT Depressurized Towing Tank

EM Electro Magnetic

FAT Factory Acceptance Test

FPP Fixed Pitch Propeller

GPS Global Positioning System

GT Gas Turbine

HNLMS Her Netherlands Majesty's Ship

I/O Input/Output

IMO International Maritime Organisation

LDV Laser Doppler Velocimetry

LES Large Eddie Simulation

MARIN Maritime Research Institute Netherlands

MCS Monte Carlo Simulation

M-frigate Multipurpose Frigate

MoTher Motor Thermodynamics

MQK Marine Quality Kit

NLDA Netherlands Defence Academy

OD box Oil Distribution box

PCS Propulsion Control System

PPC Propeller Pitch Controller

PROSA Program for Online Signal Acquisition

RAN Royal Australian Navy

RANS Reynolds Averaged Navier-Stokes

RAS Replenishment at Sea

RNLN Royal Netherlands Navy

RTBO Reduced Time Between Overhaul

S-frigate Standard Frigate

SUA System Uncertainty Analysis

SCS Society for Computer Simulation

SFC Specific Fuel Consumption

TOA Time Of Arrival

UPS Uninterruptible Power Supply

WPNL Wärtsilä Propulsion Netherlands

Summary

Control of Propeller Cavitation in Operational Conditions

by **Arthur Vrijdag**

Because of the shift of naval operations towards shallow coastal waters and the associated increasing mine threat, underwater signature management is of growing importance for naval ships. At the same time the number of countries that operate submarines is growing, suggesting that navies should be prepared for possible increased torpedo threat.

Due to the resulting strict demands on inboard as well as outboard noise levels, increasing effort is being put into the investigation, monitoring and control of noise sources, such as vibrating machinery and cavitation of the propellers.

Propeller cavitation is an important contributor to the acoustic underwater signature of a ship. Therefore, aside from other important aspects such as efficiency and strength, the design of (naval) propellers focuses on maximum avoidance of cavitation. Over the years, this has led to an increase of the cavitation inception speed, especially in calm water. However, from full scale measurements it is known that off-design conditions have a considerable influence on cavitation performance of ships propellers, and thus on the ships acoustic signature.

To increase the cavitation free time in operational conditions, it was decided to design a dedicated propulsion control system in this project. First this control system was tested in a simulation environment, after which the controller was tested on full scale. Use of a simulation environment has many advantages. However, a big disadvantage is that one has to asses the validity of a simulation model before one can rightfully use it to make predictions. The latter especially holds if the model is used to design equipment.

To increase and asses the model validity, a systematic modelling, verification, calibration and validation approach is applied to the ship propulsion system under consideration. Only after the validity is quantified and considered as sufficient, the model is used for the development of the propulsion controller.

When controlling a ship propulsion system with a Controllable Pitch Propeller (CPP), one in principle has the freedom to choose from many shaft speed-pitch combinations that all result in the same ship speed. By choosing one of these possible combinations, a secondary goal (besides ship speed) can be pursued. In search of an effective cavitation control variable, it is observed that cavitation inception on blade sections is strongly related to the angle of attack. However, in case of a propeller this angle of attack is not unambiguously defined, since each section has its own pitch and inflow angle. Nevertheless, an effective angle of attack with certain desirable properties is proposed, which is representative for all sectional profiles out of which the propeller is built up.

To estimate (and control) this effective angle of attack onboard, it is necessary to continuously measure/ estimate the axial velocity in the propeller disc. For this purpose an axial velocity estimation algorithm, based on measurement of thrust, was developed and tested.

A simple controller, aiming at keeping the angle of attack at the desired value was subsequently developed, and thoroughly tested in a simulation environment. The predictions that were shown for various parameter settings gave a good idea of initial parameter settings and did show how, if necessary, the dynamic behaviour of the plant could quickly be adjusted during the full scale trials.

To verify the performance of the newly developed propulsion control system, full scale trials were carried out onboard the M-frigate HNLMS van Galen, in February and March 2008. The operating area was the Caribbean Sea, where the ship was deployed at that time. The main improvement of cavitation free time was obtained during the acceleration and deceleration tests. The forced overloading test showed that engine-overloading can be prevented in increased ship resistance conditions, without loss of propulsive power. The seaway test revealed a very small gain in cavitation behaviour, but further improvements are considered possible. The quality of the turning circle measurements is negatively affected by seaway, and by a too high ship speed. This complicates the comparison of the two systems with regards to the cavitation behaviour in a turning circle.

Although the validated simulation model is mainly used for the development of a propulsion controller, it can be used for many other studies. On the one hand other propulsion controllers aiming at other dedicated goals might be developed with the help of the simulation model. On the other hand, even without making modifications to the simulation model, the understanding of the system behaviour can be increased, especially due to the virtually unlimited amount of test-cases that can be run in a simulation environment. Some introductory examples of such applications are given.

Samenvatting

Het Regelen van Schroef Cavitatie in Dienstomstandigheden
(Control of Propeller Cavitation in Operational Conditions)
door **Arthur Vrijdag**

Door de verschuiving van maritieme operaties richting de ondiepe kustwateren, en de hieraan gerelateerde verhoogde mijnendreiging is de akoestische onderwater signatuur van toenemend belang voor marineschepen. Tegelijkertijd groeit het aantal landen dat onderzeeërs gebruikt, hetgeen suggereert dat marines voorbereid moeten zijn op eventuele verhoogde torpedodreiging.

De resulterende toenemend strenge eisen die aan zowel de binnenboord- als buitenboord geluids niveaus gesteld worden, hebben geleid tot een toename van onderzoek van, toezicht houden op, en regelen van geluidbronnen zoals trillende machinerie en schroef cavitatie.

Schroef cavitatie levert een grote bijdrage aan de akoestische onderwater signatuur van een schip. Tijdens het ontwerpen van de (marine)schroef wordt hier dan ook rekening mee gehouden, naast andere aspecten zoals rendement en sterkte. Dit heeft reeds geleid tot een toename van de cavitatie inceptie snelheid in vlak water. Echter, uit ware grootte metingen is gebleken dat werkelijke dienstomstandigheden een aanzienlijke invloed hebben op het cavitatie gedrag van scheepsschroeven, en dus op de akoestische signatuur van een schip.

Om de tijd dat een schroef in dienstomstandigheden cavitatie-vrij kan opereren te vergroten is er in dit project voor gekozen om een op dit regeldoel toegespitste voortstuwingsregeling te ontwikkelen. Deze regeling is eerst getest in een simulatie omgeving, voordat hij op ware grootte is getest. Het gebruik van een simulatieomgeving heeft vele voordelen. Echter, een groot nadeel is dat zo'n simulatiemodel gevalideerd moet worden voordat het gebruikt kan worden voor het maken van voorspellingen. Dit laatste is in het bijzonder van belang wanneer het model ingezet gaat worden voor het ontwerp van een (sub)systeem.

Om de validiteit van het model te vergroten en te beoordelen is gebruik gemaakt van een systematische modelleer-, verificatie-, kalibratie- en validatiecyclus. Pas nadat de validiteit gekwantificeerd is en voldoende is bevonden, is het model gebruikt voor het ontwikkelen van een voortstuwingsregeling.

Bij het regelen van een scheepsvoortstuwingsinstallatie met een verstelbare schroef heeft men in principe de vrijheid om te kiezen uit een groot aantal schroefspoed-astoeren combinaties, die allen leiden tot eenzelfde scheepssnelheid. Door deze vrijheidsgraad te benutten kan men, naast de scheepssnelheid, een tweede doel nastreven. In de zoektocht naar een tweede te regelen (cavitatie gerelateerde) variabele is de invalshoek van het bladprofiel een belangrijke speler gebleken. Echter, in het geval van een propeller is deze invalshoek niet eenduidig te definiëren omdat elke bladsectie een eigen instroom en spoedhoek heeft.

Desalniettemin wordt er in dit onderzoek een effectieve invalshoek met bepaalde gewenste eigenschappen voorgesteld, die representatief is voor alle secties van de propeller.

Om deze effectieve invalshoek aan boord te schatten en te regelen is het nodig om de instroomsnelheid in de schroefschijf continue te meten of te schatten. Hiertoe is een instroomsnelheidsschatter, gebaseerd op meting van stuwkracht, ontwikkeld en getest.

Om de geschatte effectieve invalshoek constant te houden is er een eenvoudige regelaar ontwikkeld, die uitvoerig is getest in de simulatieomgeving. Middels parameter-studies zijn de initiële instellingen van de regelaar bepaald. Tevens is via deze studies onderzocht hoe, door parameterwijzigingen, het gedrag van het scheepssysteem doelmatig en snel aan boord aangepast kon worden wanneer dit nodig zou blijken gedurende de ware grootte proeven.

Om de prestatie van het nieuwe voortstuwingsregelsysteem te verifiëren zijn in februari en maart 2008 ware grootte proeven uitgevoerd aan boord van het M-fregat Hr. Ms. Van Galen. De proeven zijn in het Caraibische gebied uitgevoerd waar het schip destijds gestationeerd was.

De belangrijkste verbetering van het cavitatiegedrag is bereikt bij de acceleratie en deceleratie proeven. De geforceerde overbelastingsproef toonde aan dat overbelasting van de motor werd voorkomen zonder prestatieverlies van de installatie. De zeegangs test liet slechts een kleine verbetering van het cavitatiegedrag zien, hoewel verdere verbetering mogelijk wordt geacht. De kwaliteit van de metingen tijdens de draaicirkel proeven is slecht. Dit is veroorzaakt door de aanwezige golven, en door een te hoog gekozen aanvangssnelheid van het schip. Beide aspecten bemoeilijken een eerlijke vergelijking van het cavitatiegedrag in een draaicirkel tussen het bestaande en het nieuwe voortstuwingsregelsysteem.

Alhoewel het gevalideerde simulatiemodel voornamelijk gebruikt is voor de ontwikkeling van de nieuwe regeling, kan het ook gebruikt worden voor vele andere doeleinden. Aan de ene kant kunnen er op andere regeldoelen toegespitste voortstuwingsregelingen mee ontwikkeld worden. Aan de andere kant kan het gedrag van het scheepsvoortstuwingssysteem nader onderzocht worden zonder enige wijziging aan het model aan te brengen. De mogelijkheid om een nagenoeg ongelimiteerd aantal simulaties uit voeren is hierbij van groot belang. Enige voorbeelden van ”overige toepassingen” van het simulatiemodel zijn uitgewerkt.

Acknowledgements

This PhD-research has primarily been made possible by the sponsorship of the Netherlands Defence Academy (NLDA), for which I am thankful. Besides the financial contribution, the NLDA also made available the controller hardware that was essential for the execution of the full scale trials.

The full scale trials including background research were made possible by a joint project group consisting of the Royal Netherlands Navy (RNLN), Maritime Research Institute Netherlands (MARIN), Wärtsilä Propulsion Netherlands (WPNL), IMTECH, Defence Research and Development Canada (DRDC) and the Royal Australian Navy (RAN).

During the past few years many people made this project to what it finally has become. It would be impossible to mention all that have contributed. There are however few people that I would like to mention explicitly here.

On the organisatory field I would like to thank Peter van Terwisga, who initiated the joint project, and was the project manager during the first year. The role of project manager was taken over by LTZT1 Paul Schulten, who managed the greater part of the project, and participated in one of the preparatory full scale trials. His role was taken over by Michèle Nieuwenhuis, who was involved in the hectic preparations of the final trials. The final project manager was Joop van Son, who was involved in the finalization of the project.

Although the formal role of project manager was often handed over, there was one constant force that ensured continuity: during the four years Bert Koops (MARIN) never failed to be involved, both in organizational and in technical issues.

Both during the on-shore preparations and during the various trials the help of André Marinus and Ton Bruinhout of the Navy Dockyard (Marine Bedrijf) was indispensable. Together with LTZT2OC Fimme Hilverda (Naval Operational Command) they came first, left last, and in the meanwhile never stopped nor gave up. Their input and good spirit cannot be emphasized enough.

During the various full scale trials I often witnessed the flexibility and expertise of the crew of HNLMS van Galen. Despite all setbacks, overtime and hydraulic oil, their professional skills made the trials possible. Although my gratitude goes out to the complete crew, I am particularly thankful to SGTMJR Jan Mosterd, LTZT2OC Peter Steentjes and LTZT1 Rick Fransbergen. Furthermore I am grateful for the help of LTZT1 Danny van den Bosch during the first preliminary trial onboard HNLMS van Amstel. I also thank all VAF, WPNL, IMTECH and MARIN participants of the various full scale trials for ”walking the extra mile”.

I am thankful for the input and patience of professor Van Terwisga. I can only hope that the chapter and our discussions on the importance of uncertainty analysis of cavitation inception predictions and observations will contribute in that direction.

Finally I would like to thank professor Stapersma for his seemingly never ending enthusiasm, involvement and energy. Inspiration often came from our inspiring Friday-afternoon brainstorm sessions, which helped me to stay enthusiastic during the inevitable ”calms” in a four year research project.

Curriculum Vitae

Arthur Vrijdag was born on the 12th of July 1979, in Hellevoetsluis. There he went to secondary school "GSG Helinium", where he received his VWO diploma in 1997. After finishing the propaedeutic year of the Maritime Officer's (MAROF) education at Maritime Institute "De Ruyter" in Vlissingen in 1998, he became a midshipman at the Royal Netherlands Naval College in Den Helder. In 2001 he received his officer's rank, and was further trained in practical watch officer skills onboard the M-frigate HNLMS van Nes.

After this, he continued his studies both at the Naval College and at the Faculty of Marine Technology, Delft University of Technology. He wrote his thesis titled "Cavitation Inception in Operational Conditions" at MARIN, after which he received his Master of Science degree in 2004. After that he shortly taught fluid mechanics at the Netherlands Defence Academy (former Royal Netherlands Naval College). In May 2005 he started his PhD research in Delft, of which the results are presented in this dissertation.